DOCTORAL THESIS

Architecture, Building, and Construction Engineering Department

Politecnico di Milano

2020

Title

Recycled Rubber-Fiber Reinforced Elastomeric Isolators for Seismic Protection in Developing Countries

PhD Candidate

Ahmad Basshofi Habieb

Supervisors
Prof. Gabriele Milani

Co-Supervisors
Prof. Virginio Quaglini
Prof. Marco Valente

The present doctoral thesis is dedicated to the people of Indonesia who live with high risk of devastating earthquakes.

It was finally submitted in a very difficult time in all around the world, particularly in Italy, due to Covid-19 pandemic.

Together, we will win!

Acknowledgements

My distinguished thanks go to Professor Milani G., who gives me valuable supports and constructive advice during my PhD period. I am grateful to him, for giving me the opportunity to become part of his research team. Special thanks to all the research team member; Shehu R., Tiberti S., Stockdale G., Bertolesi E., and Silva L. C., who support my work and create a friendly atmosphere in the research team.

The present work has been developed at the Department of Architecture, Built Environment and Construction Engineering, Politecnico Di Milano. I would like to address my special thanks to all the professors, particularly to Professor Quaglini V. and Professor Valente M., who kindly supervised my work. To my colleges in the PhD student room, with whom I have shared moments of joy, challenges, surprises, and achievements. I am also very grateful for the genuine friendship.

To my beloved small family who accompanied me during my study in Milan, nine months old Gazali and his mother, Rosalinda H.M., I am very grateful for having you two in my life, giving much more energy and joy in many stressful and difficult times. Many thanks to my parents in Indonesia who support me always with great motivation and inspiration.

<div align="right">

Ahmad Basshofi Habieb
Politecnico Di Milano
March 15, 2020

</div>

Table of Contents

P

PREFACE

Numerous earthquakes in the past often caused severe damages to infrastructures and loss of life. The conditions are becoming worse since many high-seismic zones are located in developing countries such as Indonesia, where a huge number of buildings are not designed properly and do not have adequate seismic protections. In many cases of earthquake events, low class housing experienced severe damages, causing many casualties. These facts justify the importance of conceiving a low cost seismic protection system for low-class housing, generally applicable in all those developing countries subjected to strong earthquakes.

Poor reinforced concrete and masonry buildings that are susceptible to shear loads are commonly found in developing countries, particularly in rural areas. Indonesian non-engineered construction mostly consists of masonry structures confined or unconfined. It is therefore the preferred material in the countryside, which typically consists of clay bricks bonded by mortar joints. Without resisting moment frames, masonry can withstand seismic loads only thanks to the in-plane shear and flexural strength of piers and spandrels, but unfortunately, conventional brick masonry exhibits poor tensile strength, so its capacity to carry horizontal loads is considerably lower than standard reinforced concrete and steel frames.

In general, in order to reduce the damaging effects on the building due to earthquakes, some techniques commonly used are; (a) increase the seismic-resistant capacity of the structure (b) involve bracing system (c) use of added damping system and (d) reduce the seismic demands on the structure by incorporating the base isolation system. The seismic base isolation is considered as the efficient seismic protection system. Generally speaking, the base isolators can be classified as frictional and elastomeric isolators. Some types of elastomeric base isolators have been developed by researchers around the world in the last three decades, e.g imposing leads and high damping rubbers.

Since the cost of commercial elastomeric isolators is relatively expensive due to the need for steel reinforcement and thick steel plate supports, and they are not so suitable for common building such as housing in developing countries, scientific works in the field of low-cost elastomeric devices have been conducted in the last years. Fiber reinforced elastomeric isolator (FREI) are nowadays considered as a promising device because it costs significantly less thanks to the absence of steel reinforcements.

This PhD thesis presents a series of experimentations and comprehensive numerical modeling on fiber reinforced elastomeric isolators (FREIs) mainly made from recycled

rubber from industrial waste, aiming to drop down the cost of the isolator device. Several technical detailing are proposed so that the isolation system works effectively for the isolation of low resistant buildings such as masonry housing. The proposed FREI system is mainly applied in unbonded condition to improve the deformability of the isolation device. The study presents several promising performances of the proposed isolation system with favorable production cost.

Chapter
1

Introduction

It is an unfortunate fact that many developing countries with huge population are located in high seismicity regions. As many residential or public buildings are not designed properly nor sufficiently protected against earthquakes, the number of deaths is always feared high when earthquakes strike. For instance in Indonesia, almost every year, earthquakes take place in various zones of that archipelago. In the last two decades, severe earthquakes were recorded causing thousands of casualties [1]. In December 2004, an earthquake with large magnitude 9.3 Richter scale (RS) struck Aceh and Northern Sumatra, followed by a huge tsunami wave, killing 170.000 people. In Java island, the most important land in Indonesia, an earthquake 5.0 RS hit Jogjakarta city in May 2006, causing 6.500 dead, and 1.115 people were killed due to Padang earthquake in September 2009. Recently, in August and September 2018, two big earthquakes stroke Lombok Island and the city of Palu, causing 555 and more than 2000 casualties, respectively.

However, despite the impact of regional economic and development, prevention and mitigation for the future earthquakes seem not done much. Many casualties caused by the collapse of housing and buildings that are not designed properly [2] (see Fig. 1.1). This fact justifies the importance of conceiving a low-cost seismic protection system for residential housing, generally applicable in all those developing countries subjected to strong earthquakes.

Poor reinforced concrete and masonry buildings that are susceptible to shear loads are commonly found in developing countries, particularly in rural areas. Indonesian non-engineered construction mostly consists of masonry structures confined or unconfined. It is therefore the preferred material in the countryside, which typically consists of clay bricks bonded by mortar joints. Without resisting moment frames, masonry can withstand seismic loads only thanks to the in-plane shear and flexural strength of piers and spandrels, but unfortunately, conventional brick masonry exhibits poor tensile strength, so its capacity to carry horizontal loads is considerably lower than standard reinforced concrete and steel frames.

Generally, in order to reduce the damaging effect on building due to earthquake, some techniques commonly used are: (a) increase the seismic-resistant capacity of the structure [3][4]; (b) involve bracing system [5][6]; (c) use of added damping system [7][8]; and (d) reduce the seismic demands on the structure by incorporating the base isolation system [9][10][11][12]. Increasing a seismic-resistant capacity can be done by increasing the dimension of structures and upgrading the quality of materials used to

achieve the expected target strength. Undoubtedly, this attempt will increase the total cost of structures significantly. The second option, bracing system, enhances the horizontal stiffness of the building and can localize the plastic hinge to improve the seismic behavior of structure, but does not decrease the seismic force on the structures. For an economical reason, it is not suitable to implement the bracing system for ordinary residential buildings. Use of damping devices can be a solution to reduce the seismic force at the upper structure but increase the overall cost significantly, so cannot be adopted for common buildings.

In the last three decades, the interesting topic is towards the reduction of seismic demand rather than increasing the seismic resistant capacity of the structure. The seismic demand of structure can be reduced by installing the devices having a low horizontal stiffness to provide a certain degree of flexibility in the structure. This device is well-known as the seismic base isolator, which is considered as the most efficient device. Some types of base isolators have been developed by researchers around the world. Elastomeric isolators and sliding isolators are the well-known seismic isolation devices used for constructions.

Fig. 1. 1. Severe collapses of residential building in Yogyakarta, Indonesia, after an earthquake in May 2006 [3].

The elastomeric isolator is considered as the most widely used devices to isolate the seismic energy propagation in the building. Applying the elastomeric isolator can restore the horizontal seismic force and does not cause residual displacements of the isolated building after an earthquake. The elastomeric isolators are produced in different types such as laminated rubber bearings, lead rubber, and high damping rubber bearings. This

technology satisfies well the need of seismic isolation for certain kinds of buildings and remains an attractive research topic among the construction engineers.

Since the cost of commercial elastomeric isolators is relatively expensive and not so suitable for common building such as housing, particularly in developing countries, researches in the field of low-cost devices should be conducted. Therefore, in this thesis, a research work called experimental and analytical studies on low-cost elastomeric bearings is carried out. The objective of the study is to develop an effective but low-cost rubber isolation system and guidelines of its optimal application for housing in developing countries, particularly masonry.

1.1. Base isolation system

The damage potential on an earthquake is basically due to the lack of harmony between the fundamental periods of vibration of the majority of structures and the frequency of the ground motions. During a seismic event, the structure acts as vibration amplifier, magnifying the acceleration at the upper-structure. This amplification may result in severe damage to structural and non-structural elements of the building, and in the worst case, the collapse of the structure. Seismic base isolation is an effective technical solution to reduce the vulnerability of new and existing structures. Indeed, it can mitigate the negative impact of an earthquake, because it shifts the period of the structure in that range of the spectrum where the spectral acceleration is small. This method isolates the propagation of seismic energy from the ground, protecting the upper-structure from extensive damage. Interstory drifts can be significantly reduced by the presence of base isolation devices, see Fig. 1.2. The isolation is achieved by decoupling the upper-structure and foundation, and putting the base isolators in between.
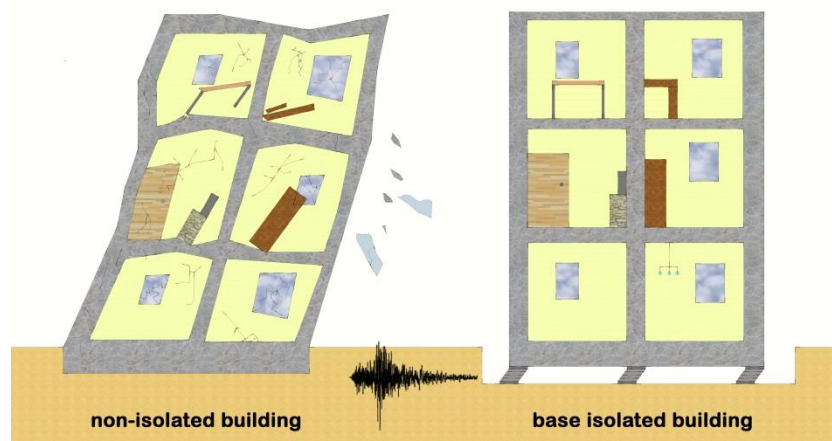
Fig. 1. 2 A basic concept of base isolation, reducing significantly the inter-story drifts of the building. (left) without isolation, (right) with isolation

Base isolation system can be provided by inserting elastomeric devices such as rubber or sliding surfaces between foundation and upper-structures to decouple the

structure from ground motions. These types of base isolation will be briefly explained in this section.

1.2.   History of base isolation system

There is a unique history behind the idea of protecting building structures from severe damages due to earthquake through base isolation system. Instead of a structural engineer, the first documented innovative base isolation design belongs to an English medical doctor, proposing a construction of building on a layer of fine sand, mica, and talc, which allow the building to slide in case of strong earthquake [13][14].

Friction base isolation system apparently has been applied for housing over hundred years ago. Some traditional house, even in developing countries, sometimes have sliding interfaces between columns and foundation. Observation has been conducted on Indonesian traditional housing [15][13]. Some houses were built by not fixing the timber columns to the foundation, Fig. 1.3, allowing the upperstructure to slide during earthquake motion and can reduce the damage of the structure.

The base isolation system was first recommended as a seismic-resistant design strategy by the Italian government after the great Massimo-Reggio earthquake in 1908, which killed about 160.000 people due to collapses of unreinforced masonry buildings. Almost all of the construction of this type were collapsed **Error! Reference source not found.**. The commission formed by Italian government at that time proposed two options in earthquake-resistant design methods; (1) isolate the building by providing a sand layer in its foundation or using roller under the column to allow the horizontal movement, (2) construct a fixed base design with height limitations and a lateral force design requirements.
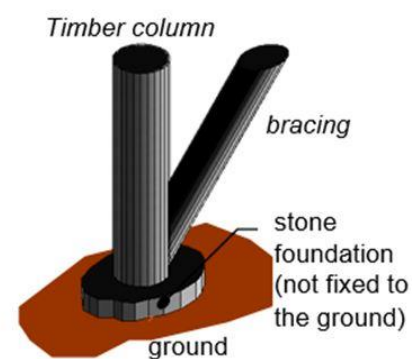
Fig. 1. 3. Sliding foundation of a timber traditional house in Nias Island, Indonesia [8].

Concerning the elastomeric base isolators, they have been used since the 1950s as thermal expansion bearings for highway bridges and as vibration isolation bearings for building in severe acoustic environments. Steel reinforced elastomeric isolators have been used in the early 1980s. The flexibility of rubber compounds in the

isolator is the main principle of this device. Therefore it has considerably low horizontal stiffness.

Before becoming popular as earthquake isolation system, rubber firstly used on building as the vibration isolator. The first construction isolated from vibration using rubber is the apartment Albany Court in London, completed in 1966. The other important buildings in the United Kingdom are also isolated to protect some sensitive devices which need extremely high precision such as in laboratories and hospitals. Vibration isolation is also essential equipment for concert hall building to avoid noises from external environments, like vibration from underground trains[17].

J.M Kelly, a Professor Emeritus at the University of California at Berkeley in 1971 started his comprehensive research in the field of energy-dissipating devices to be used in earthquake-resistant structures [15]. He led the way in experimental and analytical investigations of seismic-isolation rubber bearings, conducting many pioneering studies of seismically isolated structures . In testing hundreds of bearings, he achieved numerous advances, including the application of high-damping rubber for seismic isolation, used many buildings and bridges around the world. Most of his research discuss the elastomeric isolators reinforced by steel lamina. Through some developments of the isolator design, manufacturers of elastomeric isolators produce different type of modern isolators.

1.3. Elastomeric isolators

Some commercial base isolators mainly from rubber (elastomeric) materials have been introduced in the last two decades to protect buildings from vibration and earthquake. Buildings, bridges, and nuclear power plants often require the application of rubber base isolators. Typically, it is constituted by several layers of rubber (pads) and steel or fiber lamina interposed by two continuous pads, having the role of limiting vertical deformability. At the same time, such isolator exhibits good deformation capacity in the horizontal direction when subjected to a seismic load, thanks to the small shear stiffness of the pads. This system can isolate the energy transmission of the earthquake from the foundation to the upper-structure, see Fig. 1.4. Some recent researches [18] in the field employed glass fiber laminas instead of thin steel plate to make the cost of the isolator even cheaper sometimes in combination with used recycled rubber, from tires or industrial waste to further drop down costs [21][20][22].

(a)   (b)

Fig. 1. 4 Elastomeric isolators applied at the ground level of earthquake-resistant buildings, source: www.ibec.or.jp/jsbd/AR/tech.htm.

An effective seismic elastomeric isolation shall satisfy the following main function: (1) Performance under all service loads, vertical and horizontal; shall be effective as conventional structural bearings, (2) Provide enough horizontal flexibility in order to reach the target natural period for the isolated structure, (3) Re-centering capability after the ground motion of a severe earthquake so that no residual horizontal displacement can downgrade the serviceability of the structure, and (4) Provide an adequate level of energy dissipation or damping ability in order to control the displacement that could otherwise damage other structural members.

Horizontal stiffness is determined by the hyperelastic behavior of rubber material, and the ability of damping can be improved by engineering the mixture technology of rubber compound during fabrication [22]. The rubber typology, the compound, the thickness, and the process of vulcanization of the rubber pads are crucial issues for obtaining desired isolator performance. In fabrication processes for conventional isolators, the compounded rubber sheets with the interleaved steel plates are put into a mold and heated under pressure for a couple of hours to complete the manufacturing process.

Rubber pads can be produced from natural or artificial rubber. Natural rubber (NR) is the most used, but artificial rubber seems promising for the fabrication of isolators since NR is vulnerable from quick aging and its industrial production capability is limited. Synthetic rubber is usually neoprene. Less frequently it is ethylene propylene diene monomer (EPDM) or a nitrile-butadiene rubber-EPDM (NBR-EPDM) blend vulcanized with or without an increasing amount in weight of carbon black[24].

1.3.1. Low damping rubber bearing (LDRB)

Low-damping rubber bearing (LDRB) is the first elastomeric isolators which are used to mitigate buildings from earthquake effect. Rubber compound in LDRB is produced without any particular fabrication process. This type of bearing has the equivalent damping ratio within the range of 2% to 5%. LDRBs produced from natural and or synthetic rubber are used in combination with supplemental damping devices, such as lead or steel bars and viscous dampers or frictional devices. The

isolators should be placed on thick steel plates as supports at top and bottom of isolators, bonded by heating and pressuring processes. The steel lamina between rubber layers improve the vertical stiffness of the rubber pads and prevent the bulging of the rubber without affecting the horizontal stiffness of the system.

Fig. 1. 5. School building in Skopje isolated with blocks of low-damping natural rubber without reinforcements, causing the rubbers swell sideways [10]. In the last Fig., an isolator was replaced by a new high-damping rubber, next to to the original one

Low damping rubber for earthquake isolation is first used in 1969 for an elementary school building in Skopje, Yugoslav Republic of Macedonia [25]. It is a three-story concrete framed structure that relies on large block of low-damping natural rubber without any reinforcement. Thus, the vertical loading due to the weight of structure causes the rubbers swell sideways, see Fig. 1.5. Consequently, the horizontal and vertical stiffness of the rubber are about the same. These unreinforced bearing are not recommended anymore for isolation design. More recent examples of isolated buildings use multilayered rubber bearing.

1.3.2. Lead-plug rubber bearing (LRB)

The most significant advance in damping came in the 1970s with the presence of lead-plug down the center the isolator. In shear, the lead yields at the relatively low stress of 10 MPa and behaves approximately as an elastic-plastic solid. A reasonable size insert of about 100 mm in diameter is required to produce the need of plastic damping force of about 100 kN. Then, at room temperature when lead is plastically deformed, it is being 'hot worked' and the mechanical properties of the lead are being continuously restored by the interrelated processes of recovery, recrystallization, and grain worth which are occurring simultaneously. Plastically deforming lead at room temperature is equivalent to plastically deforming steel at a temperature of greater than 450°C [26].

Fig. 1. 6. Detail of lead rubber bearings (LRB) (source:http://www.oiles.co.jp), and the William Clayton Building in New Zealand isolated with LRB.

This system has been recommended worldwide for isolation of buildings and bridges. It was first used in New Zealand in the William Clayton Building, completed in 1981, see Fig. 1.6. The system effectively results in a nearly rectangular hysteresis loop thanks to the lead on to the linear spring characteristic of the rubber, with consequent absorption of earthquake energy, and control of oscillations [27].

A study reported in [28] investigates the effect of lead rubber bearing (LRB) isolator and ground motion characteristics on the response of seismic isolated bridges. Several optimum LRB parameters were proposed in order to maximize the performance of the isolation system against different earthquake types.

The LRB isolation system presents a temperature-dependant behavior. A numerical study was conducted in [29] to predict the temperature rise of the lead core and the reduction in characteristic strength and energy dissipation history of lead rubber bearings subjected to cyclic motion. On the basis of the presented results, it is concluded that testing at quasistatic conditions (as often done due to limited availability of high-speed testing machines) results in a lesser increase in the lead core temperature and in a lesser reduction of dissipated energy per cycle and characteristic strength of lead-rubber bearings. This difference in reduction in EDC is dependent on the geometry of the bearing, the conditions of testing, and the number of cycles imposed.

In case of high-rise isolated buildings, tensile stresses in laminated rubber bearings can create expandable cavities and cause damage to spread inside the rubber, which may lead to inestimable impact on the mechanical performance of the isolators. A new type of tension restraining device to be used in conjunction with LRBs is proposed in [30] which can keep the tensile stress in the rubber under the limit value, while adapting to horizontal deformation of the rubber bearing by interactionand sliding between the components of the device, see Fig. 1.7 and 1.8. The results indicate that the tension-restraint device can help protect the rubber from large tensile stresses and improve the tensile resistanceof the isolator, while having little influence on the horizontal shear behavior of the bearings and their effect on the global behavior of the structure.
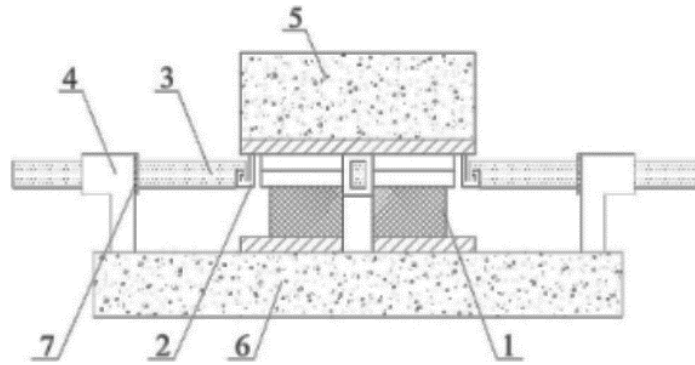
Fig. 1. 7. Isolation bearing with tension-restrain device: (1) isolation bearing; (2) shacke bar; (3) active part; (4) fixed part; (5) upper column; (6) bottom column; (7) damper.
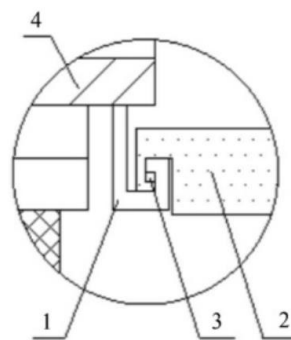
Fig. 1. 8. Connection details between shackle bar and active part: (1)Shackle bar; (2) active part; (3) Gap; (4) upper plate.

A study carried out on [31] to investigate the effect of thermal aging on the mechanieal properties of laminated lead rubber bearings (LRB) in accelerated exposure condition of 70°C temperature for 168 hours. The compressive-shear test was carried out to identify the variation of compressive and shear properties of the rubber bearings before and after thermal aging. In contrast to tensile strength and elongation tests, the hardness of rubber materials showed the increasing tendency dependent on exposure temperature and period. Compressive stiffness of LRB decreased as an about 2 to 3% after thermal aging. In the compressive-shear properties test, shear modulus and equivalent damping ratio of all specimens decreased and the change in shear modulus of LRB appeared to be clear. In the 50 times cyclic loading test, shear modulus of LRB and NRB decreased as a 2.7 % and 3.6%, respectively and it was found that NRB was much more deteriorated than LRB in thermal exposure condition because the change of equivalent damping ratio of LRB is 1.9% and NRB is 10.9%.

In the literature [32], non-destructive inspection of a lead rubber bearing using ultrasonic wave is demonstrated. Two kinds of miniature LRB models are prepared, one model has normal lead damper, the other has abnormal one. The proposed method using ultrasonic waves successfully identify the internal states of LRB. The feature vectors are created by calculation of second power average of the amplitude. These vectors are used for pattern recognition. The accuracy of the pattern

recognition is significantly enhanced if the components that have strong correlation with the conditions are selected.

1.3.3. High-damping Rubber bearing (HDRB)

The higher performance of rubber isolators can be achieved by increase the ability of energy dissipation, represented by damping ratio. The damping can be increased by adding extra-fine carbon black, oil, or resins, and other fillers. The damping is increased to levels between 10 to 20% of the critical damping, at 100% shear strain range.
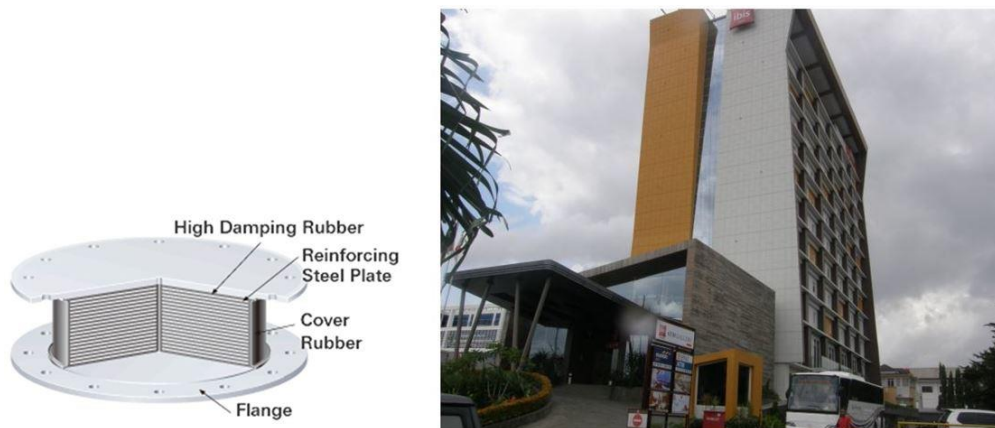
Fig. 1. 9 Detail of high-damping rubber bearings (HDRB)
source:http://www.bridgestone.com/products), and the Ibis Hotel in Padang, Indonesia isolated with HDRB.

Although HDRB is considered as an effective isolation device, the utilization of elastomeric isolators such as HDRB in developing countries such as Indonesia is still few due to the considerably high invesment cost and lack of experiences. The demonstration building isolated by high-damping natural rubber bearing in Indonesia is located in the southern part of West Java, about 1 km southwest of Pelabuhan Ratu. This project was completed in 1994, funded by The United Nations Industrial Development Organization (UNIDO) in order to introduce base isolation technology to developing countries. The building is a four-story moment-resisting reinforced concrete structure, accommodating eight low-cost apartment units. The isolation bearings are located at the ground level and are connected to the upperstructure using innovative recessed end-plate connection, unlike the more usual bolted connection. This use of recessed end-plate connection decreases the cost of isolation system and is very easy to install [14]. A recent building isolated with HDRB in Indonesia is the Ibis Hotel with 12-story in Padang, completed in 2013, Fig. 1.9.

Heat-mechanic interaction behavior of high damping rubber bearings was investigated in the literature [33]. For the elastomeric bearings such as LRB and HDRB, the seismic energy they absorb is fundamentally transformed into thermal energy, so heat is generated causing higher temperatures in the lead plug or in the high damping rubber. Dynamic loading tests were conducted using full-scale and

reduced-scale rubber bearing specimens under large deformation conditions assuming long-period ground motion to ascertain the effects of increased temperatures on the mechanical behavior of rubber bearings. In a test using a reduced-scale HDB with diameter of 500 mm, sine wave input caused the yield load to drop to about 80%. The temperature inside the rubber rose uniformly by about 30 °C. Since HDBs absorb energy by generating heat throughout the rubber, the temperature increase inside the rubber was smaller than that of the LRB, and reductions in the yield load were also smaller.

A literature in [34] attempts to reveal the ageing behavior of natural natural rubber (NR) and high damping rubber (HDR) materials used in bridge rubber bearings. Using various degradation factors such as thermal oxidation, ultraviolet, ozone, low temperature ozone, salt water and acid rain, a series of environmental accelerated ageing tests were conducted to investigate the ageing characteristics at the material level. The artificial weathering tests last from 4 days to more than 300 days. Generally all exposure types result in a degradation process, which is predominately oxidative in nature. It was found that the stresses corresponding to specific strains increase with ageing while the elongation at breaking point and the tensile strength both decrease. Such deterioration not only weakens the ability of the bridge bearings to isolate the superstructure and absorb energy, but also reduces the load bearing safety factor. It is necessary, therefore, to take into account the deterioration of rubber bearing during the design and maintenance stages. Thermal oxidation is discovered to be the most significant degradation factor. The stress which applies to the 100% strain (M100) can be 200% higher after a long time, than the stress at time zero.

Cyclic behaviors of three types of high damping rubber bearings under multiaxial loading state were studied, as reported in the literature [35]. First, the characteristics of the restoring forces of these bearings in small amplitude are investigated. The experimental results show that the equivalent stiffness of high damping rubber bearings is increased and the damping ratio is decreased as the increase of the amplitude. In addition, the restoring force of a lead rubber bearing is found to highly depend on the vertical load. Second, a triaxial loading experiment, in which two-directional displacement paths are given to the bearings under a constant vertical load, is conducted. The experimental results indicate that horizontal restoring forces possess the coupling effects. The equivalent stiffness and damping ratio of high damping rubber bearings and natural rubber bearings are increased due to this coupling effect in comparison with the biaxial loading case, while the lead rubber bearing shows a slight decrease in them. Hence it is understood that the effects of the triaxial loading are not negligible and these have to be considered in a rational and reliable design.
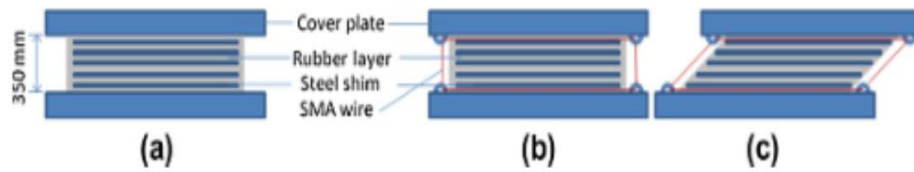
Fig. 1. 10 Description of the isolation bearing (a) HDRB; the rubber layers with high damping properties are vulcanized by steelshims, (b) SRB in un-deformed condition and (c) SRB in deformed condition.

In order to increase the energy dissipation of the isolation system, shape memory alloy (SMA) wires are proposed in the literature [36] to be combined with the HDRB device, see Fig. 1.10. Two types of SMA wires, such as Ni–Ti and Cu–Al–Be, are used in fabricating the combined isolation bearings. The numerical results have revealed that SMA-based isolation bearings (SRBs) satisfactorily restrain the residual displacement of the bridge deck and the displacement of the bridge pier for moderate earthquakes; however, for strong earthquakes the residual displacements and the pier displacements are not restrained by incorporation of Ni–Ti and Cu–Al–Be based SMA alloys in the isolation bearings. For bridge deck and bearing displacements, the bridge with HDRB has resulted in less response compared to those of SRB-1 and SRB-2 under both types of earthquakes. Similar trend is also observed in the case of deck accelerations. The constitutive properties of both types of SRBs have significant effect on the seismic responses of the system.

Irreversible deterioration in the base isolation system exposed to high temperatures during a fire has raised concerns about the reliability of elastomeric isolators. In literature [36], residual seismic load capacity of fire-damaged lead rubber bearing (LRB) and high damping rubber bearings (HDRB) of base-isolated buildings was investigated. A 200°C isotherm method is used to evaluate reduction of the mechanical properties of the fire-damaged isolators. Fire loading before earthquake confirms reduction factors of the effective shear and axial stiffnesses and primary and secondary shape factors for LRBs higher than for HDLRBs, due to their lesser initial diameter.

1.3.4. Fiber reinforced elastomeric isolator (FREI)

Commercial isolator devices like steel reinforced elastomeric isolators (SREIs) have been widely employed for protection of buildings, nuclear power-plant, and bridges. But such types of isolators tend to be too expensive due to the need of thick steel plates for their supports and the high-energy consumed for manufacturing process. And therefore it is not suitable for massive usage on low-class buildings in high seismic zones, particularly in developing countries. Potential low-cost of isolator devices exist if the steel plates are substituted with other materials having approximately the same elastic behavior as steel.
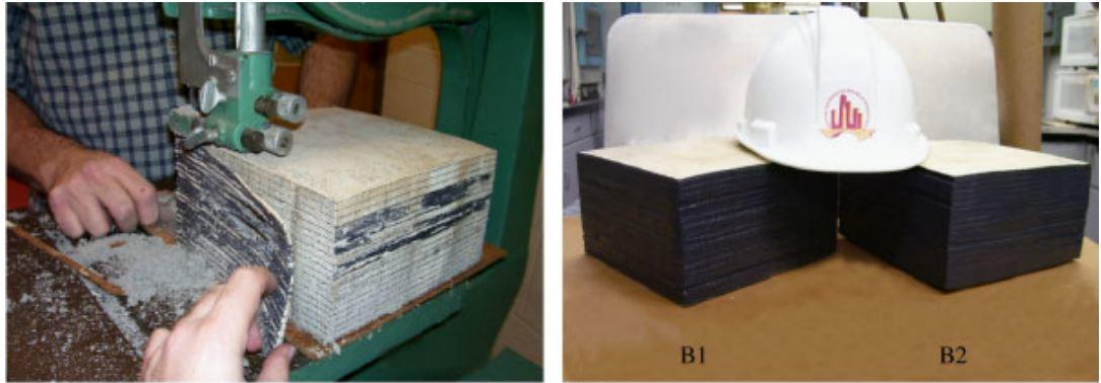
Fig. 1. 11. Prototypes of newly conceived fiber reinforced elastomeric isolators, tested in McMaster Univerity by **Error! Reference source not found.**.

Fiber reinforced elastomeric isolator (FREI) is a relatively new type of elastomeric isolator, as seen in Fig. 1.11. Instead of using steel lamina, thin fiber layers are utilized for the vertical reinforcement. Compared with SREIs, FREIs have considerably lower weight and can be manufactured through cold vulcanization. The advantage of this isolator type is that it can be fabricated without the thick end plates. FREIs can be applied on the structure in several methods, as illustrated in Fig. 1.12: bonded [38][39], unbonded [40][41][42][43], partially bonded [44], and friction (no-bonding between rubber and fiber layers). In the absence of thick steel supports, the isolators can be simply installed between the upperstructure and foundation without any bonding or fastening in an unbonded application. Thus, the shear load is transferred through the friction that is generated between the isolator and the structure surfaces. A possibility of unbonded application is a promising feature of the FREIs since the effect of rolling-over and friction may improve the dissipation energy of the isolators. The low-cost and easy application of FREIs allow engineers to introduce the possibility of non-expensive seismic isolation for low-class buildings in developing countries.
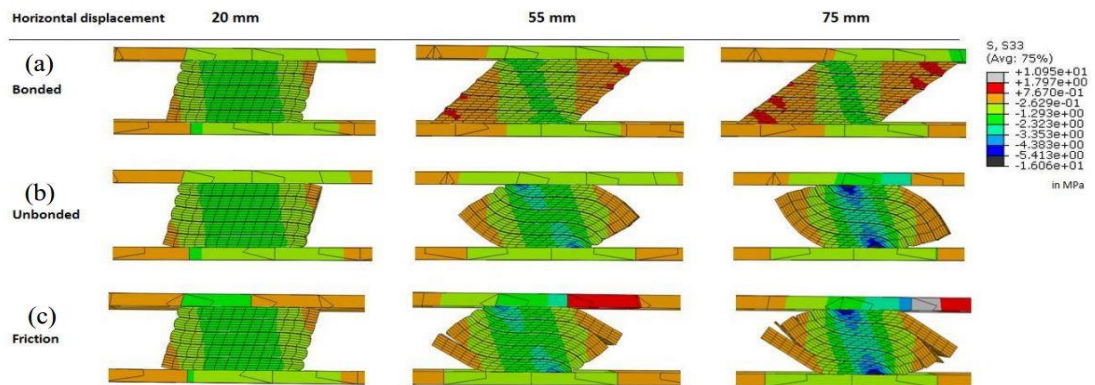
Fig. 1. 12. Three possibilities of fiber reinforced elastomeric isolators (FREIs) application: (a) bonded; (b) unbonded; (c) friction, and the deformation patterns.

Initial researches reveal that it is possible to achieve adequate vertical and horizontal stiffness in bonded FREIs. Researchers in **Error! Reference source not found.** carried out experimental works to investigate the behavior of square carbon FREIs using low damping natural rubber compounds in unbonded application, which

is considered as a new method of isolation systems. The unbonded application can result in a stable rollover lateral deformation, which reduces the horizontal stiffness and increases the efficiency of the bearing as a seismic isolation device. Comparing to the identical specimen but in bonded condition, the unbonded FREIs result in superior performance concerning the damping ability. A significant increase in the damping values of FREIs due to higher vertical pressure is a unique feature not found in SREIs. In attempt to lower the cost of FREIs, some researchers employed recycled rubber derived from tires or industrial waste [20]**Error! Reference source not found.**[21].

The first full-scale building prototype in the world isolated with unbonded FREIs is a two-story masonry housing in Tawang, India, see Fig. 1.13 [52]. This attractive research is aimed to develop suitable isolation methods for housing in developing countries. To achieve an optimal isolation using unbonded FREIs, the masonry structure must be equipped with elevated foundation beams to support the placement of the isolators.

In parallel, an experimental shake table test on masonry model isolated with unbonded FREIs was conducted as reported in [45]. Acceleration response amplification and peak response values of test model with and without base isolation system are compared for different intensities of table acceleration. Distribution of shear forces and moment along the height of the structure and response time histories indicates significant reduction of dynamic responses of the structure with unbonded FREI system. The results demonstrated that the base isolation system using unbonded FREIs can improved remarkably the seismic performace of the isolated unreinforced masonry structure.

Fig. 1. 13. The first prototype of masonry building isolated with unbonded FREIs in Tawang, India [52].

The sliding instability of the unbonded FREI system has been studied in [42]. The study describes the experimental study on the unbonded FREIs reinforced by bi-directional carbon fiber fabrics performed to investigate the static friction at contact surfaces. Friction behavior was analyzed in terms of isolator sliding with respect to the concrete sub- and super-structure. The tests revealed that, regarding the value of the applied compressive stress, uncontrolled sliding of the isolator can occur with the increase of the shear force. It is found that the minimum compressive stress 0.5 MPa should be applied to the unbonded FRI to avoid sliding instability of the isolators.

The roll-out instability of small size FREIs in unbonded applications was investigated in [46]. The study proposed a model for prediction of roll-out instability based on the applied forces equilibirium condition and on the ssumption that a triangular distribution for the compressive stress acts on the isolator. The model is developed considering that the isolator contact area varies with the applied displacement, and consequently the compressive stress vary. It was found that for equal levels of applied compressive stress, the roll-out displacement increases by increasing the specimen aspect ratio. For specimens with the same aspect ratio, by increasing the applied compressive stress, the roll-out displacement first increases and then decreases. Under dynamic testing, values of roll-out displacement are always higher than values obtained from quasi-static tests. The roll-out displacement values and the corresponding forces from quasi-static tests are therefore conservative as regards the phenomenon of roll-out instability.

1.4. Friction pendulum isolators

Providing sliding interfaces between the foundation and structure can eliminate the horizontal load transmission during an earthquake. This approach is based on the concept that the lower the friction coefficient, the less the shear load transmitted. In typical sliding isolator, two pure flat stainless steel plates or spherical surface and friction slider slide over each other during seismic excitation, see Fig. 1.14. To initiate sliding, the horizontal force should be more than frictional force of isolator. After cyclic horizontal loading, the friction isolator causes a residual sliding displacement, which is the drawback of this system. To deal with this problem, researchers develop pendulum-sliding isolator to reduce the residual displacement of the sliding system significantly. However, this isolation system is less popular than the elastomeric devices. Researchers in [53] adapt this system using low-cost materials to provide the frictional isolation for low-rise masonry housing in rural areas.
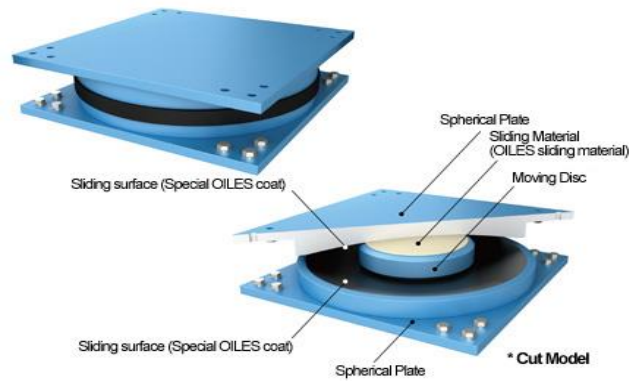
Fig. 1. 14. Detail of a commercial friction pendulum system, source:http://www.archiexpo.fr/prod/fip-industriale

In the literature [47], the thermal-mechanical response of a Curved Surface Slider isolator (or friction pendulum isolator) to cyclic loading was investigated through the implementation of a three-dimensional finite element analysis of the complete bearing. It was found that the temperature-dependent formulation of the bearing material allows to capture the self-limiting mechanism of frictional heating and to provide realistic predictions of temperature histories under high speed motion. The procedure predicts the change of the mechanical properties of the isolator during cyclic loading, confirming that decrease in stiffness and dissipation capacity of the sliding isolators during seismic excitation is a potential issue related to heating of the sliding surfaces.

An innovative uplift restraining friction pendulum system was proposed in [48]. Termed as XY-FP isolator, the new isolaiton device consists of two orthogonal opposing concave beams interconnected through a sliding mechanism that permits tension to develop in the bearing, thereby preventing uplift, see Fig. 1.15. The XY-FP isolator provides unique properties for a seismic isolator, including uplift or tension restraint, decoupling of the bi-directional motion along two orthogonal directions, and capability of providing independent stiffness and energy dissipation along the principal horizontal directions of the bearing.
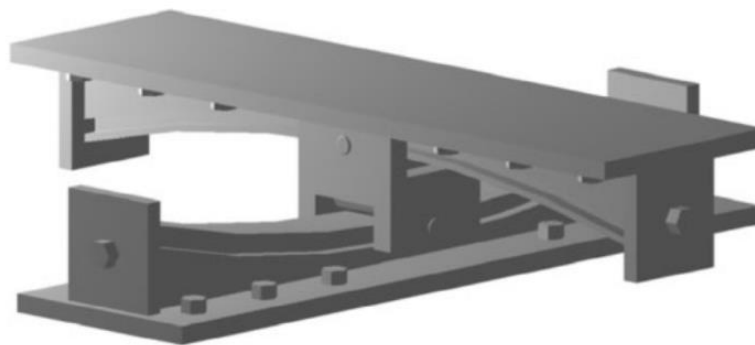
Fig. 1. 15. Three-dimensional view of the uplift-restraining XY-FP isolator.

In the literature [49], the restoring capability of double concave friction pendulum seismic isolation systems was investigated through shake table testing considering that non-negligible residual displacement may effect the serviceability of a base isolated structure. The study based on displacement control and seismic input experiments, performed under unidirectional motion. The study confirms that the maximum displacement d_{max} is mainly affected by the characteristics of the ground motion as well as tha PGA intensity. In all considered friction coefficient, the initial offset does not influence the maximum displacement when stronger eaqrthquakes occur. The results confirm the validity of the criterion dmax/drm > 0.5 proposed by [50] to ensure a good restoring capability of the FPS isolation system, where drm is the maximum static residual displacement. Such conclusions are in agreement with several previous investigations [51].

1.5. Application of seismic isolation system around the world

Up to 2013, according to the report in [16] more than 23.000 structures in the world are seismically protected using passive anti-seismic method, such as base seismic isolation (SI), energy dissipation system (ED), shape memory alloy devices (SMAD), or shoch transmitter units (STUs). They are located in more than 30 countries. The application of SI in some most active countries is reported in Fig. 1. 16 and Table 1. 1. The seismic isolation system is applied for various type of structures such as large buildings, houses, bridges and viaducts, and industrial structures. Japan so far is the leading country for the number of seismic isolation system; it is followed by China, the USA, Russia, and Italy (see Fig. 1. 17). However, it is clearly shown that the application of isolation system is still limited to developed countries.

There are numerous developing countries with high seismicity and huge population that left behind in terms of number of seismically isolated sructures such as, Indonesia, India, Turkey, Nepal, etc.. Indeed, the cost of commercial isolation system until now is considered expensive for massive application in those developing countries. In Indonesia for instance, where about 184 million inhabitans are at high risk of severe earthquakes, the number of seismically isolated buildings is less than ten. Only three of them are located in Jakarta, the Indonesian capital and business center. The application of base isolation system in this country was initiated in 1994 by the UNIDO-sponsored project to introduce base isolation technology to developing countries. A four-storey moment resisting reinforced concrete buildings located in the southern part of West Java, about 1 km southwest of Pelabuhan Ratu, was protected using 16 high-damping natural rubber bearings at the base floor level [15].
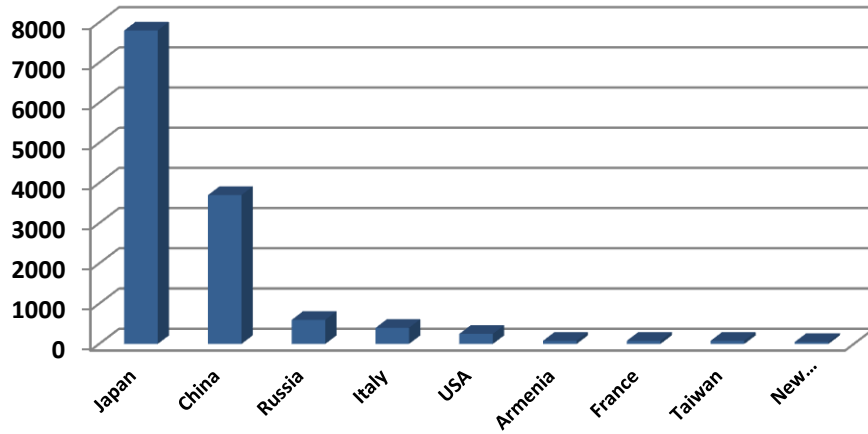
Fig. 1. 16 Numbers of seismically isolated buildings in the most active countries (data of September 2013)[16]

Table 1. 1 Application of anti-seismic systems [16]: n.a=no data

Country	Seismic isolation				Energy dissipation and other			
	Large buildings	Houses	Bridges	Industrial structure	Large buildings	Houses	Bridges	Industrial structure
Japan	3,000	5000	1000	some	1000	5000	n.a	n.a
China	4,000	n.a	400	50	500	n.a	200	50
Russia	600	0	100	-	8	0	100	0
USA	250	n.a	hundreds	some	hundreds	n.a	n.a	n.a
Italy	400	n.a	tens	3	tens	n.a	300	0
Taiwan	29	n.a	20	n.a	85	n.a	n.a	n.a
Armenia	43	2	10	0	3	0	0	0
New Zealand	15	0	3	2	2	0	1	2
Turkey	18	0	11	2	2	0	0	0

Most of SI systems rely on the use of rubber bearings [16], such as high damping rubber bearings (HDRBs), lead rubber bearings (LRBs), or low damping rubber bearings (LDRBs) in combination with dampers that are particularly common in Japan. Another type of isolators is the frictional base isolator such as US friction pendulum system (FPS) and curved surface slider (CSS). Recently, rolling isolators in the form of ball bearings and sphere bearings are also applied, especially in Japan with more than 200 applications for buildings. However rolling isolators are considered too costly when applied to large structures. Therefore, in Italy, such isolators are used for protection of precious masterpieces and expensive equipment such as operating-room in hospitals.
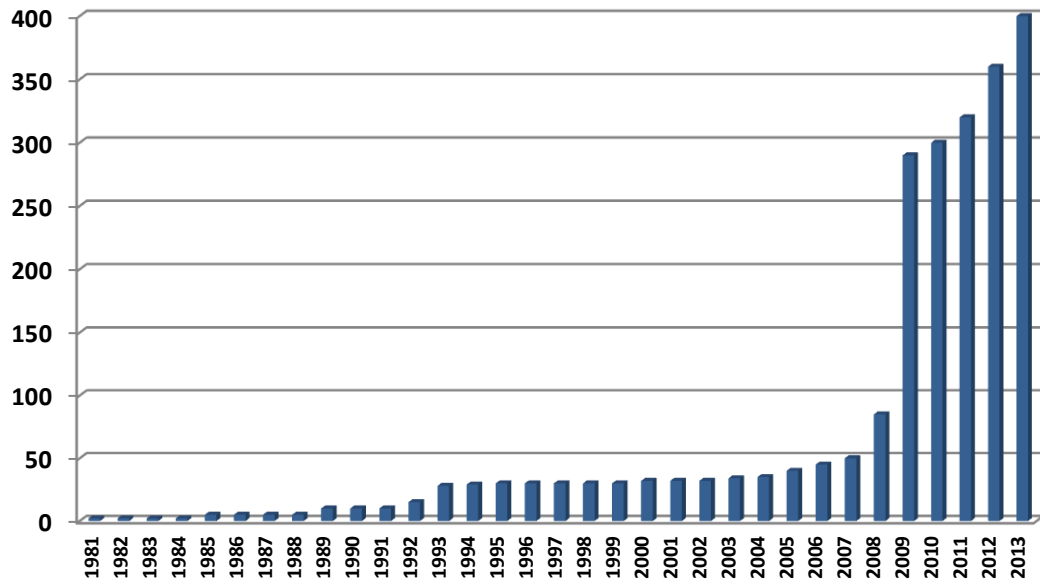
Fig. 1. 17 Overall number of Italian buildings protected by seismic isolation during years [16].

As reported in [16], all structures protected by rubber isolation system in regions that hit by even large earthquakes performed an excellent behavior, in spite of the fact that the intensity of some earthquakes was frequently underestimated. However, very few number of seismically buildings particularly in developing countries having high seismicity reveals the importance of developing a low cost seismic isolation system, such as fiber reinforced elastomeric isolators (FREIs) in combination with recycled rubber.

1.6. Research objectives

Considering some significant benefits in utilizing fiber reinforced elastomeric isolators (FREIs), particularly for developing countries, this study focuses on the production and application of fiber reinforced elastomeric isolators (FREIs) using recycled rubber. In order to assure the clarity of the present research, several research objectives are set as the following:

1. To obtain the mehcanical properties of the rubber compounds under study, particularly the recycled rubbers.

2. To obtain a proper method to fabricate fiber rienforced elastomeric isolators (FREIs) using recycled rubbers.

3. To obtain the mechanical behavior of FREIs (e.g: displacement-shear force relationship, compressive modulus).

4. To evaluate the effect of ageing on the mechanical properties of the rubber compounds and the FREIs under study.

5. To obtain a suitable element model in Abaqus envirentment to represent the behavior of the FREIs in unbonded and bonded condotions.

6. To evaluate the performance of the FREI system in isolating several type of buildings.

7. To evaluate the performance of the FREI system in combination with dadditional damping device such as shape memmory alloy wires.

1.7. Research methodologies

The schema of the research methodologies is presented in Fig. 1.18. The experimental work starts with the characterization of the rubber material, mainly recycled rubber, through experimental tests: uniaxial tensile and shear test to characterize the hyperelasticity behavior, and relaxation test to characterize its viscosity. Numerical models on hyperelasticity and viscosity are also presented.

The experimental part then continues with the investigation on the unbonded fiber reinforced elastomeric isolators (FREIs) as the focus of this research. A series of compression and shear tests are performed to characterize the axial and lateral behavior of the FREIs. Aging effects are also observed to evaluate the durability of such isolators under long-term usage.
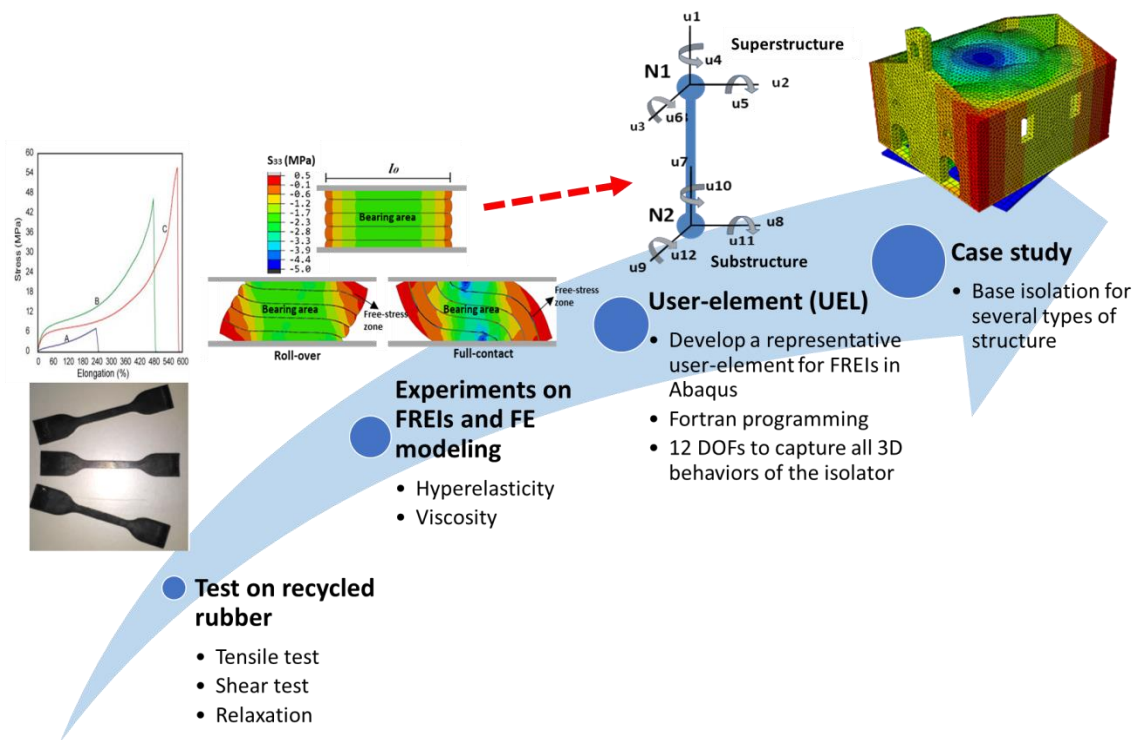
Fig. 1. 18. Schema of the research methodologies

The geometry of the three FREI products in the present project are illustrated in Fig. 1.19. The FREIs consist of several rubber pads made of either recycled rubber 30 or 60 ShA. Specimen 1 and specimen 2 have different shape factor but identical aspect ratio in order to investigate the effect of shape factor. Meanwhile, specimen 2 and 3 have different aspect ratio but similar shape factor to observe the effect of aspect ratio. Fig. 1.20 presents the technological details of the unbonded FREI

system applied in a masonry structure. The upper and bottom surfaces of the FREIs are not bonded to the superstructure and the fundation. This configuration will allow a "rolling-over" deformation of the unbonded FREI, as shown in Fig. 1.20, increasing the displacement capacity of the isolation system.

Based on the results of experimental tests and 3D FE modeling, a simplified Abaqus user element (UEL) is developed to represent the complex behaviors of the unbonded FREIs. Thus, the computational time in nonlinear time-history analyses can be dramatically reduced, when compared with using a detailed 3D FE model for a single unbonded FREI. This part requires a skill in Fortran programming.

Several case studies are then performed to evaluate the performances of the FREIs when applied in low seismically resistant buildings, such as masonry. Technological detailings are proposed so that the unbonded isolation system using unbonded FREIs can work effectively to protect new or existing masonry buildings against earthquakes.
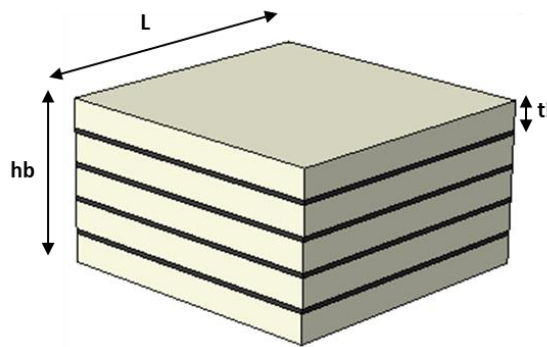
			Specimen 1	Specimen 2	Specimen 3	
	size		150.150.54	150.150.52	75.75.65	
side	L	mm	150	150	75	
single rubber thickness	ti	mm	5	10	5	
Glass fiber thickness	tf	mm	0.50	0.50	0.50	
no. rubber layer	nr	-	10	5	12	
total rubber thickness	hr	mm	50	50	60	
total height	hb	mm	54.50	52.00	65.50	
Shape factor	S	-	7.50	3.75	3.75	S = b/4ti
Aspect ratio	R	-	2.75	2.88	1.15	R = b/hb

Fig. 1. 19. Preliminary designs of FREI prototypes in the present research works
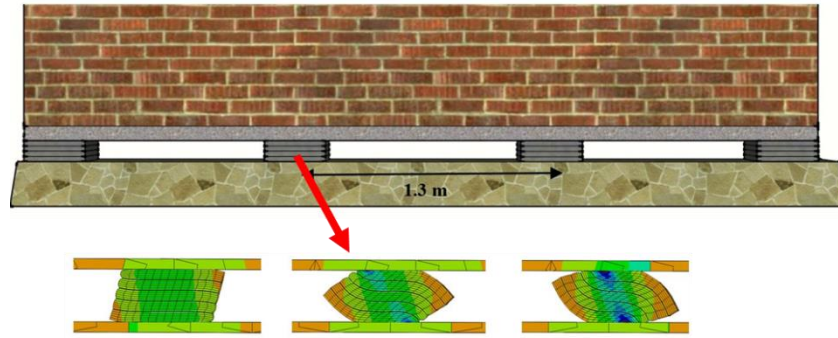
Fig. 1. 20. Detail of unbonded FREI system in masonry structure and the deformation modes under seismic excitation.

1.8. Thesis structure

The first chapter of this thesis presents a state of the art of the research project, history and development of seismic isolation technology. Research methodologies and research product are also described in this part.

In the second chapter, the constitutive models of rubber hyperelasticity and viscosity are briefly described to understand well the nonlinearity behavior of rubber material. A series of simple uniaxial tensile tests and relaxation tests are performed to evaluate the rubber constitutive models available in the literatures.

The third chapter presents a series of experimental tests and comprehensive FE modeling on unbonded fiber reinforced elastomeric isolators (UFREIs) which made from recycled rubber from industrial waste. The performances and durability of the proposed UFREIs are investigated through a set of compression tests and cyclic shear tests in fresh and aged conditions. The main feature of such UFREI device is the large deformability thanks to the roll-over deformation and the favorably lower lateral stiffness compared to the bonded isolator.

In the fourth chapter, a development of phenomenological model of UFREIs is comprehensively discussed. Because there is no proper representative element for UFREIs in Abaqus FE code, the proposed phenomenological model is then implemented in an Abaqus user element (UEL) to represent the complex behavior of a UFREI. Such a procedure dramatically decreases the computational time for a structural analysis of an isolated structure rather than using a detailed 3D FE model for a single UFREI in isolation system.

The applications of the UFREI devices for several types of structure are then discussed in the next chapters. Comprehensive numerical analyses are presented to evaluate the performance of the proposed UFREI device for application in residential masonry housing, historical masonry church, and masonry tower. A series of full-scale nonlinear time-history analyses are carried out in the Abaqus FE software. The application of additional dissipation device is also presented. The UFREI isolation system is combined with shape memory alloy (SMA) wires to increase the energy dissipation of the isolation

system, applied in a large historical masonry church. A particular configuration and technical detailing are proposed so that the hybrid isolation system works effectively under seismic excitation.

1.9. Research limitation

In the present research, several limitations are considered, as following:

1. This research does not discuss the production cost of the FREIs based on large scale production

2. This research discusses briefly the construction method to insert the isolation system into an existing masonry building based on the literatures and does not discuss the construction cost of such an intervention.

3. In the FE analysis, the fiber reinforcement is considered isotropic elastic.

4. The masonry material in the FE model is assumed homogeneous.

5. No sliding is assumed in the unbonded FREI system

References

[1] Boen, T. (2014). Challenges and Potentials of Retrofitting Masonry Non-Engineered Construction in Indonesia. PhD Thesis, Kyoto University, 2014.

[2] Elnashai, A. S., Kim, S. J., Yun, G. J., & Sidarta, D. (2007). The Yogyakarta Earthquake of May 27, 2006. *MAE Center CD Release 07-02*.

[3] Promis, G., Ferrier, E., & Hamelin, P. (2009). Effect of external FRP retrofitting on reinforced concrete short columns for seismic strengthening. *Composite structures*, *88*(3), 367-379.

[4] Ilki, A., Peker, O., Karamuk, E., Demir, C., & Kumbasar, N. (2008). FRP retrofit of low and medium strength circular and rectangular reinforced concrete columns. *Journal of Materials in Civil Engineering*, *20*(2), 169-188.

[5] Formisano, A., Lombardi, L., & Mazzolani, F. M. (2016). Perforated metal shear panels as bracing devices of seismic-resistant structures. *Journal of Constructional Steel Research*, *126*, 37-49.

[6] Badoux, M., & Jirsa, J. O. (1990). Steel bracing of RC frames for seismic retrofitting. *Journal of Structural Engineering*, *116*(1), 55-74.

[7] Lee, S. K., Park, J. H., Moon, B. W., Min, K. W., Lee, S. H., & Kim, J. (2008). Design of a bracing-friction damper system for seismic retrofitting. *Smart Structures and Systems*, *4*(5), 685-696.

[8] Martinez-Rodrigo, M., & Romero, M. L. (2003). An optimum retrofit strategy for moment resisting frames with nonlinear viscous dampers for seismic applications. *Engineering Structures*, *25*(7), 913-925.

[9] Matsagar, V. A., & Jangid, R. S. (2008). Base isolation for seismic retrofitting of structures. Practice Periodical on Structural Design and Construction, 13(4), 175-185.

[10] Mezzi, M., Comodini, F., & Rossi, L. (2011, September). A base isolation option for the full seismic protection of an existing masonry school building. In *Proc. 13th International Conf. on Civil, Structural Engineering Computing. Civil-Comp Press. Stirlingshire, Scotland.*

[11] Melkumyan, M. G. (2007). Base and roof isolation for earthquake retrofitting and protection of existing buildings in Armenia. In *Proceedings of the International Symposium on Seismic Risk Reduction (the JICA Cooperation Project in Romania), Bucharest, Romanian* (pp. 593-600).

[12] Mazza, F., Mazza, M., & Vulcano, A. (2017). Nonlinear response of rc framed buildings retrofitted by different base-isolation systems under horizontal and vertical components of near-fault earthquakes. Earthq. Struct, 12(1), 135-144.

[13] Naeim, F., & Kelly, J. M. (1999). Design of seismic isolated structures: from theory to practice. John Wiley & Sons.

[14] Kelly, J. M., & Konstantinidis, D. (2011). *Mechanics of rubber bearings for seismic and vibration isolation*. John Wiley & Sons.

[15] Lumantarna, B., & Pudjisuryadi, P. (2013, September). Learning from local wisdom: Friction damper in traditional buildings in Indonesia. In Proceedings of the Thirteenth East Asia-Pacific Conference on Structural Engineering and Construction (EASEC-13) (pp. Keynote-Lecture). The Thirteenth East Asia-Pacific Conference on Structural Engineering and Construction (EASEC-13).

[16] Martelli, A., Clemente, P., De Stefano, A., Forni, M., & Salvatori, A. (2014). Recent development and application of seismic isolation and energy dissipation and conditions for their correct use. In *Perspectives on European earthquake engineering and seismology* (pp. 449-488). Springer, Cham.

[17] Kelly, J. M. (1993). Earthquake-resistant design with rubber.

[18] Calabrese, A., Spizzuoco, M., Serino, G., Della Corte, G., & Maddaloni, G. (2015). Shaking table investigation of a novel, low-cost, base isolation technology using recycled rubber. *Structural Control and Health Monitoring*, *22*(1), 107-122.

[19] Toopchi-Nezhad, H., Tait, M. J., & Drysdale, R. G. (2008). Testing and modeling of square carbon fiber-reinforced elastomeric seismic isolators. *Structural Control and Health Monitoring: The Official Journal of the International Association for Structural Control and Monitoring and of the European Association for the Control of Structures*, *15*(6), 876-900.

[20] Mishra, H. K. (2018). Experimental and analytical studies on scrap tire rubber pads for application to seismic isolatiion of structures (Doctoral dissertation).

[21] Spizzuoco, M., Calabrese, A., & Serino, G. (2014). Innovative low-cost recycled rubber–fiber reinforced isolator: experimental tests and finite element analyses. *Engineering Structures*, *76*, 99-111.

[22] Turer, A., & Özden, B. (2008). Seismic base isolation using low-cost Scrap Tire Pads (STP). *Materials and Structures*, *41*(5), 891-908.

[23] Markou, A. A., & Manolis, G. D. (2016). Mechanical models for shear behavior in high damping rubber bearings. *Soil Dynamics and Earthquake Engineering*, *90*, 221-226.

[24] Milani, G., & Milani, F. (2012). Stretch–stress behavior of elastomeric seismic isolators with different rubber materials: numerical insight. *Journal of engineering mechanics*, *138*(5), 416-429.

[25] Martelli, A., & Forni, M. (2010). Seismic isolation and other antiseismic systems: recent applications in Italy and worldwide. *Seismic Isolation And Protection Systems*, *1*(1), 75-123.

[26] Robinson, W. H. (1982). Lead-rubber hysteretic bearings suitable for protecting structures during earthquakes. Earthquake engineering & structural dynamics, 10(4), 593-604.

[27] Tyler, R. G. (1991). Rubber bearings in base-isolated structures. *Bulletin of the New Zealand Society for Earthquake Engineering*, *24*(3), 251-274.

[28] Hameed, A., Koo, M. S., Dai Do, T., & Jeong, J. H. (2008). Effect of lead rubber bearing characteristics on the response of seismic-isolated bridges. *KSCE Journal of Civil Engineering*, *12*(3), 187-196.

[29] Kalpakidis, I. V., & Constantinou, M. C. (2009). Effects of heating on the behavior of lead-rubber bearings. II: Verification of theory. *Journal of Structural Engineering*, *135*(12), 1450-1461.

[30] Hu, K., Zhou, Y., Jiang, L., Chen, P., & Qu, G. (2017). A mechanical tension-resistant device for lead rubber bearings. *Engineering Structures*, *152*, 238-250.

[31] Kim, D., Oh, J., Do, J., & Park, J. (2014). Effects of thermal aging on mechanical properties of laminated lead and natural rubber bearing. *Earthquakes and Structures*, *6*(2), 127-140.

[32] Yoneda, Y., & Mita, A. (2006, April). Nondestructive inspection of a lead rubber bearing using ultrasonic wave. In *Smart Structures and Materials 2006: Sensors and Smart Structures Technologies for Civil, Mechanical, and Aerospace Systems* (Vol. 6174, p. 61740J). International Society for Optics and Photonics.

[33] Takaoka, E., Takenaka, Y., Kondo, A., Hikita, M., & Kitamura, H. (2008, October). Heat-mechanics interaction behavior of laminated rubber bearings under large and cyclic lateral deformation. In *Proceedings of the 14th Conference on Earthquake Engineering, Beijing, China* (pp. 12-17).

[34] Gu, H. S., & Itoh, Y. (2010). Ageing behaviour of natural rubber and high damping rubber materials used in bridge rubber bearings. *Advances in Structural Engineering*, *13*(6), 1105-1113.

[35] Abe, M., Yoshida, J., & Fujino, Y. (2004). Multiaxial behaviors of laminated rubber bearings and their modeling. I: experimental study. *Journal of Structural Engineering*, *130*(8), 1119-1132.

[36] Bhuiyan, A. R., & Alam, M. S. (2013). Seismic performance assessment of highway bridges equipped with superelastic shape memory alloy-based laminated rubber isolation bearing. *Engineering Structures*, *49*, 396-407.

[37] Mazza, F. (2017). Residual seismic load capacity of fire-damaged rubber bearings of rc base-isolated buildings. *Engineering Failure Analysis*, *79*, 951-970.

[38] Moon, B. Y., Kang, G. J., Kang, B. S., & Kelly, J. M. (2002). Design and manufacturing of fiber reinforced elastomeric isolator for seismic isolation. *Journal of Materials Processing Technology*, *130*, 145-150.

[39] Kelly, J. M. (1999). Analysis of fiber-reinforced elastomeric isolators. Journal of Seismology and Earthquake Engineering, 2(1), 19-34.

[40] Habieb, A. B., Valente, M., & Milani, G. (2019). Base seismic isolation of a historical masonry church using fiber reinforced elastomeric isolators. *Soil Dynamics and Earthquake Engineering*, *120*, 127-145.

[41] Toopchi-Nezhad, H., Tait, M. J., & Drysdale, R. G. (2008). Lateral response evaluation of fiber-reinforced neoprene seismic isolators utilized in an unbonded application. Journal of Structural Engineering, 134(10), 1627-1637.

[42] Russo, G., & Pauletta, M. (2013). Sliding instability of fiber-reinforced elastomeric isolators in unbonded applications. *Engineering Structures*, *48*, 70-80.

[43] Osgooei, P. M., Van Engelen, N. C., Konstantinidis, D., & Tait, M. J. (2015). Experimental and finite element study on the lateral response of modified rectangular fiber-reinforced elastomeric isolators (MR-FREIs). *Engineering Structures*, *85*, 293-303.

[44] Van Engelen, N. C., Osgooei, P. M., Tait, M. J., & Konstantinidis, D. (2015). Partially bonded fiber-reinforced elastomeric isolators (PB-FREIs). *Structural Control and Health Monitoring*, *22*(3), 417-432.

[45] Das, A., Deb, S. K., & Dutta, A. (2016). Shake table testing of un-reinforced brick masonry building test model isolated by U-FREI. *Earthquake Engineering & Structural Dynamics*, *45*(2), 253-272.

[46] Pauletta, M., Cortesia, A., & Russo, G. (2015). Roll-out instability of small size fiber-reinforced elastomeric isolators in unbonded applications. *Engineering Structures*, *102*, 358-368.

[47] Quaglini, V., Bocciarelli, M., Gandelli, E., & Dubini, P. (2014). Numerical assessment of frictional heating in sliding bearings for seismic isolation. *Journal of Earthquake Engineering*, *18*(8), 1198-1216.

[48] Roussis, P. C., & Constantinou, M. C. (2006). Uplift-restraining friction pendulum seismic isolation system. *Earthquake engineering & structural dynamics*, *35*(5), 577-593.

[49] Ponzo, F. C., Di Cesare, A., Leccese, G., & Nigro, D. (2017). Shake table testing on restoring capability of double concave friction pendulum seismic isolation systems. *Earthquake Engineering & Structural Dynamics*, *46*(14), 2337-2353.

[50] Katsaras, C. P., Panagiotakos, T. B., & Kolias, B. (2008). Restoring capability of bilinear hysteretic seismic isolation systems. *Earthquake engineering & structural dynamics*, *37*(4), 557-575.

[51] Tsopelas P, Constantinou MC (1994) NCEER-TAISEI corporation research program on sliding seismic isolation systems for bridges-experimental and

analytical study of a system consisting of sliding bearings and fluid restoring force/damping devices. Technical Report NCEER-94-0014, University of New York at Buffalo, Buffalo, NY.

[52] Thuyet, V. N., Deb, S. K., & Dutta, A. (2018). Mitigation of Seismic Vulnerability of Prototype Low-Rise Masonry Building Using U-FREIs. *Journal of Performance of Constructed Facilities*, *32*(2), 04017136.

[53] Nanda, R. P., Shrikhande, M., & Agarwal, P. (2016). Low-cost base-isolation system for seismic protection of rural buildings. Practice Periodical on Structural Design and Construction, 21(1), 04015001.

Reactivated EPDM for production of
fiber reinforced elastomeric isolators

Rubber material is widely used either for household or industrial needs. Since the prehistoric era, rubber has been involved in human life by exploiting the latex from particular trees. In the industrial sector, natural rubber was firstly used at the beginning of 18th century [1]. Nowadays, rubber is commonly used for tires, marine fenders, vibration or seismic isolator, impermeable layers, and also for sports equipment. In general, rubber can be in the form of natural and synthetic materials. A natural rubber can be traditionally harvested in the form of latex from the rubber three. The latex is then refined into rubber sheet ready for commercial processing. Thailand and Indonesia so far are the leading natural rubber producing countries in the world. Later on, synthetic rubber was introduced to overcome a high demand of rubber materials starting in the 1900s due to a massive production of vehicles[2]. Some of the popular synthetic rubber types include: hypalon, ethylene propylene diene monomer (EPDM), viton, neoprene, silicone rubber (SiR), and styrene butadiene rubber (SBR).

To be ready for application, rubber should be processed through several stages; mixing or milling, and vulcanization [3]. In the mixing process, some additives are added to obtain the expected behavior of the rubber compound. In the vulcanization process, the rubber is heated with sulfur, accelerator, and activator at around 140-160 C. The process triggers the formation of cross-links between long rubber molecules, thus improving elasticity, resilience, tensile strength, viscosity, hardness, and weather resistance.

In civil engineering field, rubber is the main material for production of seismic or vibration isolation system. The isolator generally consists of several high damping rubber pads (HDRB) with steel shims interposed in between to improve the vertical stability. In lead rubber bearing (LRB), cylindrical lead core is used to increase significantly the damping ratio. Thanks to the low horizontal stiffness and favorable damping ratio of the rubber isolator, the fundamental period of a structure can be

shifted and the propagation of earthquake energy from foundation to superstructure can be prevented. One of inexpensive rubber isolators is fiber reinforced elastomeric isolator (FREI). Instead of steel, carbon or glass fiber lamina are used as vertical reinforcement of the isolator to reduce the cost. In addition, the fiber polymer does not need any particular treatment against corrosion as experienced by its steel counterpart. Such a device is considered suitable for seismic protection in developing countries.

Along with the rapid development of vehicle industries that produce rubber based products in the past decades, huge amount of rubber waste has polluted the environment. Therefore, researchers in the field have investigated the possibility of using rubber waste for various applications, particularly in construction industry. The recycled rubber has been used not only in rubber based equipment such as seismic isolator but also in cementitious materials or concrete. When dealing with the problem of rubber recycling, waste rubber can be reduced to powder and melt in blends with thermoplastic resins to produce thermoplastic elastomers (TPE) compounds. As a matter of fact, the utilization of waste EPDM appears very interesting, because EPDM backbone remains essentially the same of the starting materials.

Gregori et al in [4] investigated the effects of the partial replacement of natural concrete aggregates with waste tire rubber on the concrete compressive strength. The proposed material, so called as rubberized concrete has mechanical and rheological properties suitable for civil engineering applications and leads to an effective solution of recycling discarded tires. However, rubberized concrete remains a suitable material mostly for nonstructural component such as lightweight wall panels, insulating screeds, and filling materials due to the high uncertainty of the predicted strength reduction factor.

An investigation was conducted in [5] on the flexural behavior of reinforced beams made from crumbed rubber concrete (CRC) mixes where the beam specimens were tested up to failure. The results in this study show that the flexural behavior of reinforced CRC beam is very similar to the normal concrete beam of the same strength. It is also found in [6] that the ultimate shear capacities of CRC beams are 0-15% lower than that of an idealized beam of conventional concrete.

In [7], an innovative seismic isolation method was proposed by means of recycled scrap tire rubber-soil mixtures. It is found that the proposed method can reduce the shaking level of ground motion not only in horizontal direction but also in vertical direction. Such a method can be considered as a low cost solution for seismic protection of buildings, particularly in developing countries.

In the production of rubber base isolation system, the use of recycled rubber has attracted high interest from researchers. In[8], recycled rubber derived from used tires and industrial waste is used to produce rubber pads for fiber reinforced elastomeric isolators (FREIs). Unlike the commercial base isolators, the proposed FREIs can be applied in unbonded condition [9][10], in which the upper and bottom

surface of the isolator are not bonded to the superstructure and foundation. Therefore, the presence of steel end-plate is not required, reducing the construction cost of the isolation system. In addition, the unbonded application may increase the deformability capacity and damping ratio of the isolator [11]. A test on shaking table [12][13] shows that the FREI system can effectively reduce the top displacement and the acceleration response of an isolated structure, competing with the available commercial devices. A successive research in [14] was conducted by combining the recycled rubber isolation system with additional magnetorial damper to improve significantly the seismic performance of the isolated structure again severe earthquakes. The cost of the recycled rubber isolators using fiber reinforcement is estimated about one tenth of which of commercial isolators.

In [15] and [16], scrap tire rubber pads (STRP) are used as an alternative seismic base isolation. Additional steel shims or fiber laminas are not required because the reinforcing cords provided in manufacturing the tire can be considered as the vertical reinforcement. The STRP layers were just stacked one on top of another without applying the adhesive. These proposed STRP isolators have several advantages compared to conventional elastomeric isolator including superior damping properties, lower cost, and easily available material.

A simple seismic isolation system was proposed in [17] by simply using some half pieces of recycled tire applied in particular configuration. Such a simple isolation system is designed to isolate critical rooms in health care facilities such as emergency rooms and essential care units. The experimental test shows that the proposed system demonstrates a feasible solution for improving the seismic response of non-structural components in critical rooms of hospital facilities.

The aforementioned researches reveal the important benefits of utilizing rubber waste from vehicle tires or industries both to drop down the cost of isolation system and to save the environment. Such a consideration is particularly essential when dealing with seismic protection in developing countries where the cost of commercial isolation system is considered too expensive for massive application.

Based on similar motivation, the present study investigates the use of recycled rubber in the form of reactivated ethylene propylene diene monomer (EPDM) from industrial waste to fabricate rubber pads for building seismic isolation system. This paper discusses the fabrication process and composition of the recycled rubber, chemical characterization, mechanical properties, and the resistance against aging. The chemical characteristic is evaluated through rheometer tests at different temperatures, while the mechanical properties are examined trough several tests including hardness test, compression set, uniaxial tensile test, and relaxation test.

Hyperelasticity and viscosity of rubber, which can be derived from tensile test and relaxation test, respectively, are the main parameters to perform numerical models of rubber material in finite element (FE) analyses. Therefore, several numerical models of hyperelasticity and viscosity available in the literatures are discussed to define the most suitable models applied to the proposed recycled material.

2.1. Regenerated rubber compounds

Four rubber batches using regenerated EPDM as shown in are produced in this experimental campaign. Two commercial virgin rubbers Vistalon 3666 and Dutral 4038 are used to be blended with the regenerated EPDM to obtain blends with hardness 30±5 ShA and 60±5 ShA. The first is a product with extended oil and medium/large distribution of molecular weight, an ENB content equal to 4.5% and a propylene content in weight of 30%; the latter has a narrow/medium molecular weight distribution, an ENB content of 4.1% and a propylene content of 29%. The detail composition of Vistalon 3666 and Dutral 4038 can be seen in Table 2.1.

The detail composition of the four batches can be seen in : batch 1 and 2 are designed as soft rubber with the target of hardness 30 Sh A, while batch 3 and 4 are expected to have hardness about 60 Sh A. The regenerated EPDM is used to partially replace the virgin rubbers. As shown, the difference between batch 1 and 2 is the source of the regenerated EPDM: two sources A and B are considered. This difference applies also for batch 3 and 4.

Table 2. 1. Composition of two virgin rubber Vistalon 3666 and Dutral 4038

Vistalon 3666		Dutral 4038	
Product	Phr	Product	Phr
Vistalon 3666	175	Dutral 4038	100
FEF N550	80	FEF N550	70
Silitin Z	80	ZnO	5
Flexon 876	120	Stear. Ac.	1
ZnO	5	SRF C.B.	40
Silitin Z	0.5	Paraff. Oil	80
MTB	1.5	Rodrtax 2	4.5
TMTDS	0.8	ZDBDC	1
ZDEDC	0.8	S	2
DTDM	2		
Total	465.6	Total	303.5

Fig. 2. 1. Four recycled rubber specimens under study.

Table 2. 2. Composition of four rubber specimens.

Batch 1A		Batch 2B		Batch 3A		Batch 4B	
INGREDIENT	gr	INGREDIENT	gr	INGREDIENT	gr	INGREDIENT	gr
EPDM VISTALON 3666 OG	175.00	EPDM VISTALON 3666 OG	175.00	EPDM DUTRAL 4038 NCS	100.00	EPDM DUTRAL 4038 NCS	100.00
EPDM REGENERATED A	300.00	EPDM REGENERATED B	300.00	EPDM REGENERATED A	300.00	EPDM REGENERATED B	300.00
ZNO PREMIX	9.52	ZNO PREMIX	9.52				
STEARINA	1.52	STEARINA	1.52				
PEG 4000	4.00	PEG 4000	4.00	OSSIDO DI ZINCO S.V.	4.00	OSSIDO DI ZINCO S.V.	4.00
RESINA PETROLICA	5.00	RESINA PETROLICA	5.00	STEARINA	1.00	STEARINA	1.00
SILLITIN N 85	68.00	SILLITIN N 85	68.00				
CARBONATO	100.00	CARBONATO	100.00	CARBONATO	40.00	CARBONATO	40.00
N550 FEF II	72.80	N550 FEF II	72.80	N550 FEF II	185.00	N550 FEF II	185.00
OLIO PARAFFINICO	142.00	OLIO PARAFFINICO	142.00	OLIO PARAFFINICO	95.00	OLIO PARAFFINICO	95.00
MBT PREMIX	1.92	MBT PREMIX	1.92				
ZDBC PREMIX	1.92	ZDBC PREMIX	1.92				
TDEC PREMIX	0.80	TDEC PREMIX	0.80	MBT PREMIX	1.50	MBT PREMIX	1.50
TMTD PREMIX	1.12	TMTD PREMIX	1.12	ZOLFO PREMIX	2.50	ZOLFO PREMIX	2.50
DPTT PREMIX	1.12	DPTT PREMIX	1.12	TMTD PREMIX	2.00	TMTD PREMIX	2.00
ZOLFO PREMIX	3.80	ZOLFO PREMIX	3.80				
total	888.52	total	888.52	total	731.00	total	731.00

2.2. Chemical characterization

2.2.1. Rheometer test at four temperatures

Rubbers in raw state have to undergo a vulcanization process in order to crosslink the molecular chains and to improve the rubber properties. A rheometer measures the viscoelastic properties of rubber compounds during the vulcanization process. In order to evaluate the effect of different temperatures, the recycled rubber specimens in this study are subjected to rheometric test at four different temperatures: 150, 160, 170 and 180°C. Fig. 2. 2 presents the rheometric curves of four batches at different temperatures. In Table 2. 3, some important rheometric parameters are summarized.

When a specimen in the rheometer gets heated under pressure, the viscosity drops and the torque decreases. The lowest torque recorded on the curve is called ML (Moment Lowest). It represents the stiffness of uncured rubber at a given temperature.

As the curing begins, the torque rises. TS2 is the time from the beginning of the test to the time the torque has increased 2 units above ML value. It represents the scorch time or at which point the curing actually starts. As the curing progresses, the torque increases further. The gradient depends on the compound and curing method used. After some period, the torque reaches a maximum value and tends to be constant. The highest recorded torque on the curve is called MH (Moment Highest). Time from the start of the test to the point where 90% of the MH value is reached is called T90. Such a description applies also for T10 and T50. As shown in Fig. 2. 2 and Table 2. 3, the increase of vulcanization temperature accelerates the vulcanization time. However, vulcanization at 150°C seems to be the most optimum method because it results in the highest MH. On the other hand, the lowest MH is resulted in the vulcanization at 180°C.
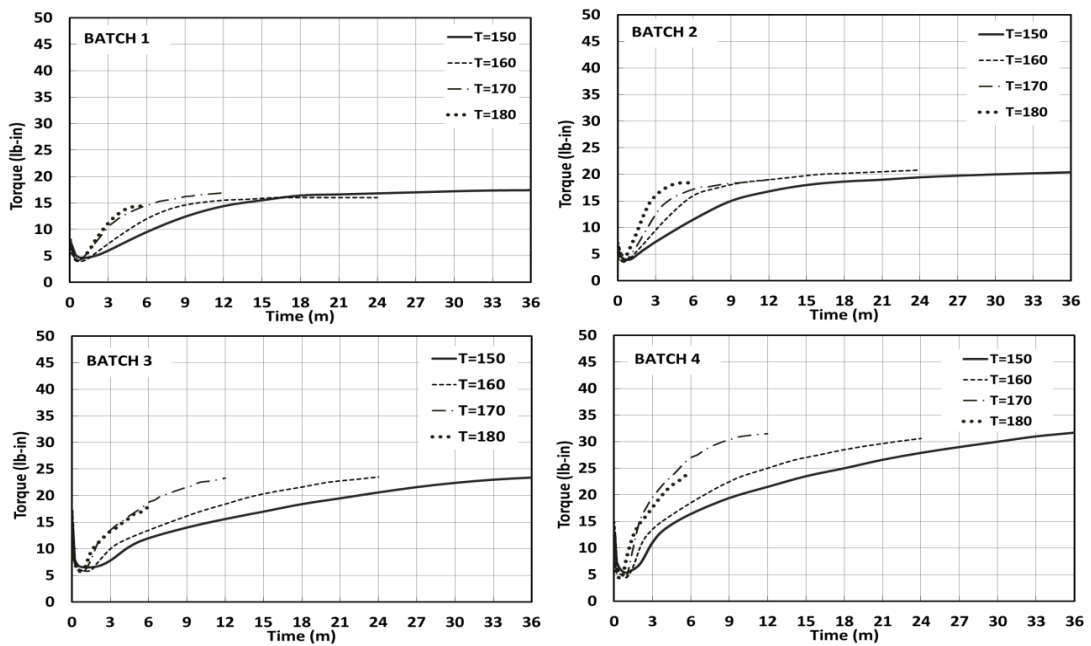

Fig. 2. 2. Rheometer curves of four rubber specimens at different temperatures.

Table 2. 3. Several important parameters in the rheometer test on four rubber specimens at different temperatures.

Test temp.	Batch 1								Batch 2							
	ML	Ts1	Ts2	T10	T50	T90	MH	Final	ML	Ts1	Ts2	T10	T50	T90	MH	Final
°C	lb-in			mm:ss			lb-in	lb-in	lb-in			mm:ss			lb-in	lb-in
150	4.81	02:37	03:30	02:47	07:20	16:13	16.72	16.72	3.9	01:33	02:07	01:56	06:25	21:20	20.99	20.98
160	4.45	01:49	02:23	01:56	04:44	09:44	16.27	15.97	3.71	01:12	01:35	01:28	04:08	12:26	20.61	20.52
170	4.39	01:16	01:32	01:19	03:00	07:37	16.53	16.53	3.51	00:54	01:10	01:04	02:40	06:19	19.32	19.30
180	3.96	01:06	01:24	01:07	02:20	04:19	14.62	14.62	3.43	00:41	00:53	00:47	01:49	03:38	18.44	18.44

Test temp.	Batch 3								Batch 4							
	ML	Ts1	Ts2	T10	T50	T90	MH	Final	ML	Ts1	Ts2	T10	T50	T90	MH	Final
°C	lb-in			mm:ss			lb-in	lb-in	lb-in			mm:ss			lb-in	lb-in
150	6.67	02:50	03:25	03:14	10:38	04:01	23.29	23.29	5.35	01:46	02:03	02:10	07:37	01:35	30.54	30.54
160	6.21	01:52	02:13	02:07	06:59	17:49	23.15	23.15	4.98	01:16	01:27	01:32	04:56	15:55	29.71	29.71
170	6.16	01:16	01:27	01:24	03:27	08:53	23.39	23.39	4.67	01:05	01:13	01:17	02:34	07:25	30.54	30.54
180	5.46	01:02	01:12	01:04	02:22	04:59	17.45	17.45	4.51	00:42	00:48	00:48	01:52	04:40	23.63	23.63

2.3. Mechanical characterization of the compounds

2.3.1. Shore A hardness test

Shore (durometer) hardness is a measure of the resistance of a material to penetration of a spring loaded needle-like indenter. In rubbers, the hardness is usually measured by shore A scales. In rubber test for seismic isolation purpose, the hardness is measured before and after accelerated ageing. The accelerated aging is conditioned by storing the speciments in oven at 70 °C for 24x7 hours. The aged specimens are then tested after 24 hours of storage at room temperature. According to EN 15129 [18], the variation of the hardness after aging is recommended to not exceed -5 or +8. Table 2. 4 presents the measured hardness of four recycled rubber batch before and after aging and the hardness of the virgin rubbers provided by the supplier. Batch 3 and 4 satisfy the maximum variaton of rubber hardness after accelerated aging.

Table 2. 4. Shore A hardness of four recycled rubber specimens before and after aging.

Rubber	Shore A Hardness		ΔH
	Unaged	Aged	
Vistalon 3666*	34	-	-
Batch 1A	27	37	10
Batch 2B	33	43	10
Dutral 4038*	55	-	-
Batch 3A	56	62	6
Batch 4B	66	69	3

*provided by supplier

2.3.2. Compression set

In compression set testing, the ability of rubber to return to its original thickness after prolonged compression at defined temperature and deflection is examined.

When the rubber is compressed over time, it loses its ability the original thickness. This loss of resiliency may degrade the performance of rubber based equipment such as seal or elastomeric gasket. Compressions set results are expressed in a percentage. A rubber which has lower percentage has better resistance to permanent deformation under a defined deflection and temperature range. In compression set, the rubber specimens as shown in Fig. 2. 3 are subjected to compression at 70 °C for 24 hours. According to EN 15129 [18] in case of rubber material for seismic isolation, the maximum value of compression set result is 30%. In the present experimental test, the results of compression set of rubber Batch 1A, 2B, 3A, and 4B are 23, 12, 28, and 25 %, respectively. Therefore, all four compounds satisfy the requirement of compression set for rubber seismic isolators.
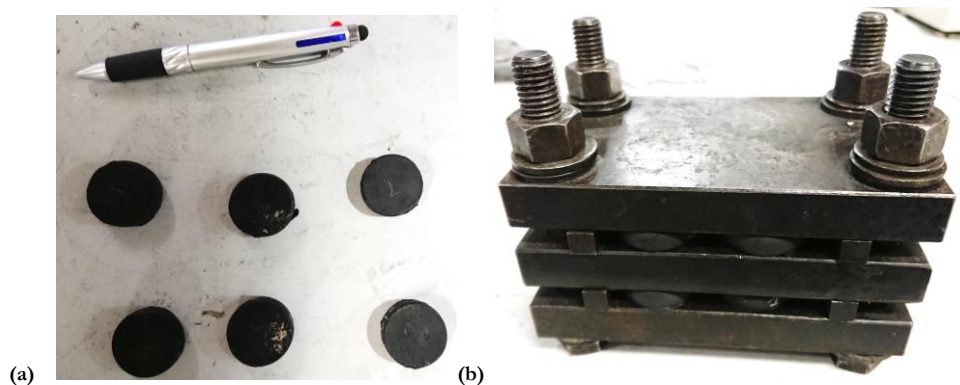

(a)   (b)

Fig. 2. 3. (a) Rubber specimens for compression set; (b) standard device for compression set.

2.3.3. Uniaxial tensile test

Rubber is well-known as an ideal example of perfectly elastic material. However, nonlinear elasticity of rubber at moderate to large strain is clearly remarkable. Such a nonlinearity is often called as hyperelasticity. In order to characterize the hyperelastic properties of the proposed recycled rubber, uniaxial test based on ISO 37 [19] is performed in this study.

For each rubber batch, three specimens in the form of dumb bell pieces as shown in Fig. 2. 4 are tested in the uniaxial tensile test device. The specimens are stretcthed up to failure to define the tensile strength and the strain at failure.

Fig. 2. 5 presents the results of the uniaxial tensile test on four rubber batches. A single curve represents the average of three identical specimens. Results from the test of fresh specimens are presented by black curves, while the red curves present the results after aging. The accelerated aging is conditioned by storing the speciments in oven at 70 °C for 24x7 hours. The aged specimens are then tested after 24 hours of storage at room temperature.
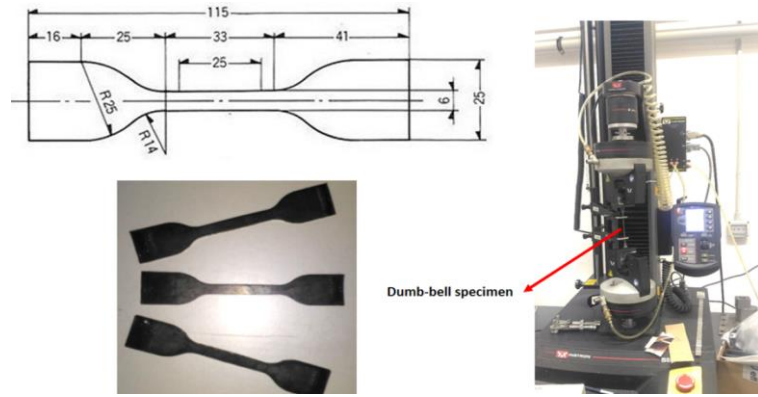
Fig. 2. 4. Dumbbell specimens of rubber and the uniaxial tensile test device.

In case of unaged soft rubber compounds, Batch 1 exhibits larger failure strain yet lower tensile strength when compared to Batch 2. Both soft batches present an identical shape of the hyperelastic curves. For hard rubber compounds, Batch 3 experiences larger failure strain yet lower tensile strength compared to Batch 4. The tensile strength of four batches varies from 5.4 to 6.5 MPa, while the failure strain ranges from 310 to 840 MPa. In general, the values of tensile strength of four batches under study are significantly lower than the requirements stated in EN 15129 for commercial seismic isolators. However, the proposed recycled rubbers are intended to be used for unbonded isolators which exhibit much lower tensile stress under large shear displacement when compared to the commercial ones, as reported in the literatures [20].

In Fig. 2. 5, the results of tensile test after aging are presented by red curves. In genereal, the aging increases the stiffness of the rubber. Table 2. 5 shows the quantity of difference of tensile strength and strain at failure, before and after aging. According to EN 15129, the maximum changes of tensile strength and failure strain are 15% and 25%, respectively. Therefore, Batch 2 and 4 satisfy the aging test requirements in terms of tensile properties.
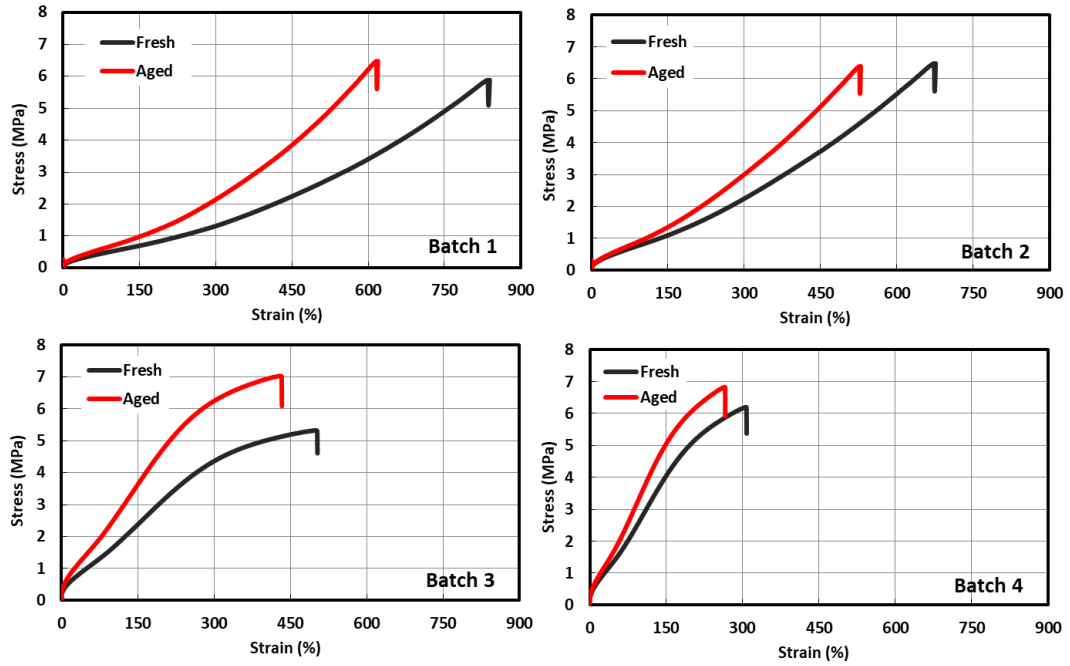
Fig. 2. 5. Strain stress curves of four rubber batches before and after aging.

Table 2. 5. Tensile strength and failure strain of four recycled rubber specimens before and after aging.

	Tensile strength (MPa)		Δ (%)	Strain at break (%)		Δ (%)
	unaged	aged		unaged	aged	
Vistalon3666*	9.3	-	-	730	-	-
Batch 1A	5.89	6.48	10.01	839	619	-26.22
Batch 2B	6.48	6.39	-1.38	676	529	-21.74
Dutral 4038*	11	-	-	400	-	-
Batch 3A	5.32	7.03	32.14	503	433	-13.91
Batch 4B	6.2	6.83	10.16	308	266	-13.63

*provided by the producer

Fig. 2.6 summarizes the experimental results obtained for the different receipts investigated at at failure. On the horizontal axis the Elongation at Break (EB) in % is represented, whereas on the vertical axis the ultimate strength (TS) in MPa is depicted. The data in correspondence with two virgin rubbers Vistalon 3666 and Dutral 4038 and four mixed regenerated rubbers are presented. In this way, the comparison with reference compound made exclusively by virgin rubber is straightforward.

From Fig. 2.6, it can be deduced that the different formulations with regenerated rubber, having comparable hardness with that of the virgin materials, generally exhibit a lower ultimate strength. However, blends with type B regenerated rubber (RRB) exhibits a much better performance than type A regenerated rubber (RRA).

As expected, adding regenerated rubber results into a decrease of the strength with similar elongation at break.
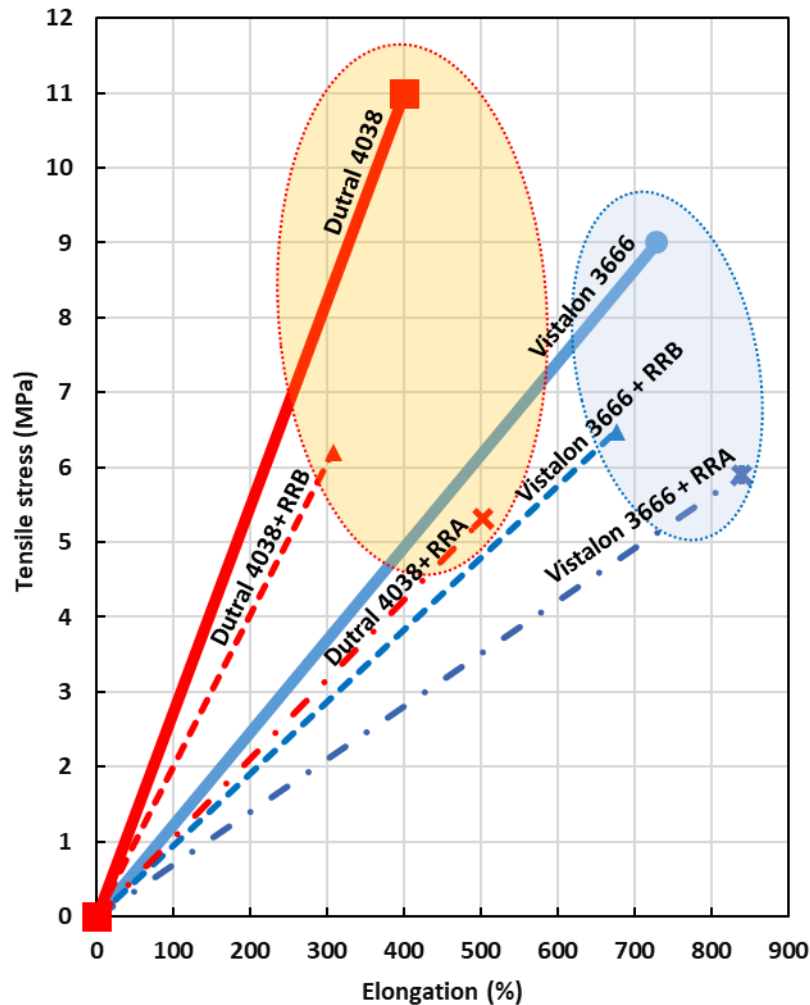

Fig. 2. 6. comparison between first group (red colors: Vistalon 3666, 1A and 2B) and second group (blue colors: Dutral 4038, 3A and 4B) elongation at break (EB) and tensile strength (TS)

In Fig. 2.7, the diagrams of the tensile strength (TS) as a function of the ultimate elongation at break (EB) after ageing at 70°C for 128 hours are presented. From Fig. 2.7, it is possible to notice that, in the presence of ageing, the elongation at break decreases and the tensile strength slightly increases. Considering the theoretical behavior of the observed EB and TS as a function of the vulcanization degree depicted in 2.8b, it can be argued that the compounds are slightly undervulcanized. From a chemical point of view, ageing has the effect to promote an additional crosslinking, confirmed by the fact that Shore A also increases, see Fig. 2.7. Ageing results therefore into an increase of the vulcanization degree, i.e. non-cured polymer was present at the end of the vulcanization process that reticulates further during ageing. The slight increase of the tensile strength shows how the initial curing condition is however near the optimal one, i.e. not far from the point of maximum obtainable.
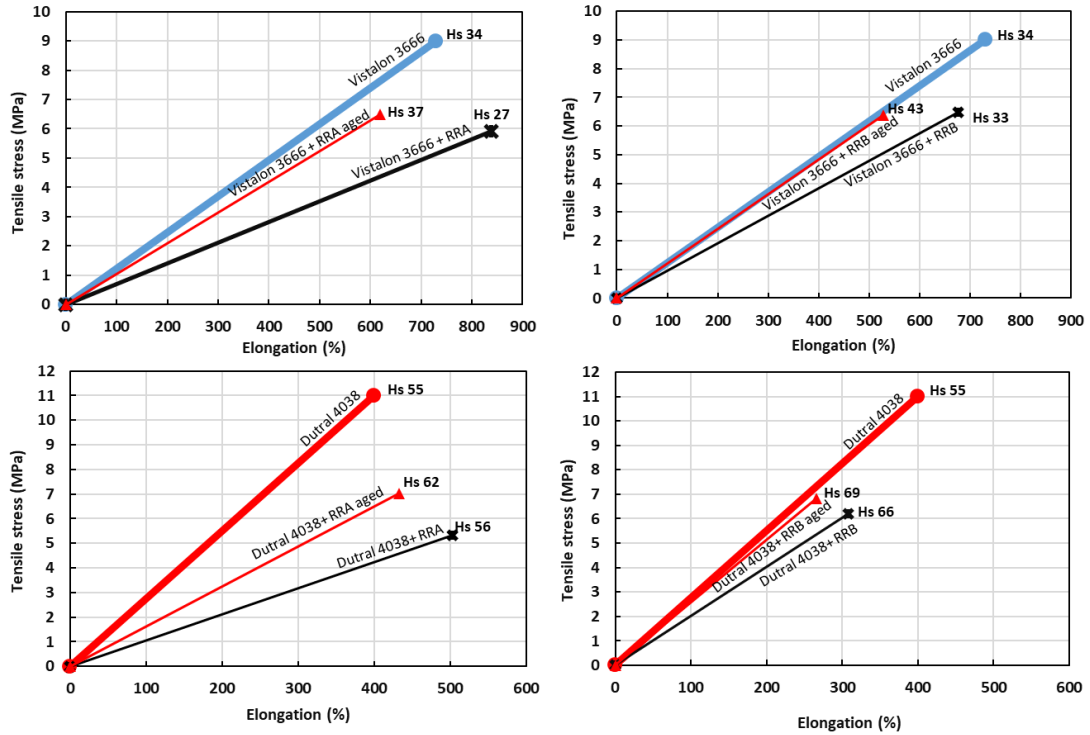
Fig. 2. 7. comparison between first group (red colors: Vistalon 3666, 1A and 2B) and second group (blue colors: Dutral 4038, 3A and 4B) elongation at break (EB) and tensile strength (TS)

Fig. 2.8a shows that compound 4B (Dutral 4038 + regenerated rubber B) is that one exhibiting the best performances among all those investigated. As a matter of fact, compound 4B is the blend approximating better the behavior of the virgin material. Values of EB and TS for Dutral 4048 are scaled in the figure by a factor 26/33, because in the blends a Dutral 4038 with 26% in weight of polymer was utilized, whereas data furnished by the producer, see Table 2.1, for the virgin material refer to an amount of polymer equal to 33%.

It is finally worth mentioning that quite satisfactory is also the behavior of blend 2B (re-generated rubber with Vistalon 3666), but with a still slightly better performance of 4B.

Having obtained the strain stress relations, several numerical models of rubber hyperelasticity are discussed. Rubber is a material having an ideally elastic behavior for which the stress-strain relationship can be derived from a strain energy density function. Rubber is a perfect material to model the hyperelasticity because it is almost perfectly isotropic and nearly incompressible. Many researchers have developed the hyperelastic models, based on the strain energy density function, (W), which is the contribution of the isochoric elastic part, W_{iso}, and the volumetric elastic part, W_{vol}, as follows:

$$W = W_{\text{iso}}(I_1, I_2, I_3) + W_{\text{vol}}(J_{\text{el}}) \tag{1}$$
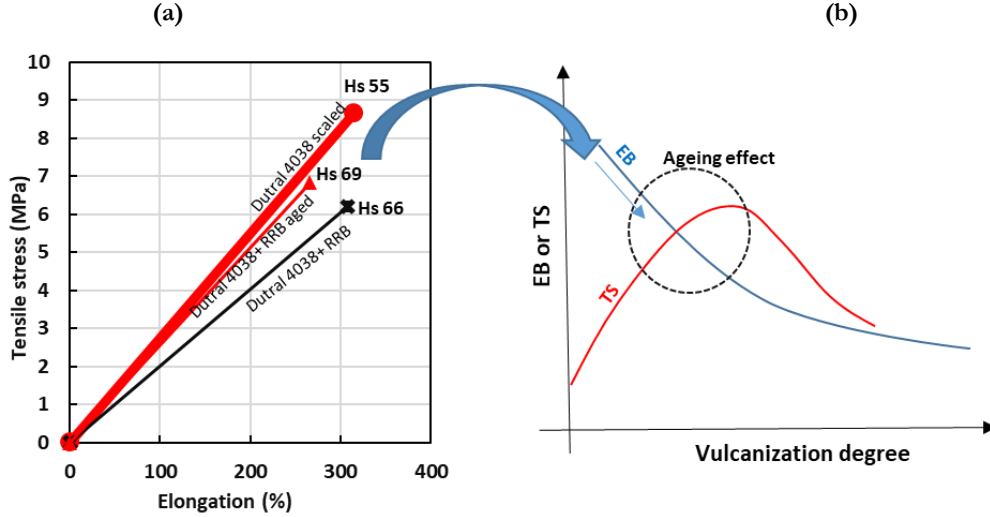
Fig. 2. 8. (a) Scaled Dutral 4038 values and 4B values (with and without ageing) comparison in terms of elongation at break (EB) and tensile strength (TS). (b): theoretical behavior of EB and TS as a function of the vulcanization degree.

Where W is strain per unit reference volume, and I_1, I_2, and I_3 are three invariants of left Cauche-Green deformation tensor which can be calculated in terms of principal stretch ratios, given by equation 2-4:

$$I_1 = \lambda_1{}^2 + \lambda_2{}^2 + \lambda_3{}^2 \tag{2}$$

$$I_2 = \lambda_1{}^2 \lambda_2{}^2 + \lambda_2{}^2\lambda_3{}^2 + \lambda_3{}^2\lambda_1{}^2 \tag{3}$$

$$I_3 = \lambda_1{}^2 \lambda_2{}^2\lambda_3{}^2 \tag{4}$$

Where $\lambda_1, \lambda_2,$ and λ_3 are the three elongation ratios, and J_{el} is the elastic volume ratio.

For isotropic material, the principal stretches in uniaxial tensile test can be expressed in equation 11.

$$\lambda_1 = \lambda; \quad \lambda_2 = \lambda_3 = \frac{1}{\sqrt{\lambda}} \tag{5}$$

And the corresponding stress of uniaxial tension can be expressed by equation 6.

$$\sigma_1 = \sigma = \lambda\frac{\partial W(\lambda)}{\partial \lambda}; \quad \sigma_1 = \sigma_2 = 0 \tag{6}$$

Where $W(\lambda) = W(\lambda, \lambda^{-0.5}, \lambda^{-0.5})$

In this section, several well-known hyperelastic models are briefly described:

- **Neo-Hookean model**

The simples form of hyperelastic polynomial models is the Neo-Hookean model. It is suitable for 20 to 30 percent strain and its strain energy function, as expressed in equation [21].

$$W = C_{10}(I_1 - 3) + \frac{1}{D_1}(J_{el} - 1)^2 \tag{7}$$

Where $C_{10} = \mu_0/2$, μ_0 is the initial shear modulus, I_1 is the first invariant of the left Cauche-Green deformation tensor, and D_1 is the material constant presenting compressibility.

- **Mooney-Rivlin model**

 This model was proposed in 1940 by Melvin Mooney with a linear combination of two invariants of the left Cauchy-Green deformation tensor. The strain energy density function of this model is expressed in equation 8 [22].

$$W = C_{10}(I_1 - 3) + C_{01}(I_2 - 3) + \frac{1}{D_1}(J_{el} - 1)^2 \tag{8}$$

where C_{10} and C_{01} are the material constants, and I_1 and I_2 are the first and second invariant of the left Cauchy-Green deformation tensor.

The accuracy of the Mooney-Rivlin model is quite consistent with that of the Neo-Hookean model in case of small strain. In particular, the Mooney-Rivlin model fits well the experiment result for a small to mederate strain: 100% tensile strain and 30% compressive strain [23].

- **Yeoh model**

This model is also called the reduced polynomial model as for incompressible rubber, it uses only the strain invariant I_1 with higher order. Equation 9 expresses the Yeoh model[24].

$$W = \sum_{i=1}^{3} C_{i0}(I_1 - 3)^i + \sum_{i=1}^{3} \frac{1}{D_1}(J_{el} - 3)^{2i} \tag{9}$$

The initial shear modulus and bulk modulus are given by equation 10.

$$\mu_0 = 2C_{10}; \quad K_0 = \frac{2}{D_1} \tag{10}$$

The Yeoh model is particularly suitable for a much wider range of deformation and able to predict the shear-strain behavior in different deformation modes [25].

- **Ogden model**

Proposed by Raymond Ogden in 1972, the Ogden model can be expressed by the equation 11, for incompressible materials [26].

$$W = \sum_{i=1}^{N} \frac{2\mu_i}{\alpha_i^2}\left(\lambda_1^{\alpha_i} + \lambda_2^{\alpha_i} + \lambda_3^{\alpha_i} - 3\right) + \sum_{i=1}^{N} \frac{1}{D_1}(J_{el} - 1)^{2i} \tag{11}$$

Where $\lambda_1^2 . \lambda_2^2 . \lambda_3^2 = 1$, I_1 and I_2 determine the first part of the strain energy function in Ogden model. I_1 and I_2 do not necessarily represent the function. The accuracy of this model depends on the value of N. The Ogden model suits for large strain up to 700 percent.

- **Arruda-Boyce model**

Arruda-Boyce model was proposed based on representative volume element [27], expressed by the equation 12.

$$W = \mu_0 \sum_{i=1}^{5} \frac{C_i}{\lambda_m^{2i-2}}\left(I_1^i - 3\right) + \frac{1}{D}\left[\frac{J_{el}^2-1}{2} - \ln(J_{el})\right] \tag{12}$$

Where C_1=1/2, C_2=1/20, C_3=11/1050, C_4=19/7000, C_5=519/673750, and λ_m is the locking stretch at which the upturn of stress-strain curve rises significantly.The Arruda-Boyce model can fit well the experimentation for the strain up to 300% [28].

Through optimization procedures based on the experimental results, the hyperelsticity coefficients of each model are defined, as summarized in Table 2. 6. The hyperelastic parameters obtained are then implemented in the uniaxial tensile test simulation to evaluate the performance of the models. The dimension of the specimen is the same with that in the experimental test. The element used is C3D20R (quadratic) to facilitate excessive deformation. Fig. 2. 9 presents the FE model of dumb-bell specimen undergoing a tensile loading.

Table 2. 6. Hyperelastic parameters of four recycled rubber batches before and after aging.

Rubber	Model	Unaged	Aged
Batch 1	Neo Hookean	C_{10}= 0.191; D=0	C_{10}= 0.266; D=0
	Mooney Rivlin	C_{10}=0.295; C_{01}= -0.362; D=0	C_{10}=0.442; C_{01}=-0.511; D=0
	Yeoh	C_{10}=0.152; C_{20}=0.00079; C_{30}=1.98E-06; D=0	C_{10}=0.208; C_{20}=0.0024; C_{30}=9.56E-06; D=0
	Ogden	μ_1= -0.843; μ_2=0.461; μ_3=1.188 α_1=3.293; α_2=3.452; α_3=-5.776; D=0	μ_1= -0.684; μ_2=0.127; μ_3=1.642 α_1=3.621; α_2=4.081; α_3= -6.585; D=0
	Arruda-Boyce	μ=0.317; μ_0=0.322; λ_m=6.208; D=0	μ=0.432; μ_0=0.444; λ_m=4.640; D=0
Batch 2	Neo Hookean	C_{10}= 0.292; D=0	C_{10}= 0.347; D=0
	Mooney Rivlin	C_{10}=0.423; C_{01}= -0.414; D=0	C_{10}=0.532; C_{01}=-0.507; D=0
	Yeoh	C_{10}=0.238; C_{20}=0.00172; C_{30}= -5.3E-08; D=0	C_{10}=0.28; C_{20}=0.0033; C_{30}=2.1E-06; D=0
	Ogden	μ_1= 0.459; μ_2= -0.448; μ_3=0.792 α_1=5.082; α_2=5.094; α_3= -3.988; D=0	μ_1=0.464; μ_2= -1.632; μ_3=3.264 α_1=2.425; α_2= 7.894; α_3= -15.78; D=0
	Arruda-Boyce	μ=0.494; μ_0=0.504; λ_m=5.567; D=0	μ=0.576; μ_0=0.594; λ_m=4.407; D=0
Batch 3	Neo Hookean	C_{10}= 0.512; D=0	C_{10}= 0.759; D=0
	Mooney Rivlin	C_{10}=0.497; C_{01}= -0.049; D=0	C_{10}=0.743; C_{01}=0.048; D=0
	Yeoh	C_{10}=0.496; C_{20}=0.0035; C_{30}= -9.1E-05; D=0	C_{10}=0.73; C_{20}=0.0071; C_{30}=-2.3E-04; D=0
	Ogden	μ_1= -2.436; μ_2=0.918; μ_3=4.146 α_1=4.589; α_2=4.874; α_3= -8.265; D=0	μ_1= -3.542; μ_2=1.383; μ_3=5.929 α_1=4.873; α_2= 5.173; α_3= -8.731; D=0
	Arruda-Boyce	μ=1.025; μ_0=1.025; λ_m=5609; D=0	μ=1.518; μ_0=1.518; λ_m=4959; D=0
Batch 4	Neo Hookean	C_{10}= 0.8; D=0	C_{10}= 0.984; D=0
	Mooney Rivlin	C_{10}=0.9; C_{01}= -0.217; D=0	C_{10}= 1.117; C_{01}= -0.271; D=0
	Yeoh	C_{10}=0.722; C_{20}=0.019; C_{30}= -8.5E-04; D=0	C_{10}=0.891; C_{20}=0.0288; C_{30}= -1.64E-03; D=0
	Ogden	μ_1= 1.421; μ_2= -3.542; μ_3=5.772 α_1=6.061; α_2=5.71; α_3= -10.21; D=0	μ_1= 1.728; μ_2= -4.257; μ_3=6.927 α_1=6.497; α_2= 6.116; α_3= -10.878; D=0
	Arruda-Boyce	μ=1.522; μ_0=1.551; λ_m=5.742; D=0	μ=1.86; μ_0=1.91; λ_m=5.034; D=0

Fig. 2. 10 and Fig. 2. 11 present comparative curves between the experimental data and the five numerical models of four batches, before and after aging, respectively. It can be seen that Yeoh and Ogden models gives the most accurate fitting results

compared to the three other models. Neo-Hookean and Mooeney-Rivlin model seem to not catch very well the high degree of nonlinearity exhibited by the rubber compounds at moderate to large strain, while the Arruda-Boyce model results in too stiff models at large strains. In any case, according to author's experiences, the Yeoh model gives more stable computation during the FE analyses at large deformations.
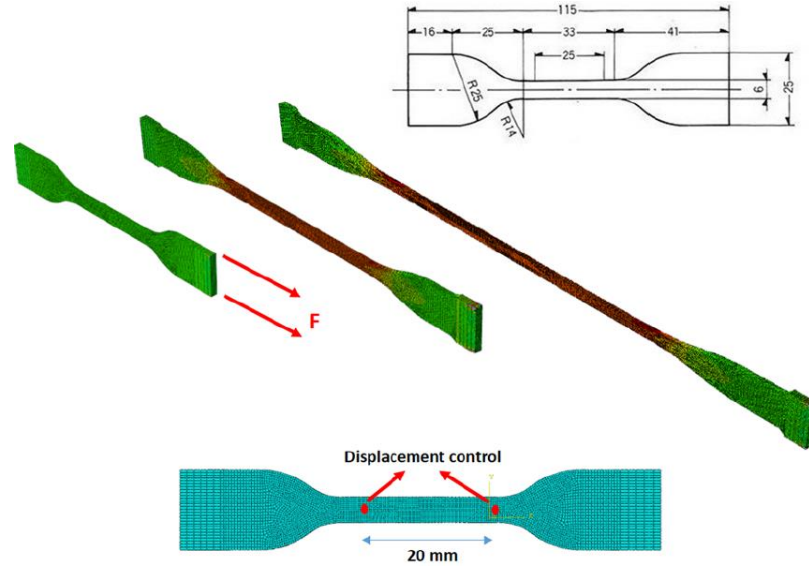

Fig. 2. 9. 3D finite element model of the rubber specimen undergoing uniaxial tensile test.
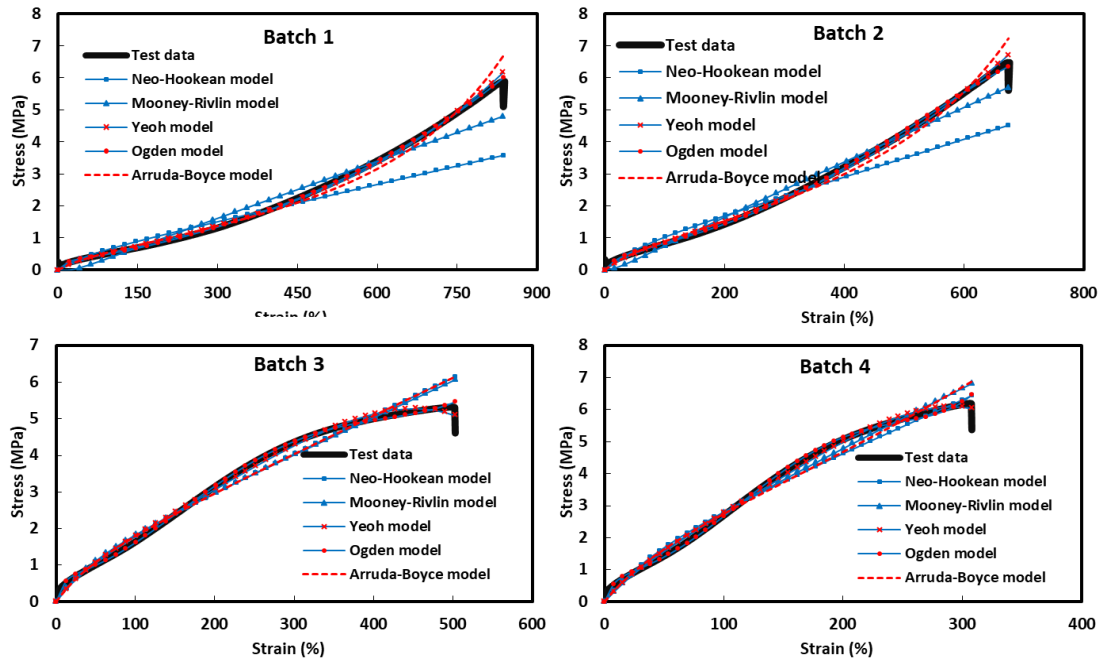

Fig. 2. 10. Comparative strain-stress curves of unaged specimens obtained through experimental test and numerical modeling.
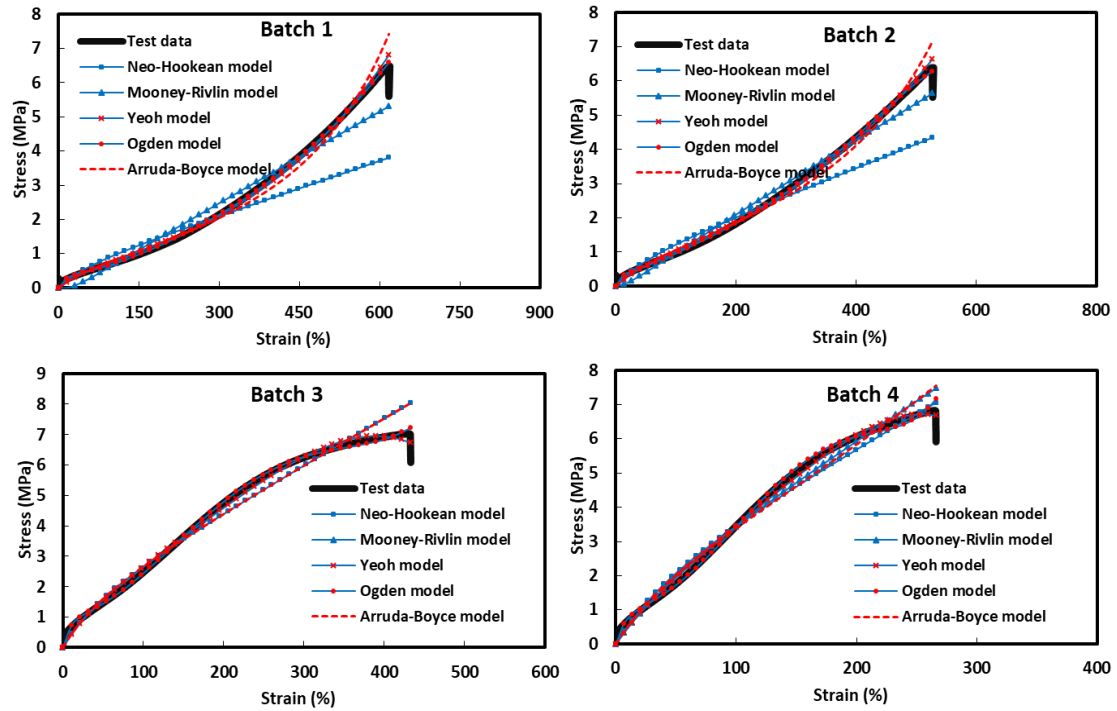
Fig. 2. 11. Comparative strain-stress curves of aged specimens obtained through experimental test and numerical modeling.

2.3.4. Viscoelasticity

The viscoelasticity parameters of rubber material can be derived from a relaxation test. In a one-dimensional relaxation test, the material is subjected to a sudden strain that is kept constant over the duration of the test, while the stress is recorded over time. The initial stress measured is due to the elastic response of the material. Over the time, the stress relaxes due to the viscous effects exhibited by the material. The device for relaxation test is the same as that for the uniaxial test. Rubber with higher damping ratio is represented by larger difference between the initial stress and the final stress at the end of relaxation period. The resulting stress versus time data can be fitted through Prony series model [29][30]. In the relaxation test, defining the strain-rate at sudden stretching phase is an important consideration. For seismic isolation purpose, a literature [30] suggests to stretch the specimen as quickly as possible to adjust the condition under seismic motion. High strain-rate about 50 mm/sec is recommended for the relaxation test. However, the device used in this study has a maximum strain rate about 40 mm/sec. Later on, such a maximum loading rate is observed sufficient to predict the damping behavior of the rubber isolator under seismic action.

In order to define the most suitable method for relaxation test, a series of preliminary tests are performed. Fig. 2. 12 presents the strain time history during the relaxation test: five relaxation tests are performed on similar low damping rubber. The first term of the specimen nomenclature describes the targeted strain: four different target strains are chosen: 50, 75, 100, and 150 %. The second term represents the strain rate at loading phase: 40mm/sec and 50 mm/min. For instance,

the specimen named "100%_40mm/s" is the test which is performed with 100% of target strain and 40 mm/s of strain rate at loading phase. The stress is then recorded over 600 seconds while the strain is kept constant to observe as long as possible the relaxation curve. The last specimen is tested under very low strain rate, 50 mm/min to see how the viscous effect varies with the change of the loading rate.
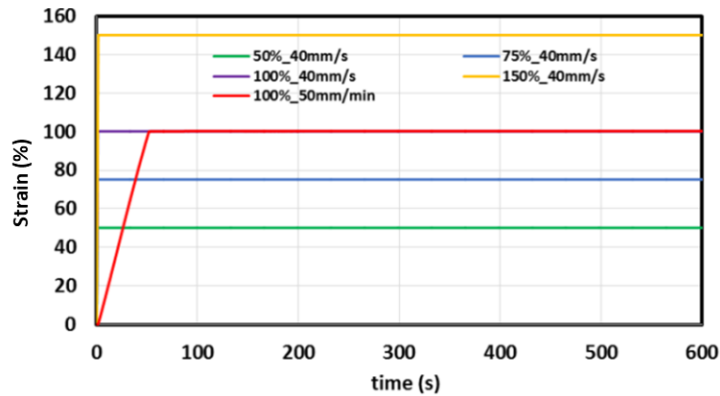

Fig. 2. 12. Strain time history performed in relaxation tests.

The recorded stresses over the relaxation period are presented in Fig. 2. 13a. The viscous effects are shown by the decrease of the recorded stress, particularly in the first seconds of relaxation periods. However, due to the high strain rate, remarkable inertia effects are observed when the specimens reach the targeted strain, see Fig. 2. 13b: the time axis is zoomed to 0-10 seconds. Two unexpected data points are observed and shall be removed in data post-processing. On the other hand, such an inertia effect is not present in case of low loading rate, as shown in the specimen 100%_50mm/min, see Fig. 2. 13c. Fig. 2. 13d presents the relaxation curves after data post processing.
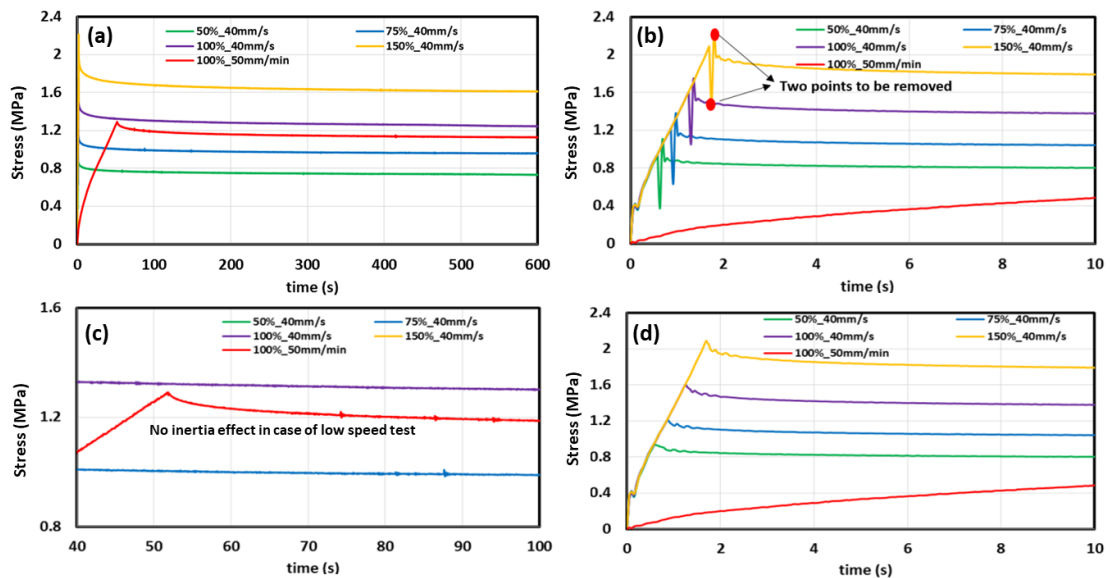

Fig. 2. 13. (a) Stress time history during relaxation period; (b) Unexpected data due to inertia effect in high rate stretching; (c) No inertia effect observed in low rate stretching; (d) Stress time history during relaxation period after post-processing.

Having established the post-processed data of relaxation tests as seen in Fig. 2. 13d, the next step is to transform the data in the form of normalized stress, see Fig. 2. 14 (red line). Later on, such normalized curves are used for Prony series fitting. In the normalized curve, the initial stress at t=0 is the value of stress, recorded right when the specimen reaches the target strain, that is normalized to 1. The relaxation period presented in Fig. 2. 14 is only up to 100 seconds because no remarkable stress reduction is observed after such period.

As shown in Fig. 2. 14, in case of relaxation tests with high strain rate, the stress relaxed up to 80% after 100 seconds. It applies for all tests with different target strain. On the other hand, in case of low strain rate, the stress relaxed up to 90% after 100 seconds of relaxation period. These results reveal thhat viscous effect is a rate dependent phenomenon: under low strain rate, the material is less viscous.
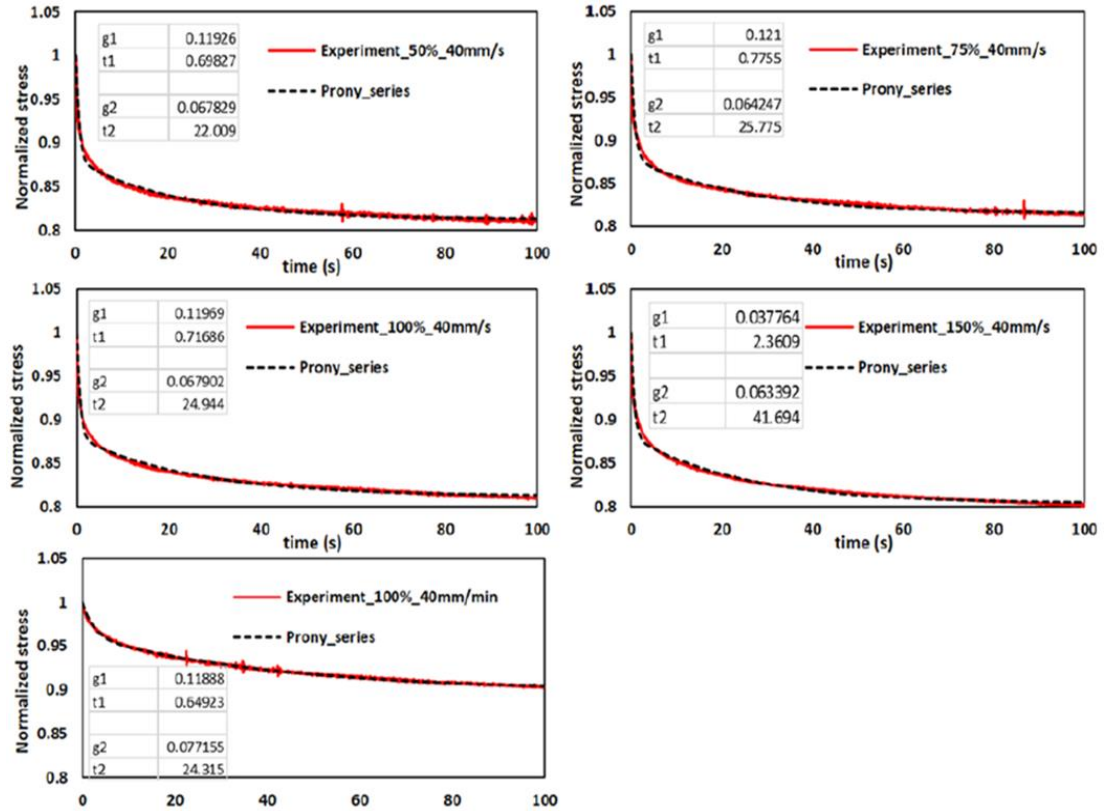

Fig. 2. 14. Relaxation curves obtained trough five relaxation tests and Prony model.

The relaxation curves presented in Fig. 2. 14 can be fitted by Prony series based on the viscoelastic generalized Maxwell model. It is a time-domain viscoelasticity available in Abaqus to determine te time-dependent stress-strain relation, as expressed below:

$$G(t) = G_\infty + \sum_{k=1}^{K} G_k e^{-t/\tau_k} = G_0 \left[1 - \sum_{k=1}^{K} g_k \left(1 - e^{-t/\tau_k}\right) \right] \tag{13}$$
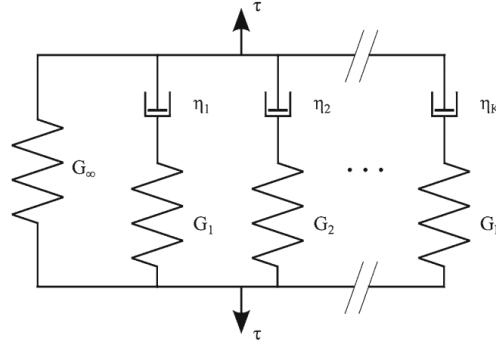
Fig. 2. 15. Rheological model of the generalized Maxwell model.

The generalized Maxwell model in Fig. 2. 15 represents the rheological model of the stress relaxation function G(t). The model is composed of a nonlinear elastic spring related to the hyperelastic part and a finite number of maxwell elements (spring and dashpots) that describes the viscoelasticity [31]: G_∞ is the final or equilibrium modulus; G_k and η_k are the modulus and viscosity of the kth element, respectively; τ_k is the relaxation time defined as $\tau_k = \eta_k/G_k$. In the software code Abaqus, the right hand side of Eq. 13 is applied: G_0 is the shear modulus at time t=0 and g_k is the dimensionless Prony coefficient. The parameters g_k and τ_k can be determined experimentally through relaxation test. For hyperelastic material, the relaxation coefficients are applied to the constants that define the energy function. For example, for the Yeoh hyperelastic model, the relaxation function is given by the equation 14:

$$C_{i0}^R(t) = C_{i0}^0 \left[1 - \sum_{i=1}^{N} g_k \left(1 - e^{-\frac{t}{\tau_k}} \right) \right] \tag{14}$$

The Prony series models for five relaxation data are presented also in Fig. 2. 14 (dashed black lines). The Prony series coefficients are shown inside the corresponding chart. In order to validate the obtained viscous parameters, five shear test simulations are performed using those five Prony models in Abaqus FE code. The simulation results are then compared to the experimental shear test performed in the laboratory. The shear test is performed based on ISO 1827: a rubber block with dimension 20x20x20 mm is subjected to three cycles of shear test with 0.5 Hz of frequency. In the numerical simulation, the hyperelastic properties follows the Yeoh model, which is found as the most efficient model. For the viscous parameters, five Prony series obtained in Fig. 2. 14 are applied to the five FE simulations in order to examine the accuracy of each model in fitting the shear test data.

The rubber part is meshed using C3D8R linear element, and the size of the mesh is about 1.5 mm, as shown in Fig. 2. 16. The description of five FE simulations are described in Table 2. 7: for instance, model 1 uses the Prony series coefficients obtained from the relaxation test 50%_40mm/s. As described in the previous section, such relaxation test is performed with 50% of target strain and 40 mm/s of strain rate.

Table 2. 7. Properties of the shear test FE simulation.

FE model	Viscous parameters	Damping ratio in FE model (%)	Damping ratio in experiment (%)	Error (%)
Model 1	50%_40mm/s	4.04		8.31
Model 2	75%_40mm/s	4.09		9.65
Model 3	100%_40mm/s	3.97	3.73	6.43
Model 4	150%_40mm/s	4.01		7.5
Model 5	100%_40mm/min	0.74		80.16

The comparative results between the provided experimental shear test data and the five FE simulations are presented in Fig. 2. 16. In can be clearly seen that model 5, which uses the Prony series coefficients from the low strain rate relaxation test, exhibits the worst curve compared to other four models. The viscous effect of the rubber in model 5 is barely observed. Table 2. 7 presents the error calculation of each FE model. The error is defined as the difference of resulted damping ratio between the experimental data and the simulation results. The computation of the shear modulus G and damping ratio ξ follows Eqs 15-18. The shear modulus and damping ratio are calculated based on the last loop of the cyclic shear test, when the curve in the experimental data remains stable. As shown in the Table 2. 7, model 3 using Prony series obtained from the relaxation test with target strain 100% and strain rate 40 mm/s results in the most accurate curve with 6.4% of error. Therefore, shear test model 3 is considered as the most suitable method in this study.

$$G = (F/A)/(u/hr) \tag{15}$$

$$\xi = W_d/(4\pi W_s) \tag{16}$$

$$W_s = \frac{1}{2} k_{H,eff} \Delta^2_{max,ave} \tag{17}$$

$$\Delta_{max,ave} = \frac{1}{2}\left(\Delta_{max} + |\Delta_{min}|\right) \tag{18}$$

where F is shear force force; A is rubber area parallel to the force; u is displacement; hr is height of rubber; W_d represents the dissipated energy (area within the loop) and W_s is the restored energy.
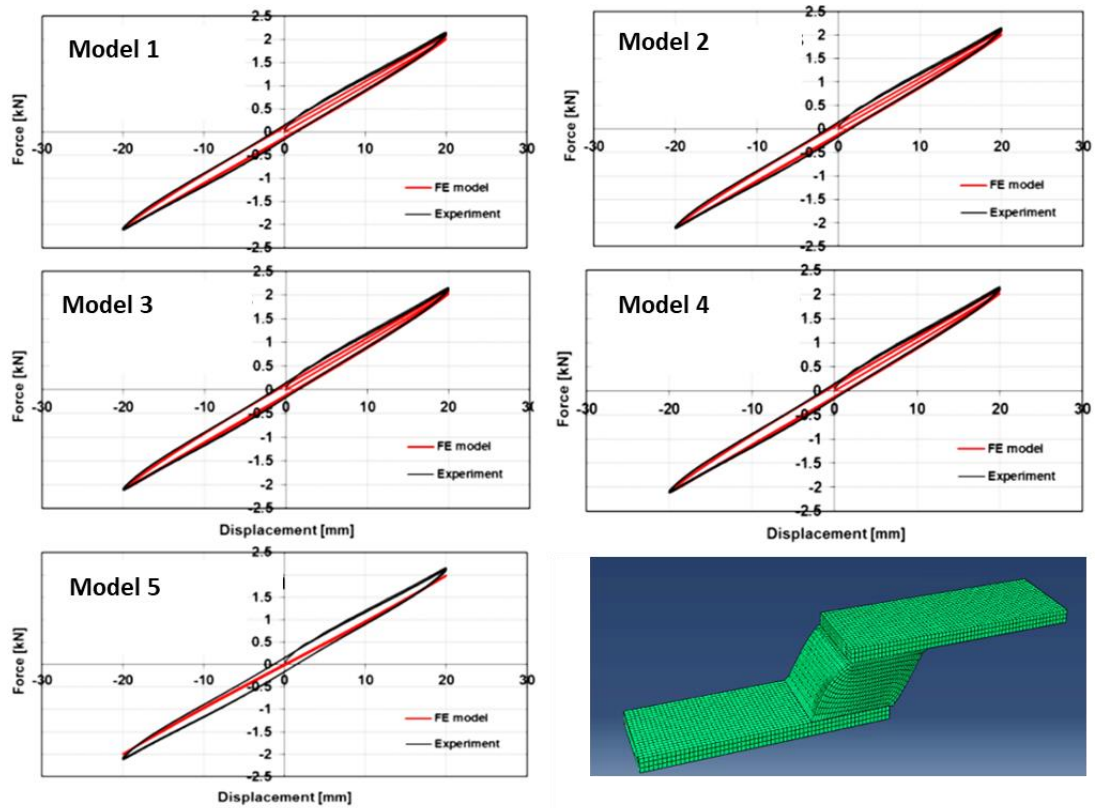
Fig. 2. 16. Displacement-force relations obtained from experimental test and five FE models.

Having defined the most accurate method for relaxation test, the viscoelasticity of four recycled rubber compounds under study is evaluated thourgh relaxation test. Fig. 2. 17 presents the normalized relaxation stress time history of four rubber batches before and after aging effect. The hard compounds, Batch 3 and 4, exhibit more viscous effects compared to the soft compounds, Batch 1 and 2, because the differences between the initial and final stress are larger. No significant difference is observed between Batch 1 and 2, and between Batch 3 and 4. For all specimens, aging causes a slight reduction of the viscous efffect on rubber. Those relaxation curves are well fitted by the Prony series model, see Fig. 2. 17 (dashed line): the Prony constants of four batches before and after aging are presented in Table 2. 8.

Table 2. 8. Coefficients of the Prony-series adopted for four recycled rubber batches

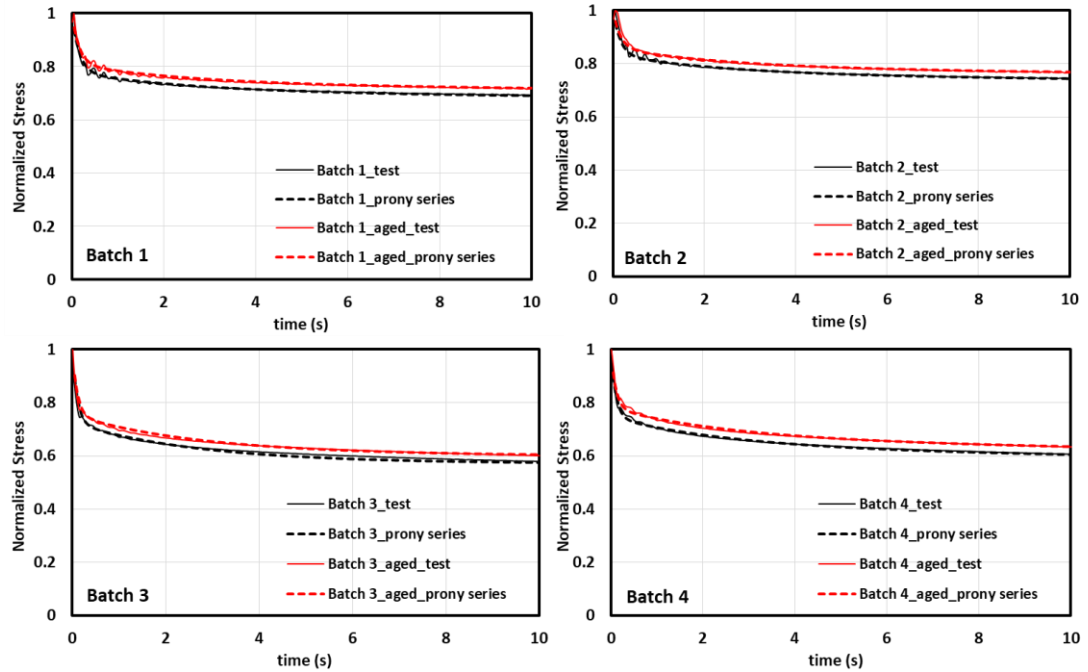| Rubber	Unaged				Aged			
	g_1	τ_1	g_2	τ_2	g_1	τ_1	g_2	τ_2
Batch 1	0.22	0.156	0.082	2.56	0.19	0.156	0.084	2.2
Batch 2	0.166	0.156	0.085	2.56	0.14	0.156	0.085	2.56
Batch 3	0.275	0.103	0.15	2.664	0.245	0.103	0.145	2.664
Batch 4	0.254	0.103	0.145	3	0.22	0.103	0.14	2.664

Fig. 2. 17. Relaxation curves of four recycled rubber batches before and after aging.

2.4. FE simulation on the reactivated EDPM rubber

After having defined the hyperelastic and viscous parameters of four recycled rubber compounds, a series of shear test simulations are performed to predict the shear modulus and damping ratio of the recycled rubbers. The FE model is similar to which described in Fig. 2. 16. Rubber blocks with dimension 20x20x20 mm are subjected to three cycles of shear test with 0.5 Hz of frequency. Fig. 2. 18 presents the results of shear test simulation on four recycled rubber batches, before and after aging. It can be seen that the aging effect causes the rubber stiffer. The differences of shear modulus and damping ratio before and after aging are computed and presented in Table 2. 9. Large stiffness changes are shown in Batch 1 and 3. Meanwhile, the change of damping ratio of four specimens are quite similar.
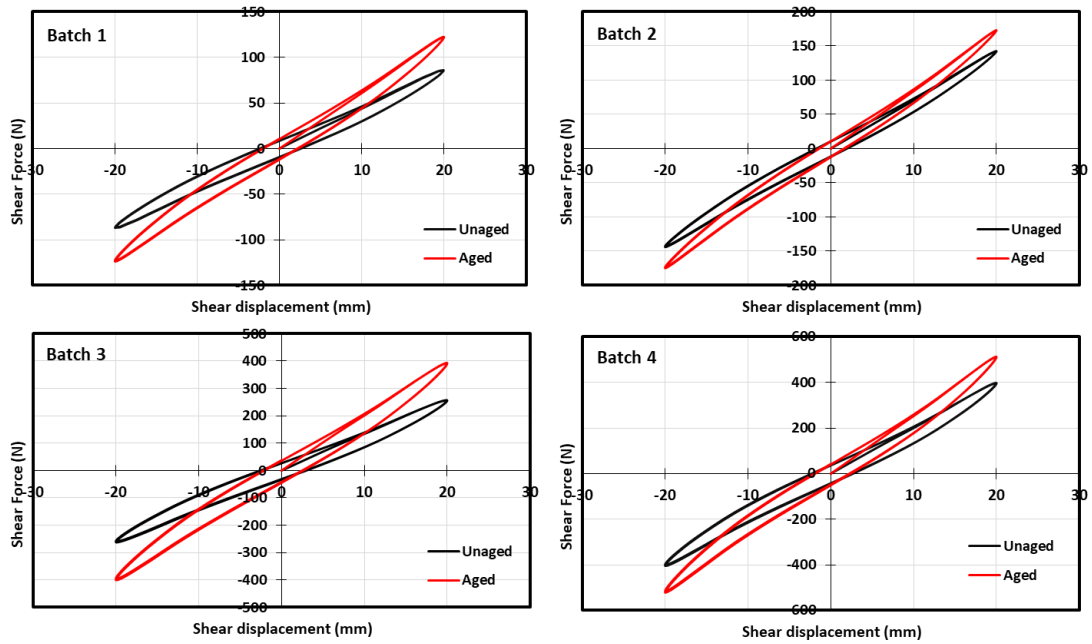
Fig. 2. 18. Shear displacement-force curves of four recycled rubber batches before and after aging.

Table 2. 9. Properties of four recycled rubber batches obtained from the shear test FE simulations.

Rubber	Unaged		Aged		ΔG (%)	Δξ (%)
	G (MPa)	ξ (%)	G (MPa)	ξ (%)		
Batch 1	0.215	5.43	0.305	4.539	41.96	-16.46
Batch 2	0.355	3.885	0.432	3.251	21.53	-16.30
Batch 3	0.639	5.925	0.98	5.15	53.1	-13.0
Batch 4	0.981	5.205	1.27	4.50	29.1	-13.53

2.5. Production and characterization of fiber reinforced elastomeric isolators (FREI)

After having fabricated the different rubber compounds, the fiber reinforcements and the vulcanization devices are prepared. Pre-treated woven glass fibers are used in this project. The fibers are dried with a primer to improve adhesion (chemical grip), see Fig. 2.16. The product is a commercial cover-coat adhesive (Megum 538 by Dupont), used in combination with an adhesive primer (Thixon by Dupont), commonly adopted for bonding rubber compounds to metals and other rigid substrates during vulcanization.

Fig. 2. 19. Relaxation curves of four recycled rubber batches before and after aging.

Fig. 2.17a presents the preparation of the rubber pads and fiber reinforcements having dimension 75x75 mm to be vulcanized in the mold, see Fig. 2.17b. As can be noted in 2.17d, the Shore A hardness is measured in the middle vertical section after knife cut. Some tribological damage of the cut surface is observed near the boundary for the utilization of a toothed knife. Five hardness measures were reported, four points near the section corners (point 2, 3, 4 and 5) and one in the center. A hardness of 58±2 in correspondence of the corners and of 48 ± 2 in the center is reported during measurement. On the other hand, rubber cube without fiber sheets provides a homogeneous hardness from the skin to the core of 62± 2.

Considering that an analogic durometer is used and due to non-flat and damaged surface obtained, the following considerations can be drawn:

▪ Mold and vulcanization temperature (130°C) are roughly suitable to obtain industrial items vulcanized in a proper and uniform manner.

▪ The lower hardness registered in correspondence of the center of the section confirms that the presence of GFRP sheets is detrimental, since it isolates further the core of the samples.

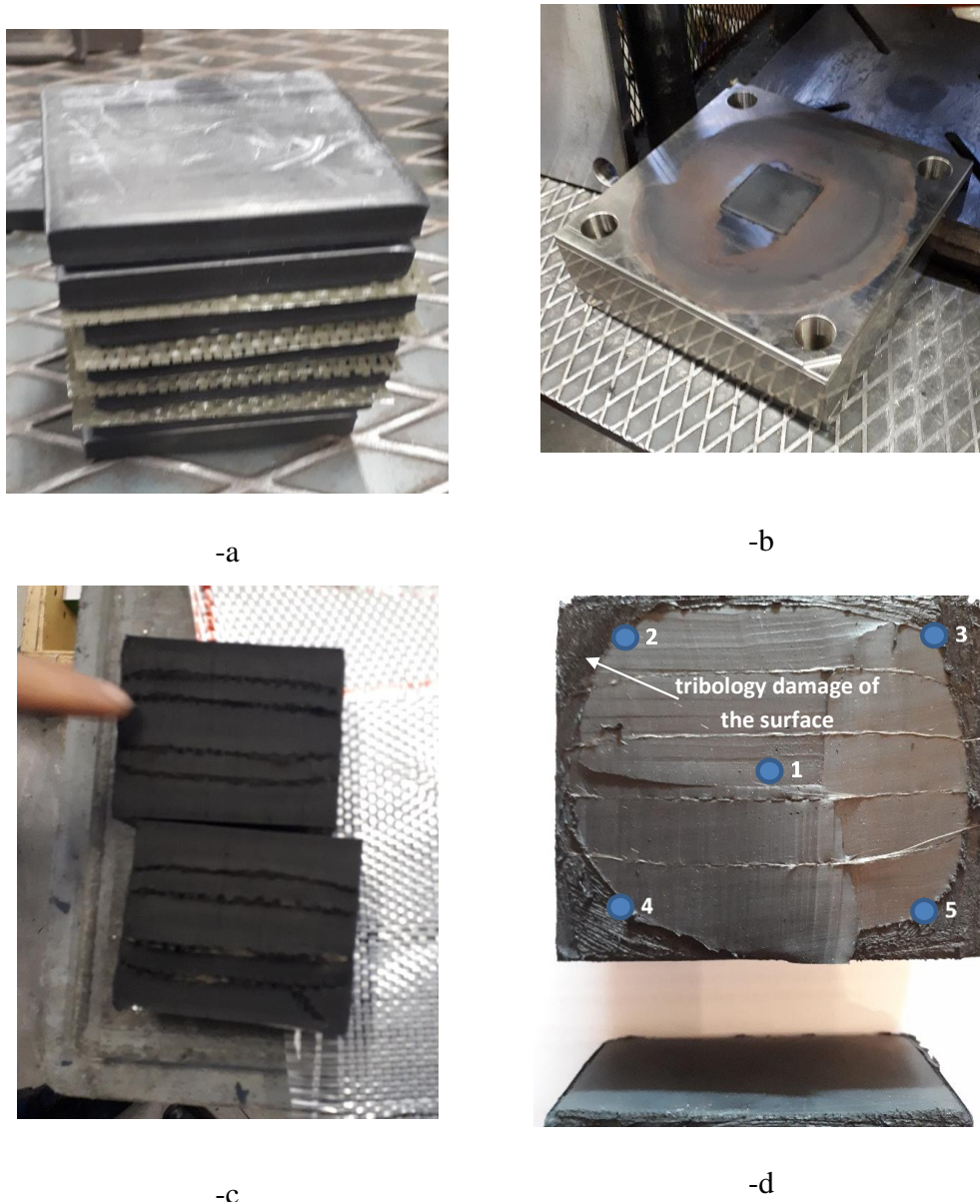▪ Final hardness is acceptable both in the core and near the skin.

-a

-b

-c

-d

Fig. 2. 20. Relaxation curves of four recycled rubber batches before and after aging.

2.6. Conclusions

A series of experimental tests on four different rubber compounds made of reactivated EPDM have been carried out including rheometer test, compression set, hardness test, uniaxial tensile test, and relaxation test.. Two commercial virgin rubbers Vistalon 3666 and Dutral 4038 are used to be blended with the regenerated EPDM to obtain blends with hardness 30±5 ShA and 60±5 ShA. Two different sources of reactivated EDPM (type A and B) are considered in this study to find the best receipt of the compound. Aging test is performed to evaluate the durability of the rubbers.

Regarding the rheometer test, the vulcanization at 150°C seems to be the most optimum method indicated by the highest MH obtained (moment highest) when

compared to other vulcanization temperatures. From the hardness test, it is found that compound 3A and 4B satisfy the requirement of the hardness variation before and after aging, indicated by their hardness variation after ageing below the range -5 to +8 Sh A. In the compression set test, all four compounds satisfy the requirement of compression set for rubber seismic isolators, where all the thickness variations after test are less than 30%.

In the uniaxial tensile test, the performance of four compounds containing regenerated EDPM are also compared to the virgin rubbers. It is found that the different formulations with regenerated EPDM, having comparable hardness with that of the virgin materials, generally exhibit a tensile strength. However, blends with type B regenerated rubber exhibits a much better performance than type A regenerated rubber. As expected, adding regenerated rubber results into a decrease of the strength with similar elongation at break. In the presence of ageing, the elongation at break decreases and the tensile strength slightly increases. A slight increase of hardness after ageing indicates that additional crosslinking is provided during ageing process, increasing the vulcanization degree of the compound.

Compound 4B (Dutral 4038+regenerated EPDM type B) presents the most satisfactory results before and after aging. It approximates better the performance of the corresponding virgin material, Dutral 4038. Quite satisfactory result is provided by compound 2B (Vistalon 3666 + regenerated EPDM type B), which presents alowable variation of tensile strength and elongation at break after ageing.

Finite element (FE) analyses are performed to predict the mechanical behavior of the considered compounds. The hyperelastic properties in the FE model are derived form the results of uniaxial tensile test, while the damping properties are derived from the results of relaxation test. Yeoh hyperelastic model seems to be the most accurate model in predicting the strain-stress relationship at moderate to large imposed strain. The relaxation test performed with 100% of strain and 40mm/s of strain rate results in the most accurate data used in predicting the damping behavior of the rubber through FE modeling.

In the production of the fiber reinforced elastomeric isolators (FREIs), the bonding between GFRP and rubber pad is provided by cover-coat adhesive used in combination with an adhesive primer. After the vulcanization, hardness test is performed at several points on the sliced FREI specimen. The shore A hardness at the middle of the pad is found considerably lower than which near the edge of the pad. On the other hand, a rubber cube without GFRP presents an identical hardness at any point. It confirms that the presence of GFRP sheets isolates further the core of the samples. However, the variation of the hardness in the rubber core are still in the acceptable range. It indicates that the performed production method in fabricating FREIs is suitable to produce standardized industrial items.

References

[1]   Coates, A. (2015). The commerce in rubber: the first 250 years.

[2]   Morawetz, H. (2000). History of rubber research. Rubber chemistry and technology, 73(3):405–426.

[3]   Guise-Richardson, C. (2010). Redefining vulcanization: Charles goodyear, patents, and industrial control, 1834-1865. Technology and Culture, 51(2):357–387.

[4]   Gregori, A., Castoro, C., Marano, G. C., & Greco, R. (2019). Strength Reduction Factor of Concrete with Recycled Rubber Aggregates from Tires. Journal of Materials in Civil Engineering, 31(8), 04019146.

[5]   Mendis, A. S., Al-Deen, S., & Ashraf, M. (2017). Effect of rubber particles on the flexural behaviour of reinforced crumbed rubber concrete beams. Construction and Building Materials, 154, 644-657.

[6]   Mendis, A. S., Al-Deen, S., & Ashraf, M. (2018). Flexural shear behaviour of reinforced Crumbed Rubber Concrete beam. Construction and Building Materials, 166, 779-791.

[7]   Tsang, H. H., Lo, S. H., Xu, X., & Neaz Sheikh, M. (2012). Seismic isolation for low-to-medium-rise buildings using granulated rubber–soil mixtures: numerical study. Earthquake engineering & structural dynamics, 41(14), 2009-2024.

[8]   Spizzuoco, M., Calabrese, A., & Serino, G. (2014). Innovative low-cost recycled rubber–fiber reinforced isolator: experimental tests and finite element analyses. Engineering Structures, 76, 99-111.

[9]   Habieb A.B., Valente M., Milani G. Base seismic isolation of a historical masonry church using fiber reinforced elastomeric isolators. Soil Dynamics and Earthquake Engineering 2019;120:127-145.

[10] Habieb A.B., Milani G., Tavio T. Two-step advanced numerical approach for the design of low-cost unbonded fiber reinforced elastomeric seismic isolation systems in new masonry buildings. Engineering Failure Analysis 2018;90:380-396.

[11] De Raaf M.G.P., Tait M.J., Toopchi-Nezhad H. Stability of fiber-reinforced elastomeric bearings in an unbonded application. Journal of Composite materials 2011;45:1873-1884.

[12] Calabrese A., Spizzuoco M.C., Serino G., Della Corte G., Maddaloni G. Shaking table investigation of a novel, low-cost, base isolation technology using recycled rubber. Structural Control and Health Monitoring 2015;22:107-122.

[13] Das A., Deb S.K., Dutta A. Shake table testing of un-reinforced brick masonry building test model isolated by U-FREI. Earthquake Engineering & Structural Dynamics 2016;45:253-272.

[14] Maddaloni, G., Caterino, N., & Occhiuzzi, A. (2017). Shake table investigation of a structure isolated by recycled rubber devices and magnetorheological dampers. Structural Control and Health Monitoring, 24(5), e1906.

[15] Mishra, H. K., Igarashi, A., & Matsushima, H. (2013). Finite element analysis and experimental verification of the scrap tire rubber pad isolator. Bulletin of Earthquake Engineering, 11(2), 687-707.

[16] Turer, A., & Özden, B. (2008). Seismic base isolation using low-cost Scrap Tire Pads (STP). Materials and Structures, 41(5), 891-908.

[17] Morales, E., Filiatrault, A., & Aref, A. (2017). Sustainable and low cost room seismic isolation for essential care units of hospitals in developing countries. In 16th World Conference on Earthquake Engineering. Santiago.

[18] UNI EN 15129: 2009 Anti-seismic devices.

[19] ISO 37: 2005. Rubber, vulcanized or thermoplasticdetermination of tensile stress-strain properties. International Organization for Standardization, Geneva.

[20]   Toopchi-Nezhad H., Tait M.J., Drysdale R.G. Bonded versus unbonded strip fiber reinforced elastomeric isolators: finite element analysis. Composite Structures 2011;93:850-859.

[21]   Ogden, R. W. Non-linear Elastic Deformations. Dover Publications, New York (1997): 560.

[22]   Mooney, M. (1940). A theory of large elastic deformation. Journal of applied physics, 11(9):582–592.

[23]   Bol, M., and S. Reese. Finite Element Modeling of Polymer Networks Based on Chain Statistics. in Constitutive Models for Rubber III, edited by Busfield, J.; and Muhr, A., A Balkema Publishers, UK (2003): 203-211

[24]   Yeoh, O. (1993). Some forms of the strain energy function for rubber. Rubber Chemistry and technology, 66(5):754–771.

[25]   Ghosh, P., A. Saha, and R. Mukhopadhyay. Prediction of Tyre Rolling Resistance using FEA in Constitutive Models for Rubber III, edited by Busfield, J., and A. Muhr, A Balkema Publishers, UK (2003): 141-145.

[26]   Ogden, R. W. (1972). Large deformation isotropic elasticity–on the correlation of theory and experiment for incompressible rubberlike solids. In Proc. R. Soc. Lond. A, volume 326, pages 565–584. The Royal Society.

[27]   Arruda, E. M. and Boyce, M. C. (1993). A three-dimensional constitutive model for the large stretch behavior of rubber elastic materials. Journal of the Mechanics and Physics of Solids, 41(2):389–412.

[28]   Seibert, D. J., and N. Schoche. (2000) Direct Comparison of Some Recent Rubber Elasticity Models. Rubber Chemistry and Technology, Volume 73: 366-384.

[29]   Tzikang, C. (2000). Determining a prony series for a viscoelastic material from time varying strain data.

[30]   Dalrymple, T., Choi, J., and Miller, K. (2007). Elastomer rate-dependence: A testing and material modeling methodology. In 172nd Technical Meeting of the Rubber Division of the American Chemical Society (ACS), Cleveland, OH, Oct, pages 16–18.

[31]   Kraus MA, Schuster M, Kuntsche J, Siebert G, Schneider J. Parameter identification methods for visco-and hyperelastic material models. Glass Struct Eng 2017;2(2):147–67.

Implementation of a simple novel Abaqus User Element to predict the behavior of unbonded fiber reinforced elastomeric isolators in macro-scale computations

The need for seismic protection of structures located in earthquake prone areas of developing countries has motivated several investigations of low-cost seismic isolators in recent years. One of the most promising device is the unbonded fiber reinforced elastomeric isolator (UFREI): in UFREIs no bonding or fastening is provided between the bearing and top-bottom supports and expensive thick steel plates are not required. The behavior of UFREIs is characterized by rollover and full-contact deformations under horizontal loads: the former decreases the effective stiffness of the isolation system, thus reducing the seismic demand, while the latter plays a key role in generating a hardening phase, thus limiting the horizontal displacement of the isolator under severe earthquakes. Such remarkable advantages highlight a great potential for world-wide UFREIs application. However, until now there is no representative UFREI model available in structural analysis software codes. In this work, a comprehensive but simple UFREI model is implemented in an ABAQUS user element (UEL), taking into account non-linear, hardening and hysteretic behavior of the bearing: in addition, multiple DOFs are considered to simulate the complex 3D behavior of UFREIs, which is characterized by horizontal and vertical displacements, rotation and torsion. The effectiveness of the UEL model is evaluated performing 3D FE dynamic time history analyses on a rigid slab supported by four different types of UFREI. The results show that the UEL model can reasonably fit the behavior of the detailed FE model, significantly reducing the computational efforts of the analyses. The UEL model proposed in this study can be particularly suitable for 3D dynamic time history analyses of complex base isolated structures.

Keywords: Fiber reinforced elastomeric isolator, Phenomenological model, ABAQUS user element, FE analysis.

3.1. Introduction

Different seismic protection strategies based on traditional or innovative approaches can be used to mitigate the effects of earthquakes on new and existing structures [1]-[5]. Conventional approaches are generally aimed at increasing the seismic capacity and ductility of the structure, using reinforced concrete shear walls, traditional or dissipative steel bracings, additional rigid frame systems and fiber reinforced polymer (FRP) materials [6]-[10]. Conversely, base isolation is an approach to earthquake resistant design and retrofitting that is based on the concept of reducing the seismic demand rather than increasing the seismic capacity of the structure [11][12]. It is a well-known method, widely used in structural seismic design, for reducing structural response and minimizing possible damage to structures due to strong earthquakes. The isolation devices, typically placed at the base of the structure, increase the flexibility of the structure and shift its fundamental frequency away from the dominant frequency of seismic excitations, thus significantly reducing displacements and accelerations. During the seismic event, the base isolated structure is expected to have negligible inelastic deformation and most of the energy is dissipated at the isolation level.

Conventionally, steel reinforced elastomeric and friction based devices are used for base isolation of structures and actually represent the most straightforward method of seismic isolation. In particular, a typical elastomeric isolator consists of a number of rubber pads and steel layers to provide high stiffness in the vertical direction along with large deformability in the horizontal direction. However, commercial rubber seismic isolators are generally too expensive for seismic protection of structures located in earthquake prone areas, above all in developing countries. For this reason, some investigations on different types of low-cost seismic isolator devices have been performed in recent years; in particular, some studies have focused on Unbonded Fiber Reinforced Elastomeric Isolators (UFREIs) [13]-[15]. In such typology of device, the top and bottom end steel connector plates of conventional isolators are removed. Moreover, fiber layers are used to substitute the steel shims and reduce the weight and cost of the bearing: the utilization of recycled rubber materials for UFREIs is also proposed in the literature [16][17].

Another remarkable advantage of UFREIs is the large deformability ensured by the so-called rollover deformation, followed by a hardening phase due to an increase of the contact zone with the substructure and superstructure. The rollover phenomenon initially decreases the horizontal stiffness, then favors the hardening phase at large deformations: such a hardening phase plays an advantageous role in limiting displacements during strong earthquakes [18]. Moreover, the combination of these features increases the effective damping of the bearing device [13][16].

At present, the application of UFREIs for seismic protection of structures is very limited: it is reported that the first UFREI-supported prototype masonry building constructed anywhere in the world is located in Tawang, India [20]. However, some experimental tests on shaking tables have proved that the application of UFREIs in

low-rise building may provide satisfactory results [21]-[23]. On the other hand, until now, several seismic codes permit only the utilization of bonded seismic isolators [24][25], indicating a need for a more advanced research on UFREIs.

Another important issue is related to the strategies of modeling UFREIs in structural analyses. As a matter of fact, the utilization of detailed 3D FE models of UFREIs is computationally expensive, with results not easily achievable for macro-scale computations in the non-linear dynamic range: therefore, the development of a simple and representative model is of paramount importance. Some works have recently presented a simplified numerical model of the horizontal behavior of UFREIs [26]-[28]. However, the behavior in compression, rotation and torsion is not taken sufficiently into account.

The aim of this work is to present a comprehensive but simple model for UFREIs: the model is implemented in Abaqus as user element (UEL) and takes into account the most important features exhibited by UFREIs, such as non-linear behavior and hardening phase. The UEL for UFREIs discussed in this paper is the extension of a UEL for commercial bonded isolators available in literature [29]. The extended UEL can be very useful for full 3D dynamic time history analyses of complex isolated structures through advanced FE codes, such as Abaqus [31], which allow accounting for material and geometric non-linearities. The application of the developed UEL for seismic protection of a historical masonry church is reported in a companion paper of the authors, [30].
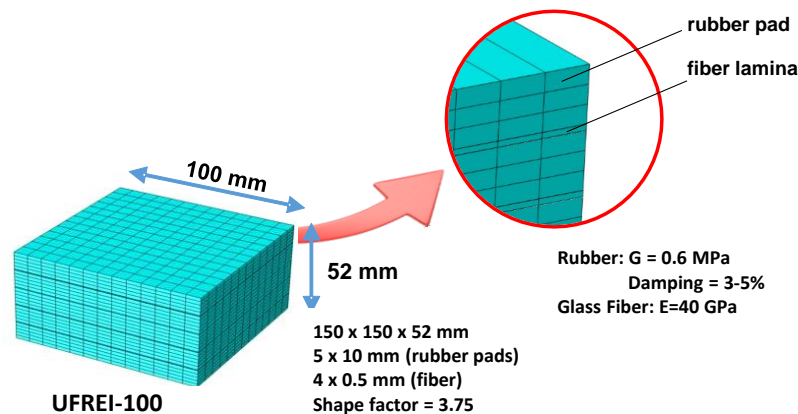

Fig. 3.1 3D FE model with indication of the main geometrical and mechanical characteristics of UFREI-100.

3.2. Phenomenological model of UFREIs behavior

In order to calibrate the mechanical properties of the UEL, a detailed 3D FE model of a newly conceived low-cost UFREI is developed. The isolator under study consists of few rubber pads from recycled tires and uses glass fiber reinforcements instead of steel laminas to improve the vertical stiffness; in addition, it presents unbonded boundary conditions (i.e. the upper and lower edges do not exhibit any bond with the supports), which significantly reduce manufacturing cost and weight. Fig. 3.1 shows the FE model and the main geometrical and mechanical

characteristics of the UFREI along with the refined discretization consisting of 8-node brick elements. The isolator, denoted as UFREI-100, presents a square section with sides equal to 100 mm and is 52 mm high: it consists of five 10 mm thick rubber pads and four 0.5 mm thick fibers. The mesh used for the rubber pad consists of C3D8R elements with dimensions equal to approximately 7.6 x 7.6 x 1.6 mm, while in the hardening analysis (section 2.2) the thickness is reduced to 1 mm because higher strain takes place. The meshing method validation has been discussed in a previous work by the authors [32] in order to fit the shear displacement-force curve obtained from an experimental test. The Yeoh strain-energy model is employed as hyperelastic material model for rubber pads. For a compressible rubber the model is expressed by Eq. (1):

$$W = \sum_{i=1}^{3} C_{i0}(I_1 - 3)^i + \sum_{i=1}^{3} \frac{1}{D_i}(J_{el} - 1)^{2i} \qquad (1)$$

where W is the strain energy density, C_{i0} and D_i are material coefficients, I_1 is the first deviatoric strain invariant and J_{el} is the elastic volume strain. In the present study, the values of the material coefficients are assumed by referring to the results of experimental and numerical studies on rubbers with different hardness, [33][34]. The values of the material coefficients for the Yeoh model adopted in this study are indicated in Table 3.1, corresponding to rubber with shear modulus G=0.6 MPa. The viscous damping is evaluated through the Prony-series model: the values of the coefficients of the model are presented in Table 3.2, corresponding to rubber with damping ratio equal to approximately 8%. The value of the shear modulus G and the damping ratio are initially obtained through a series of uniaxial tensile tests and relaxation tests, respectively. The fiber reinforcement is treated as a linear elastic isotropic material with Young modulus E=40 GPa and Poisson's ratio ν=0.20, in accordance with many references [20][35][14].
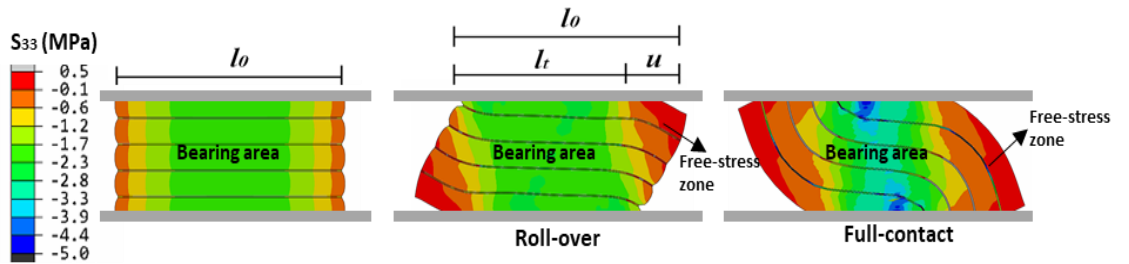

Fig. 3.2 Deformation modes and vertical stress distribution of UFREI-100 under constant vertical pressure equal to 1.17 MPa.

Table 3.1 Coefficients of the Yeoh hyperelastic model for UFREI-100 used in the numerical analyses.

C_{10}	C_{20}	C_{30}	D_1	D_2	D_3
0.47	0.0044	0.00013	0	0	0

Table 3.2 Coefficients of the Prony-series model for UFREI-100 used in the numerical analyses.

g_1	t_1	g_2	t_2
0.333	0.04	0.333	100

In the FE analysis presented in this study, the UFREI model is subjected to a 1 Hz cyclic horizontal displacement applied at the top under a constant vertical pressure equal to 1.17 MPa: such a pressure corresponds to the axial load carried by a single UFREI used for the isolation system of a masonry housing [36][37]. To provide an unbonded condition in the 3D FE model, a penalty friction coefficient equal to $\mu=0.85$ is introduced between the supports and the isolator. The maximum horizontal displacement imposed during the analysis is equal to $1.2h_r$ (h_r is the total thickness of rubber layers in the isolator). Fig. 3.2 shows the deformation modes and the vertical stress distributions of the UFREI under constant vertical pressure and Fig. 3.3 illustrates the corresponding cyclic horizontal behavior (lateral load - horizontal displacement curve) of the UFREI. The results highlight a remarkable non-linear behavior due to rollover deformations: it is worth mentioning that the non-linear behavior occurs when the horizontal stiffness of the UFREI decreases with increasing rollover deformations. A non-linear behavior is also observed in the compressive response of the UFREI under increasing horizontal displacements: Fig. 3.4 illustrates the evolution of the vertical stiffness during the last cycle of the lateral force – horizontal displacement curve.

These results indicate that the non-linearity occurs both in the horizontal and vertical behavior of the UFREI. Thus, the constant horizontal and vertical stiffness governed by the classical equations available in the literature [38] is not applicable anymore. A model of unbonded bearing proposed by Constantinou et. al and based on equilibrium and compatibility requirements can be found in the literature [39]. In this section, a phenomenological model to represent the behavior of UFREIs is proposed and described in detail.
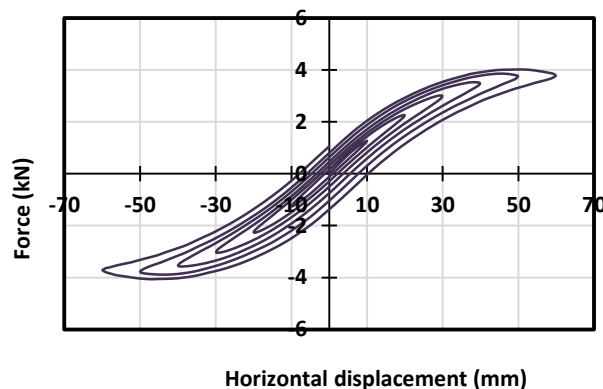

Fig. 3.3 3D FE model: lateral force – horizontal displacement curve of UFREI-100 under constant vertical pressure equal to 1.17 MPa.
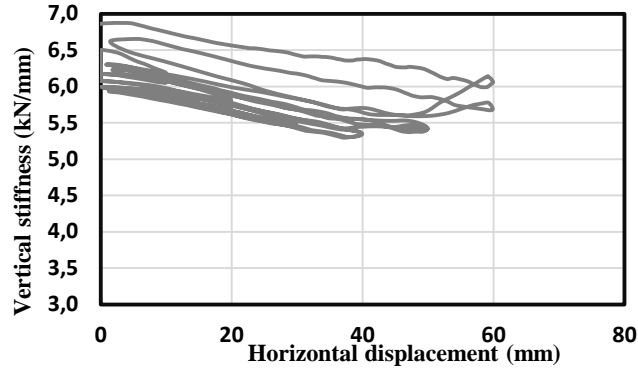
Fig. 3.4 3D FE model: evolution of the vertical stiffness during the lateral force – horizontal displacement curve.

3.2.1. Non-linear behavior

The horizontal response of UFREIs is non-linear and is affected by vertical loading and horizontal displacement: in this study it is described by using the equations (Eq. (2)-(11)). Such equations derive from the classical solution for commercial bonded isolators available in previous studies, [38][40], and modified by the authors for unbonded isolators. The main parameters involved are the following (see Fig. 3.2): b and l_0 are the sides lengths of a rectangular bearing (in 2D analyses, l_0 corresponds to the side parallel to the horizontal displacement); l_t is the effective length; S is the bearing shape factor; A_r is the bearing plan area; u is the horizontal displacement; m_l is the modification factor; t_r is the thickness of a single rubber pad; h_r is the total height of rubber; G is the shear modulus of rubber; h_b is the total height of the isolator; EI is the flexural rigidity of the isolator; EI_{eff} is the effective flexural rigidity of the isolator; E_r is the elastic modulus of rubber; P_e is the Euler load for the standard elastic element; GA_r is the shear rigidity of the isolator; k_H is the horizontal stiffness of the isolator. To take into account the vertical load effects, Eq. (11) considers the value of the square ratio of the existing load (P_L) to the critical load (P_{cr}), [38][40].

$$S = \frac{b \times l_t}{2(b+l_t) \times tr} \tag{2}$$

$$Ar = b \times l_t \tag{3}$$

$$l_t = l_0 - |\bar{u}| \tag{4}$$

$$l_t = l_0 - (|\bar{u}| \times m_l) \tag{5}$$

$$I = \frac{2}{3} l_t \left(\frac{b}{2}\right)^3 \tag{6}$$

$$Er = 4G(1 + 0.742\, S^2) \tag{7}$$

$$EI_{eff} = Er \times I\, \frac{h_b}{tr} \tag{8}$$

$$P_e = \pi^2 \times \frac{EI_{eff}}{h_r^2} \qquad (9)$$

$$P_{cr} = 2 \times \frac{P_e}{1+\sqrt{\left(1+4\pi^2\left(\frac{EI_{eff}}{G.Ar.h_r^2}\right)\right)}} \qquad (10)$$

$$k_{H=} G.Ar \frac{\left(1-\left(\frac{P_L}{P_{cr}}\right)^2\right)}{h_r} \qquad (11)$$

When the bearing undergoes horizontal displacements, the UFREI area Ar carrying vertical load decreases. Eq. (11) shows that the bearing area Ar gives a direct contribution to the horizontal stiffness of the bearing. In unbonded application, the value of the bearing area Ar varies as expressed in Eqs. (3)-(4) [41]. The remaining part is considered as a free-stress zone (Fig. 3.2), which does not experience any notable compressive and tensile stress [42]. However, the free-stress zone seems to contribute partially to the horizontal stiffness of the bearing. Fig. 3.5 shows the results obtained through the 3D FE model and the analytical model for the horizontal behavior of UFREI-100 under constant vertical pressure equal to 1.17 MPa. It can be noted that if Eq. (4) is directly used (it means that m_L=1 in Eq. 5), the horizontal stiffness seems too low when compared with that of the FE model. Thus, a modification factor m_L is introduced in order to partially involve the effect of the free-stress zone (Eq. (5)). In the present case, the optimum value of m_L is found to be 0.75, meaning that approximately 25% of the free-stress zone contributes to the horizontal stiffness during rollover deformations. The value of 0.75 for m_L is also recommended in [42].
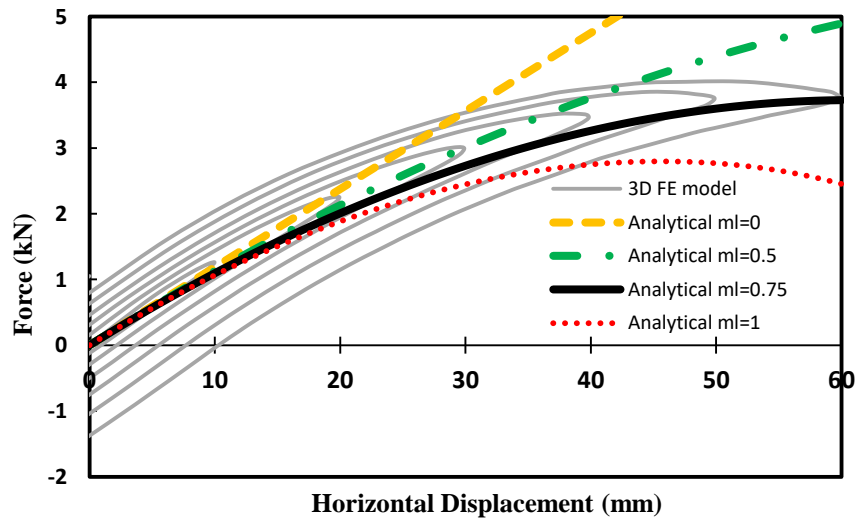

Fig. 3.5 3D FE model and analytical results for the horizontal behavior of UFREI-100 under constant vertical pressure equal to 1.17 MPa.
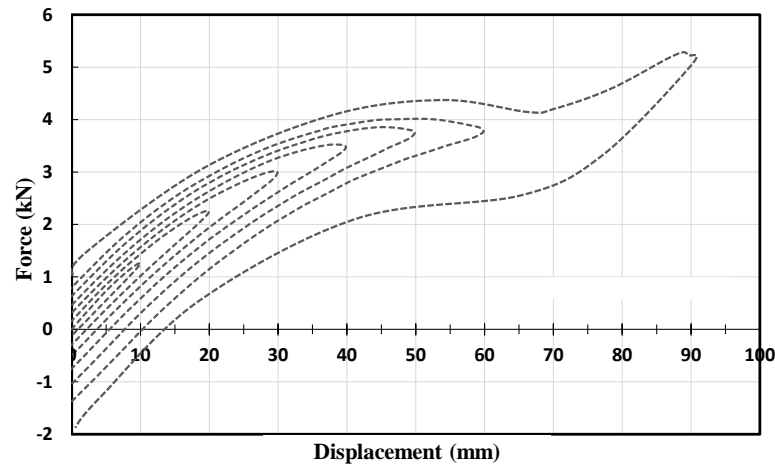
Fig. 3.6 Lateral force - horizontal displacement curve obtained through the 3D FE model for UFREI-100 up to a horizontal displacement equal to 1.75hr (90mm): detail of the hardening behavior at horizontal displacement equal to 1.35hr (70mm).

3.2.2. Hardening

At large lateral displacements, the UFREI experiences the so-called full-contact deformation: it means that the vertical faces of the isolator are in contact with the upper and bottom support surfaces, causing an increase of the horizontal stiffness of the isolator. Such a hardening phase of UFREIs is an open issue. Some researchers consider it as an unstable point that should be avoided because of the analysis complexity [20]. On the other hand, such a hardening phase is considered beneficial to limit horizontal displacements during strong earthquakes [18], behaving like a stopper device. Furthermore, some experimental tests have indicated that in presence of hardening up to horizontal displacements equal to $3h_r$ no remarkable damage is observed in the bearing [43]. Such a value of horizontal displacement is surprisingly higher than that of commercial bonded isolators, which is equal to only $1.5h_r$ [25][24]. Such a large deformability allows for the application of UFREIs with small height.

The hardening behavior of UFREIs has been implemented in the UEL code. To predict the hardening phase, a 3D FE cyclic analysis of UFREI-100 has been performed by increasing the horizontal displacement up to $1.75h_r$. It is worth mentioning that the model requires a fine mesh of the rubber and fiber elements to avoid excessive distortions at large displacements. Fig. 3.6 presents the lateral force-horizontal displacement curve of UFREI-100: the hardening behavior can be observed at horizontal displacements equal to $1.4h_r$ (70 mm). However, in other references [13][44], a higher value of the hardening point (about 1.6 h_r) is observed. A solution to predict when full rollover would occur in an isolator with fiber reinforcement can be found in the literature [45].
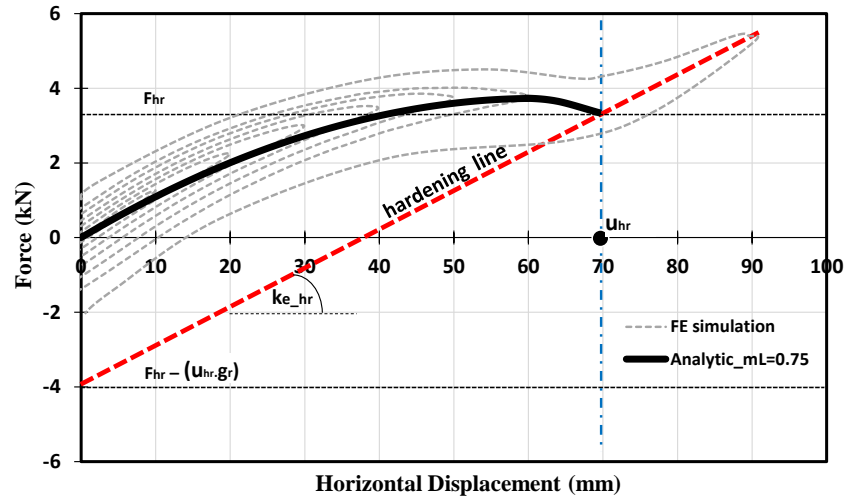
Fig. 3.7 Hardening line generated by the proposed procedure in the analytical model.

To simulate the results obtained from the FE analysis, some adaptations in Eqs. (2)-(11) should be performed once the hardening point is reached. Fig. 3.7 presents the analytical model (black line) discussed in previous section 2.1 and an additional hardening model (red line). The procedure to generate the hardening phase is explained as follows:

- The hardening point (u_{hr}) is set equal to $1.4h_r$ (70 mm).

- The gradient (gr) of the hardening line is estimated visually because it is highly complicated to compute analytically due to the irregular shape of a UFREI after exhibiting a full-contact deformation.

- The variable u (horizontal displacement) in Eq. (5) is replaced by the value of u_{hr}, see Eq. (12). Then, Eqs. (6)-(10) are subsequently used to obtain the horizontal stiffness k_{hr} (Eq. (13)).

- The horizontal stiffness k_{hr} (Eq. (13)) is introduced in Eq. (14) to compute F_{hr}, which is the value of the force corresponding to the hardening point, see Fig. 3.7.

- Finally, when the horizontal displacement u is larger than u_{hr}, the effective horizontal stiffness k_{e_hr}, see Eq. (15), is used to compute the horizontal force of the model, see Fig. 3.7.

$$l_t = l_0 - (|u_{hr}| \times m_l) \qquad (12)$$

$$k_{hr} = G.Ar \frac{\left(1-\left(\frac{P_L}{P_{cr}}\right)^2\right)}{h_r} \qquad (13)$$

$$F_{hr} = k_{hr} \times u_{hr} \qquad (14)$$

$$k_{e\_hr} = gr.\frac{F_{hr}-(u_{hr}.\,gr\,)}{u} \qquad (15)$$

3.2.3. Bouc-Wen hysteresis

Once the stiffness variation of the bearing is known, the next step is to reproduce the hysteretic behavior under cyclic displacements. Some references [46][47] represent the behavior of commercial isolators by adopting a bilinear model, which is the simplest one. However, this model is not so accurate to describe the non-linear behavior of an isolator. On the other hand, the classical Bouc-Wen model has been widely implemented to effectively represent the hysteretic behavior of seismic isolators. An extended version of the classical Bouc-Wen model is also reported in the literature: the force of the isolator has been modeled with a second and third order polynomial in terms of the lateral displacement of the isolator [28]. Moreover, other authors have proposed a fifth order polynomial to capture the non-linear behavior and the hardening phase [27]. In this study the authors develop a UFREI model based on the classical form of the Bouc-Wen model, taking into account both the non-linear behavior and the hardening phase. As aforementioned, this behavior is simulated by varying the bearing stiffness as a function of the horizontal displacement. This procedure is more suitable to explain the evolution of the macro-scale bearing behavior than using a high-degree polynomial equation. In addition, the computational effort is less because the latter requires more optimization steps to determine more unknown coefficients.

In the Bouc-Wen model used in this study, Eqs. (16)-(17), the biaxial interaction between the X and Y directions is taken into account for 3D analyses [29][48].

$$\begin{bmatrix} F_x \\ F_y \end{bmatrix} = k_H \cdot \begin{bmatrix} u_x \\ u_y \end{bmatrix} + c_d \cdot \begin{bmatrix} \dot{u}_x \\ \dot{u}_y \end{bmatrix} + w \begin{bmatrix} z_x \\ z_y \end{bmatrix} \tag{16}$$

$$Y \begin{bmatrix} \dot{z}_x \\ \dot{z}_y \end{bmatrix} = \left(A[I] - \begin{bmatrix} z_x{}^2(\gamma \cdot sign(\dot{u}_x z_x) + \beta) & z_x z_y(\gamma \cdot sign(\dot{u}_x z_x) + \beta) \\ z_x z_y(\gamma \cdot sign(\dot{u}_x z_x) + \beta) & z_y{}^2(\gamma \cdot sign(\dot{u}_y z_y) + \beta) \end{bmatrix} \right) \begin{bmatrix} \dot{u}_x \\ \dot{u}_y \end{bmatrix} \tag{17}$$

The main parameters involved are the following: F is the restoring force, k_H is the horizontal stiffness of the bearing, c_d is the damping coefficient and u is the horizontal displacement. Moreover, w, Y, γ and β are the Bouc-Wen constants controlling the shape of the hysteretic loop. The variable z is a non-physical parameter governing the hysteretic loop of the isolator based on a differential equation (Eq. (17)). To solve numerically the Bouc-Wen equation, a standard Newton-Raphson procedure is executed.

3.2.4. Vertical stiffness

Another main feature of a base isolator is the vertical stiffness, which influences the global behavior of the isolated structure, especially in the case of moment-resisting frames. A classical expression to predict the vertical stiffness of BFREIs can be found in the literature [38]: an adaptation is required for the case of UFREIs. In fact, the vertical stiffness of UFREIs varies significantly with the horizontal displacement. When the bearing starts to deform, the bearing area carrying the

vertical load decreases (see Fig. 3.2). However, as in the case of the horizontal stiffness, the free-stress zone partially contributes to the vertical stiffness, as expressed in Eq. (18). In this case, the modification factor m_C is found to be equal to 0.25, meaning that 75% of the free-stress area contributes to the vertical stiffness.
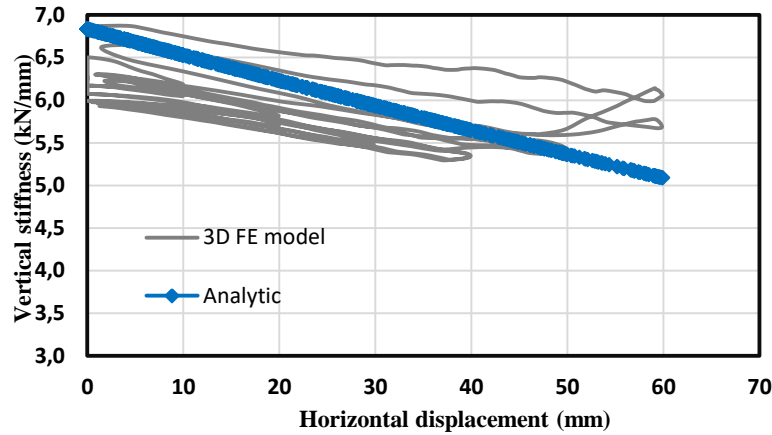

Fig. 3.8 Vertical stiffness as a function of the horizontal displacement: 3D FE model and analytical results.

As shown in Eqs. (18)-(20), the vertical stiffness (k_v) varies because the values of the shape factor S (Eq. (2)) and effective length (l_{t_c}) change as a function of the horizontal displacement u. Fig. 3.8 shows the variation of the vertical stiffness of UFREI-100 as a function of the horizontal displacement: it is obtained through the 3D FE model and the analytical solution. The hysteretic behavior of the bearing in the vertical direction is neglected as the dissipation in the vertical direction does not significantly influence the global behavior of an isolated structure: thus, the application of the Bouc-Wen model is not strictly required. The proposed solution for the vertical stiffness is activated only when the bearing is under compression. As the UFREI does not present any bonding with the superstructure, the vertical stiffness is assumed equal to zero when subjected to tensile loads. Therefore, the overturning stability of an isolated structure supported on UFREIs must be carefully checked.

$$l_{t\_c} = l_0 - (|\bar{u}| \times m_c) \qquad (18)$$

$$E_c = 6.748 \, G \times S^2 \qquad (19)$$

$$k_V = \frac{E_c \cdot b \cdot l_{t\_c}}{h_r} \qquad (20)$$

3.2.5. Rotational and torsional stiffness

The torsional and rotational behaviors of base isolators are sometimes considered in structural analyses, mainly in the case of frame structures. Classical solutions for rotational and torsional stiffness of commercial isolators are available in the literature, but limited to bonded bearings [38][39][49]. In this study, a FE approach

based on the detailed 3D FE model is used to evaluate if the classical solutions valid for BFREIs can be adopted with some modifications for UFREIs.
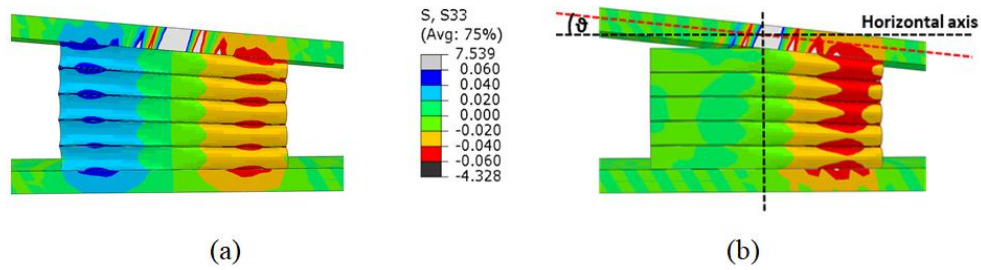

Fig. 3.9 Rotational deformation of (a) bonded and (b) unbonded FREI, corresponding vertical stress distribution (MPa) and indication of the rotational angle (ϑ).

Fig. 3.9 shows the rotational deformation of bonded and unbonded FREIs and the corresponding vertical stress distribution, along with an indication of the rotational angle (ϑ) in Fig. 3.9b. Fig. 3.10 compares the results obtained through 3D FE models and analytical solutions for the rotational behavior of bonded and unbonded FREIs. In the unbonded case, a free-stress zone arises, decreasing the rotational stiffness of the bearing. On the contrary, in the bonded case, all the parts of the bearing contribute to the rotational stiffness, in the form of compressive or tensile stress. According to the literature [50], the rotational stiffness of UFREIs may be estimated as equal to 75% of that of BFREIs, see Eq. (21) and Fig. 3.10.

According to the authors' knowledge, there are no studies reported in the literature focusing on the torsional behavior of UFREIs. Some works dealing with the analysis of base isolated structures supported on UFREIs have neglected the contribution of the torsional stiffness in the model [51][52][22]. It has to be pointed out that a classical solution to predict the torsional stiffness of a single BFREI is available [49]: thus, in the present study a 3D FE simulation is performed to evaluate an adjustment of the classical solution for UFREIs as the interfaces may slide due to bonding absence. Fig. 3.11 shows the torsional deformation of bonded and unbonded FREIs and the corresponding Mises stress distributions. A notable difference of Mises stress distribution between the two models can be observed only at the top and bottom surfaces of the FREIs, mainly at the edges. Fig. 3.12 compares the results obtained through bonded and unbonded FREIs models and the analytical model based on Eq. (22). In this case, it is found that the unbonded model does not cause any notable reduction of torsional stiffness due to friction and vertical pre-loading. On the other hand, the analytical solution based on Eq. (22) provides smaller values of torsional moment than the FE models: in any case, the difference seems negligible in a structural analysis and may be probably due to the vertical pre-loading effect, which is not taken into account in the analytical model.
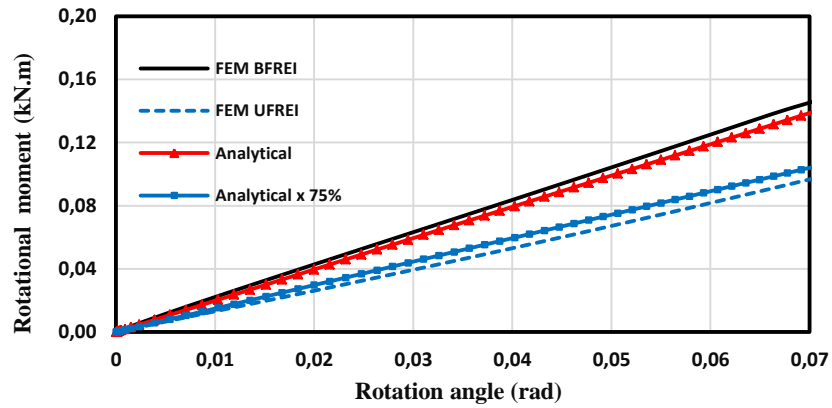
Fig. 3.10 Comparative results of the rotational behavior for bonded and unbonded FREI: 3D FE models and analytical solutions.

It has to be observed that in Eqs. (21)-(22) E_r is the rotation modulus of the bearing, I_s is the inertia moment about an axis of rotation in the horizontal plane and I_t is the inertia moment about the vertical axis. For a symmetric bearing, $I_t = 2.I_s$. A list of rotation moduli for different shapes of elastomeric bearings is available in the literature [39]. Finally, both rotational and torsional stiffnesses of UFREIs are considered as constant because they do not significantly affect the global behavior of a seismically isolated structure [49].

$$k_R = \frac{E_r.I_s}{h_r}.75\% \tag{21}$$

$$k_T = \frac{2GI_t}{h_r} \tag{22}$$
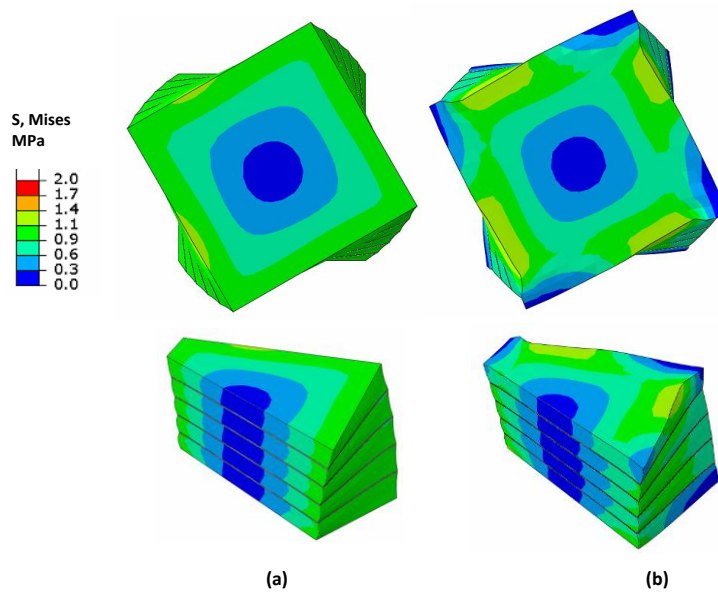

(a)   (b)

Fig. 3.11 Torsional deformation of (a) bonded and (b) unbonded FREI and corresponding Von Mises stress distribution.
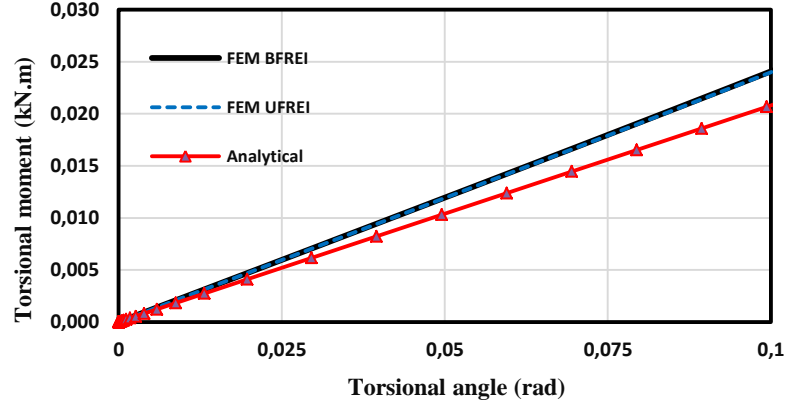
Fig. 3.12 Comparative results of the torsional behavior of bonded and unbonded FREIs: 3D FE models and analytical solution.

3.3. Implementation in ABAQUS Subroutine

To simulate the behavior of the base isolator, a 2-node 12-DOF beam element is considered as the basic form of the UEL model connecting the substructure and the superstructure [49]. Fig. 3.13 illustrates the schematic representation of the UEL with 2 nodes, each of them presenting six DOFs: axial (U1) and shear (U2 and U3) behavior, torsion (UR1) and rotation (UR2 and UR3). The analytical solutions obtained in the previous sections are then implemented into an Abaqus UEL developed in the literature only for commercial BFREIs [49]. The general form of element force vector, f_b, and element stiffness matrix, K_b, is expressed by Eq. (23).

$$f_b = \begin{bmatrix} axial(U1) \\ shear1(U2) \\ shear2(U3) \\ tors(UR1) \\ rot1(UR2) \\ rot2(UR3) \end{bmatrix} ; K_b = \begin{bmatrix} axial & 0 & 0 & 0 & 0 & 0 \\ 0 & shear1 & shear12 & 0 & 0 & 0 \\ 0 & shear21 & shear2 & 0 & 0 & 0 \\ 0 & 0 & 0 & tors. & 0 & 0 \\ 0 & 0 & 0 & 0 & rot1 & 0 \\ 0 & 0 & 0 & 0 & 0 & rot2 \end{bmatrix} \quad (23)$$

The axial behavior (U1) is governed by the solution of the vertical stiffness k_V (Eq.(20)), in which the coupling with the horizontal displacement is already taken into account. The horizontal stiffness k_H (Eq.11) in combination with the Bouc-Wen model (Eqs. (16)-(17)) are used to characterize the shear behavior (U2 and U3), which is considered as a coupled mechanism. Finally, the torsional stiffness k_T (Eq. (22)) governs the torsional behavior (UR1) and the rotational stiffness k_R (Eq. (21)) characterizes the rotational behavior (UR2 and UR3).
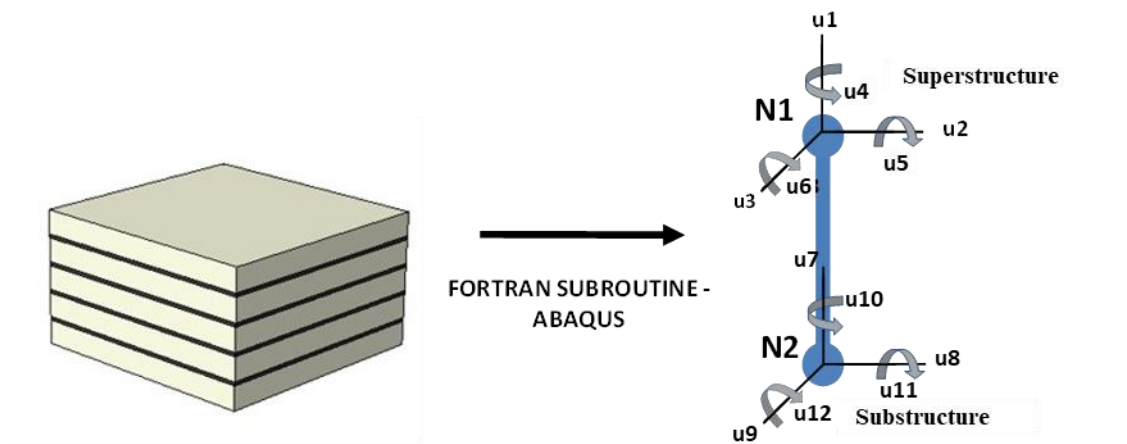
Fig. 3.13 Simplified representation of the bearing: global nodal representation of the User Element (UEL) with 2 nodes and 12 DOFs.

To solve the differential equations of the Bouc-Wen model (Eqs. (16)-(17)), a standard Newton-Raphson procedure is executed in the UEL code.

Finally, a numerical simulation is performed by applying a 1 Hz cyclic horizontal displacement and a constant vertical pressure (1.17 MPa) on the UEL and the 3D FE models of UFREI-100, Figs. 14 and 15. A satisfactory performance of the UEL model can be observed when compared with the results obtained through the detailed 3D FE model, without and with hardening. However, it can be noted that the UEL model provides thinner loops around the origin than those observed for the 3D FE model. The optimum values of the UEL and Bouc-Wen parameters for the UFREI-100 are presented in Table 3.4.
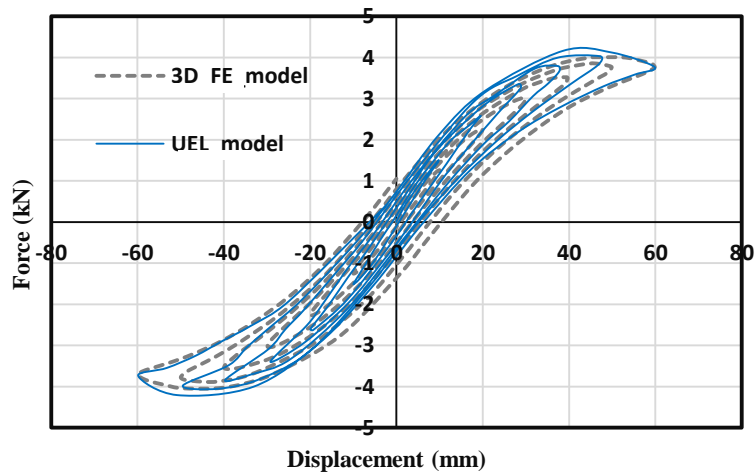

Fig.14 Lateral force – horizontal displacement curves (without hardening) obtained through UEL and 3D FE model of UFREI-100 under constant vertical pressure equal to 1.17 MPa.
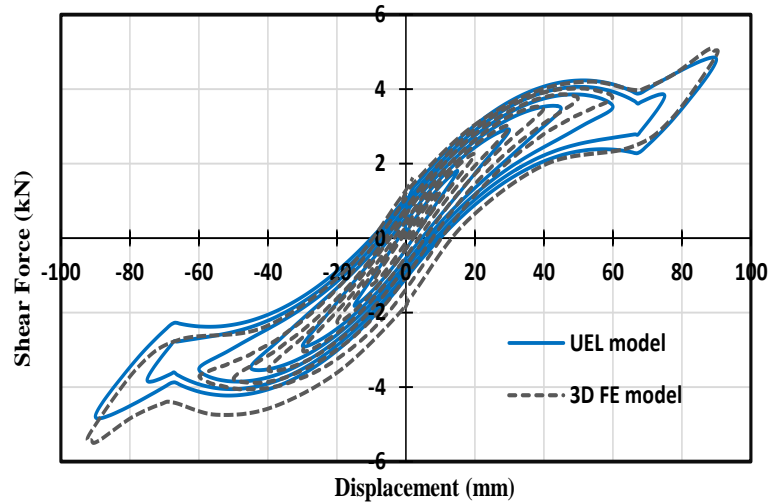
Fig. 3.15 Lateral force – horizontal displacement curves (with hardening) obtained through UEL and 3D FE model of UFREI-100 under constant vertical pressure equal to 1.17 MPa.

3.4. Validation of the proposed UEL model through experimental tests

Some results of experimental tests performed on UFREIs available in the literature are used to evaluate the applicability of the UEL model for a wide range of UFREIs geometry. The properties and geometry of the specimens considered in this study are presented in Table 3.3. It is worth mentioning that the aspect ratio R is the ratio between the length and the total height of the isolator.

The comparison of the lateral load - lateral displacement curves obtained in the experimental tests and through the UEL model is presented in Fig. 3.16, while the Bouc-Wen and UEL parameters adopted for the different models are shown in Table 3.4. Observing the results, it can be noted that the hysteretic behavior of specimens B1 and B3 is mainly characterized by viscous damping, while the hysteretic response of specimens B2 and B4 is characterized by yield strength (w). Indeed, Table 3.4 reports $w=0$ for specimens B1 and B3 and small value of damping coefficient c_d for specimens B2 and B4.

In specimen B1, the value of c_d is significantly larger than the other specimens because of the very low frequency of the shear test, see Table 3.3.

The small aspect ratio R of the specimen B4 may justify the significantly higher tangential stiffness at the first cycle than in the last cycle: in addition, specimen B4 was tested under small shear strain. The small aspect ratio and small shear strain imposed may produce the hysteretic behavior that is characterized by yield strength with a larger loop area than the other specimens.

The UEL parameter m_L varies between 0.75-0.80 for all the specimens considered, except for specimen B2. Meanwhile, the value of the hardening point u_{hr}

equal to 1.6 is obtained for specimens B2 and B3. It is worth mentioning that the other UFREIs were not tested up to the hardening phase.

Fig. 3.16 shows that, in general, the UEL model can reasonably fit the shear behavior of UFREIs with different geometries by implementing the suitable Bouc-Wen and UEL parameters. However, some negligible inaccuracies are present: for instance, the UEL model cannot capture the multiple hardening presented in specimen B2 and the larger loop area in the hardening phase experienced by specimen

Table 3.3. Properties and geometry of the UFREIs tested in the literature.

Properties	B1	B2	B3	B4
Reference	[20]	[19]	[44]	[16]
Dimension (mm)	310 x 310 x 100	70 x 70x25	60x60x 22.4	70x70x63
Single rubber thickness, t (mm)	5	1.58	3.18	5
Number of pads, n	18	12	5	12
Fiber thickness, tf (mm)	0.55	0.54	0.55	0.07
Shape factor, S	15.5	11.07	4.6	3.5
Aspect ratio, R	3.1	2.8	2.6	1.1
Rubber shear modulus, G (MPa)	0.9	0.4	0.4	0.7
Fiber Young modulus, Ef (GPa)	40	-	20	14
Applied axial load (MPa)	5.6	1.6	2	1
Cyclic shear test frequency (Hz)	0.025	1	0.75	1

Table 3.4. Bouc-Wen and UEL parameters adopted for the different models.

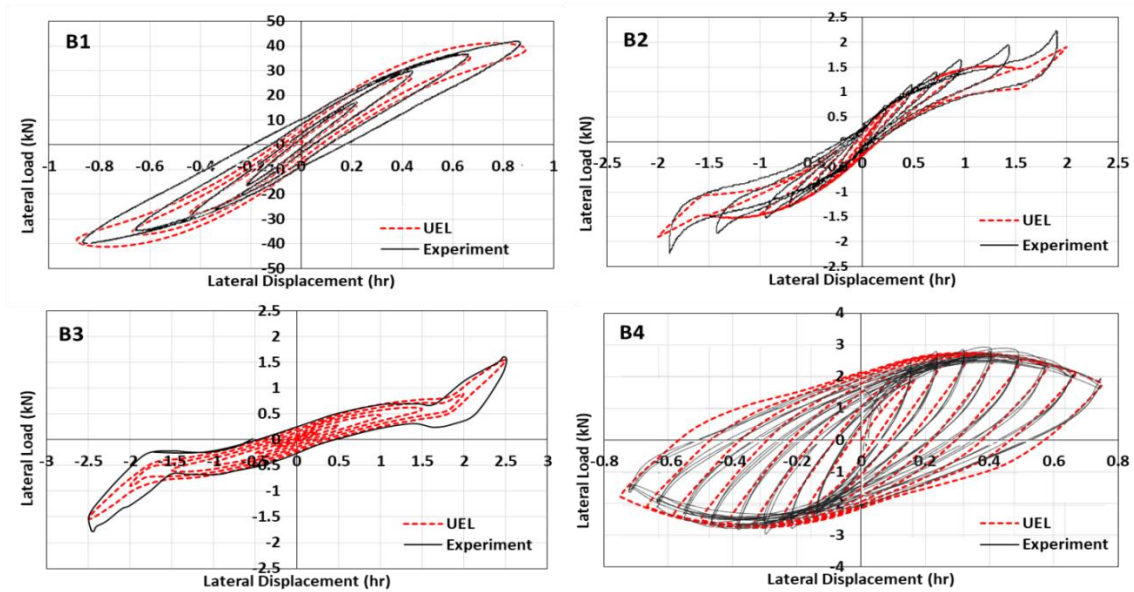| Coefficient	3D FE	Test Specimens			
	UFREI-100	B1	B2	B3	B4
A	1	1	1	1	1
n	1	1	1	1	1
w (N)	100	200	300	50	1600
β	0.15	0.15	0.15	0.15	0.15
Y	0.005	0.005	0.005	0.005	0.008
γ	0.45	0.45	0.45	0.45	0.45
c_d (N.s/mm)	7.5	625	0.5	1.5	0.5
m_L	0.75	0.75	0.55	0.80	0.75
u_{hr}	1.4 hr	-	1.6 hr	1.6 hr	-

Fig. 3.16 Comparison of results obtained from experimental tests and UEL model for different UFREIs geometry.

3.5. Verification of the UEL model for UFREIs through 3D FE dynamic analyses

To evaluate the effectiveness of the Abaqus UEL proposed in this study, 3D dynamic time history analyses of an isolated rigid square slab are performed. Fig. 3.17 shows the geometrical model of the isolated rigid square slab with sides equal to

2 m using detailed 3D FE models and Abaqus UEL models for the four isolators located at the corners. To simulate the 3D behavior of the isolation system including torsion and rotation during the seismic excitation, four UFREIs characterized by different stiffness are used. The main properties of the rubber are reported in Table 3.5 for the different types of UFREI: moreover, the reinforcement consists of a glass fiber with Young modulus E=40 GPa. The properties of hyperelasticity and viscosity of the rubbers is obtained through a uniaxial tensile test and relaxation test, respectively.

Each UFREI presents a typical square section with sides equal to 100 mm and consists of five rubber pads with thickness equal to 10 mm and four fiber laminas with thickness equal to 0.55 mm. The weight of the upper slab is about 46.8 kN: consequently, each isolator is loaded by a vertical pressure equal to about 1.17 MPa. A similar vertical pressure was supported by the low-cost rubber isolators employed for the seismic protection of a masonry building model, [37].
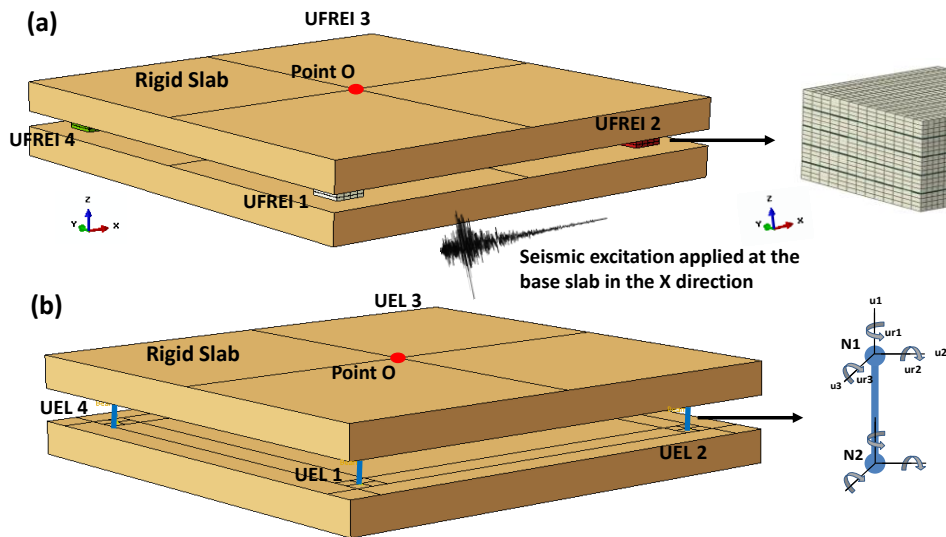

Fig. 3.17 Model of the isolated rigid slab using (a) the detailed 3D FE model and (b) the Abaqus User Element (UEL) for the isolators.
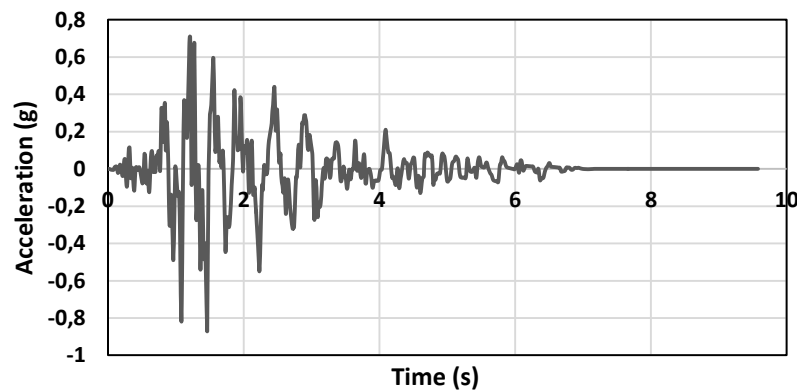

Fig. 3.18 North-South component of the Durzunbey accelerogram with PGA=0.86 g used in the numerical

simulation.

Table 3.5. Main properties of the different UFREIs

Bearing	Rubber shear modulus (MPa)	Viscous damping (%)	k_{Heff} (N/mm) (at displacement = $1h_r$)	k_{Veff} (N/mm)
UFREI-1	0.50	4	81.73	4680
UFREI-2	0.60	4	91.00	5318
UFREI-3	0.78	8	136.71	7313
UFREI-4	1.00	8	148.65	8357

As already mentioned, two different types of models are adopted for the four isolators: the detailed 3D FE model with refined mesh, which serves as a reference model, and the Abaqus UEL proposed in this study, which can predict the complex 3D behavior of UFREIs after providing the geometry of the isolator and the shear modulus and damping of the rubber.

To provide an unbonded condition in the 3D FE model, a friction coefficient equal to μ=0.85 is introduced between the supports and the isolator. Considering the high computational effort of the analysis of the detailed 3D FE model with friction contact, an accelerogram with short duration is selected for the numerical simulations. Fig. 3.18 shows the North-South component of the Durzunbey (Turkey) accelerogram (PGA=0.86g) that is applied at the bottom slab in the X direction. It is worth mentioning that three additional seconds are added at the end of the registration to assess the re-centering capability of the UFREI system.
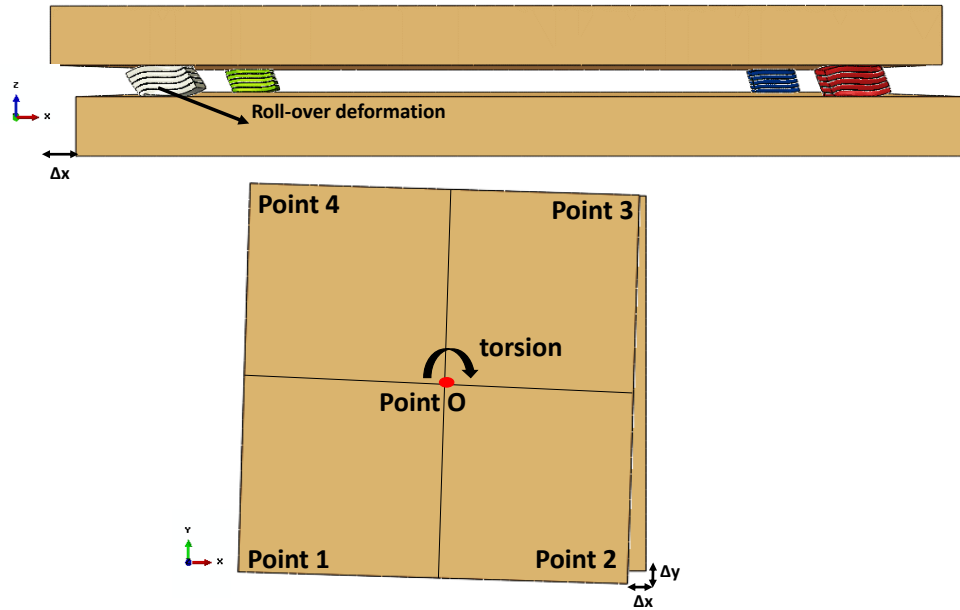
Fig. 3.19 Motion of the isolated slab during seismic excitation: elevation view and plan view.
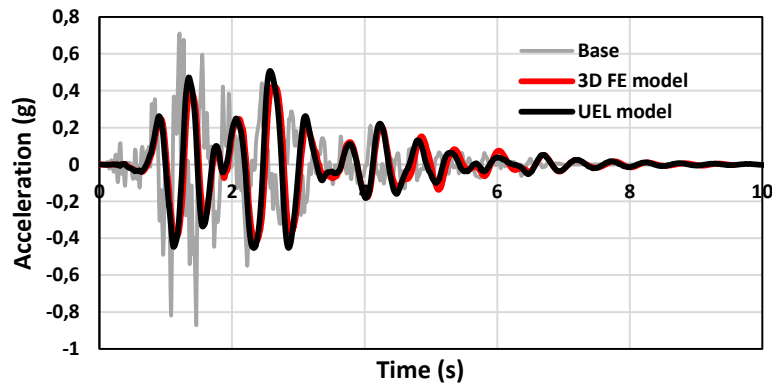

Fig. 3.20 Acceleration time history (X direction) of the upper slab (point O) for the 3D FE model and the UEL model.

The motion of the isolated slab during the seismic excitation in the case of both the models for the isolators is schematically shown in Fig. 3.19. As indicated, the 3D motions of the bearings and the upper slab centroid (point O) are registered during the numerical simulation: in particular, the global torsion is monitored through the azimuth rotation of point O. The acceleration time history of the upper slab (point O) is presented in Fig. 3.20 in the case of 3D FE models and UEL models for the isolators. It can be noted that the UEL model provides a very good prediction of the results obtained through the detailed 3D FE model. Moreover, a reduction of the peak acceleration values can be observed for the upper slab due to the low stiffness and damping of the isolation system.
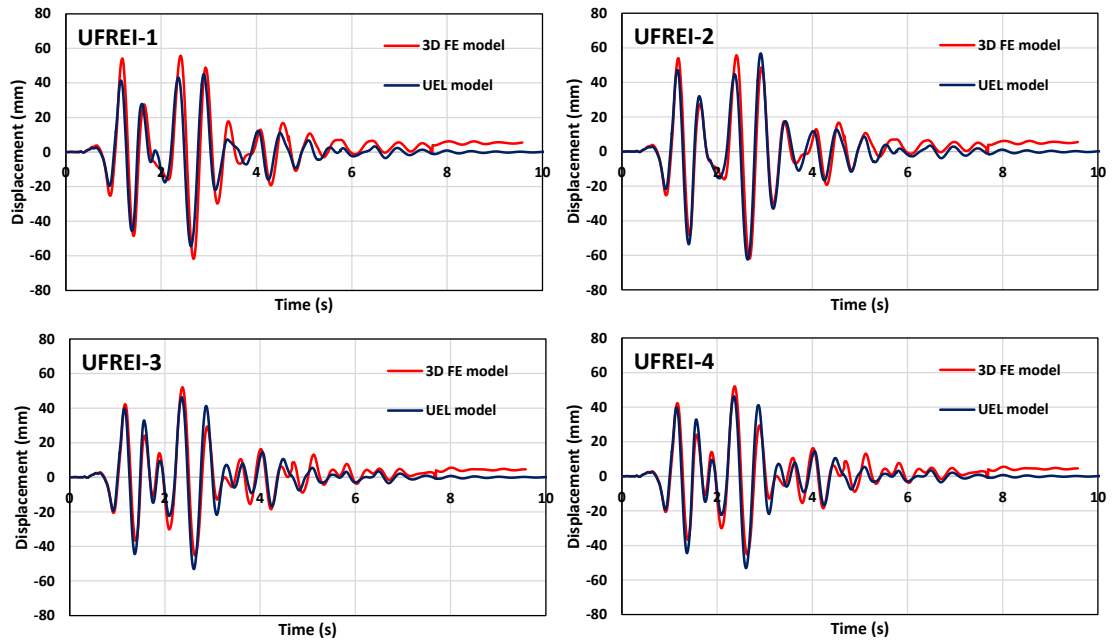
Fig. 3.21 Displacement time history (X direction) of the different types of UFREI: 3D FE model and UEL model.
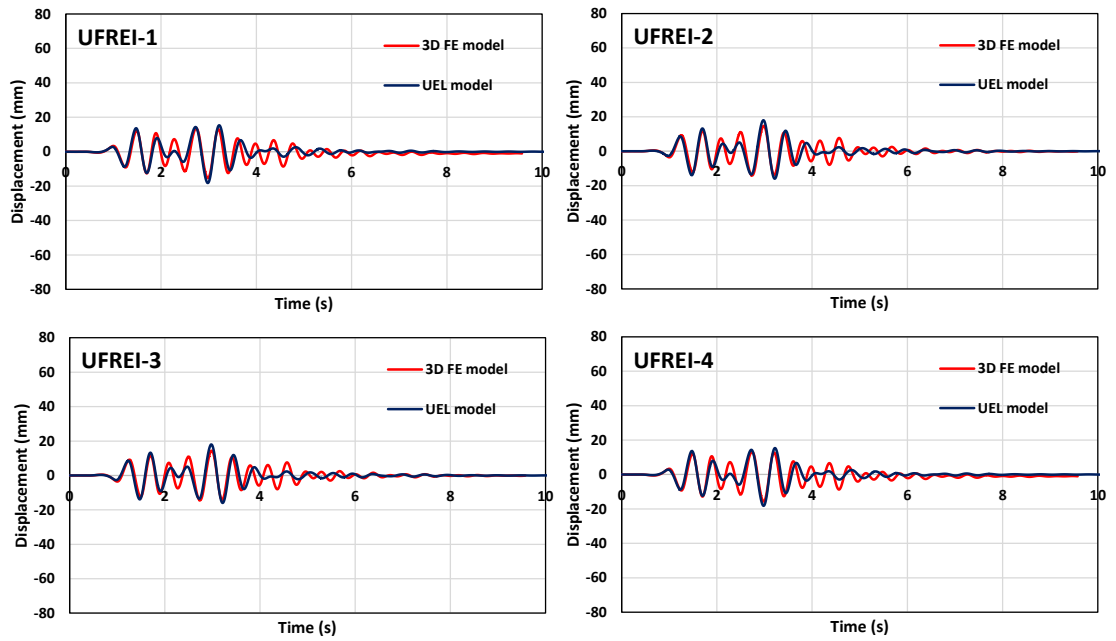

Fig. 3.22 Displacement time history (Y direction) of the different types of UFREI: 3D FE model and UEL model.
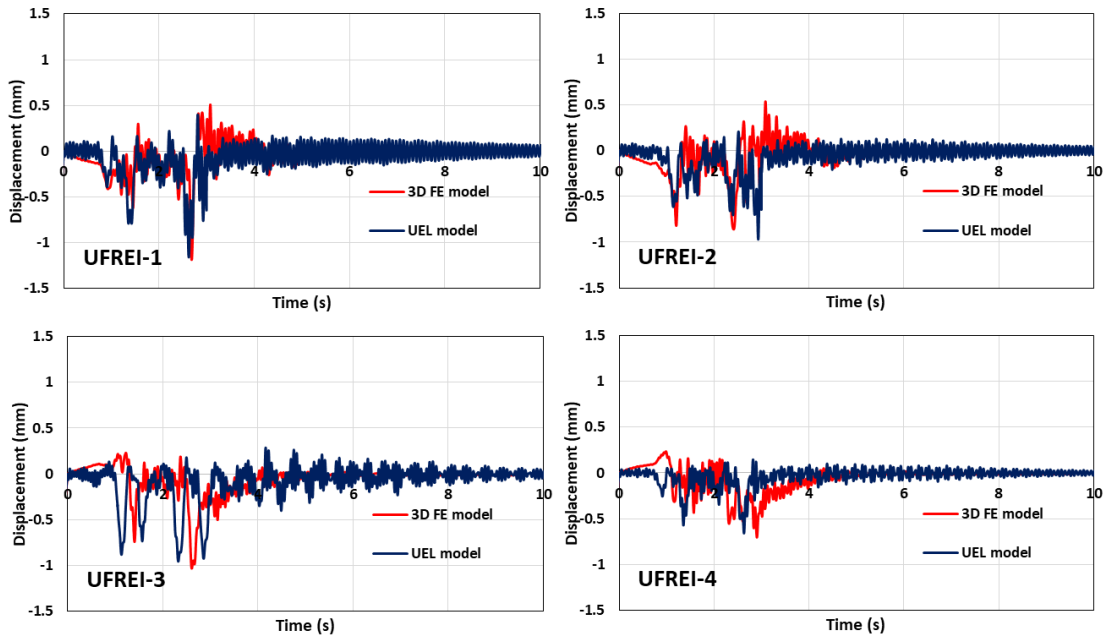
Fig. 3.23 Displacement time history (Z direction) of the different types of UFREI: 3D FE model and UEL model.
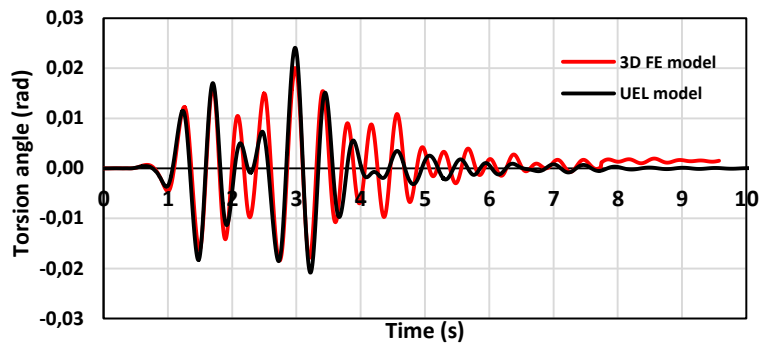

Fig. 3.24 Torsion angle time history of the upper slab (point O) during seismic excitation: 3D FE model and UEL model.

Fig. 3.25 Lateral force - horizontal displacement curves (X direction) for the different types of UFREI during seismic excitation: 3D FE model and UEL model.

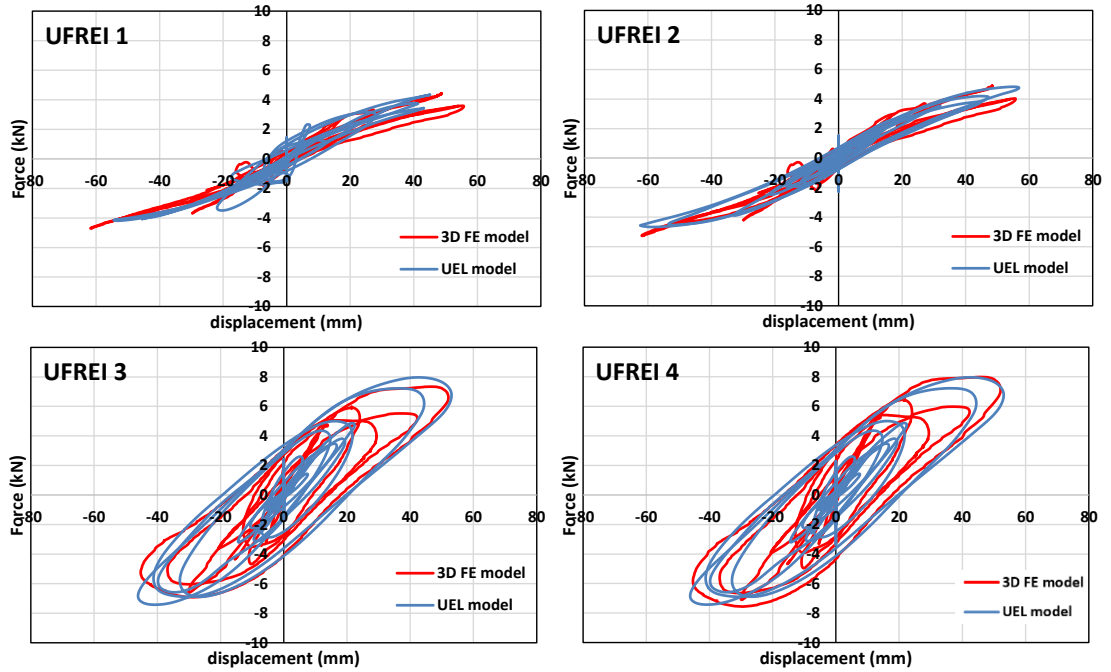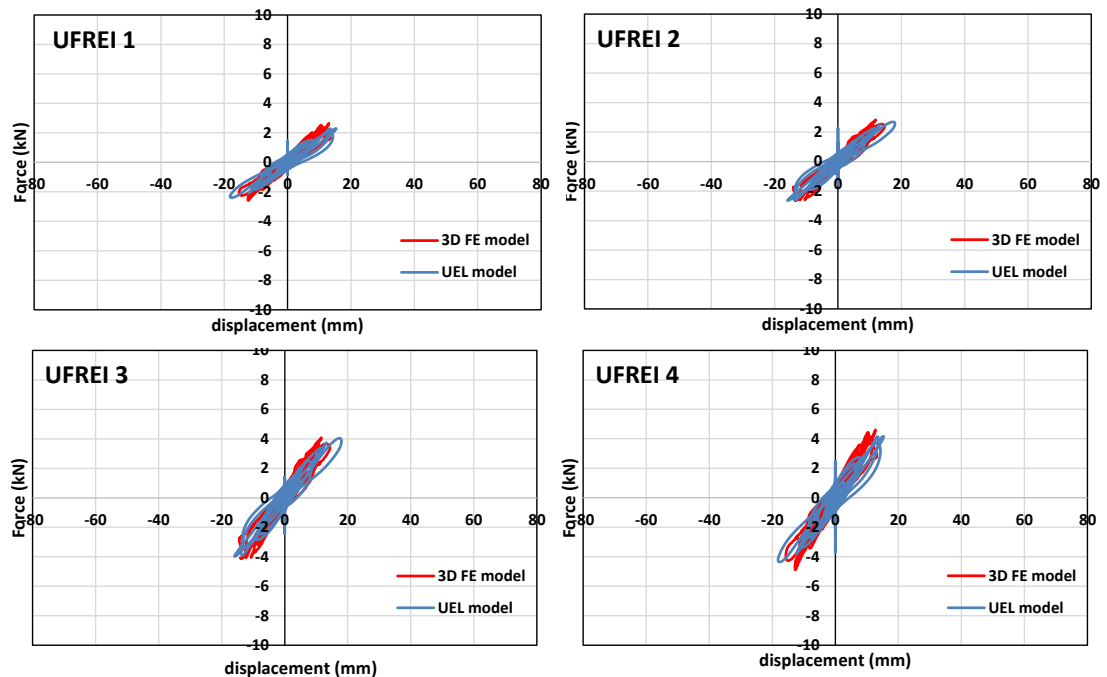Fig. 3.26 Lateral force - horizontal displacement curves (Y direction) for the different types of UFREI during seismic excitation: 3D FE model and UEL model.

Figs. 21-23 show the displacement time history obtained through the 3D FE model and the UEL model for the different UFREIs in the horizontal and vertical directions. As can be noted, a good agreement is found between the results of the two

approaches. As expected, the largest displacements are registered in the X direction, with a peak value observed for UFREI-2. Fig. 3.21 and Fig. 3.22 indicate that all the UFREIs, through both the models, present a good re-centering capacity after the seismic excitation. A small maximum sliding equal to 4 mm is registered in the X direction for the UFREIs using the 3D FE model, while no noticeable sliding is observed in the Y direction for the UFREIs using both the models. This result is in agreement with the recommendation that a vertical pressure equal to at least 0.5 MPa on UFREIs can prevent a large sliding between the isolator and concrete substructures [53][15]. Fig. 3.23 shows that the vertical displacements are smaller than 1.2 mm for both the models: as expected, the isolator with the smallest stiffness (UFREI-1) experiences the highest displacements.

Fig. 3.24 shows the torsion angle time history of the upper slab (point O) in the case of 3D FE models and UEL models for the bearings. A reasonable accuracy can be observed for the UEL model, which takes into account the UFREI torsional behavior. Although some differences can be registered during the seismic excitation, the maximum values of the torsional angle observed in the case of 3D FE models are properly captured by the UEL model.

Figs. 25-26 confirm a good agreement between the lateral force – horizontal displacement curves (both in the X and Y directions) of the different types of UFREIs using 3D FE models and UEL models. Moreover, it can be noted that the two models can capture the different characteristics of the four UFREIs in terms of energy dissipation capacity, lateral force and horizontal stiffness.

The comparison with the results obtained through a detailed 3D FE model indicates that the UEL model may provide a very good prediction of the UFREI behavior under seismic excitation, see Table 3.6, resulting a useful tool for 3D dynamic analyses of more complex isolated structures.

Table 3.6. Comparative results of the peak displacement and force obtained from 3D FE and UEL models.

	3D FE				UEL				Average of error (%)
UFREI no.	1	2	3	4	1	2	3	4	
Peak displacement-X (mm)	61.5	61.7	52.1	52.0	54.4	62.4	46.1	46.1	8.9
Peak displacement-Y (mm)	16.7	16.4	15.6	15.7	18.1	17.7	17.7	18.1	11.3
Peak displacement-Z (mm)	1.1	0.8	1.1	0.7	1.1	0.9	0.9	0.6	6.9
Peak force-X (kN)	4.4	4.8	7.3	7.9	4.3	4.8	7.9	7.9	3.1
Peak force-Y (kN)	2.6	2.8	4.1	4.6	2.2	2.7	4.1	4.1	7.07

3.6. Conclusions

A phenomenological model of unbonded fiber reinforced elastomeric isolators (UFREIs) for large scale structural analyses is proposed and described in this study. The remarkable features of the UFREI behavior are taken into account, such as non-linearity due to rollover and hardening due to full-contact: the former decreases the effective horizontal stiffness, thus reducing the seismic demand, while the latter plays an important role in limiting displacements under severe earthquakes.

Due to the absence of analytical expressions to comprehensively predict the UFREIs behavior, the classical equations available in the literature for commercial BFREIs are modified and adapted for UFREIs. The phenomenological solution is then implemented into an Abaqus user element (UEL), which is based on Fortran programming language. Using a 2-node 12-DOF beam element, the proposed model takes into account the main features of the 3D behavior of UFREIs: the hysteretic behavior is reproduced through the classical Bouc-Wen model and a standard iterative Newton-Raphson procedure is used. Some results from experimental works are used to evaluate the performance of the UEL for UFREIs under horizontal cyclic loading. It is found that the UEL is applicable for various geometries and mechanical properties of UFREIs.

The validity and effectiveness of the extended UEL model are also evaluated through 3D dynamic time history analyses. The benchmark structure is a square slab isolated using four different types of UFREIs to generate rotation and torsion. A good agreement between the results obtained through the UEL and the detailed 3D FE model is observed, indicating that the developed UEL can provide a satisfactory prediction of the UFREI behavior under seismic excitation. Moreover, it should be mentioned that the application of the UEL model significantly reduces the computational effort of the dynamic time history analysis when compared with the 3D FE model. Indeed, in the case under study, the analysis conducted through the 3D FE model of the isolation system takes a couple of days mainly due to friction contact; conversely, the UEL model requires only few minutes for the same case.

It can be concluded that the UEL model developed in this study can be particularly suitable for 3D analyses of complex isolated structures through the software code Abaqus, with a significant computational efficiency.

References

[1] CEB-FIB (Comité Européen du Béton - Fédération Internationale du Béton) (2003) Seismic assessment and retrofit of reinforced concrete buildings. CEB-FIB Bulletin no. 24. International Federation for Structural Concrete, Task Group 7.1

[2] FEMA (Federal Emergency Management Agency) (2000) (2000) FEMA 356: pre-standard and commentary for the seismic rehabilitation of buildings. FEMA, Washington

[3] Di Sarno L, Elnashai AS (2005) Innovative strategies for seismic retroftting of steel and composite structures. Prog Struct Mater Eng 7(3):115–135

[4] Bruneau M, Engelhardt M, Filiatrault A, Goel SC, Itani A, Hajjar J, Leon R, Ricles J, Stojadinovic B, Uang CM (2005) Review of selected recent research on US seismic design and retroft strategies for steel structures. Prog Struct Mater Eng 7(3):103–114

[5] Valente M, Milani G (2018) Alternative retroftting strategies to prevent the failure of an under-designed RC frame. Eng Fail Anal 89:271–285

[6] Di Sarno L, Elnashai AS (2009) Bracing systems for seismic retroftting of steel frames. J Constr Steel Res 65:452–465

[7] Fardis MN (2009) Seismic design, assessment and retroftting of concrete buildings: based on EN-Eurocode 8. Springer, Berlin

[8] Fardis MN, Schetakis A, Strepelias E (2013) RC buildings retroftted by converting frame bays into RC walls. Bull Earthq Eng 11:1541–1561

[9] Giannuzzi D, Ballarini R, Hucklebridge A, Pollino M, Valente M (2014) Braced ductile shear panel: new seismic-resistant framing system. J Struct Eng ASCE 140(2):1–11

[10] Triantafllou TC (2001) Seismic retroftting of structures with fbre-reinforced polymers. Prog Struct Mater Eng 3(1):57–65

[11] Naeim F, Kelly JM (1999) Design of seismic isolated structures: from theory to practice. Wiley, Hoboken

[12] Habieb AB, Milani G, Tavio T, Milani F (2017a) Low cost frictional seismic base-isolation of residential new masonry buildings in developing countries: a small masonry house case study. Open Civ Eng J 11:1026–1035

[13] Toopchi-Nezhad H, Tait MJ, Drysdale RG (2008a) Testing and modeling of square carbon fber-reinforced elastomeric seismic isolators. Struct Control Health Monit 15:876–900

[14] Toopchi-Nezhad H, Tait MJ, Drysdale RG (2011) Bonded versus unbonded strip fber reinforced elastomeric isolators: fnite element analysis. Compos Struct 93:850–859

[15] Russo G, Pauletta M (2013) Sliding instability of fber-reinforced elastomeric isolators in unbonded applications. Eng Struct 48:70–80

[16] Spizzuoco M, Calabrese A, Serino G (2014) Innovative low-cost recycled rubber-fber reinforced isolator: experimental tests and fnite element analyses. Eng Struct 76:99–111

[17] Mishra HK, Igarashi A, Matsushima H (2013) Finite element analysis and experimental verifcation of the scrap tire rubber pad isolator. Bull Earthq Eng 11(2):1–21

[18] Van Engelen NC, Konstantinidis D, Tait MJ (2016) Structural and nonstructural performance of a seismically isolated building using stable unbonded fber-reinforced elastomeric isolators. Earthq Eng Struct Dyn 45:421–439

[19] Toopchi-Nezhad H, Tait MJ, Drysdale RG (2008b) Lateral response evaluation of fber-reinforced neoprene seismic isolators utilized in an unbonded application. J Struct Eng 134:1627–1637

[20] Thuyet VN, Dutta A, Deb SK (2017) Evaluation of horizontal stifness of fbre-reinforced elastomeric isolators. Earthq Eng Struct Dyn 46(11):1747–1767

[21] Calabrese A, Spizzuoco M, Serino G, Della Corte G, Maddaloni G (2015) Shaking table investigation of a novel, low-cost, base isolation technology using recycled rubber. Struct Control Health Monit 22:107–122

[22] Das A, Deb SK, Dutta A (2016a) Comparison of numerical and experimental seismic responses of FREIsupported un-reinforced brick masonry model building. J Earthq Eng 20:1239–1262

[23] Das A, Deb SK, Dutta A (2016b) Shake table testing of un-reinforced brick masonry building test model isolated by U-FREI. Earthq Eng Struct Dyn 45:253–272

[24] S.N. Indonesia (2013) Persyaratan beton struktural untuk bangunan gedung, SNI 2847

[25] Eurocode 8 (2005) Design of structures for earthquake resistance-part 1: general rules, seismic actions and rules for buildings. European Committee for Standardization, Brussels

[26] Osgooei PM, Tait MJ, Konstantinidis D (2017) Non-iterative computational model for fber-reinforced elastomeric isolators. Eng Struct 137:245–255

[27] Manzoori A, Toopchi-Nezhad H (2017) Application of an extended Bouc–Wen model in seismic response prediction of unbonded fber-reinforced isolators. J Earthq Eng 21(1):87–104

[28] Love JS, Tait MJ, Toopchi-Nezhad H (2011) A hybrid structural control system using a tuned liquid damper to reduce the wind induced motion of a base isolated structure. Eng Struct 33:738–746

[29] Kumar M, Whittaker AS, Constantinou MC (2014) An advanced numerical model of elastomeric seismic isolation bearings. Earthq Eng Struct Dyn 43:1955–1974

[30] Habieb AB, Valente M, Milani G (2018c) Base seismic isolation of a historical masonry church using fber reinforced elastomeric isolators. Soil Dyn Earth Eng (accepted)

[31] Simulia (2014) ABAQUS 6.14 user's manual. Dassault Systems, Providence

[32] Habieb A, Milani G, Tavio T, Milani F (2017d) FE modelling of fber reinforced elastomeric isolators (FREI): mesh verifcation and validation. In: AIP conference proceedings, vol 1978, p 450006

[33] Shahzad M, Kamran A, Siddiqui MZ, Farhan M (2015) Mechanical characterization and FE modelling of a hyperelastic material. Mater Res 18:918–924

[34] Jerrams SJ, Kaya M, Soon KF (1998) The efects of strain rate and hardness on the material constants of nitrile rubbers. Mater Des 19:157–167

[35] Van Engelen NC, Osgooei PM, Tait MJ, Konstantinidis D (2014) Experimental and fnite element study on the compression properties of Modifed Rectangular Fiber-Reinforced Elastomeric Isolators (MR-FREIs). Eng Struct 74:52–64

[36] Habieb A, Milani G, Tavio T, Milani F (2017c) Numerical model of low cost rubber isolators for masonry housing in high seismic regions. World Acad Sci Eng Technol Int J Civ Environ Struct Constr Archit Eng 11(5):590–596

[37] Habieb AB, Milani G, Tavio T, Milani F (2018b) Practical designs and seismic performances of residential masonry building isolated with fber reinforced elastomeric isolators. In: 10th international masonry conference, Milan

[38] Kelly JM (1993) Earthquake-resistant design with rubber. Springer, London

[39] Constantinou MC, Whittaker AS, Kalpakidis Y, Fenz DM, Warn GP (2007) Performance of seismic isolation hardware under service and seismic loading. Technical Report MCEER-07-0012

[40] Cardone D, Perrone G (2012) Critical load of slender elastomeric seismic isolators: an experimental perspective. Eng Struct 40:198–204

[41] Habieb A, Milani G, Tavio T, Milani F (2017b) Seismic performance of a masonry building isolated with low cost rubber isolators. WIT Trans Built Environ 172:71–82

[42] Toopchi-Nezhad H (2014) Horizontal stifness solutions for unbonded fber reinforced elastomeric bearings. Struct Eng Mech 49:395–410

[43] De Raaf MGP, Tait MJ, Toopchi-Nezhad H (2011) Stability of fber-reinforced elastomeric bearings in an unbonded application. J Compos Mater 45:1873–1884

[44] Al-Anany YM, Van Engelen NC, Tait MJ (2017) Vertical and lateral behavior of unbonded fber-reinforced elastomeric isolators. J Compos Constr 21:04017019

[45] Kelly JM, Konstantinidis D (2007) Low-cost seismic isolators for housing in highly-seismic developing countries. In: 10th world conference on seismic isolation, energy dissipation and active vibrations control of structures, Istanbul, Turkey, pp 28–31

[46] Fragiacomo M, Rajgelj S, Cimadom F (2003) Design of bilinear hysteretic isolation systems. Earthq Eng Struct Dyn 32(9):1333–1352

[47] American Association of State Highways and Transportation Ofcials, AASHTO (2000) Guide specifcation for seismic isolation design, 2/e

[48] Nagarajaiah S, Reinhorn AM, Constantinou MC (1991) Nonlinear dynamic analysis of 3-D-base-isolated structures. J Struct Eng 117:2035–2054

[49] Kumar M, Whittaker AS, Constantinou MC (2015) Seismic isolation of nuclear power plants using elastomeric bearings. Technical Report MCEER-15-0008

[50] Al-Anany YM, Tait MJ (2015) A numerical study on the compressive and rotational behavior of fber reinforced elastomeric isolators (FREI). Compos Struct 133:1249–1266

[51] Castellano A, Foti P, Fraddosio A, Marzano S, Mininno G, Piccioni MD (2014) Seismic response of a historic masonry construction isolated by stable unbonded fber-reinforced elastomeric isolators (SUFREI). Key Eng Mater 628:160–167

[52] Habieb AB, Milani G, Tavio T (2018a) Two-step advanced numerical approach for the design of lowcost unbonded fber reinforced elastomeric seismic isolation systems in new masonry buildings. Eng Fail Anal 90:380–396

[53] Ehsani B, Toopchi-Nezhad H (2017) Systematic design of unbonded fber reinforced elastomeric isolators. Eng Struct 132:383–398

Chapter
4

Low Cost Base Isolation System for Residential Housing in Developing Countries

In developing countries, masonry is generally employed in the construction of residential buildings due to its relatively cheap cost. However, these structures are often provided with inadequate seismic protection. A low-cost base isolation aimed at decreasing the seismic vulnerability of masonry buildings is studied in this work from a numerical standpoint. The studied isolator is an unbonded fiber-reinforced elastomeric isolator (UFREI). With fewer rubber pads than conventional isolators the UFREI is a cheaper option. A 3D finite element analysis is performed to predict the behavior of the UFREI under large displacements. The isolation system is then implemented into a two-story masonry building prototype, where the 3D model of a single UFREI is substituted by a nonlinear spring and a damper. This simplification decreases the computational costs of the analysis. Seven scaled ground motions are applied to the numerical model to investigate the seismic performance of the isolated masonry building subjected to a maximum considered earthquake. Nonlinear dynamic analyses are eventually performed in Abaqus, taking into account the two horizontal components of the seismic motion. The shear deformation of the UFREIs was monitored through a later excitation for determining its overall behavior under lateral loads. The numerical results show an excellent isolation performance of the system, with a significant reduction of the inter-story drift and a suitable deformation of the UFREIs, as well as demonstrate that the simplified numerical approach adopted is useful for practical design and quick safety assessments.

Keywords: Masonry housing; low cost seismic isolation; rubber isolators; advanced FE modelling; Non-linear dynamic analyses

4.1. Introduction

Seismic isolation is an effective solution to reduce the vulnerability of new and existing structures. Isolation can mitigate the negative impact of an earthquake, because it shifts the period of the structure in the range of the spectrum where the spectral acceleration is low. Seismic isolators are especially needed for masonry

structures in developing countries, because of the limited resistance of masonry under horizontal loads. As a matter of fact, masonry is a common building method in developing countries because of its low cost and simplicity of construction, but its poor tensile strength ultimately leads to low horizontal load carrying capacities [1,2]. In high seismicity regions such as Indonesia, many affordable housing structures are built with masonry and experience severe damage during an earthquake. This consequently results in many avoidable casualties [3]. The importance of conceiving new low-cost seismic isolation systems is therefore paramount.

One of low-cost seismic isolation solutions is the so-called frictional isolation, which is basically the introduction of a pad/sheet/interface near the foundation with a suitable friction coefficient. Experimental tests on this isolation system for unreinforced masonry housing have been already carried out, see for instance [4,5]. It has been found that the vulnerability can be reduced by decoupling the superstructure from the ground using a sliding joint. Some materials for sliding interfaces have been also tested on small prototypes [6,7,8] like marble, graphite powder, screened gravel, rubber-sand, and paraffin wax. This simple and cheap isolation system is however affected by undesired drawbacks, due to the absence of re-centering capability. A pendulum frictional isolator was then introduced to overcome the re-centering issue. In the literature, base friction isolation is applied on the masonry monumental construction to protect the non-structural monolithic object [9].

An elastomeric isolator is a well-known and relatively cheap seismic isolation device. Typically, it consists of several layers of high-damping rubber (pads) and reinforced by steel lamina interposed between pads. The reinforcement has the role of limiting only vertical deformations. The horizontal deformations can be large and are controlled by the small shear stiffness of the pads. This system can isolate the energy transmission of the earthquake from the foundation to the upper-structure. However, a massive application of commercial elastomeric isolators in developing regions is not easy to be realized. It still costs too much for its widespread utilization in low-class housing, due to the need of using steel reinforcements and rigid steel plates for isolation supports.

Glass or carbon fiber laminas are now being used as an alternative reinforcement [10,11]. A glass fiber is much cheaper than its steel counterpart but has a comparable reinforcement effect. Furthermore, one may think to remove the stiff still plates connecting the isolator to ground and superstructure, so conceiving a so called unbonded device, also known as Unbonded Fiber Reinforced Elastomeric Isolator (UFREI).

Experimental works reveal the advantages of UFREI applications [12,13]. Its effective horizontal stiffness is considerably lower than that of a bonded device, decreasing the seismic force demands. This softening effect is notable in the stiffness variation of UFREIs that is caused by a roll-over deformation of the UFREI, which is a sort of quasi rigid rotation occurring at large deformation under strong earthquakes.

Another remarkable feature of a UFREI is the so called hardening at large deformation. This occurs when the vertical edges of the bearing, due to increased roll-over, touch the superstructure and the ground. It is considered as an advantageous effect because it plays an important role in limiting the shear displacement during a maximum seismic motion [14]. An innovative method was proposed to accelerate the full-contact mechanism of a UFREI by modifying the geometry of the upper and bottom supports [14]. However, this method seems to significantly increase the construction cost. The hardening feature is also found in an expensive isolation system that employs a stopper device to control the displacement [15,16].

Since a UFREI has a large deformability, some researches evaluated the stability limit at which the bearing is subjected to a state damage or delamination which should be considered as threshold for the substitution of the device. In some papers, see [17,13], such critical limit was identified as that corresponding to 170-200% of shear deformation, while, in contrast, in [18] it was shown that even 300% of shear deformability did not cause any damage of rubber-fiber interfaces. This very large critical limit facilitates the utilization of UFREIs with small height, i.e. with few pads and laminas and hence much cheaper. This remarkable feature cannot be found in a commercial-bonded isolator, that typically exhibits a critical shear displacement of around 150% [19,20].

UFREIs have been already applied for seismic isolation of low-rise masonry prototypes tested in the laboratory [10]. The experimental results show a desired behavior of the isolated structure with a significant reduction of the roof acceleration and inter-story drift. This excellent performance is also followed by an easy technical detail of the connection between the isolators and the structures. Consequently, advanced and complicated construction methods can be avoided. Basing on such promising results, a first full-scale masonry building isolated with UFREIs has been recently built in Tawang, India, a well known high seismicity region [17].

To further reduce the cost, UFREI can be also combined with pads obtained from recycled rubber tires or re-generated rubber [21,12]. With ad-hoc experimentation on the single rubber pads (tuning rubber loads and recipe), a desired horizontal stiffness and damping ratio can be easily obtained. For instance, in [21], using scrap tire pads, an unbonded bearing without any bonding between layers was obtained and tested. The friction coefficient between pads was considered high, so that the pads could be considered to act together. This cheap method however leads to a permanent sliding of the bearing when subjected to a large displacement. On the other hand, some other researches [22,11] proposed UFREIs with modified shape, by cutting the interior or exterior geometry of the bearing to decrease the material volume and the horizontal stiffness. A favorable energy dissipation was also observed through this method, but by cutting the geometry, the isolator tends to behave as two individual bearings so that the isolation system seems excessive complex and inefficient.

UFREI specimens in the literature [23,24,13] mostly consist of many thin rubber pads (15-20 pads), resulting in high shape factors, defined as known as the ratio between the load area to the force-free area of a single pad. Employing many thin pads, consequently, increases the price because of the need for adhesive on rubber-fiber interfaces. Thus, in this work, a UFREI with significantly fewer rubber pads (see Fig. 4.1) results in a cheaper isolation system. In addition, thanks to the small height of the bearing, the full-contact mechanism can be accelerated without any expensive modification.

a/b   = isolator length/width
t_r = singe rubber pad thickness
n_r = number of rubber pads
t_f = fiber thickness
S   = first shape factor = $a.b / (2.(a+b)*t_r)$

Dimensions (mm) of the isolators considered

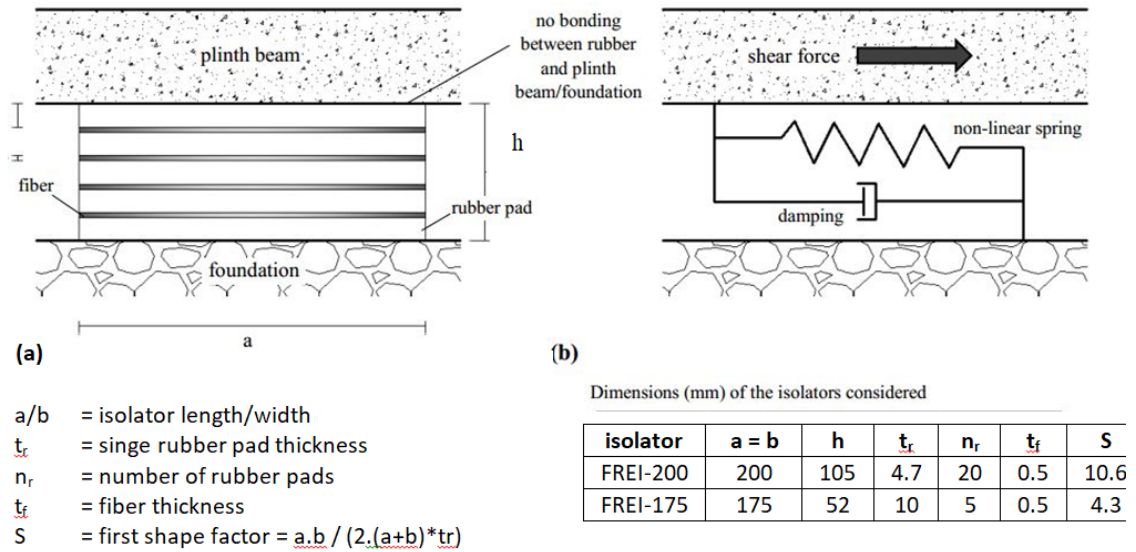| isolator	a = b	h	t_r	n_r	t_f	S
FREI-200	200	105	4.7	20	0.5	10.6
FREI-175	175	52	10	5	0.5	4.3

Fig. 4.1. (a) Geometry of the elastomeric isolator and (b) the representative damped spring model.

Another important issue is the modelling of UFREIs in structural analysis. The non-linearity model of this isolator, including the softening and hardening, is not found in the most structural analyses software available [25,26]. Some works implemented a numerical model of UFREIs only up to the softening mode [27,28,29]. The hardening branch was usually excluded because it was considered as the unstable part.

The objective of this paper is to analyze the seismic performance of a newly conceived low-cost UFREIs in real structural applications, i.e. when applied to low-rise masonry buildings. The proposed isolator, which will be tested experimentally in a dedicated research, consists of few rubber pads from recycled tires, is unbonded and uses GFRP instead of steel laminas; in addition, it has a small shape factor, all the aforementioned features intentionally forced to drop-down the cost.

First of all, a detailed 3D model of a single isolator is implemented into ABAQUS and its hysteretic behavior is numerically analyzed. A preliminary validation is provided assuming as reference some existing experimental data obtained on a standard UFREI subjected to hysteretic cycles.

Then, the proposed UFREI is identify with a single DOF system constituted by a spring exhibiting softening and occurs during a cycle, this latter is quite low and can

be disregarded without meaningful errors for structural applications. The identification of the 3D model behavior with a single DOF system (non-linear spring with damping) is mandatory to perform large scale non-linear dynamic analyses on isolated full scale buildings. hardening and a damper acting in parallel see Fig. 4.1. Whilst the 3D detailed model shows some dissipation, i.e. energy dissipation

By means of such identification and in this framework, a 3D FE model of a two-story masonry building and isolated with the proposed UFREIs is analyzed in the non-linear dynamic range, assuming different accelerograms as input data. A Concrete Damage Plasticity (CDP) model is employed to characterize the non-linearity of the masonry material.

From simulations results, it is found how the proposed UFREI is a promising and effective isolation system that can be used in developing countries. In addition, the simplified numerical approach proposed allows for a fast and reliable design of such kind of isolators in real cases.

4.2. 3D FE numerical model of a single FREI (Fiber Reinforced Elastomeric Isolator)

In this Section, detailed 3D FE analyses are performed on a typical FREI, meshing the device with a refined discretization with 8-noded brick elements, as depicted in Fig. 4.2. In Fig. 4.2, two different FREI devices are shown, namely FREI-200 and FREI-175.They differ only for the geometry; in particular they have different shape factors, cross areas (the number in the label indicates the edge length in mm of the square cross area) and number of pads used. FREI-200 is used exclusively to benchmark the 3D FE model against some existing experimental data, whereas FREI-175 is the actual low cost isolator used for large scale structural analyses.

For rubber pads, a Yeoh hyper-elastic material model is assumed. Such model is relatively simple, but is already implemented in ABAQUS and authors experienced a good stability of the numerical model under large displacement conditions and good fitting capabilities. Yeoh strain energy [25] is given by the following equation:

$$W = \sum_{i=1}^{3} C_{i0} (I_1 - 3)^i + \sum_{i=1}^{3} \frac{1}{D_i} (J_{el} - 1)^{2i} \tag{1}$$

where W is the strain energy per unit of volume, C_{i0} and D_i are material parameters, I_1 is the first deviatoric strain invariant, and J_{el} is the elastic volume ratio.

Table 4. 1 Yeoh hyperelastic coefficients adopted in the FE model

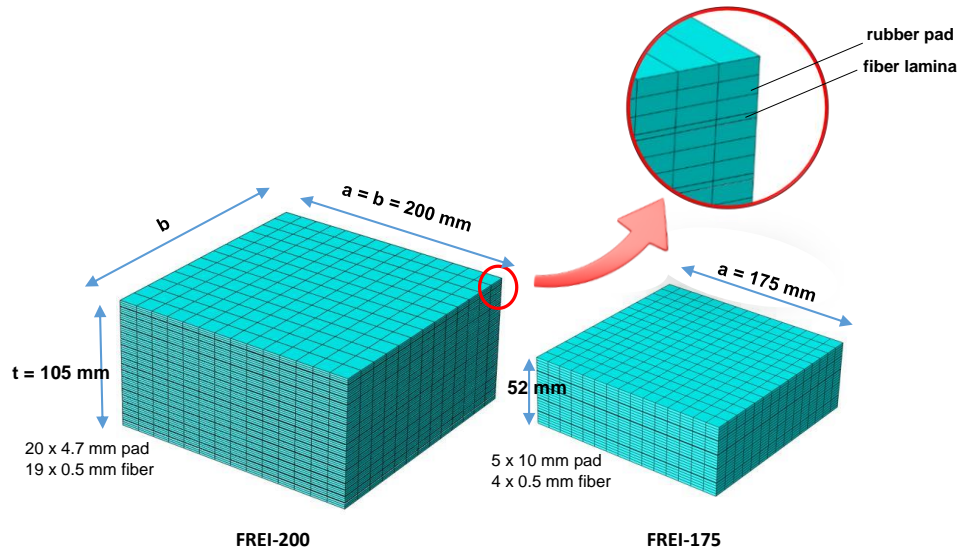| C_{10}	C_{20}	C_{30}	D_1	D_2	D_3
G035	0.0066	0.000032	0.00218	0.000086	-0.000018

C in MPa

Fig. 4.2. Size comparison of isolators FREI-200 and FREI-175 and mesh used for the 3D FE model.

Yeoh coefficients are typically estimated through best fitting of uniaxial stretch-strain experimental curves obtained from dog-bone rubber samples loaded up to failure. In particular, we use here existing literature in the field, see [30,31], which tunes numerical model coefficients using simple tests of material characterization (like the uniaxial stretch-strain test), where Yeoh coefficients of rubbers are also correlated with rubber hardness. The material considered in the present model is a natural-soft gum rubber with around 40 Shore A hardness [13]. The hyperelastic coefficients are presented in Table 4. 1.

Instead of steel laminas, glass fibers are assumed as reinforcement to improve the vertical stiffness. As mentioned previously, fiber utilization can reduce the cost of the isolator when compared with steel lamina [23]. In this numerical simulation, the fiber is assumed isotropic-elastic with Young modulus E = 40 GPa and Poisson's ratio=0.20, in accordance with many references [24,32,22].

Fig. 4.1-b shows the dimensions of the two FREI specimens analyzed. The FREI-200 is an isolator tested at McMaster University [13]. It was subjected to a 0.5 Hz cyclic shear displacement in unbonded application. An equivalent damping ratio of about 5.2% was reported in the test. This specimen is considered as the reference sample to calibrate the material properties in the FE simulation.

FREI-175 is the isolator proposed in this paper, having similar rubber properties, but much smaller dimensions than the previous one. It has only five pads of rubber with 10 mm of thickness, resulting in a much lower shape factor. Fig. 4.2 shows the geometry of the isolators and the discretization adopted for both FE models. Rubber pads and fiber laminas are modeled with 28756 and 10225 of C3D8R elements for FREI-200 and FREI-175, respectively. Direct shear numerical analyses up to 200% of shear deformation are performed, applying a constant vertical pressure of 1.75

MPa. Such vertical load corresponds to the load carried by a single isolator in the structural application discussed in the next Section.

For comparative purposes, three conditions are simulated: bonded, unbonded and frictional contact (see Fig. 4.3a). In the so-called bonded model, the elastomer surfaces are tied to the upper and bottom supports. It is the most common type of base isolators which requires thick steel plates for the supports, and hence higher costs. As a consequence, it cannot be considered as a low-cost device. Once a large displacement takes places, high values of tensile stress appear (Fig. 4.3a), leading to a damage of the rubber-fiber interface, a damage condition that is not reproducible with such FE approach. The evolution of maximum tensile stress with increasing horizontal deformation is shown in Fig. 4.3b.

The second model is the unbonded type (UFREI), where the upper and lower edges do not exhibit any bond with the supports. Under moderate shear forces, such frictional limited strength allows the isolator to roll-over and facilitates larger deformations. Unlike the previous model, the peak tensile stress on the rubbers and interfaces significantly decreases. Thus, delamination at high deformation can be avoided. In recent years, this low-cost type has been investigated with progressively increased interest by different researchers [23,10,11].
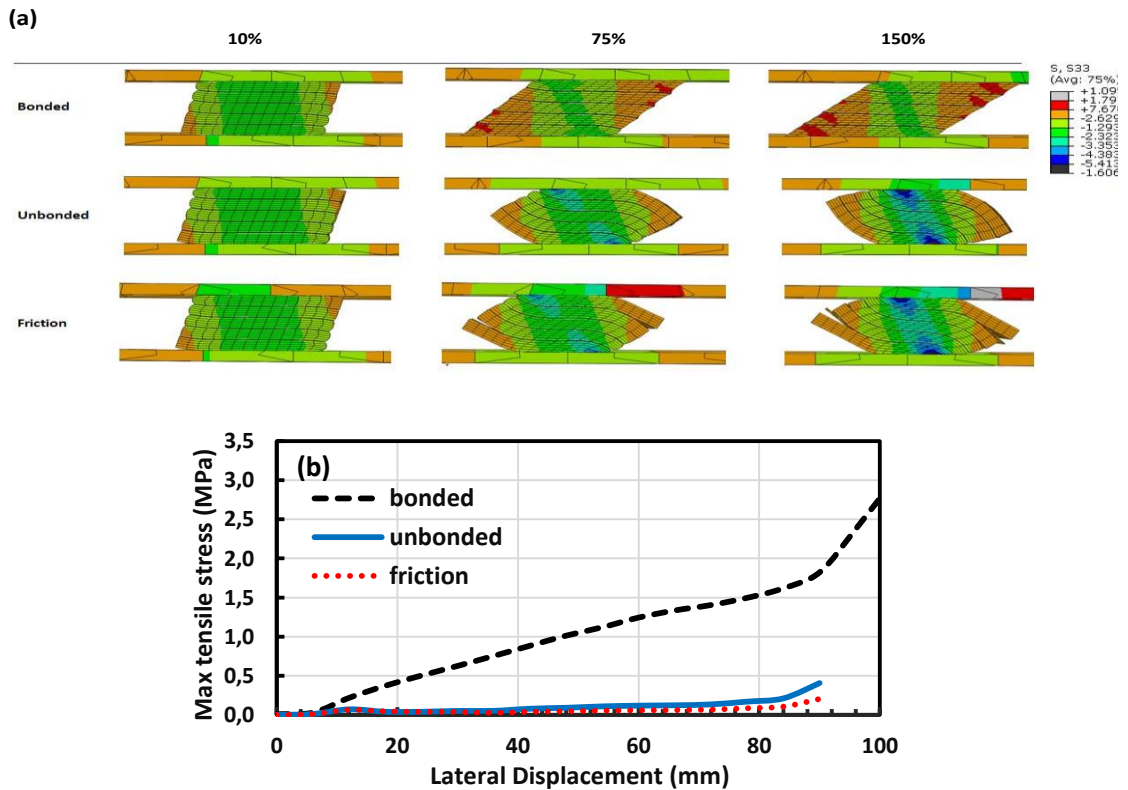

Fig. 4.3. (a) Comparative deformation and stress distribution of bonded, unbonded, and frictional FREIs, (b) evolution of the maximum tensile stress with increasing horizontal displacement.

The last type is a frictional isolator. In such case, frictional interfaces between rubber pads and fiber laminas are present. This cheap isolator can be thought as

fabricated using recycled tire rubbers [21,33]. Similarly to the unbonded device, it can exhibit roll-over deformation under moderate displacement. Nevertheless, it appears totally inadequate to carry high shear deformation, because the layers tend to slide, as clearly shown in Fig. 4.3a.

For the sake of conciseness, this paper discusses only the performance of the unbonded model in isolating a masonry structure, which seems the most realistic technical solution exhibiting good balance between cost and structural performance. UFREI-175 is considered as a potentially suitable isolation device for a low rise masonry building with two/three stories, since authors shown in previous studies [34,35] that UFREI-100 works effectively in the case of a one-story house prototype. In the FE analyses of a single isolator UFREI-175, a 1.75 MPa of constant vertical load is applied. It is because the masonry building studied in the following sections has 220 tons of weight, and 46 isolators on the foundation level are utilized.

To realistically reproduce experimental results, a hysteresis behavior of the isolator is required. One of the authors of this paper proposed a simplified hysteresis behavior of rubber to be used in a FE model by mixing elastoplastic concepts and hyperelastic properties [36]. In the present paper, a similar procedure is adopted.

First, we generate a nonlinear behavior of the 3D-FE device, as shown in Fig. 4.2. To provide an unbonded condition, a friction coefficient μ=0.85 between the supports and the isolator is introduced. A constant vertical load which corresponds to the weight of the structure carried by a single isolator is then applied on the upper surface. Finally, an increasing displacement on upper-testing plate is applied as top edge boundary condition, to simulate a simple shear test.

The result of a simple shear test simulation is then used as reference. Such output depends exclusively on the mechanical properties adopted for the constituent materials, mainly the rubber pads and in particular the hyperelasticity coefficients assumed for the rubber pads, i.e. losing the hysteretic behavior on different loading-unloading paths, see Fig. 4.4(b). The dashed line represents the shear behavior obtained by the 3D FE analysis of an UFREI-200. Such displacement-force curve is then used to calibrate the non-linear elastic properties of the springs adopted at a structural level.

Secondly, to generate a hysteresis behavior, a damper is added in parallel to the non-linear spring, with mechanical properties ad hoc calibrated so that the model can fit the experimental data. In the experiment [13], the equivalent damping of the unbonded FREI-200 was reported to be equal to 5.2%. The spring model with damping (Fig. 4.4b) shows a reasonable fitting with the experiment (Fig. 4.4a). However, it cannot catch the sudden increase of damping as seen in the last cycle of the experiment (Fig. 4.4a). Nevertheless, it is noted that this limitation does not affect the final results.
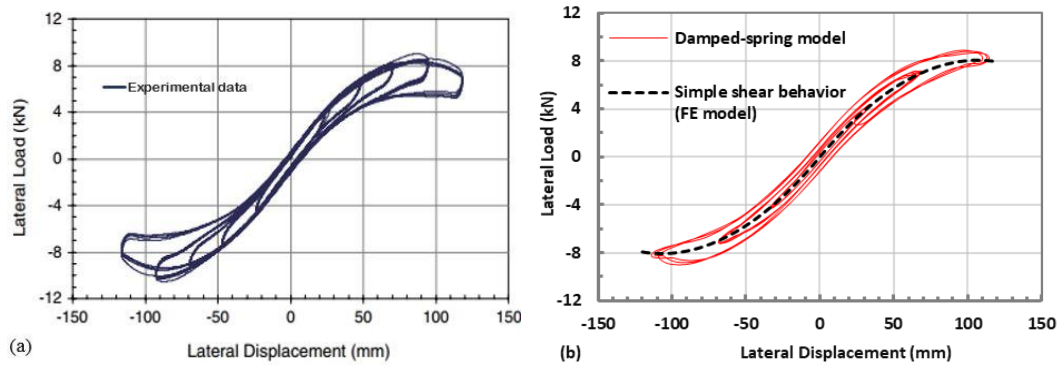
Fig. 4.4. (a) Experimental shear behavior of FREI-200 and (b) Shear behavior of FREI-200 obtained from the 3D-FE model and equivalent damped-spring model.

Consistently, that same damping coefficient is then adopted for UFREI-175 model. Fig. 4.5 shows the simple shear behavior of UFREI-175 (obtained in FE simulation) with the corresponding deformation pattern and the damped-nonlinear spring model response. The FE simulation (dashed-line) shows a remarkable softening once the shear deformation reaches 85mm (150%). When the isolator starts to deform horizontally (roll-over), its effective horizontal stiffness progressively decreases due to a reduction of the bearing area. The global curve is then followed by a hardening at 100 mm (200%), due to a full-contact deformation. The latter is an important advantage of the UFREI because it can limit the shear displacement during a severe seismic motion. The stability after hardening becomes an open issue on UFREIs that can be investigated through an experimental study. Interestingly, an instability was not observed in the shear test up to 300% [18].

As the shear behavior of the spring model is uncoupled along x and y direction, the biaxial behavior is rectangular. Fig. 4.6 shows a comparison between the dumped-spring and 3D models at 45° of load inclination. A good agreement is observed up to 120 mm of lateral displacement, while the prediction of hardening is inaccurate, due to rectangularity of the assembled springs. However, after observing the simulation results, the lateral displacement of the isolator at 45° does not exceeds 120 mm during the considered seismic motions and therefore the approximation adopted may be considered effective.

The nonlinear spring model of the UFREI-175 isolator is implemented later at structural level on a typical two-story isolated masonry building. Such identification is consistent with the simplified model depicted in Fig. 4.1. Modeling a nonlinear spring with damping instead of a real 3D isolator reduces significantly the computational time and drastically increases robustness.

It is worth also mentioning that an elastomeric isolator should be modeled with more DOFs to characterize the behavior in torsion and rotation. However, the masonry building analyzed hereafter has a regular geometry so that the local torsional effect may be considered negligible. Meanwhile, a rotational motion of the isolator is not taken into account in this work. It is acceptable because the step

between adjacent isolators is small (1.3 m) so that the flexural deformation of the foundation beam (Fig. 4.7a) is negligible.
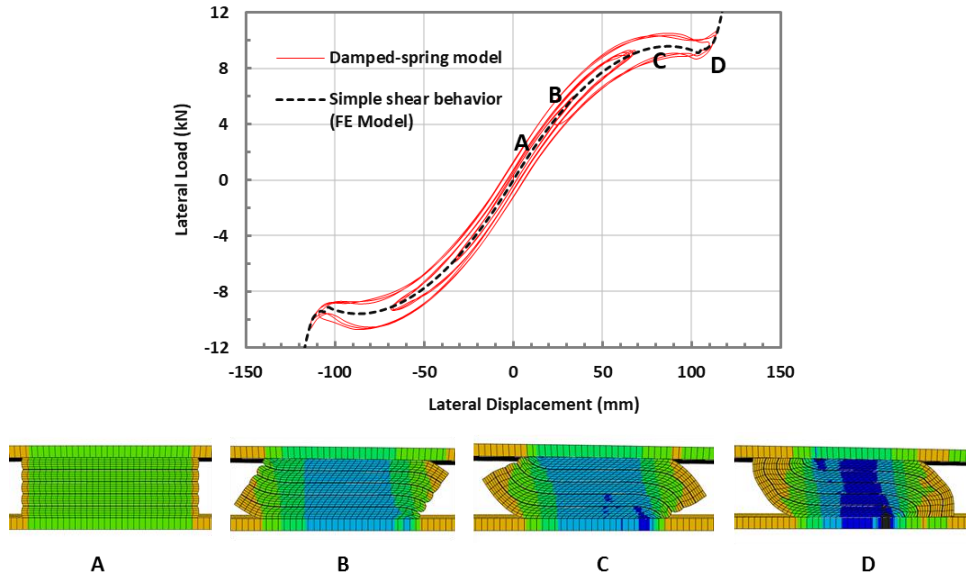

Fig. 4.5. Shear behavior obtained by means of the 3D FE modeling (dashed line) with the corresponding deformation pattern, and the equivalent damped-spring model of UFREI-175 (continuous line).
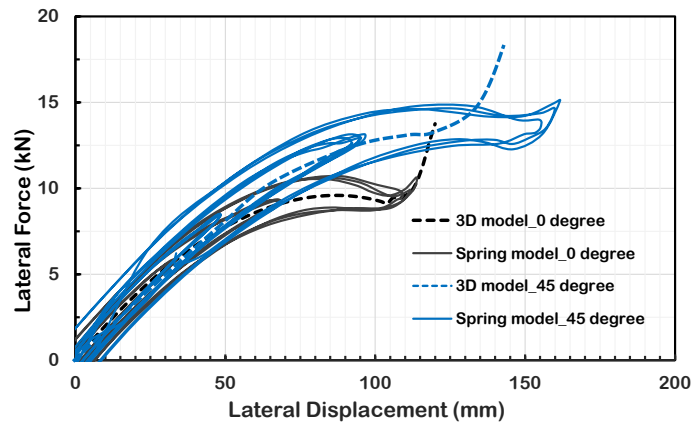

Fig. 4.6. Shear behavior at 0 and 45 degree of inclination obtained by means of the 3D FE modeling (dashed line) and the equivalent damped-spring model of UFREI-175 (continuous line).

The foundation beam is assumed made by reinforced concrete (RC) with compressive strength f_c=25 MPa. Based on the existing RC code [37], 3ø12 of steel reinforcement (f_y=275 MPa) is required at the upper and bottom side of the beam (see Fig. 4.7b), as minimum reinforcement. As the foundation beam is assumed in practice rigid in the numerical model and the spring-damper model used at a structural level loses the flexural degree of freedom, some preliminar simulations are performed for validation.
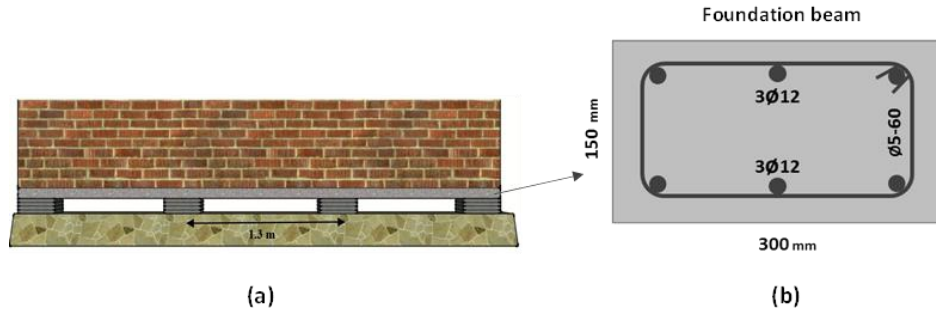
Fig. 4.7. (a) A sketch of masonry structure isolated with unbonded elastomeric isolators, (b) detail of the foundation RC beam.

Fig. 4.8a presents a detailed 3D model of an isolated RC beam resting on two UFREI-175s modelled with 3D elements, while the simplified model (Fig. 4.8b) relies into a rigid beam isolated with springs and dampers, as mentioned before. The applied mass is equivalent to the weight carried by a single span of the foundation beam in the masonry prototype, see Fig. 4.9. In the first model (Fig. 4.8a), the isolators exhibit a small but negligible rotation, due to the flexural deflection of the beam, while in the second model the beam is considered rigid. The models are then subjected to a mono-directional real accelerogram (PGA equal to 0.6g, total time equal to 12 seconds). The results reported in Fig. 4.8c, where the horizontal displacement histories of the centroid of the beam for the full 3D and the simplified damped-spring models are depicted, show an almost perfect superimposibility of the output, meaning that the simplifications introduced in the structural model are meaningful for practical purposes. As a consequence, at least in this case, an assumption of zero rotation on the isolator head may be considered reasonable. In addition, given the arrangement of the isolators, the actual structural response is dominated by the horizontal motion, which can be well represented by the present simplified damped spring model. The isolation is also quite effective, as confirmed by Fig. 4.8d where the horizontal acceleration of the RC beam in the isolated system is compared with that of the ground.
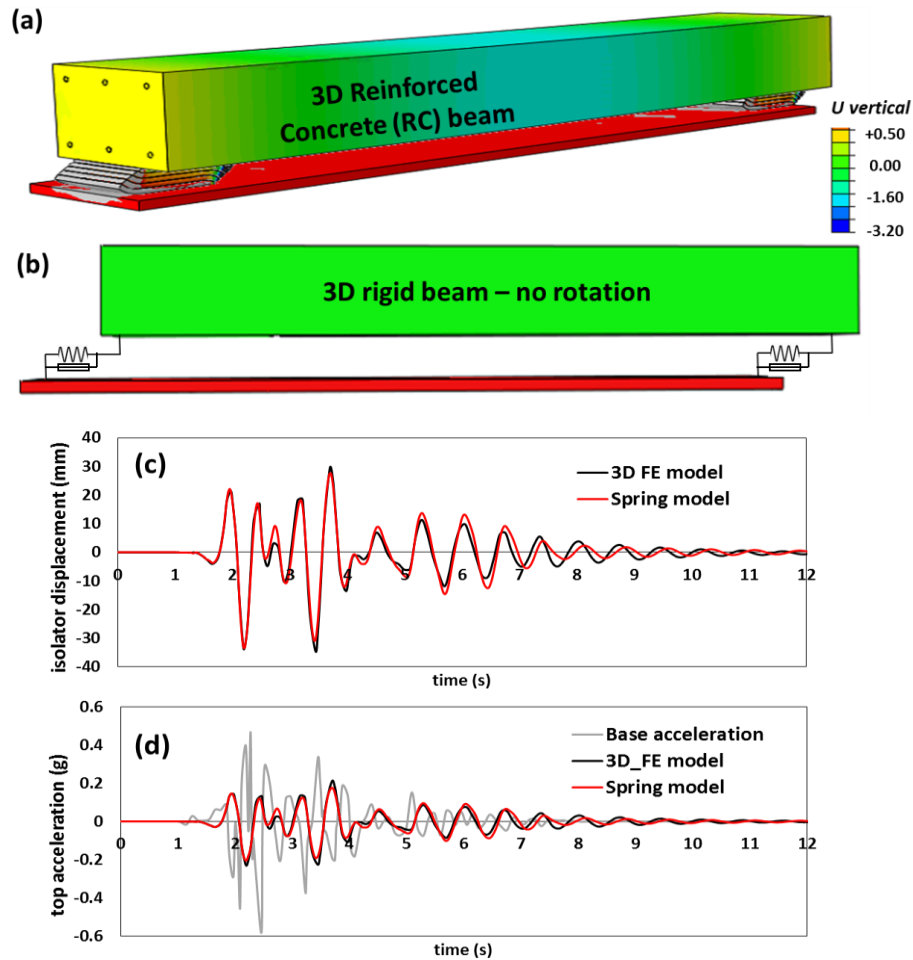
Fig. 4.8. Model validation, (a) Detailed 3D RC beam isolated with UFREIs modeled with 3D elements, (b) rigid beam (no rotation) isolated with a damped spring model. Comparative results: beam centroid horizontal displacement history (c) and comparison between ground and beam centroid acceleration (d).

4.3. FE model of an isolated masonry building

An FE model of a medium size two-story masonry house with openings and concrete diaphragms at foundation and roof levels is implemented in ABAQUS commercial code. The masonry building taken as reference is an existing one and was constructed in Tawang, India [17] to test the behavior of masonry houses isolated with UFREIs. According to authors' knowledge, this is probably one of the first examples of masonry housing isolation by means of low cost devices. Dimensions of the building are the following: thickness of the walls 300 mm, each room has 4 x 4 m plan dimensions, height of each floor is 3m, see Fig. 4.9. The weight of the roof is assumed equal to 50 kg/m^2. To prevent premature damage of the walls, rigid beams on top of windows and doors are inserted, in agreement with the real prototype. The numerical modn ufreiel has thinner walls and significantly smaller isolators compared to the real one built in India [17]. The main target of the present research, indeed, is to test the performance of a newly conceived UFREI with

very reduced dimensions, which therefore is more suited for isolation of buildings with thin walls.
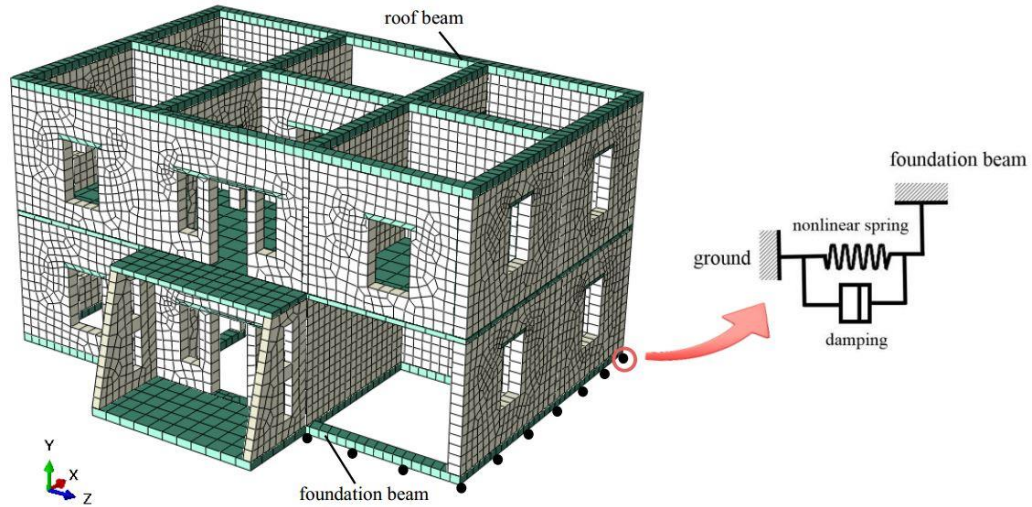

Fig. 4.9. Mesh used for the masonry prototype analyzed with isolation system and numerical model adopted at a structural scale for an isolator.

In the FE model, masonry is considered as an isotropic material exhibiting damage in both tension and compression. Although this is certainly a simplification, such assumption is commonly accepted in engineering practice [38,39,40] and, in addition, a detailed masonry modelling is not the objective of the present research. As far as the non-linear behavior is considered, a concrete damage plasticity model (CDP) is adopted. Although CDP is originally conceived for isotropic fragile materials (typically concrete) [41,42,43], it can be adapted to masonry because the orthotropy ratio in brickworks is moderate (around 1.2) under biaxial stress states in the compression–compression region [44,45]. Orthotropy is lost in CDP, but the use of isotropic model is accepted after an adaptation of the parameters to fit an average behavior between vertical and horizontal values.
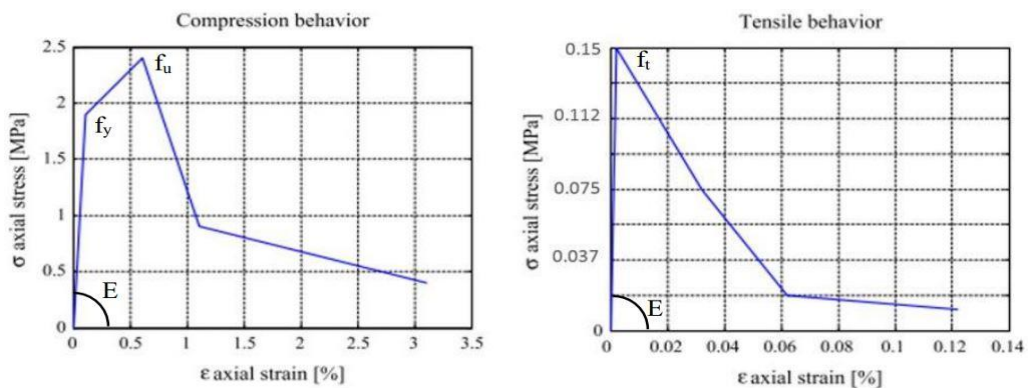

Fig. 4.10. Simplified nonlinear behavior in uniaxial tension and compression assumed for the masonry superstructure.

The CDP model requires data on the non-linear behavior in uniaxial tension and compression. In this study, the simplified axial stress-strain relationships shown in Fig. 4.10 are utilized. The tensile damage determines mainly the overall state of damage of the masonry prototype, since mortar tensile strength is considerably low. The stress-strain relation in tension exhibits a peak strength of $f_t = 0.15$ MPa. This value corresponds to the tensile strength of mortar and is taken in agreements with experimental data available in the literature for a medium/high strength mortar and codes of practice indications. Softening in tension is typically exponential and approximated in the computations with a trilinear behavior for the sake of simplicity. In compression, the response is more ductile, linear up to the yield stress $f_y = 1.8$ MPa, followed by a crushing stress $f_u = 2.4$ MPa and a softening branch which is supposed linear again for simplicity. Other parameters of CDP obtained from a previous research [40] and utilized in the computations are summarized in Table 4. 2

Table 4. 2 CDP parameters for masonry adopted in the FE model

Dilatation angle	Eccentricity	σ_{b0}/σ_{c0}	K_c	Viscosity
10	0.1	1.16	0.667	0.0001

An interesting issue that cannot be taken into account in the macroscopic FE model is the technical detail of the connection of the isolators with the superstructure. To facilitate the application of unbonded base isolators (UFREIs), rigid beams at the base of the ground floor walls must be introduced. This configuration lets the UFREIs optimally work between the foundation and the upper structure, see Fig. 4.7. In this FE analyses, the number of UFREIs used is 46 with equally stepped distance (1.3m). Damped-nonlinear springs identified through the procedure previously discussed are interposed between the foundation and the rigid beams.

The house is analyzed numerically through both non-linear static (pushover) and non-linear dynamic analyses (seven bi-directional accelerograms are applied in this latter case, as discussed in the following Sections). As a matter of fact, one of the main aims is to examine the performance of the isolated system as far as the isolation capability and reduction of damage on the upper-structure are concerned.

4.4. Pushover analyses

In the application of the horizontal load distribution within pushover, the first mode of vibration is considered. In practice, the distribution of loads is therefore reverse linear. For the sake of brevity, pushover analyses are performed along the weaker axis, namely the X-direction in Fig. 4.9. Fig. 4.11 shows the global pushover curve of the building with and without isolation. Control node is located at roof level, without the need to average horizontal displacements of different nodes, being the floors assumed sufficiently stiff. In the non-isolated building, a softening global

effect due to masonry walls diffused damage is worth noting, whereas for the isolated structure an unusual hardening at large displacements can be observed, obviously linked to the hardening exhibited by the isolators.

To classify the level of damages exhibited by the masonry building at intermediate steps of the pushover analysis, damage state limits recommended by [46] are taken into consideration. In particular DS 2, DS 3, and DS 4 points represent moderate, extensive, and collapse damage states, respectively. Such classification corresponds to the magnitude of inter-story drift observed during the analysis.
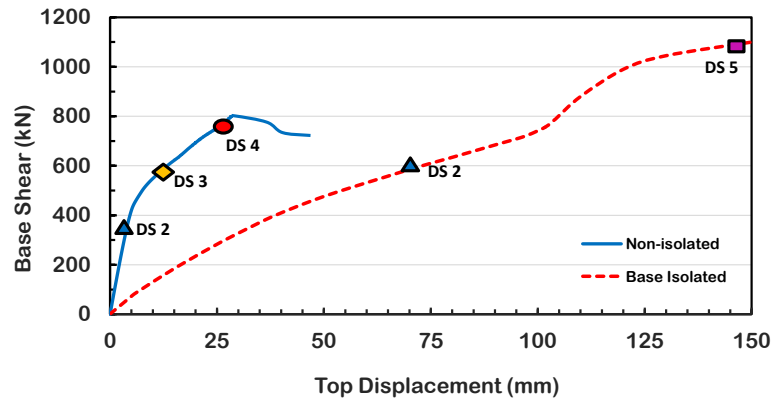

Fig. 4.11. Pushover curve of isolated (dashed) and non-isolated (continuous) two-story masonry building.

For the building without isolation (Fig. 4.11), moderate, extensive, and collapse damages occur in sequence from 2.8 to 25 mm of top displacement (Ut). Conversely, it is interesting to notice that, in the isolated model, the isolation system is able to delay the moderate damage state up to 69 mm of top displacement (Ut). As already pointed out, a hardening is recorded at Ut=100 mm for the isolated system, caused by the full-contact deformation of UFREIs. No extensive and collapse damage is observed, but a damage of the isolators appears in the end (DS 5).

DS 5 is introduced as that point where typically a damage of the isolator devices (Fig. 4.11) occurs; we defined that an isolator is damaged when the critical displacement, about 150 mm (300% shear), is exceeded. This critical limit is reported in some experimental works for UFREIs [18, 11]. It has been found that a 300% of shear deformation does not cause any noticeable delamination of UFREIs, but a roll-over that cannot be recovered after the excitation removal. This excellent feature exhibited by a typical unbonded bearing cannot be found in a bonded type with 150% of critical shear displacement [17]. Furthermore, this advantage allows the application of UFREIs with few rubber pads, so that the cost can be decreased. Fig. 4.11 reveals also that the proposed isolation system may mitigate very well the seismic vulnerability of masonry buildings in terms of damage state delay.
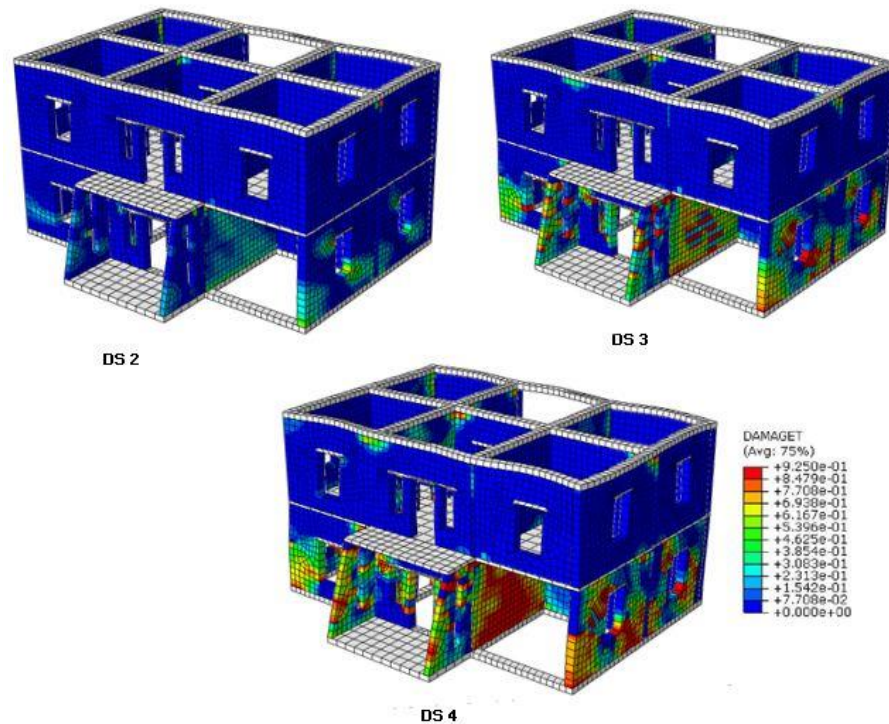
Fig. 4.12. Tensile damage distribution of masonry undergoing pushover static force.

The commercial code used in this study (ABAQUS) is capable of showing in post-processing the damage level of the elements. When the level of damage reaches 0.925, the material undergoes tensile strain equal to 0.003, which in practice corresponds to mortar total cracking. Fig. 4.12 illustrates tensile damage patches of the masonry material (building not isolated) in correspondence of the different damage states. As can be noted, tensile damages mainly propagate in the ground floor, mainly because of the perforation percentage and distribution of openings, which is typically higher than that of the first story level.

Finally, it is necessary to point out that, on masonry structures under seismic excitation, damage in compression does not play an important role in determining the failure behavior. This is the reason why a discussion on the distribution of compressive crushing is skipped.

4.5. Modal and nonlinear time history analyses

When dealing with elastic modal analysis, the implementation of FREI-175 isolation significantly shifts the natural period of the structure (Fig. 4.13) towards large values. Roughly, the period is increased almost four times in comparison with that found for the model without isolation. In order to show local vibration modes, in the FE model, RC slabs at floor level are removed. In general, from a comparison between isolated and non-isolated building without slabs, it can be observed that the proposed isolation system is quite effective and makes the natural vibration modes

shift from local to global. Fig. 4.13 shows that in the isolated structure, almost rigid eigen-modes dominate the modal behavior.

To evaluate in a more realistic manner (consistently with the actual non-linear behavior of the materials), the performance of the building (both in absence and presence of isolation), full non-linear dynamic analyses are performed by applying bi-directionally several different accelerograms [46,47]. Having in mind to implement such kind of cheap isolation in Indonesia, Indonesian seismic code is considered and seven scaled ground motions are utilized to test the performance of the structure. More in detail, the local target spectrum of Timika city, Papua Island, is considered. As the PGA of the site is more than 0.6g, the target spectrum must be generated by considering a risk-targeted maximum considered earthquake (MCE$_r$), according to the aforementioned code.

Without isolation

Mode 1	Mode 2	Mode 3
T = 0.212404 s	T = 0.204704 s	T = 0.185563 s

With isolation

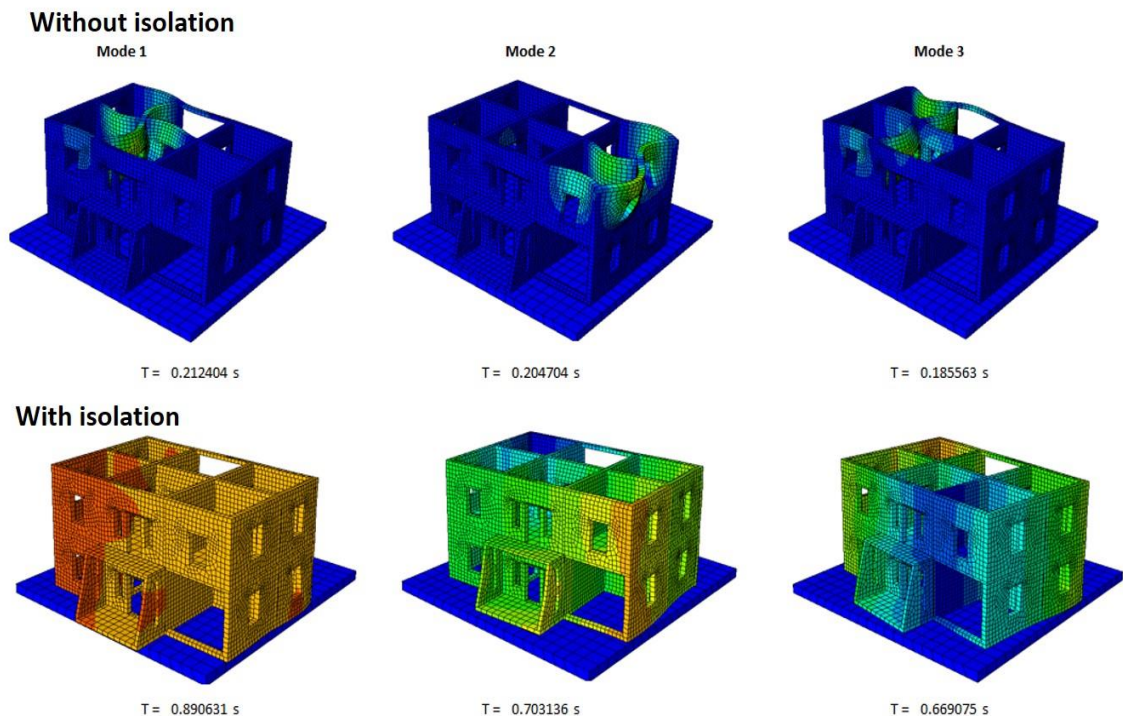|		
T = 0.890631 s	T = 0.703136 s	T = 0.669075 s

Fig. 4.13. Comparison of three first natural periods of the two-story masonry without and with isolation.

Fig. 4.14 shows the target and average spectrum of the seven accelerograms. According to the code, the average of the seven spectrums has not to be lower than the target spectrum in the range of interest, 0.5 T$_D$ - 1.25 T$_M$, where T$_D$ and T$_M$ are the effective periods of an isolated structure at design and maximum displacement, respectively. The seven selected and scaled accelerograms applied along the two geometric principal directions are depicted in Fig. 4.15.
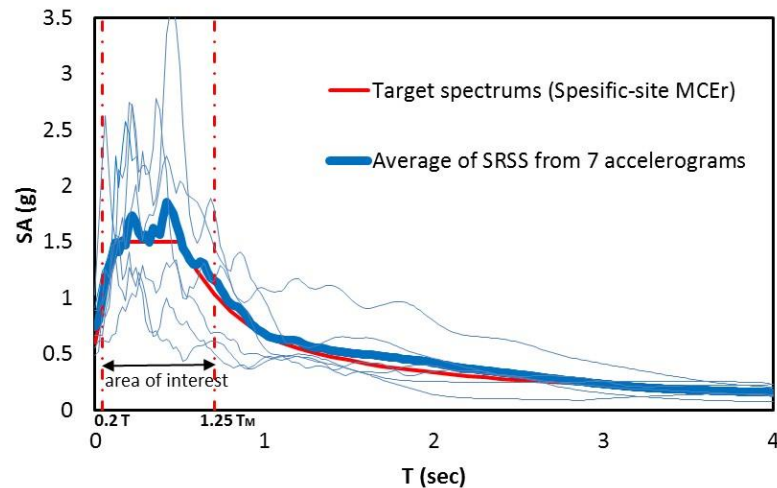
Fig. 4.14. Target spectrum according to Indonesian code and average (SRSS) of seven accelerograms considered.

The application one by one of the aforementioned seven accelerograms allows to have an insight into the structural behavior of the masonry building with and without isolation. To discuss properly and concisely the results obtained, Chi-chi accelerogram (PGA=0.5g) is taken into consideration, being the results obtained for the other excitations substantially similar. Fig. 4.16 shows few meaningful points of the accelerogram considered, used to monitor the damage cumulated. Roughly, they correspond to peaks of positive and negative accelerations at the beginning of the seismic event (which is also the most critical), which intuitively should be associated to a damage triggering. Fig. 4.17 shows tensile damage patches on masonry elements at the different instants investigated (DS2, 3, 4). Without seismic protection (fixed base), a moderate damage (DS 2) is immediately present at t=4 s, followed by extensive damage (DS 3) at t=5s, and collapse (DS 4) at the peak of the accelerogram, t=5.8s. On the contrary, the application of UFREIs helps in a significant mitigation of the building damages. No extensive and collapse damages are recorded until the end of the seismic event. Only a moderate damage occurs at t=6.5s, a few moments after the peak ground acceleration.

From Fig. 4.17 it is also interesting to notice that, in the isolated model, at the end of the numerical simulation, the volume of damaged masonry elements is much less extended than that of the model without isolation. Unlike in the static pushover analysis in Fig. 4.12, where the tensile damages are concentrated on the ground floor, tensile damage in the dynamic analyses spreads at the ground and first floors. Therefore, in case of uneven distribution of openings, instead of a pushover analysis with an equivalent frame, a time history or response spectrum analyses with 3D/plate and shell elements are recommended for seismic assessment.
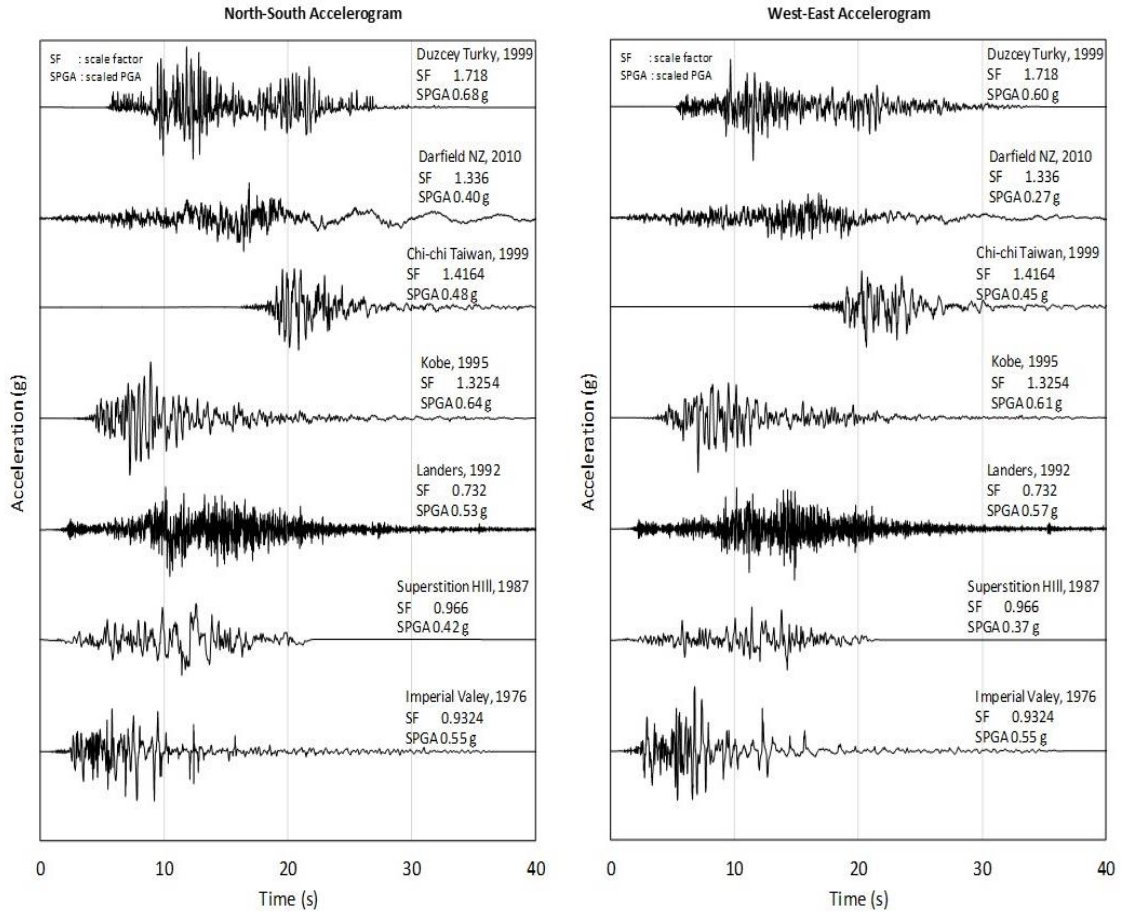
Fig. 4.15. Seven selected and scaled bidirectional acceleromgrams applied the numerical model of the building.
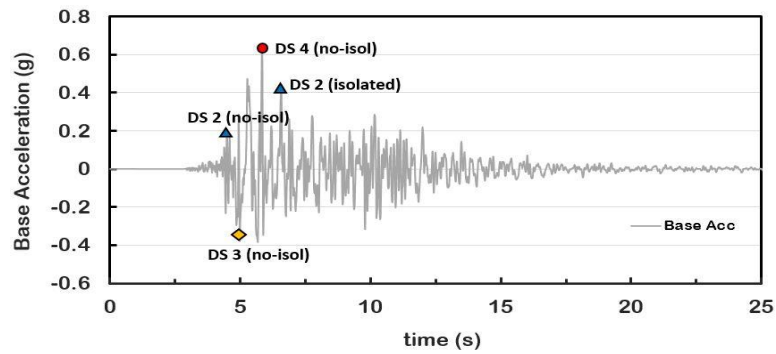

Fig. 4.16. Damage propagation of isolated and non-isolated two-story masonry housing undergoing Chi-chi accelerogram.
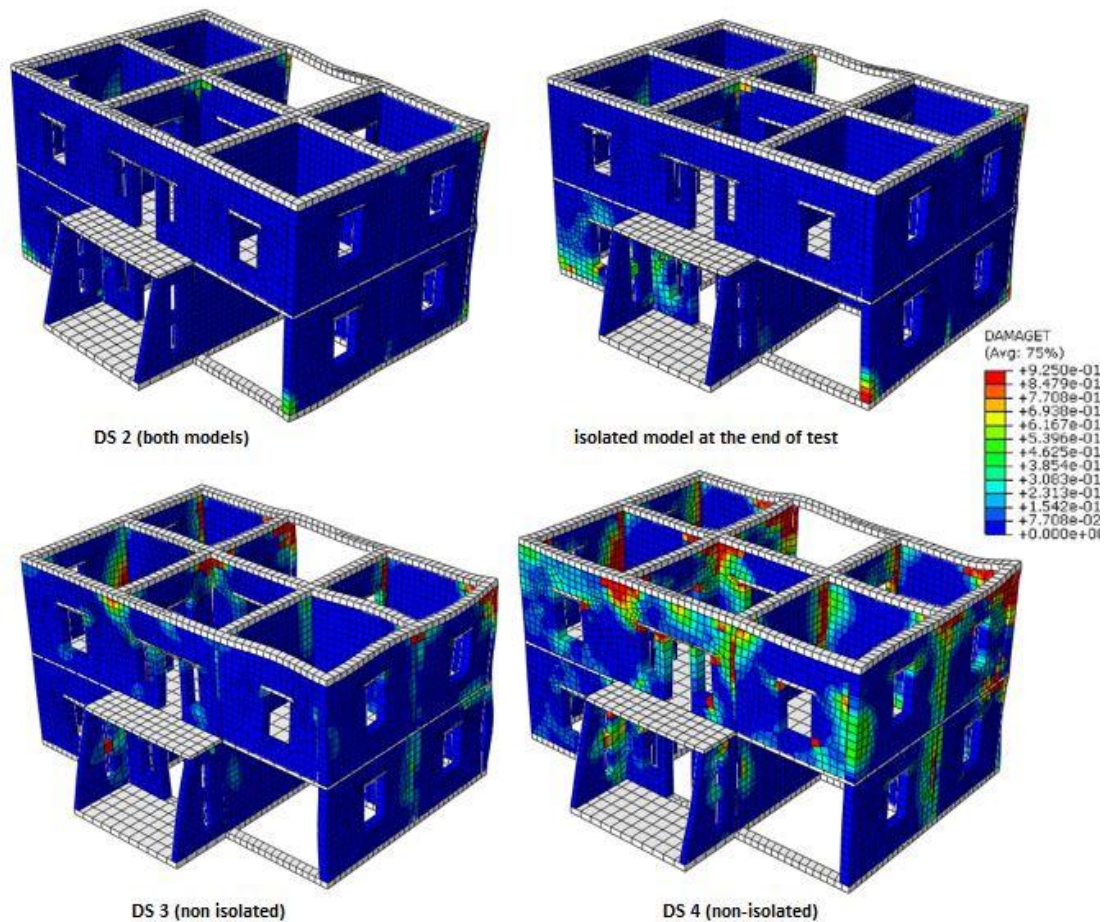
Fig. 4.17. Tensile damage distribution on masonry structures undergoing Chi-chi accelerogram with and without isolation.

Respecting the Indonesian code, the seismic performance can be assessed by averaging the outcomes obtained from the application of the seven accelerograms. Such evaluation is synoptically presented in **Error! Reference source not found.**, which shows the maximum values of the inter-story drift and the isolator deformation, two crucial parameters required by the Indonesian code.

From simulation results, it can be affirmed that the isolated masonry is safe in terms of inter-story drift. A moderate damage is present, but only 0.28% as the average of maximum drifts, an outcome which assures the suitability of a low cost isolation. Also, the isolator deformation satisfies the limit of critical deformation. The average value obtained (111 mm) is smaller than the critical shear deformation, which is 300% of total rubber thickness (or 150 mm). This critical value is found through experimental researches [11,18]. It indicates that the isolation system is capable of surviving the selected ground motions.

Table 4. 3 Performance parameters obtained from seven NLTH analyses

Accelerogram	Max. Inter-storey drift (%)	Max. Isolator deformation (mm)
Imperial Valley-06	0.49	105
Superstition Hills-02	0.7	146
Landers	0.1	118
Kobe	0.1	82
Chi-chi-04	0.32	106
Darfield	0.18	129
Duzce	0.1	92
Average	**0.28**	**111**

4.6. Conclusions

Several accurate 3D FE analyses have been carried out on a newly conceived low-cost fiber reinforced elastomeric isolator (FREI) to apply for new residential buildings in developing countries. The proposed isolator, which uses glass fibers instead of steel laminas has considerably smaller dimensions and shape factor if compared to conventional ones. The present numerical insight anticipates an ongoing experimental research and a patent of the device for real applications.

Different hypotheses have been critically compared: bonded, unbonded, and friction between pads and GFRP laminas. With the aim of applying this isolation system in areas characterized by a medium-to-high seismicity, it seems that the unbonded one (UFREI) is the most suitable for the base isolation of low-rise masonry buildings, also considering economic constraints. Such type of isolators may actually enable a wider range of horizontal deformations during an earthquake, thus fairly reducing damage on masonry elements. The special features of UFREIs are the softening and hardening branches. In fact, the former allows the achievement of a lower effective horizontal stiffness, so that the seismic force demand is decreased, whilst the latter plays an important role in limiting the shear displacement of the isolation system when subjected to a strong earthquake.

A clear methodology for the design -based on two phases of FE numerical analyses- has been proposed. The first phase is the numerical determination of the hysteretic behavior of a single device by means of a full 3D FE discretization, whereas the second phase is the advanced FE structural analysis of an isolated structure, where the isolator has been modeled as a system of a damper and a nonlinear spring, applied at the base of the structure. The passage between first and second phase relies into the classic identification of the spring-damper system from results obtained in the first phase with the detailed 3D modeling of the device.

To evaluate the performance of the proposed isolation system with a sufficient insight, pushover and time-history analyses have been performed on a real prototype of a two-story masonry building in India, where a sound model including nonlinearity and softening in tension and compression for the masonry material has been also taken into account. Time-history analyses have been performed by

considering a risk-targeted maximum considered earthquake (MCE$_r$), according to the Indonesian seismic code. It has been found that, for the selected seismic zone, the proposed isolators significantly improved the seismic behavior: the structure resulted only moderately damaged whereas collapse was avoided, and so any casualty. In addition, the maximum deformations of isolators during seismic motion did not exceed the critical limit, so allowing the re-utilization of the isolation system.

This simplified and suitably identified two-step method proved to work reasonably well and leads to faster computations when compared to a detailed modeling of the real 3D geometry of the isolators at a structural level. The present numerical approach surely needs future experimental validation to verify the accuracy of the proposed method, but yet exhibits appealing stability and predictive capabilities, revealing great potential for the design of isolated buildings in developing countries, which could employ low-cost rubber isolation systems on a large scale.

References

[1] Yuan Feng, Dan Yi, and Qiong Bi, "Seismic design analysis of the country masonry school buildings in the meizoseismal area," *Earthquake Engineering and Engineering Vibration*, vol. 10, pp. 359-367, 2011.

[2] C. V. R. Murtyl, Jayanta Dutta, and Sudhir K. Agrawal, "Twin lintel belt in steel for seismic strengthening of brick masonry buildings," *Earthquake Engineering and Engineering Vibration*, vol. 3, pp. 215-222, 2004.

[3] Teddy Boen, *Yogya Earthquake 27 May 2006: Structural Damage Report*.: EERI, 2006.

[4] Li Li, "Base isolation measure for aseismic buildings in China," in *Proceedings of the 8th World Conference on Earthquake Engineering*, vol. 6, 1984, pp. 791-798.

[5] Mohammed Qamaruddin, Rasheeduzzafar, Anand S. Arya, and Brijesh Chandra, "Seismic response of masonry buildings with sliding substructure," *Journal of Structural Engineering*, vol. 112, pp. 2001-2011, 1986.

[6] Yonglin Lou, Minquan Wang, and J. Su, "A research of sliding shock absorbing multi-storey brick building," in *Proc., 10th World Conf. on Earthquake Engineering*, vol. 4, 1992, pp. 2499-2503.

[7] Radhikesh P. Nanda, Manish Shrikhande, and Pankaj Agarwal, "Low-Cost Base-Isolation System for Seismic Protection of Rural Buildings," *Practice Periodical on Structural Design and Construction*, vol. 21, p. 04015001, 2015.

[8] Srijit Bandyopadhyay, Aniruddha Sengupta, and G. R. Reddy, "Performance of sand and shredded rubber tire mixture as a natural base isolator for earthquake protection," *Earthquake Engineering and Engineering Vibration*, vol. 14, pp. 683-693, 2015.

[9] Andrea Chiozzi, Michele Simoni, and Antonio Tralli, "Base isolation of heavy non-structural monolithic objects at the top of a masonry monumental construction," *Springer: Materials and Structures*, vol. 49, pp. 2113-2130, 2016.

[10] Animesh Das, Sajal Kanti Deb, and Anjan Dutta, "Shake table testing of un-reinforced brick masonry building test model isolated by U-FREI," *Earthquake

Engineering \& Structural Dynamics, vol. 45, pp. 253-272, 2016.

[11] N. C. Van Engelen, M. J. Tait, and D. Konstantinidis, "Horizontal behaviour of stable unbonded fiber reinforced elastomeric isolators (SU-FREIs) with holes," in *Proceedings of the 15th World Conference on Earthquake Engineering*, 2012.

[12] Mariacristina Spizzuoco, Andrea Calabrese, and Giorgio Serino, "Innovative low-cost recycled rubber--fiber reinforced isolator: experimental tests and finite element analyses," *Engineering Structures*, vol. 76, pp. 99-111, 2014.

[13] Hamid Toopchi-Nezhad, Michael J. Tait, and Robert G. Drysdale, "Testing and modeling of square carbon fiber-reinforced elastomeric seismic isolators," *Structural Control and Health Monitoring*, vol. 15, pp. 876-900, 2008.

[14] Niel C. Van Engelen, Dimitrios Konstantinidis, and Michael J. Tait, "Structural and nonstructural performance of a seismically isolated building using stable unbonded fiber-reinforced elastomeric isolators," *Earthquake Engineering \& Structural Dynamics*, vol. 45, pp. 421-439, 2016.

[15] Krzysztof Wilde, Paolo Gardoni, and Yozo Fujino, "Base isolation system with shape memory alloy device for elevated highway bridges," *Engineering structures*, vol. 22, pp. 222-229, 2000.

[16] Muhammad Tariq Amin Chaudhary, Masato Ab, and Yozo Fujino, "Performance evaluation of base-isolated Yama-agé bridge with high damping rubber bearings using recorded seismic data," *Engineering Structures*, vol. 23, pp. 902-910, 2001.

[17] Van Ngo Thuyet, S. K. Deb, and A. Dutta, "Mitigation of seismic vulnerability of a prototype low-rise masonry building using U-FREIs," *Journal of Performance of Constructed Facilities*, vol. Under Review, p. Under Review, 2017.

[18] G. P. de Raaf and Michael, Michael J. Tait, and Hamid Toopchi-Nezhad, "Stability of fiber-reinforced elastomeric bearings in an unbonded application," *Journal of Composite materials*, vol. 45, pp. 1873-1884, 2011.

[19] American Society Civil Engineers, *Minimum design loads for buildings and other structures*.: Amer Society of Civil Engineers, 2013, vol. 7-10.

[20] Badan Standarisasi Nasional, "Tata Cara Perencanaan Ketahanan Gempa untuk Struktur Bangunan Gedung dan Non Gedung (SNI 1726: 2012)," *Badan Standardisasi Nasional*, 2012.

[21] Ahmet Turer and Bayezid Özden, "Seismic base isolation using low-cost Scrap Tire Pads (STP)," *Materials and Structures*, vol. 41, pp. 891-908, 2008.

[22] Van, C. Engelen Niel, Peyman M. Osgooei, Michael J. Tait, and Dimitrios Konstantinidis, "Experimental and finite element study on the compression properties of Modified Rectangular Fiber-Reinforced Elastomeric Isolators (MR-FREIs)," *Engineering Structures*, vol. 74, pp. 52-64, 2014.

[23] Andrea Calabrese, Mariacristina Spizzuoco, Giorgio Serino, Gaetano Della Corte, and Giuseppe Maddaloni, "Shaking table investigation of a novel, low-cost, base isolation technology using recycled rubber," *Structural Control and Health Monitoring*, vol. 22, pp. 107-122, 2015.

[24] Thuyet Van Ngo, Anjan Dutta, and Sajal K. Deb, "Evaluation of horizontal stiffness of fibre-reinforced elastomeric isolators," *Earthquake Engineering \& Structural Dynamics*, vol. 46, pp. 1747-1767, 2017.

[25] D. S. Simulia, "ABAQUS 6.13 User?s manual," *Dassault Systems, Providence,*

RI, 2013.

[26] C. S. I. SAP2000 V, "8, 2002. Integrated Finite Element Analysis and Design of Structures Basic Analysis Reference Manual," *Computers and Structures, Inc., Berkeley, California, USA*, 2010.

[27] Peyman M. Osgooei, Michael J. Tait, and Dimitrios Konstantinidis, "Non-iterative computational model for fiber-reinforced elastomeric isolators," *Engineering Structures*, vol. 137, pp. 245-255, 2017.

[28] Ali Manzoori and Hamid Toopchi-Nezhad, "Application of an extended Bouc-Wen model in seismic response prediction of unbonded fiber-reinforced isolators," *Journal of Earthquake Engineering*, vol. 21, pp. 87-104, 2017.

[29] Animesh Das, Sajal Kanti Deb, and Anjan Dutta, "Comparison of Numerical and Experimental Seismic Responses of FREI-Supported Un-reinforced Brick Masonry Model Building," *Journal of Earthquake Engineering*, vol. 20, pp. 1239-1262, 2016.

[30] S. J. Jerrams, M. Kaya, and K. F. Soon, "The effects of strain rate and hardness on the material constants of nitrile rubbers," *Materials \& design*, vol. 19, pp. 157-167, 1998.

[31] Majid Shahzad, Ali Kamran, Muhammad Zeeshan Siddiqui, and Muhammad Farhan, "Mechanical Characterization and FE Modelling of a Hyperelastic Material," *Materials Research*, vol. 18, pp. 918-924, 2015.

[32] Hamid Toopchi-Nezhad, Michael J. Tait, and Robert G. Drysdale, "Bonded versus unbonded strip fiber reinforced elastomeric isolators: finite element analysis," *Composite Structures*, vol. 93, pp. 850-859, 2011.

[33] Huma Kanta Mishra, Akira Igarashi, and Hiroshi Matsushima, "Finite element analysis and experimental verification of the scrap tire rubber pad isolator," *Bulletin of Earthquake Engineering*, pp. 1-21, 2013.

[34] A. B. Habieb, G. Milani, Tavio, and F. Milani, "Low cost rubber seismic isolators for masonry housing in developing countries," in *AIP Conference Proceedings*, vol. 1906, 2017, p. 090012.

[35] A. B. Habieb, G. Milani, Tavio, and F. Milani, "SEISMIC PERFORMANCE OF A MASONRY BUILDING ISOLATED WITH LOW-COST RUBBER ISOLATORS," *WIT Transactions on The Built Environment*, vol. 172, pp. 71-82, 2017.

[36] G. Milani and F. Milani, "Stretch--stress behavior of elastomeric seismic isolators with different rubber materials: numerical insight," *Journal of Engineering Mechanics*, vol. 138, pp. 416-429, 2011.

[37] Standar Nasional Indonesia, *Persyaratan beton struktural untuk bangunan gedung*.: SNI 2847, 2013.

[38] Gabriele Milani and Gennj Venturini, "Safety Assessment of Four Masonry Churches by a Plate and Shell FE Nonlinear Approach," *Journal of Performance of Constructed Facilities*, vol. 27, pp. 27-42, 2011.

[39] Simone Tiberti, Maurizio Acito, and Gabriele Milani, "Comprehensive FE numerical insight into Finale Emilia Castle behavior under 2012 Emilia Romagna seismic sequence: damage causes and seismic vulnerability mitigation hypothesis," *Engineering Structures*, vol. 117, pp. 397-421, 2016.

[40] Thainswemong Choudhury, Gabriele Milani, and Hemant B. Kaushik, "Comprehensive numerical approaches for the design and safety assessment of

masonry buildings retrofitted with steel bands in developing countries: The case of India," *Construction and Building Materials*, vol. 85, pp. 227-246, 2015.

[41] Maurizio Acito, Massimiliano Bocciarelli, Claudio Chesi, and Gabriele Milani, "Collapse of the clock tower in Finale Emilia after the May 2012 Emilia Romagna earthquake sequence: Numerical insight," *Engineering Structures*, vol. 72, pp. 70-91, 2014.

[42] Marco Valente and Gabriele Milani, "Non-linear dynamic and static analyses on eight historical masonry towers in the North-East of Italy," *Engineering Structures*, vol. 114, pp. 241-270, 2016.

[43] Giovanni Castellazzi, Antonio Maria D?Altri, Stefano de Miranda, and Francesco Ubertini, "An innovative numerical modeling strategy for the structural analysis of historical monumental buildings," *Engineering Structures*, vol. 132, pp. 229-248, 2017.

[44] A. W. Page, "8487 The biaxial compressive strength of brick masonry," 1981.

[45] G. Milani, Paulo B. Lourenço, and A. Tralli, "Homogenised limit analysis of masonry walls, Part I: Failure surfaces," *Computers \& structures*, vol. 84, pp. 166-180, 2006.

[46] Satish Bhagat and Anil C. Wijeyewickrema, "Seismic response evaluation of base-isolated reinforced concrete buildings under bidirectional excitation," *Earthquake Engineering and Engineering Vibration*, vol. 16, pp. 365-382, 2017.

[47] Deepak R. Pant and Manika Maharjan, "On selection and scaling of ground motions for analysis of seismically isolated structures," *Earthquake Engineering and Engineering Vibration*, vol. 15, pp. 633-648, 2016.

[48] Gian Michele Calvi, "A displacement-based approach for vulnerability evaluation of classes of buildings," *Journal of Earthquake Engineering*, vol. 3, pp. 411-438, 1999.
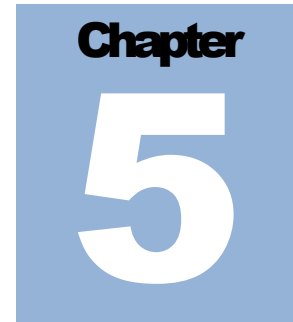
Chapter

5

Base Seismic Isolation of A Historical Masonry Church using Fiber Reinforced Elastomeric Isolators

This work investigates the possibility of improving the seismic performance of a small historical masonry church using fiber reinforced elastomeric isolators in bonded (BFREI) and unbonded (UFREI) applications. Detailed three-dimensional (3D) finite element (FE) models are used to characterize the behavior of the two types of FREIs. An Abaqus User Element (UEL) is developed to simulate the 3D behavior of FREIs for large scale seismic analyses of complex isolated structures. The results of cyclic shear analyses show that the proposed UEL model can accurately predict the behavior obtained through detailed 3D FE models. A series of non-linear dynamic analyses are performed to investigate the seismic response of a small historical masonry church in the original and base-isolated configurations employing both BFREIs and UFREIs. Numerical results show that the fixed-base model experiences severe and widespread damage, while UFREIs are observed to be very effective in significantly reducing the damage level of the masonry church when subjected to moderate-to-high seismic actions. Both the isolator types satisfy the maximum lateral displacement requirements reported in the literature.

5.1. Introduction

In Italy, a large number of historical masonry constructions, in particular churches, are highly vulnerable to damage and prone to partial or total collapse under seismic actions, as demonstrated by recent earthquakes [1]-[4]. Different seismic protection strategies and techniques are available to increase the seismic capacity of existing masonry constructions, as widely reported in the literature: among many others, see [5]-[8]. Common retrofitting techniques are often invasive and generally based on a strengthening approach, increasing the seismic demand on the structure.

On the other hand, innovative retrofitting strategies, such as base isolation system and supplemental damping, can be used to mitigate the effects of earthquakes on new and existing structures: such techniques are aimed at decreasing the seismic demand on the structure or increasing its energy dissipation capacity. In particular, base

isolation has been widely accepted as an effective method for the protection of structures against seismic actions: the isolation devices, typically placed at the base of the structure, increase the flexibility of the structure and shift its fundamental frequency away from the dominant frequency of seismic excitations, thus significantly reducing inter-story drifts and accelerations.

Base isolation has become increasingly popular among engineers in designing important structures in high seismicity regions: however, although base isolation has been recognized as a promising alternative to protect structures against earthquakes, engineering research and practices on seismic isolation of historical masonry constructions remain limited. Moreover, seismic isolators are especially needed for masonry structures, where the poor tensile strength may lead to low horizontal load carrying capacities [9]-[11].

The applications of isolation systems have increased also in high seismic regions of developing countries through the use of economical devices. Fiber reinforced elastomeric isolators (FREIs) have been introduced as a potential low-cost alternative to conventional steel reinforced elastomeric ones: they can be unbonded (UFREI) or bonded (BFREI) to both the superstructure and substructure. Conventional elastomeric isolators usually consist of several layers of high-damping rubber (pads) reinforced by interposed steel shims: the reinforcement has the role of improving the stability and limiting vertical deformations, while the horizontal deformations are controlled by the shear stiffness of the pads. Glass or carbon fiber material can be used as alternative reinforcement because it is more economical than its steel counterpart and provides comparable reinforcement effects [12]-[14]. The fiber reinforcement allows the application of UFREIs, in which the upper and bottom surfaces are not glued to the structure: furthermore, steel reinforcing plates for the supports are not required. A shaking table test on a new masonry building supported on UFREIs has provided promising results, with a significant reduction of inter-story drifts and accelerations [15]. Moreover, a first full-scale application of base isolation to a new two-story masonry building supported on UFREIs has been carried out in Tawang, India [16]. On the other hand, the application of base isolation in existing or historical masonry buildings seems a challenging task due to the need of separating the superstructure and foundation. The difficulty typically derives from the large thickness and the massive weight of masonry walls. However, several construction methods have been proposed to implement the base isolation system into old masonry buildings [17][18].

The main advantages of UFREIs application are described in the literature [12][19][20]. The effective horizontal stiffness of UFREIs is considerably lower than that of BFREIs, thus decreasing the seismic demand. The reduction of the effective lateral stiffness is the result of the rollover deformation of the UFREI due to the absence of bonding. Some researchers have evaluated the UFREI stability limit at which the isolator can be subjected to damage or delamination. Lateral displacements equal to $1.7\text{-}2t_r$ (where t_r is the total thickness of rubber layers in the isolator) are considered as critical values [21], while it is reported in [22] that even lateral

displacements equal to $3t_r$ don't seem to cause any damage in the rubber-fiber interfaces. Such large critical values facilitate the utilization of UFREIs with small height. Moreover, such a remarkable feature cannot be found in commercial BFREIs that typically exhibit critical lateral displacements equal to $1.5t_r$ [23][24].
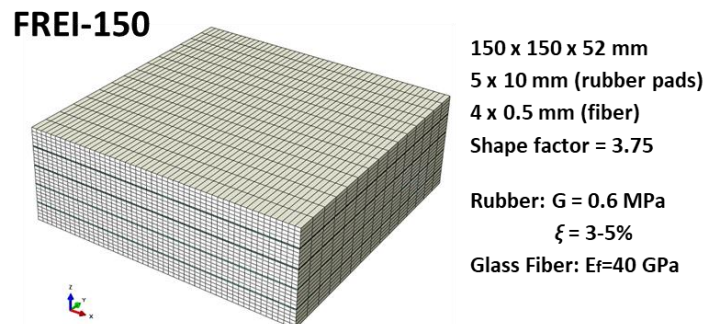

FREI-150

150 x 150 x 52 mm
5 x 10 mm (rubber pads)
4 x 0.5 mm (fiber)
Shape factor = 3.75

Rubber: G = 0.6 MPa
ξ = 3-5%
Glass Fiber: Ef=40 GPa

Fig. 5.1. FE model of FREI-150 with indication of the main geometrical and mechanical characteristics

In the literature [21][25], FREI specimens generally consist of several thin rubber pads (15-20 pads), resulting in a high shape factor that is defined as the ratio of the plan area to the perimeter stress-free area of a single pad. Employing several thin pads, consequently, increases the cost of the bearing because of the need for adhesive on rubber-fiber interfaces. Thus, in this work, a FREI with only a few rubber pads (see Fig. 5.1) is proposed to obtain a more economical isolation system. In addition, the FREIs used are significantly smaller than the isolators commonly found in the market. The small isolators considered in the present research project are primarily used for seismic protection of unreinforced masonry buildings. The dimensions of the reinforced concrete beams for the base isolation support can be reduced due to the arrangement of several FREIs of small sizes. Moreover, the use of several small FREIs (two small isolators along the wall thickness) can improve the overturning stability of the wall.

Another important issue is related to the strategies of modeling UFREIs in 3D seismic analyses of complex isolated structures. The utilization of detailed 3D FE models of UFREIs is computationally demanding, with results not easily achievable for macro-scale computations in the non-linear dynamic range: therefore, the development of a simple and representative model is of paramount importance.

The implementation of a base isolation system in existing masonry structures is not yet popular due to the lack of references and construction methods: therefore, comprehensive numerical and experimental studies are required to develop practical design guidelines for the application of the base isolation method. The main objectives of the paper are: 1) to propose a new Abaqus User Element (UEL) to represent the 3D behavior of a single UFREI for global seismic analysis of complex isolated structures, such as masonry churches, thus reducing computational effort; 2) to analyze the seismic performance of a small historical masonry church with the newly conceived low-cost FREIs; 3) to assess and compare the effectiveness of the application of bonded and unbonded FREIs.

The chapter is organized as follows. In Section 2 detailed 3D FE models are developed and cyclic shear FE analyses are performed to investigate the behavior of FREIs. In Section 3 a new Abaqus User Element (UEL) is proposed and validated through the detailed 3D FE models to represent the 3D behavior of FREIs for large scale seismic analysis of complex isolated structures. In Section 4 the detailed FE model of the historical masonry church with base isolation system is described. Section 5 presents and discusses the main results of non-linear dynamic analyses performed on the historical masonry church in the original and base-isolated configurations.

5.2. 3D FE analyses of fiber reinforced elastomeric isolators (FREIs)

Detailed 3D FE models are developed and cyclic shear FE analyses are performed through the software code Abaqus [26] to investigate the behavior of FREIs. In the software code Abaqus, different types of hyperelastic material models are available and each model defines the strain energy function in a different way. In this study the Yeoh hyperelastic material model is used to represent the properties of rubber due to its simplicity. For a compressible rubber the model is expressed by Eq. (1):

$$W = \sum_{i=1}^{3} C_{i0}(I_1 - 3)^i + \sum_{i=1}^{3} \frac{1}{D_i}(J_{el} - 1)^{2i} \qquad (1)$$

where W is the strain energy density, C_{i0} and D_i are material coefficients, I_1 is the first deviatoric strain invariant and J_{el} is the elastic volume strain. In the present study, the values of the material coefficients are assumed by referring to experimental studies reported in [27][28], where coefficients of rubbers with different hardness were evaluated. The rubber considered in this study presents a shear modulus G equal to 0.6 MPa. Tablr 5. 1 shows the values of the coefficients adopted for the Yeoh hyperelastic material model in the present FE simulations.

Tablr 5. 1. Coefficients of the Yeoh hyperelastic model for FREI-150 used in the numerical analyses.

C_{10}	C_{20}	C_{30}	D_1	D_2	D_3
0.42	0.0044	0.00013	0	0	0

C in Mpa

Tablr 5. 2. Coefficients of the Prony-series model for FREI-150 used in the numerical analyses.

$g1$	$t1$	$g2$	$t2$
0.1	0.4	0.1	0.2

To characterize the damping behavior of rubber, the Prony-series model is used. It is a time-domain viscoelasticity available in Abaqus [26] to determine the time-dependent stress-strain relation. The rubber considered in this study is a low-

damping rubber, which is characterized by an equivalent damping ratio equal to about 3-5%. Tablr 5. 2 shows the coefficients values of the Prony-series viscosity model adopted for rubber in this study: such coefficients values can be obtained through relaxation tests on rubber specimens.

The isolator investigated in this study uses glass fibers as reinforcement to improve the vertical stiffness. As already explained, the utilization of fibers may reduce the cost of the isolator when compared with steel laminas [13]. In the present numerical simulations, the glass fiber is assumed isotropic-elastic with Young modulus E_f equal to 40 GPa and Poisson's ratio equal to 0.2, in accordance with many studies reported in the literature, [14][29].
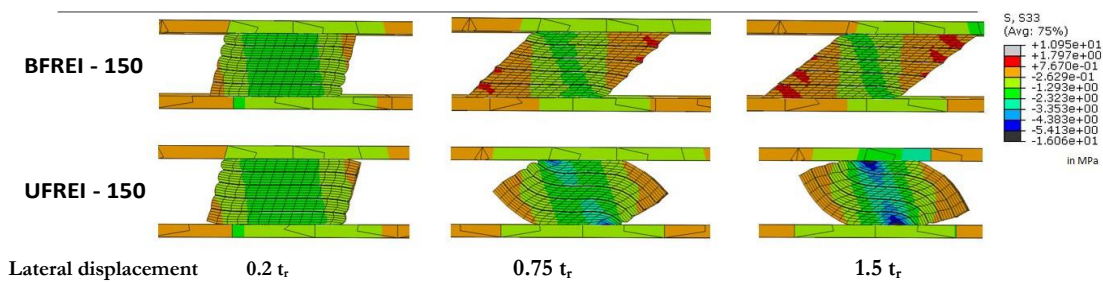
Fig. 5.2. Deformation patterns and vertical stress distribution of the bonded (BFREI) and unbonded (UFREI) isolators (FREI-150) under constant vertical pressure equal to 2.4 MPa.
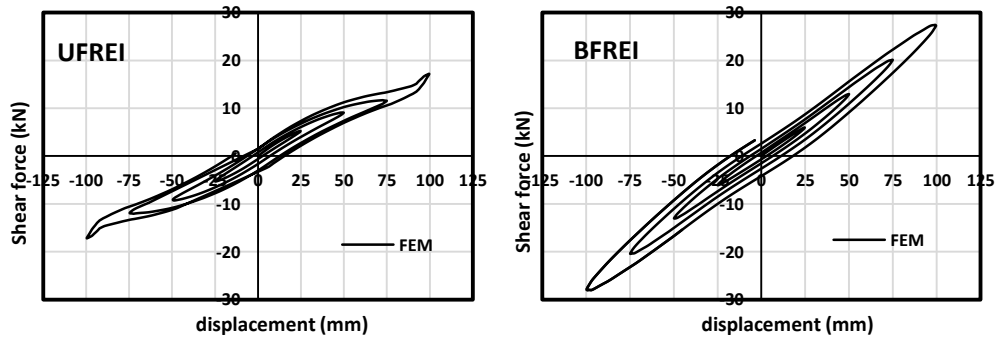
Fig. 5.3. Shear force – horizontal displacement curves obtained through 3D FE models for the unbonded (UFREI) and bonded (BFREI) isolators (FREI-150).

Fig. 5.1 illustrates the FE model of the FREI investigated in this study, denoted as FREI-150, with indication of the main geometrical and mechanical characteristics: it consists of only five rubber pads that are 10 mm thick, resulting in a low shape factor (S). The shape factor (S) is identified as the ratio of load area to load free area of the elastomer layer, see Eq. (2), where a and b are the sides lengths of rubber pads and t is the thickness of a single rubber pad.

$$S = \frac{a.b}{2(a+b) \times t} \qquad (2)$$

It is worth mentioning that the cost of the isolator decreases with decreasing values of the shape factor because the need for adhesive material and manufacturing processes are reduced. However, the consequences of small values of the shape factor should be assessed, resulting in lower vertical stiffness and critical load. The isolator is modelled using about 77000 eight-node brick elements with reduced integration (C3D8R): a perfect bond between rubber and fiber is adopted in the model.

In this study, two conditions characterized by bonded and unbonded contact are simulated and compared. In the bonded condition (BFREI), the elastomer surfaces are tied to the upper and bottom supports: it is the most common type of base isolator, which requires thick steel plates for the supports. In the unbonded condition (UFREI), the upper and bottom edges do not present bond with the supports. A penalty surface-interaction model available in Abaqus is introduced between the supports and the isolator to provide an unbonded condition in the FE model: a friction coefficient equal to μ=0.85, which is a typical value between rubber and concrete surface [30], is adopted.

Cyclic shear analyses are conducted on the detailed 3D FE models of FREIs up to lateral displacements equal to about $1.8t_r$, applying a constant vertical pressure equal to 2.4 MPa: such a pressure approximately corresponds to the load carried by a single isolator when inserted into the model of the masonry church that is analyzed in the following sections.

The deformation patterns and the vertical stress distributions of bonded and unbonded FREIs are illustrated in Fig. 5.2. Fig. 5.3 shows the shear force - horizontal displacement curves obtained through 3D FE analyses for unbonded and bonded FREIs. In bonded condition, at large horizontal displacements high values of tensile stresses are registered, leading to the delamination of the rubber-fiber interface, which is a failure that is not reproducible through such FE approach. Conversely, in unbonded condition, under moderate shear forces, the limited friction strength allows the isolator to rollover and facilitates larger deformations. The rollover mode causes a non-linear behavior, resulting in a decrease of the effective horizontal stiffness. Unlike the BFREI model, the peak tensile stress on the rubbers and interfaces significantly decreases: consequently, delamination at high deformation can be prevented. At large lateral displacements equal to $1.7t_r$, a hardening phase takes place due to the partial contact between the vertical edges of the isolator and the supports.

Tablr 5. 3 shows a comparison between UFREI and BFREI in terms of effective horizontal stiffness ($K_{h,eff}$) and damping ratio (ξ) for each cycle, obtained from the 3D-FE analyses. The calculation of the stiffness and damping ratio is based on the equation (3)-(6).

$$K_{h,eff} = (F_{max} - F_{min})/(\Delta_{max} - \Delta_{min}) \qquad (3)$$
$$\xi = W_d/(4\pi W_s) \qquad (4)$$

$$W_s = \frac{1}{2} K_{h,eff} \, \Delta^2{}_{max,ave} \tag{5}$$

$$\Delta^2{}_{max,ave} = (\Delta_{max} + |\Delta_{min}|)/2 \tag{6}$$

where F_{max}, F_{min}, Δ_{max} and Δ_{min} are the peak value of horizontal force and displacement, respectively, W_d represent the dissipated energy (area within the loop) and W_s is the restored energy.

Tablr 5. 3. Comparative results of the effective horizontal stiffness and damping ratio between UFREI and BFREI obtained from 3D FE analyses.

Shear strain	$K_{h,eff}$ (N/mm)		ξ (%)	
	UFREI	**BFREI**	**UFREI**	**BFREI**
0.5tr	211.93	249.35	5.42	5.19
1.0tr	185.03	260.34	7.03	5.24
1.5tr	158.62	270.58	9.37	5.95
2.0tr	208.99	278.36	11.45	6.37

In Tablr 5. 3, at shear strain 0.5tr, both UFREI and BFREI show a quite close effective horizontal stiffness, indicating an identical initial behavior between two specimens at initial stage. A significant decrease of the effective horizontal stiffness is shown by the UFREI up to shear strain 1.5tr, while in contrast, the BFREI results in a regular increase until the maximum imposed shear strain due to the hyperelasticity of the rubber. In the hardening phase of the UFREI, the effective stiffness seems returning back to the initial stiffness. This result reveals an advantage of the UFREI, with significant low effective stiffness at medium shear strain levels.

Another promising feature of the UFREI is depicted by the variation of the effective damping ratio. The damping in the UFREI model increases dramatically with the increase of the shear displacement, while the BFREI exhibits a lower variation. The higher damping ratio provided by the UFREI reveals excellent energy dissipation by the isolation system during an earthquake event.

5.3. Representative Abaqus User Element (UEL) for FREIs

In the previous section, a detailed 3D FE analysis of a single FREI specimen using the software code Abaqus has been presented. However, for large scale seismic analysis of complex isolated structures, the use of detailed 3D FE models of isolators is very time-consuming because several isolator devices are generally inserted at the base of the building. Unfortunately, in the software code Abaqus there is no representative element available to model isolators in an effective way. Therefore, in this study a new Abaqus User Element (UEL) is proposed and implemented to

represent the 3D behavior of a single isolator with the aim of significantly reducing the computational effort in FE modeling and analysis, thus avoiding the use of a detailed 3D FE model for each single isolator. The proposed UEL is in the form of a beam element, characterized by 12 degrees of freedom (DOF), which is able to capture the 3D behavior of a single isolator. The UEL developed for a single FREI along with the corresponding DOFs are shown in Fig. 5.4.
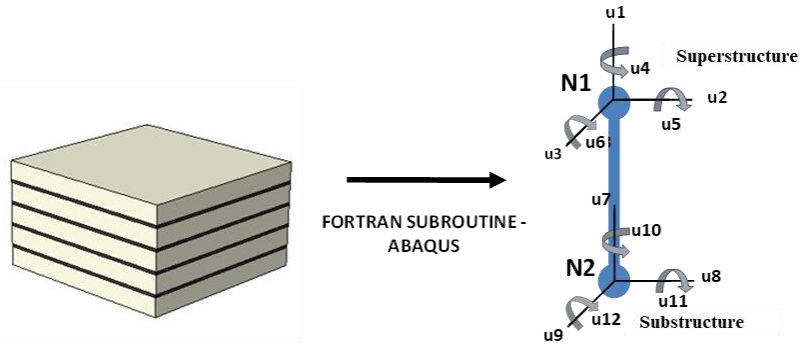

Fig. 5.4. Representative Abaqus user element (UEL) for a single FREI.

In the Chapter ??, comprehensive analyses are presented to explain how the UEL formulation is established. The proposed UEL is addressed to represent the UFREI behavior, which is characterized by a marked non-linear and hardening phase in the horizontal components and non-linear phase in the vertical component. The rotational and torsional stiffness of the UFREI is also analyzed. It is worth mentioning that the UEL formulation is based on the classical solution for BFREIs, as reported in the reference [31]. On the basis of the results obtained from 3D FE simulations, analytical solutions are proposed to simulate the behavior of UFREIs, by suitably modifying the classical equations available for BFREIs.

The proposed solutions are then implemented into a two-node beam element connecting the superstructure and the substructure, see Fig. 5.4 and Eq.7. Each node of the beam element has six DOFs: U1 is the axial DOF, U2 and U3 are the translational DOFs along the two horizontal axes, UR1 is the torsional DOF, UR2 and UR3 are the rotational DOFs around the two horizontal axes.

$$f_b = \begin{bmatrix} axial(U1) \\ shear1(U2) \\ shear2(U3) \\ torsion(UR1) \\ rotation1(UR2) \\ rotation2(UR3) \end{bmatrix};$$

$$K_b = \begin{bmatrix} axial & 0 & 0 & 0 & 0 & 0 \\ 0 & shear1 & shear12 & 0 & 0 & 0 \\ 0 & shear21 & shear2 & 0 & 0 & 0 \\ 0 & 0 & 0 & torsion & 0 & 0 \\ 0 & 0 & 0 & 0 & rotation1 & 0 \\ 0 & 0 & 0 & 0 & 0 & rotation2 \end{bmatrix} \tag{7}$$

To simulate the hysteretic behavior in horizontal components, a Bouc-Wen model is implemented into the UEL code, taking into account a coupling mechanism between damping forces in the X and Y directions, as proposed in [33], see equation (8)-(9):

$$\begin{bmatrix} F_x \\ F_y \end{bmatrix} = k_H . \begin{bmatrix} u_x \\ u_y \end{bmatrix} + c_d . \begin{bmatrix} \dot{u}_x \\ \dot{u}_y \end{bmatrix} + w \begin{bmatrix} z_x \\ z_y \end{bmatrix} \tag{8}$$

$$Y \begin{bmatrix} \dot{z}_x \\ \dot{z}_y \end{bmatrix} = \left(A[I] - \begin{bmatrix} z_x{}^2(\gamma . sign(\dot{u}_x z_x) + \beta) & z_x z_y(\gamma . sign(\dot{u}_x z_x) + \beta) \\ z_x z_y(\gamma . sign(\dot{u}_x z_x) + \beta) & z_y{}^2(\gamma . sign(\dot{u}_y z_y) + \beta) \end{bmatrix} \right) \begin{bmatrix} \dot{u}_x \\ \dot{u}_y \end{bmatrix} \tag{9}$$

where F is the restoring force, k_H is the horizontal stiffness of the bearing, c_d is the damping coefficient, u is the shear displacement and w, Y, γ, β are the Bouc-Wen parameters that control the shape of the hysteresis loop and are tuned on the basis of the results obtained from detailed 3D FE simulations of the proposed UFREI. The equations of the Bouc-Wen model are then executed numerically using a standard Newton-Raphson procedure. The UEL procedure is implemented as Fortran Abaqus subroutine. The hysteretic behavior is only applied to the orthogonal horizontal displacement components of the isolator model.

Fig. 5.5 shows the shear force - horizontal displacement curves obtained through both the 3D FE model and the proposed UEL for FREI-150 in unbonded and bonded applications. In addition, Fig. 5.6 presents the shear force-displacement curves for different lateral displacements levels. It can be noted that a very good prediction is obtained by using the UEL model, which is able to simulate the non-linear and hardening behavior as well as the hysteresis loop for different lateral displacements levels. The hardening phase in the UFREI model is depicted at lateral displacement equal to about 1.7-1.8tr. Tablr 5. 4 summarizes the value of effective horizontal stiffness and damping ratio obtained through 3D FE and UEL models. A difference smaller than 10% reveals a good accuracy of the proposed UEL model when compared with the 3D FE simulation. In the following sections, the representative UEL model is employed for the seismic analysis of a historical masonry church isolated with FREIs.
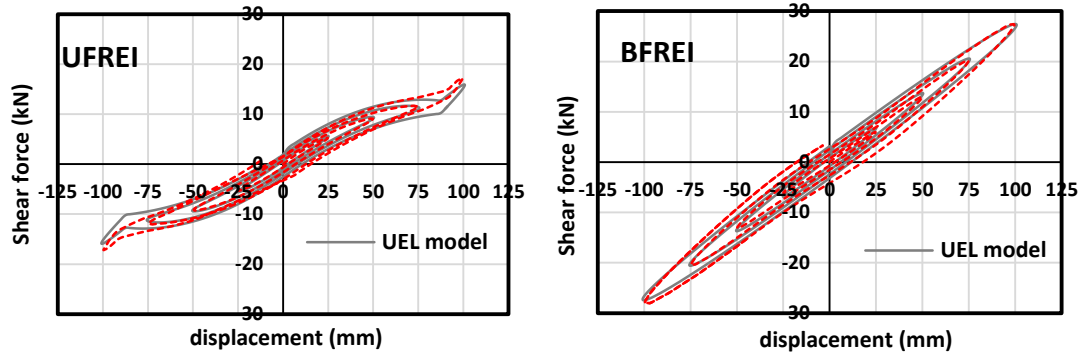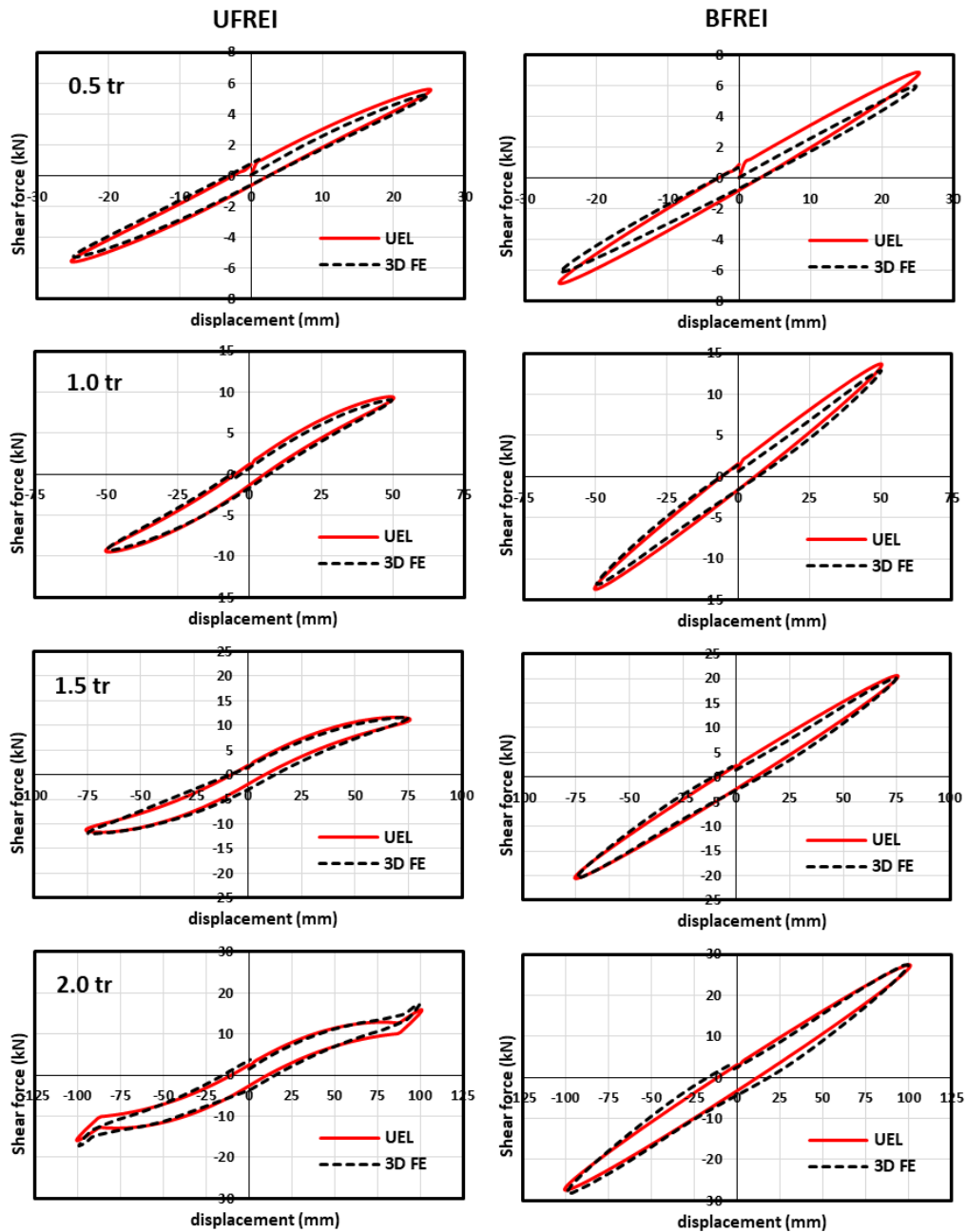
Fig. 5.5. Shear force – horizontal displacement curves obtained through 3D FE models and Abaqus User Element (UEL) for the unbonded (UFREI) and bonded (BFREI) isolators (FREI-150).

It is worth mentioning that the developed UEL model can be adopted also for the case of BFREIs, by simply neglecting the evolution of l_t (Eq. (4)) and using the classical solution, while the other Bouc-Wen parameters are set equal to those of UFREIs: such a procedure results in a relatively constant horizontal stiffness of the UEL model, as seen in Fig. 5.5 and Fig. 5.6.

Tablr 5. 4. Comparative results of the effective horizontal stiffness and damping ratio obtained from 3D FE and UEL model.

| Shear strain | UFREI | | | | | | BFREI | | | | | |
| | kH.eff (N/mm) | | | ξ (%) | | | kH.eff (N/mm) | | | ξ (%) | | |
	3D FEM	UEL	error (%)	3D FEM	UEL	error (%)	3D FEM	UEL	error (%)	3D FEM	UEL	error (%)
0.5 tr	211.93	222.38	4.93	5.42	5.67	4.67	249.35	272.27	9.19	5.19	5.74	10.6
1.0 tr	185.03	187.43	1.30	7.03	6.75	3.91	260.34	272.26	4.58	5.24	5.76	9.87
1.5 tr	158.62	154.32	2.71	9.37	8.64	7.75	270.58	272.24	0.61	5.95	5.76	3.13
2.0 tr	208.99	196.29	6.08	11.45	12.3	7.22	278.36	272.21	2.21	6.37	5.76	9.50

Fig. 5.6. Shear force – horizontal displacement curves obtained through 3D FE models and Abaqus User Element (UEL) for UFREI and BFREI at each strain level

5.4. FE model of a masonry church isolated with FREIs

In this study the seismic performance of a small historical masonry church located in Lazio region, Central Italy, is investigated. The church dates back to the XIX century and presents a rectangular plan with two naves: it is 11.4 m long and 9.9 m width. The facade presents two side doors and a tympanum that is surmounted by a bell gable that is about 2 m high: the overall maximum height is 10.25 m. The naves longitudinal walls present two rectangular openings and are about 0.6 m thick. The

two naves are covered by four cross vaults and present a central square column with sides equal to 0.5 m. The building is composed of masonry bricks and lime mortar.
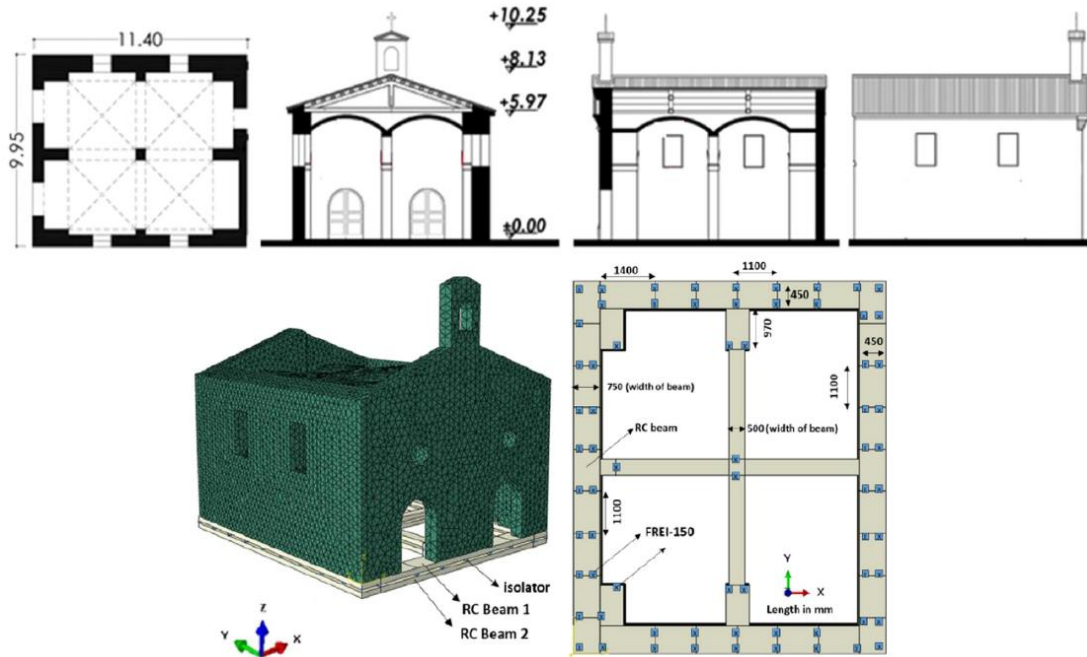
Fig. 5.7. Top: drawings of the masonry church: plan, two sections and an elevation lateral view. Bottom: FE model of the isolated masonry church and arrangement of FREIs.

Advanced numerical analyses of the church under study were performed through a detailed 3D FE model created by means of the software code Abaqus [26]. Fig. 5.7 shows a general view of the FE model of the church, consisting of about 110000 tetrahedron elements. To simulate the non-linear response of masonry, the Concrete Damaged Plasticity (CDP) model available in the software code ABAQUS is used. In this model, masonry is considered as an isotropic material exhibiting damage in both tension and compression. Although this is a simplification, such an assumption is commonly accepted in engineering practice [35]-[37]. It is worth mentioning that discrete element approaches are suitable mainly for detailed models used in the interpretation of experimental tests results or damage observed in the field: however, their use as a structural analysis tool is becoming increasingly widespread [38].

The CDP model is originally conceived for isotropic fragile materials (typically concrete), but it can be adapted to masonry because the orthotropy ratio in brickworks is moderate (around 1.2) under biaxial stress states in the compression–compression region. Orthotropy is lost in CDP but the use of the isotropic model is accepted after an adaptation of the parameters to fit an average behavior between vertical and horizontal values.

The tensile damage is considered to evaluate the overall damage state of masonry since mortar tensile strength is considerably low. The stress-strain curve in tension exhibits a peak stress $f_t = 0.19$ MPa, see Fig. 5.8: this value corresponds to the tensile

strength of mortar and is taken in agreement with experimental data available in the literature for a medium/high strength mortar and codes of practice indications. After the peak stress, micro-cracks start to propagate within the material, leading to a macroscopic softening. Softening in tension is typically exponential and approximated in the computations with a trilinear behavior for the sake of simplicity. In compression, the response is linear up to the yield stress $f_c = 1.9$ MPa: in the plastic range the response is characterized by stress hardening followed by strain softening beyond the ultimate stress $f_{cu} = 2.4$ MPa. The values of the CDP model parameters assumed according to previous studies, [3][7][39], and used in the numerical analyses are summarized in Tablr 5. 5.
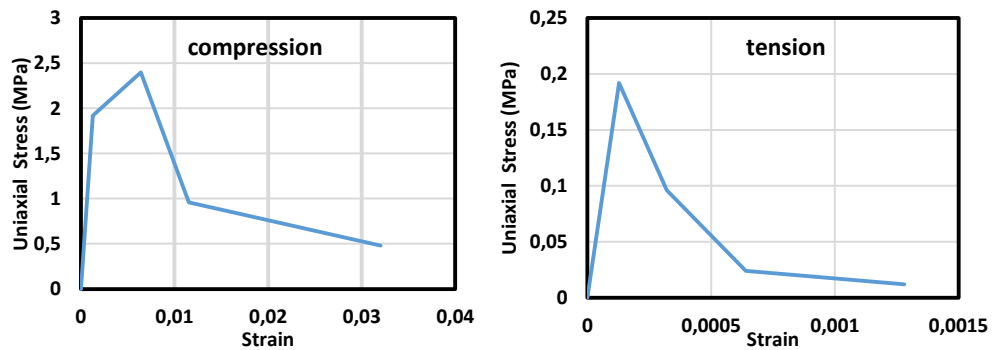
Fig. 5.8. Simplified uniaxial behavior of masonry material in compression (left) and tension (right).

Tablr 5. 5. Values of the parameters used for the CDP model in the numerical analyses.

E (MPa)	v	Dilation angle	Eccentricity	σ_{b0}/σ_{c0}	K_c	Viscosity
1800	0.2	10	0.1	1.16	0.667	0.0001

The masonry church is base isolated using isolators FREI-150, **Error! Reference source not found.**: as already mentioned, Fig. 5.5 shows the shear behavior of FREIs up to lateral displacements equal to $1.85t_r$ in unbonded and bonded conditions. To facilitate the application of the base isolators, reinforced concrete beams are placed at the base of the walls, as shown in Fig. 5.7: such a configuration allows the FREIs to work properly between the foundation and the superstructure. The proposed method to decouple the superstructure and the substructure and to insert the unbonded isolation system at the base of an existing masonry building can be found in the literature [40].

The target period of the isolation system is initially set to 1.0 second. The number of FREIs inserted into the numerical model is equal to 73, as shown in Fig. 5.7. It is worth mentioning that the number of required isolators depends on both the weight of the isolated structure and the target period of the isolation system. A single isolator should be loaded by a stress value not larger than 3 MPa to avoid buckling of the isolator, resulting in a negative horizontal stiffness. At the same time, the vertical load should be also large enough to prevent any sliding between unbonded isolators

and supports: to this aim, some researchers suggest a minimum value of vertical stress on unbonded FREIs equal to 0.5 MPa, [41].

5.5. Numerical simulations

5.5.1. Modal analyses

A modal analysis is performed to obtain the first mode shapes and the corresponding natural frequencies of the masonry church with and without base isolation, see Fig. 5.9. In the fixed-base model (FBM), the first mode (f=7.94 Hz) involves the bell gable in the longitudinal direction, the second (f=9.73 Hz) and third (f=14.7 Hz) modes concern the whole church in the transversal and longitudinal directions, respectively. On the contrary, in the isolated models the first three mode shapes are dominated by longitudinal (mode 1) and transversal (mode 2) displacements and rotation (mode 3) of the isolation system. The natural frequencies are significantly reduced: in particular, the fundamental natural frequency decreases from 7.94Hz for the fixed-base model (FBM) to 0.86 Hz and 1.07 Hz for the unbonded and bonded cases, respectively. Consequently, the seismic demand on the structure is expected to be considerably reduced.
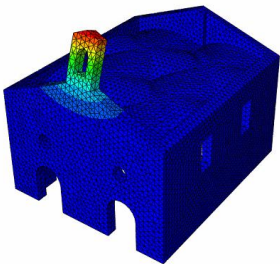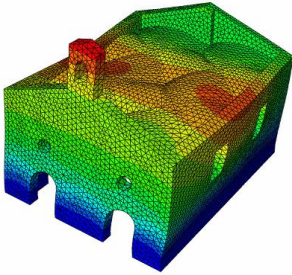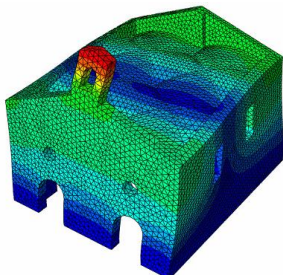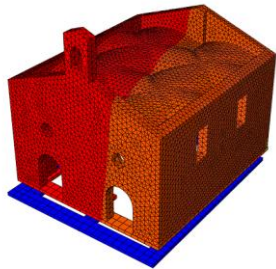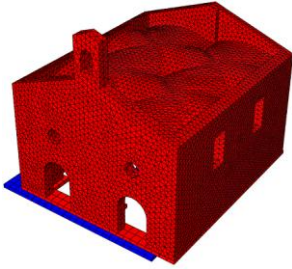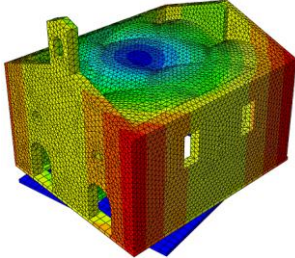

		Mode 1	Mode 2	Mode 3
FB				
UFREI & BFREI				
f (Hz)	BF	7.94	9.73	14.7
	UFREI	0.86	0.87	1.20
	BFREI	1.07	1.10	1.50

Fig. 5.9. Modal deformed shapes and corresponding frequencies of the first three vibration modes for the fixed-base (FB) model and the base isolated (UFREI and BFREI) models.

5.5.2. Non-linear dynamic analyses with PGA=0.25

To evaluate the seismic performance of the church in the three different configurations, full-scale non-linear time-history (NLTH) analyses are performed using the accelerogram registered during the 2009 L'Aquila earthquake, Central Italy. The two horizontal components of the accelerogram with Peak Ground Acceleration (PGA) equal to 0.25g are illustrated in Fig. 5.10: a part (10 s) of the real registration is used in the numerical simulations. The structural behavior of the church and the damage distribution in the different macro-elements are investigated in the case of fixed-base and isolated models.

Fig. 5.11 illustrates the tensile damage contour plots for the three models at different time instants during the non-linear dynamic analyses: red color is associated to full damage and blue color to zero damage. In the fixed-base model (FBM), tensile damage initially develops in the bell gable at the top of the façade and then propagates in the cross vaults, the façade and lateral walls, especially near the openings: at the end of the non-linear dynamic analysis, significant damage is registered in the model, mainly in the masonry cross vaults. It can be noted that in the base isolated models tensile damage is significantly reduced. In the model with UFREIs, small damage appears only near the openings of the façade: it is worth mentioning that in the first part of the analysis no damage is observed. In the model with BFREIs, the façade presents evident damage near the openings and the left cross vault experiences a severe crack. These results show the effectiveness of the isolation system in reducing damage, particularly in the case of UFREIs.
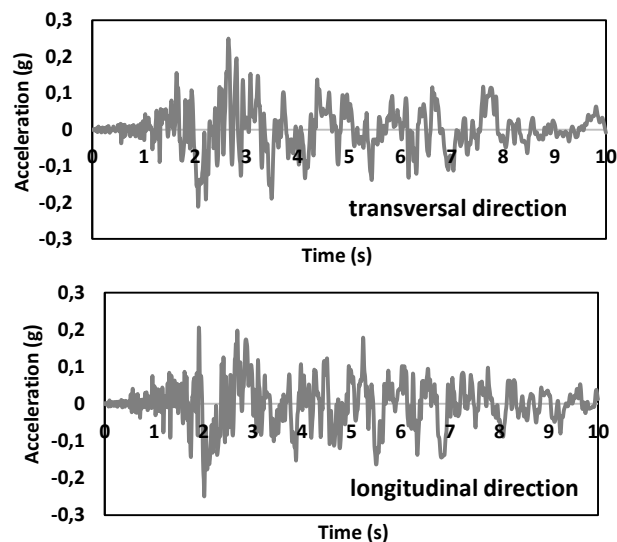

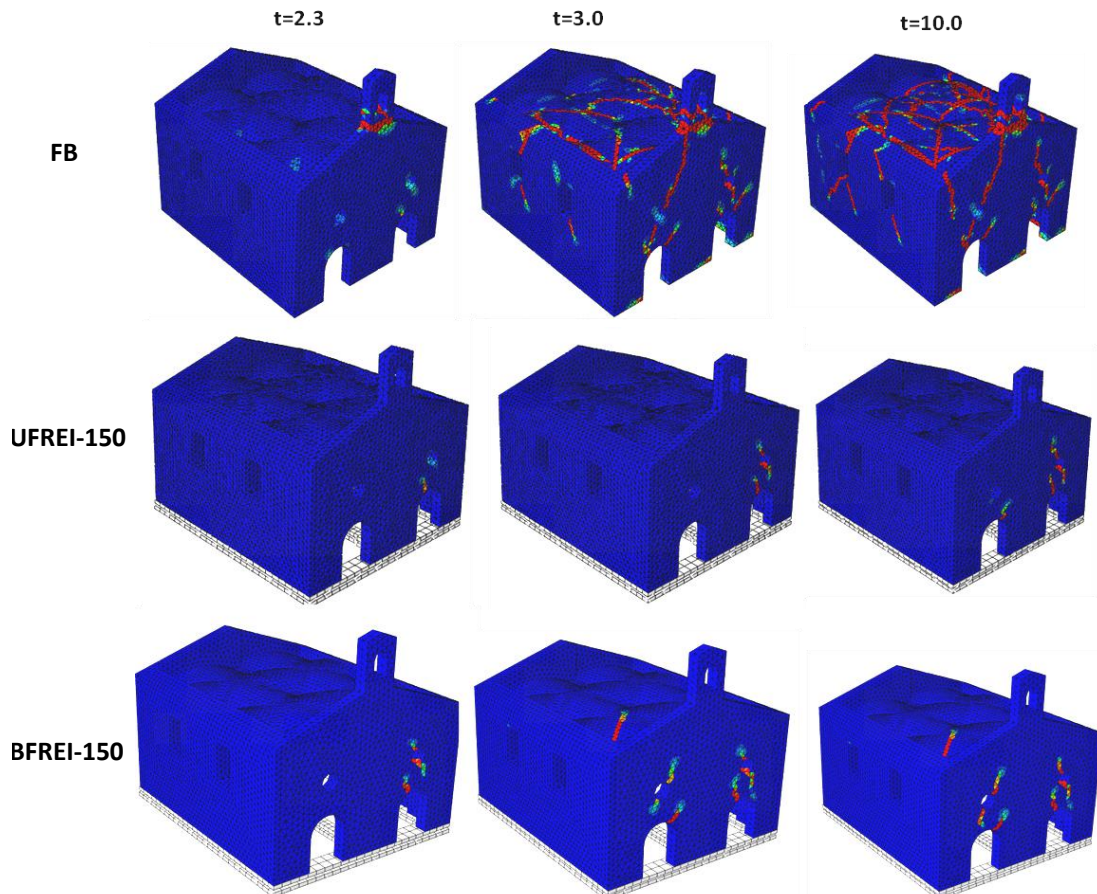Fig. 5.10. Horizontal components of the accelerogram used in the numerical simulations.

Fig. 5.11. Tensile damage contour plots for the fixed-base (FB) model and the base isolated (UFREI and BFREI) models at different time instants during the non-linear dynamic analyses with PGA=0.25g.

Fig. 5.12 compares the displacement time history of some reference points obtained from non-linear dynamic analyses for the three models. It is important to point out that the measured displacement is the relative displacement between the reference point and the base of the superstructure. The fixed-base model (FBM) shows very large displacements (about 9 cm) in the longitudinal direction at the top of the bell gable (P5), indicating that a probable collapse of such element can occur: large displacements (1.4 cm) in the longitudinal direction are registered also at the top of the façade in correspondence with the base of the bell gable (P1). It can be noted that notable residual displacements are computed at the end of the non-linear dynamic analyses, revealing significant permanent damage: such results are consistent with the damage concentration observed in the bell gable. In the transversal direction the largest displacement (about 1 cm) is registered for the right lateral wall. In the base isolated models a remarkable reduction of the peak displacements can be observed, mainly at the top of the bell gable (P5) and at the top of the façade (P1): in particular, residual displacements are negligible for both the base isolated models at the end of the non-linear dynamic analyses. It can be noted that the response of the base isolated models is characterized by a significant frequency reduction.
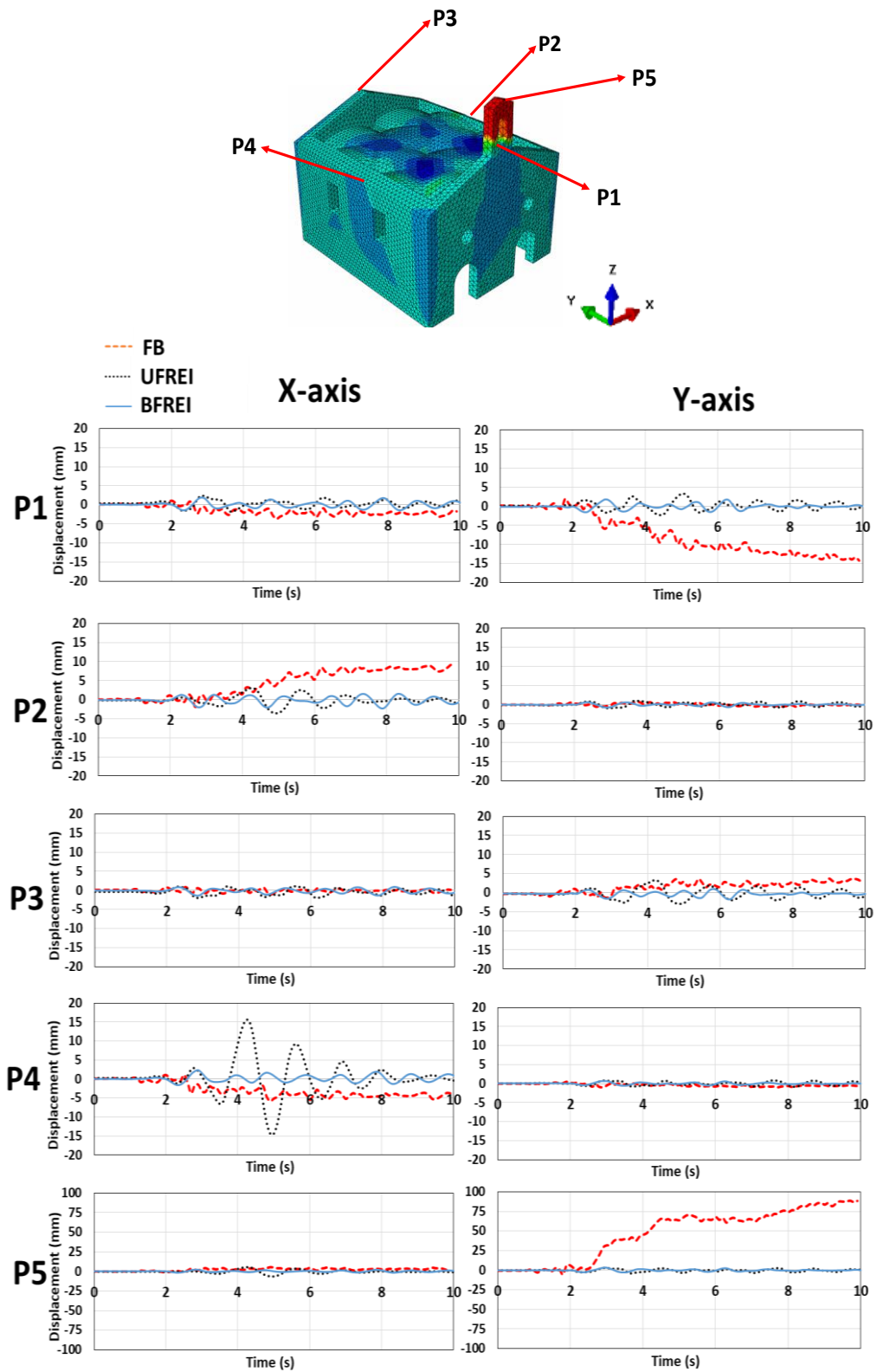
Fig. 5.12. Displacement time history of different reference points in the longitudinal and transversal directions obtained from non-linear dynamic analyses with PGA=0.25g for the fixed-base (FB) model and the base isolated (UFREI and BFREI) models.

Fig. 5.13 compares the vertical displacement time history of some reference points of the cross vaults (the center of the four cross vaults) obtained from non-linear dynamic analyses for the three models. In the fixed-base model (FBM),

residual displacements of about 0.5 cm are registered: conversely, in the base isolated models residual displacements are negligible.
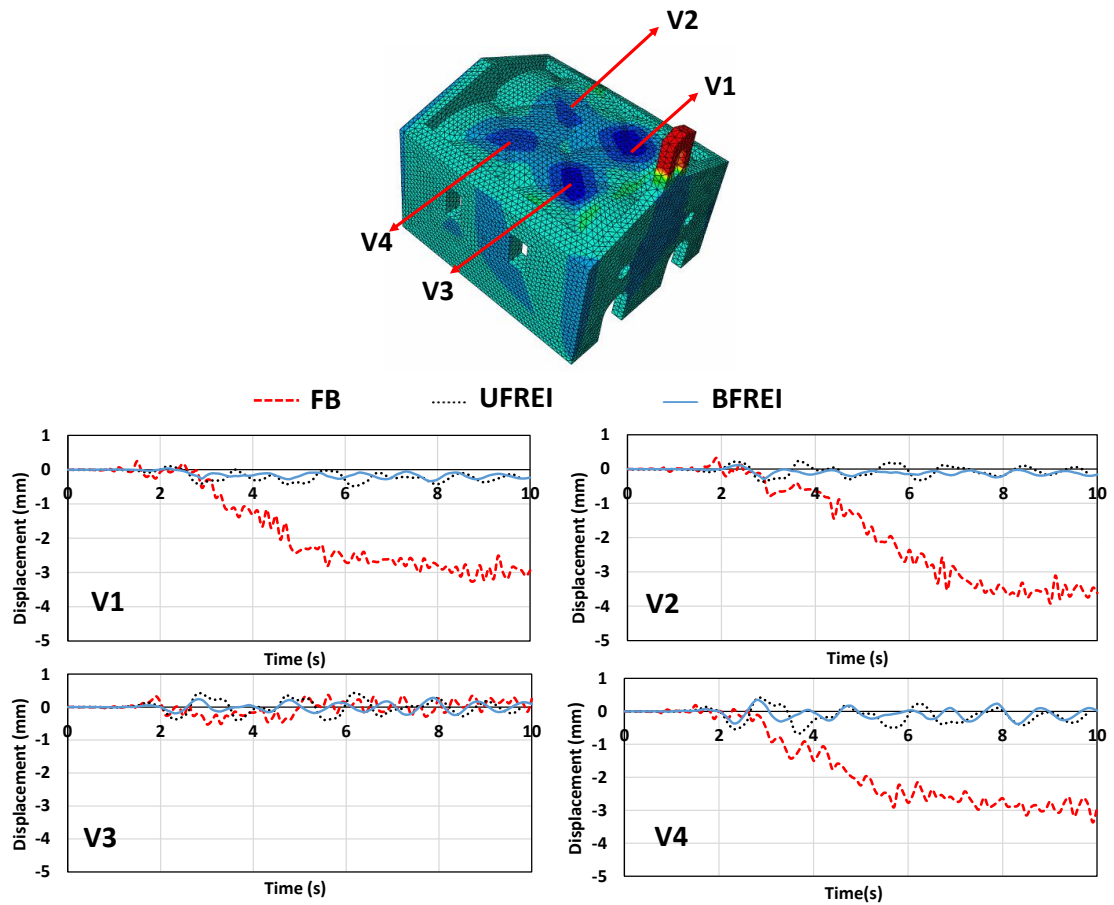

Fig. 5.13. Vertical displacement time history of different reference points of the vaults obtained from non-linear dynamic analyses with PGA=0.25g for the fixed-base (FB) model and the base isolated (UFREI and BFREI) models.

Another interesting parameter is the acceleration, typically responsible for the damage of non-structural components inside the building [32]. Fig. 5.14 shows the acceleration time history of some reference points (base, cross vaults and bell gable) obtained from non-linear dynamic analyses for the three models. Numerical results show that the acceleration values at the cross vaults and at the bell gable are significantly reduced due to the application of the isolation system, both in the unbonded and bonded cases: consequently, the use of base isolation can fairly mitigate the damage of non-structural components inside the building, such as historical furniture, lamps and paintings.

Finally, the horizontal displacements of the base isolators are computed to check the maximum displacement requirements. Fig. 5.15 and Fig. 5.16 show the displacement time history in the X and Y directions for four representative isolators (denoted as B1, B2, B3 and B4) in the unbonded (UFREI) and bonded (BFREI) cases, respectively, during the non-linear dynamic analyses.
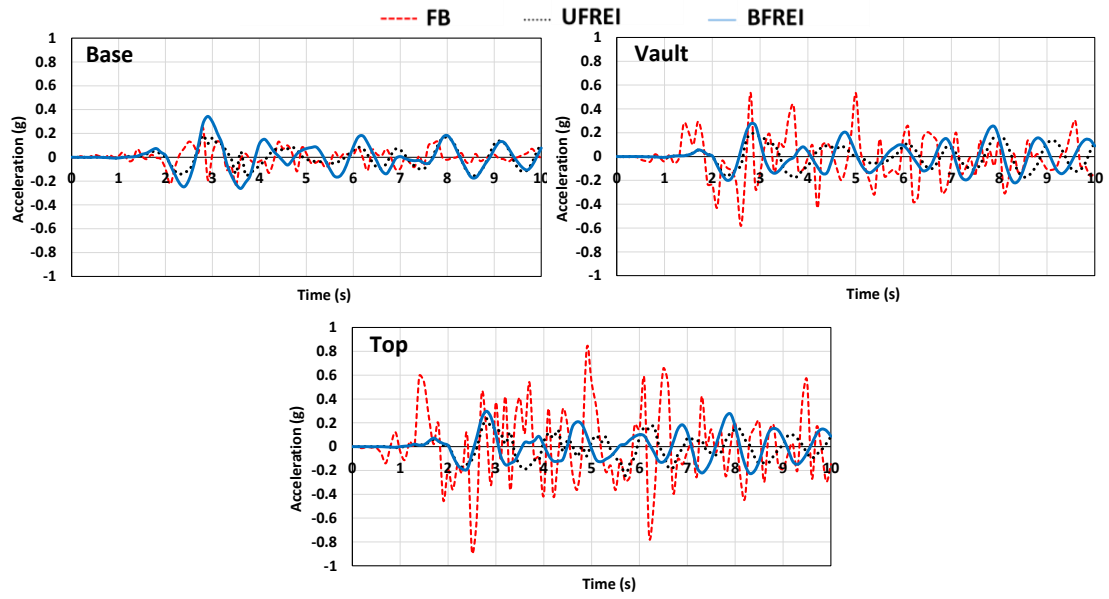
Fig. 5.14. Acceleration time history of different reference points (floor, vault and top level) in the transversal direction obtained from non-linear dynamic analyses with PGA=0.25g for the fixed-base (FB) model and the base isolated (UFREI and BFREI) models.
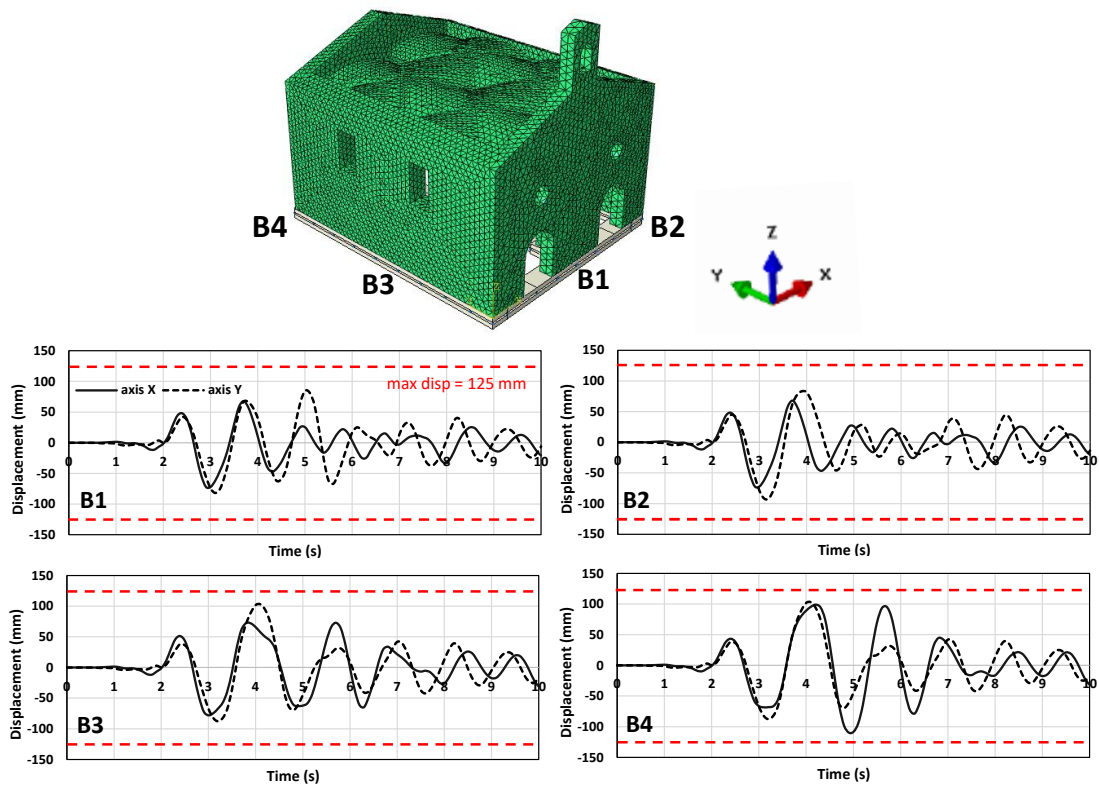

Fig. 5.15. Displacement time history in the X and Y directions obtained from non-linear dynamic analyses with PGA=0.25g for four representative isolators (UFREIs).

Fig. 5.16. Displacement time history in the X and Y directions obtained from non-linear dynamic analyses with PGA=0.25g for four representative isolators (BFREIs).
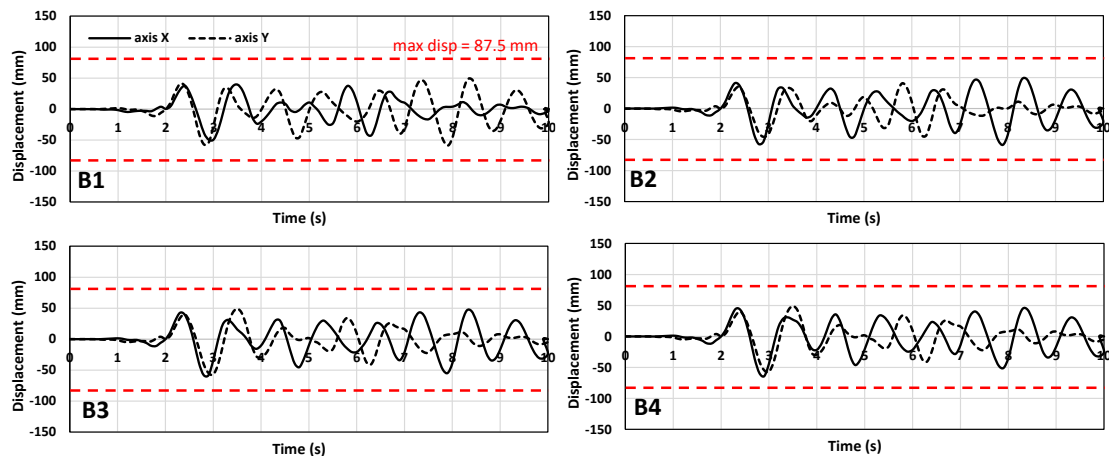
In the unbonded (UFREI) case, according to some experimental works [22], the critical displacement can be assumed equal to about 2.5-3t_r: consequently, in this study it may be assumed equal to 125 mm because the total height of rubber is 50 mm. In the bonded (BFREI) case, as reported in some seismic codes [23][24], the critical displacement is about 1.75t_r (consequently, in this study it is equal to 87.5 mm). The numerical results show that all the isolators satisfy the maximum displacement requirements; moreover, each isolator tends to return to the initial position with negligible residual displacements. It is worth mentioning that the sliding displacement of the UFREI is not taken into account in the UEL model because it can be considered as negligible under a vertical pressure larger than 0.5 MPa, as reported in [41].

These observations highlight a remarkable advantage of UFREIs: using a similar geometry and dimension of the device, the critical displacement of UFREIs is significantly larger than that of BFREIs. In addition, as already mentioned, the construction costs of UFREIs may be significantly reduced due to the absence of steel plates for the supports.

5.5.3. Non-linear dynamic analyses with PGA=0.35

To evaluate the effectiveness of the proposed isolation system under higher seismic intensity levels, the seismic performance of the masonry church in the three different configurations is investigated performing non-linear dynamic analyses with PGA=0.35g.

Fig. 5.17 illustrates the tensile damage contour plots for the three models at three different time instants during the non-linear dynamic analyses with PGA=0.35g. As in the previous dynamic analyses with PGA=0.25g, in the fixed-base model (FBM) damage starts from the bell gable and then propagates in the masonry lateral walls, in the façade and in the cross vaults. As expected, damage is significantly larger than

the previous case: it is widespread in all the parts of the church and is particularly considerable in the cross vaults, indicating a possible collapse. A significant damage reduction can be observed in the model with UFREIs: small damage is registered only in the façade and in the cross vaults. It is interesting to observe that widespread damage can be registered in the façade and in the cross vaults of the model with BFREIs, in any case smaller than that in the fixed-base model (FBM).
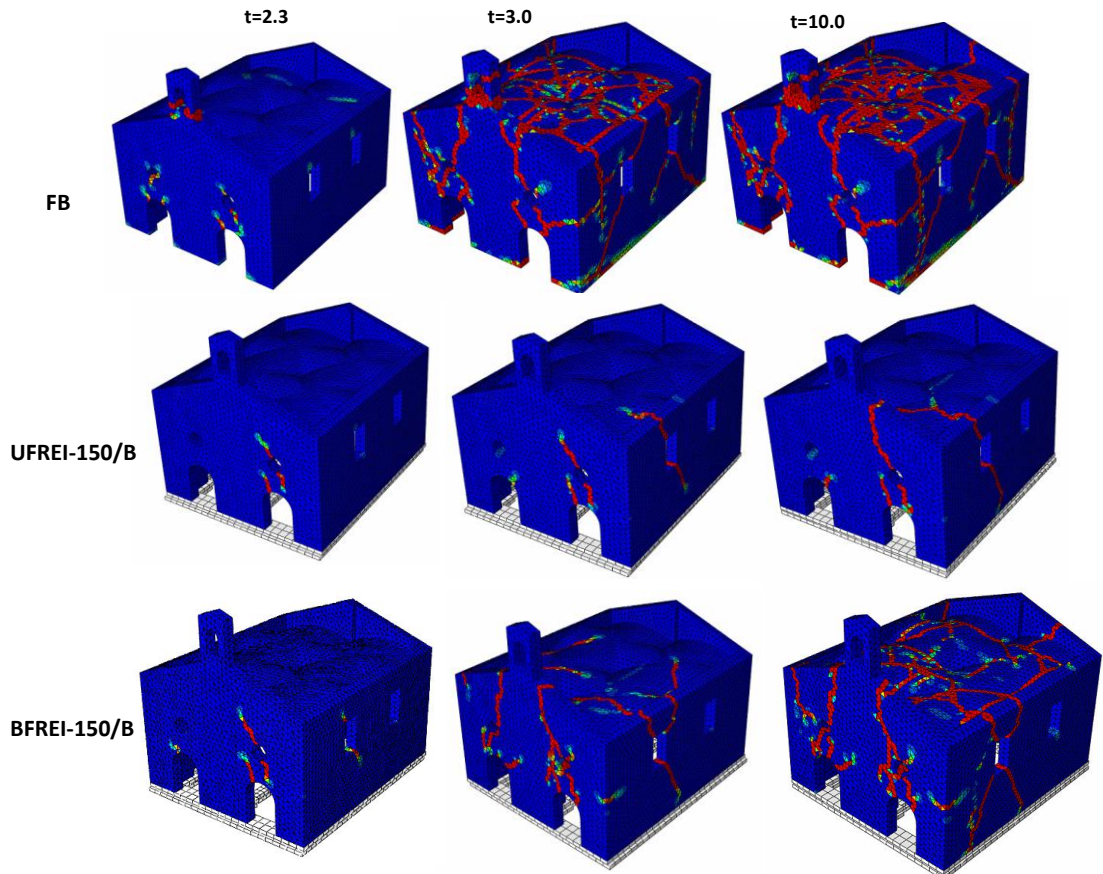

Fig. 5.17. Tensile damage contour plots for the fixed-base (FB) model and the base isolated (UFREI and BFREI) models at different time instants during the non-linear dynamic analyses with PGA=0.35g.

Fig. 5.18 compares the displacement time history of some reference points obtained from non-linear dynamic analyses with PGA=0.35g for the three models. In the fixed-base model (FBM) a large increase of displacements can be registered for the façade in the longitudinal direction and for the lateral walls in the transversal direction, when compared with the results obtained from the previous dynamic analyses with PGA=0.25g. Residual displacements equal to about 4 cm are observed for the façade and the right lateral wall, which correspond to drift ratios equal to 0.5% and 0.65%, respectively. It is worth mentioning that drift ratios equal to 0.5% are assumed to be the collapse limit for masonry elements [42]. In the model with BFREIs, the maximum displacements are reduced to about 2 cm for the façade and the right lateral wall, corresponding to drift ratios equal to 0.24% and 0.33%, respectively. These values are consistent with the moderate damage level observed

from the contour plots in Fig. 5.17. Conversely, in the model with UFREIs, the façade experiences negligible displacements and the lateral walls exhibit displacements smaller than 1 cm (drift ratio equal to 0.15%), which correspond to a slight damage level. These results indicate that the application of UFREIs can mitigate damage significantly, passing from collapse to slight damage level. It has to be noticed that the seismic performance of the church model with UFREIs is significantly better than that of the model with BFREIs, using similar dimensions and properties of the device.
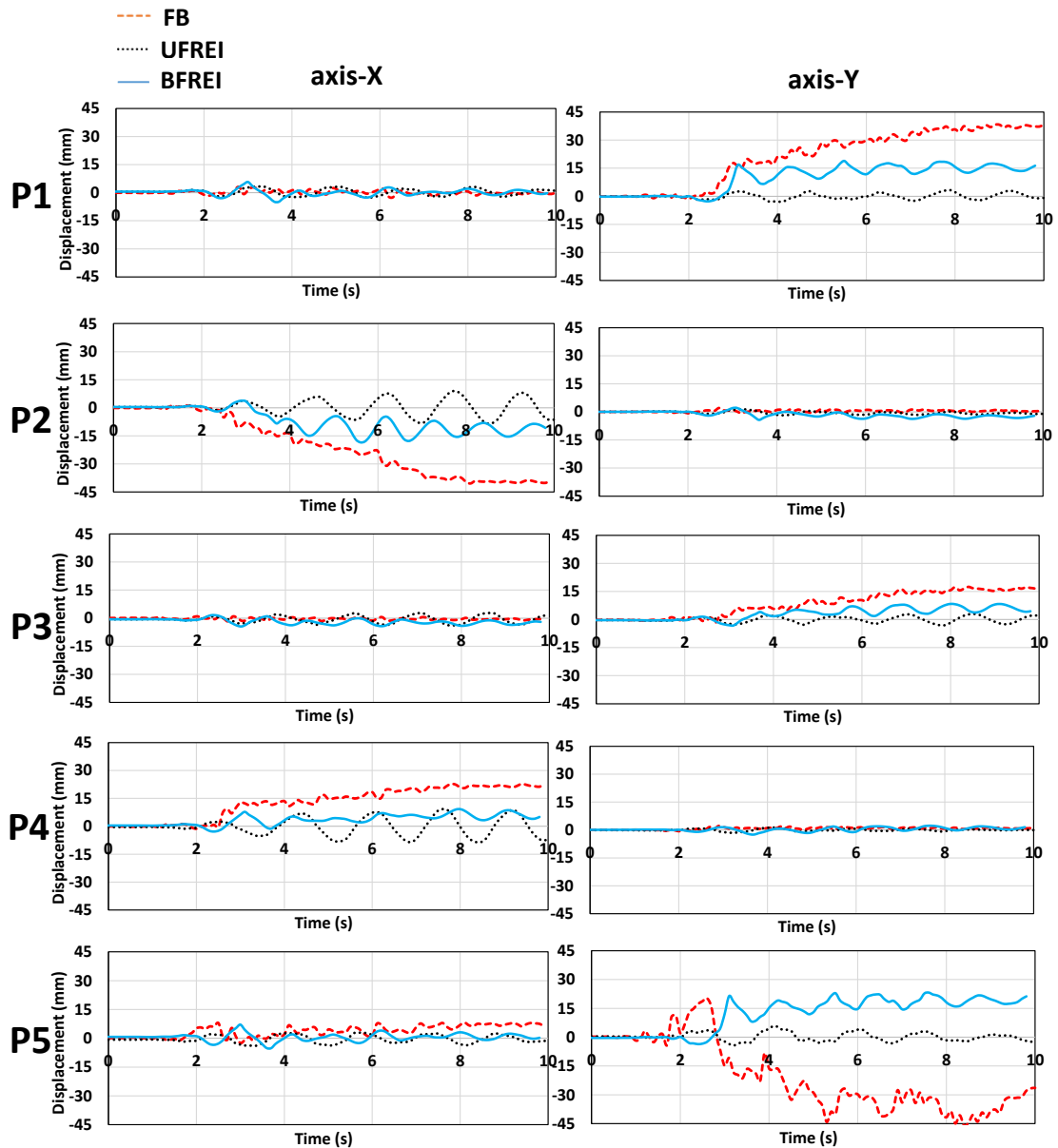

Fig. 5.18. Displacement time history of different reference points in the longitudinal and transversal directions obtained from non-linear dynamic analyses with PGA=0.35g for the fixed-base (FB) model and the base isolated (UFREI and BFREI) models. See Figure 8 for legend.

Fig. 5.19 compares the vertical displacement time history of some reference points of the cross vaults obtained from non-linear dynamic analyses with PGA=0.35g for the three models. In the fixed-base model (FBM) a large increase of

vertical displacements is observed, when compared with the results obtained from the previous dynamic analysis with PGA=0.25g. Peak residual displacements equal to about 3 cm are registered in two cross vaults, indicating an onset of collapse. In the base isolated models, a significant reduction of vertical displacements can be observed: in particular, vertical displacements smaller than 0.8 cm and 0.3 cm are computed for the models with BFREIs and UFREIs, respectively. Consequently, it can be affirmed that the use of UFREIs significantly reduces damage and residual vertical displacements of the cross vaults.
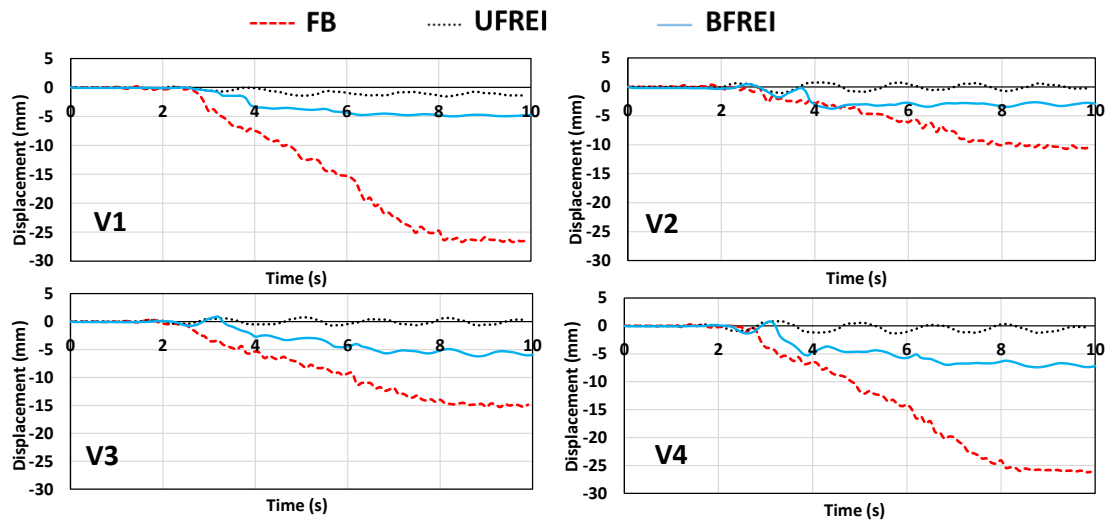

Fig. 5.19. Vertical displacement time history of different reference points of the vaults obtained from non-linear dynamic analyses with PGA=0.35g for the fixed-base (FB) model and the base isolated (UFREI and BFREI) models. See Figure 9 for legend.

Fig. 5.20 shows the acceleration time history of some reference points obtained from non-linear dynamic analyses with PGA=0.35g for the three models. In the fixed-base model (FBM), large acceleration values are recorded in the cross vaults (0.8g) and at the bell gable (1.2g) of the church. On the other hand, the application of base isolation significantly reduces the acceleration values in the cross vault and at the bell gable: in this case, there is no significant difference between the models with BFREIs and UFREIs.

Fig. 5.21 and Fig. 5.22 show the displacement time history of four different isolators (UFREIs and BFREIs, respectively) obtained from non-linear dynamic analyses with PGA=0.35g. Both the critical values are not reached in the unbonded and bonded cases.
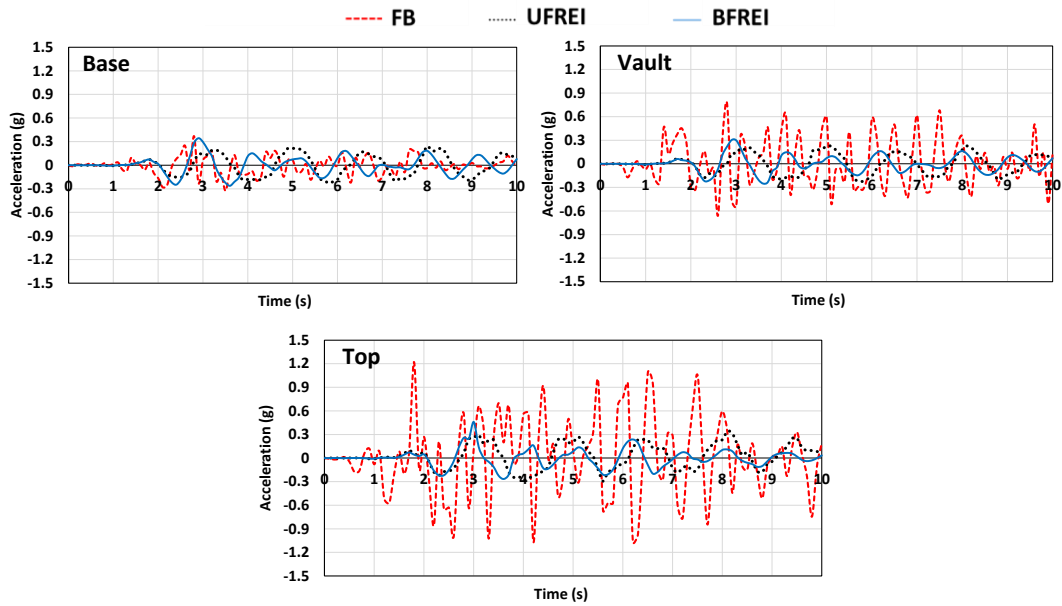
Fig. 5.20. Acceleration time history of different reference points (floor, vault and top level) obtained from non-linear dynamic analyses with PGA=0.35g for the fixed-base (FB) model and the base isolated (UFREI and BFREI) models.
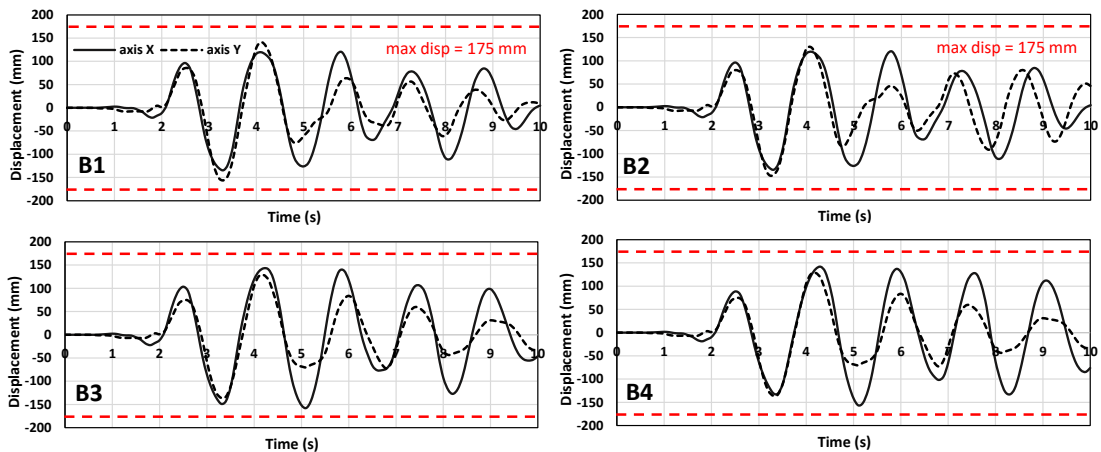

Fig. 5.21. Displacement time history in the X and Y directions obtained from non-linear dynamic analyses with PGA=0.35g for four representative isolators (UFREIs). See Figure 10 for legend.

5.6. Conclusions

This paper has investigated the possibility of improving the seismic performance of a small historical masonry church through base isolation system using FREIs with small height and low shape factor. The FREIs are arranged in such a way that the isolation system can work effectively under permissible vertical loads due to the church weight. The use of FREIs significantly reduces the cost of the isolation system due to the absence of thick steel plates for the supports. In particular, this paper has investigated the UFREIs behavior that is characterized by a marked non-

linear range and hardening phase: the former allows for a decrease of the effective horizontal stiffness, thus reducing the seismic demand, while the latter plays an important role in limiting the shear displacement of the isolation system under strong earthquakes. A series of cyclic shear analyses on detailed 3D FE models are performed to evaluate the behavior of FREIs in unbonded and bonded application. The non-linearity and damping properties are described by the Yeoh hyperelastic model and the Prony-series model, respectively. Both unbonded and bonded FREIs are then implemented into the FE model of a small historical masonry church. To avoid a high computational effort in structural analysis, a single unit of FREI is modeled as a beam element with 12 DOFs in the form of a new Abaqus user element (UEL) developed by the authors. The UEL code is based on the evolution of the isolator geometry under shear deformation and vertical pressure. Finally, the seismic performance of the masonry church in the three different configurations is evaluated performing non-linear dynamic analyses with different seismic intensity levels.
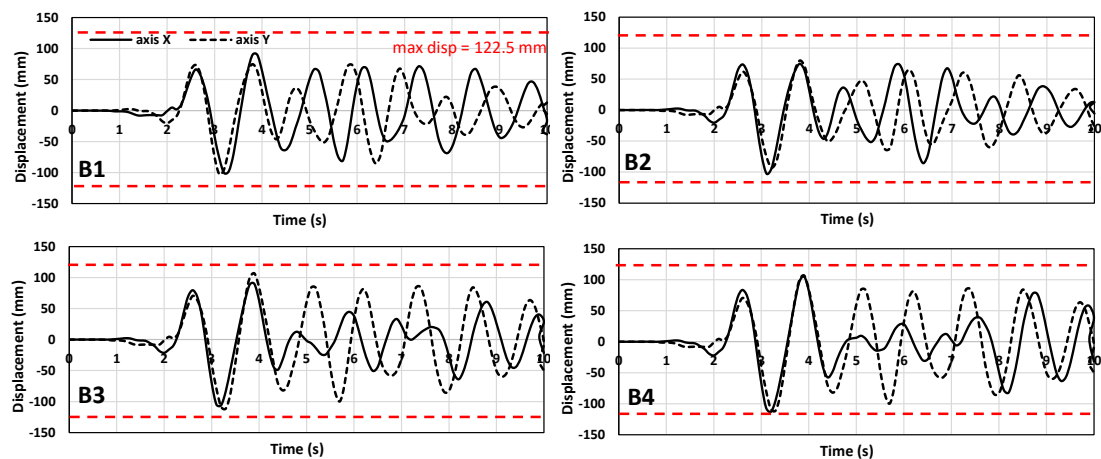

Fig. 5.22. Displacement time history in the X and Y directions obtained from non-linear dynamic analyses with PGA=0.35g for four representative isolators (BFREIs). See Figure 10 for legend.

On the basis of the results presented in this study, the following conclusions can be drawn.

- A new Abaqus User Element (UEL) is proposed and implemented to represent the 3D behavior of a single isolator in large scale structural analyses. The results obtained through the detailed FE model and the developed UEL of the FREI are found to be in a good agreement. In particular, the results of the cyclic analyses show that the use of FREIs in unbonded application significantly decreases the horizontal stiffness of the isolator due to rollover deformations. The use of the proposed UEL for FREIs is observed to be very effective for global seismic analysis of complex isolated structures, such as masonry churches, thus significantly reducing computational effort when compared with the case of detailed FE modelling of the isolators.

-The historical masonry church under study exhibits extensive damage in the façade, in the lateral walls and in the cross vaults under seismic excitation with PGA=0.25g. Large displacements can be observed in the longitudinal direction at the top of the bell gable and in the transversal direction for the lateral walls. The non-linear dynamic analysis with PGA=0.35g shows that the church exhibits very large displacements, mainly at the top level of the church, indicating a collapse of the bell gable.

-Base isolation system can be effectively used to protect the small historical masonry church against severe seismic actions, reducing damage considerably. In the non-linear dynamic analyses with PGA=0.25g, the church does not present any significant damage for both unbonded and bonded FREIs. However, in the non-linear dynamic analyses with PGA=0.35g, some evident damage can be observed in the case of bonded FREIs, while only a very limited damage is registered in the case of unbonded FREIs. The analysis of the displacements of some reference points of the church shows that both the isolation systems significantly reduce the residual drifts of the different macro-elements.

- Both the types of isolators satisfy the maximum lateral displacement requirements reported in the literature, indicating a safe applicability of the devices. However, the limits of lateral displacement for unbonded FREIs should be determined precisely through experimental works, which are still on going within this research.

-The acceleration response of the church is significantly reduced through the application of the isolation system. Both bonded and unbonded FREIs lead to similar reduction of the acceleration values, indicating that damage of non-structural components and artistic assets inside the church can be prevented.

It can be concluded that the numerical results obtained in this study show a good performance of UFREIs to protect a small historical masonry church when subjected to moderate-to-high seismic actions.

REFERENCES

[1] Lagomarsino S. Damage assessment of churches after L'Aquila earthquake (2009). Bulletin of Earthquake Engineering 2012;10(1):73-92.
[2] Brandonisio G., Lucibello G., Mele E., De Luca A. Damage and performance evaluation of masonry churches in the 2009 L'Aquila earthquake. Engineering Failure Analysis 2013;34:693-714.
[3] Valente M., Barbieri G., Biolzi L. Seismic assessment of two masonry Baroque churches damaged by the 2012 Emilia earthquake. Engineering Failure Analysis 2017;79:773-802.
[4] Valente M., Milani G. Damage assessment and partial failure mechanisms activation of historical masonry churches under seismic actions: Three case studies in Mantua. Engineering Failure Analysis 2018;92:495-519.
[5] Choudhury T., Milani G., Kaushik H.B. Comprehensive numerical approaches for the design and safety assessment of masonry buildings retrofitted with steel

bands in developing countries: The case of India. Construction and Building Materials 2015;85:227-246.

[6] Murtyl C.V.R., Dutta J., Agrawal S.K. Twin lintel belt in steel for seismic strengthening of brick masonry buildings. Earthquake Engineering and Engineering Vibration 2004;3:215-222.

[7] Milani G., Shehu R., Valente M. A kinematic limit analysis approach for seismic retrofitting of masonry towers through steel tie-rods. Engineering Structures 2018;160:212-228.

[8] Milani G., Shehu R., Valente M. Possibilities and limitations of innovative retrofitting for masonry churches: Advanced computations on three case studies. Construction and Building Materials 2017;147:239-263.

[9] Feng Y., Yi D., Bi Q. Seismic design analysis of the country masonry school buildings in the meizoseismal area. Earthquake Engineering and Engineering Vibration 2011;10:359-367.

[10] Barbieri G., Valente M., Biolzi L., Togliani C., Fregonese L., Stanga G. An insight in the late Baroque architecture: an integrated approach for a unique Bibiena church. Journal of Cultural Heritage 2017;23:58-67.

[11] Valente M., Milani G. Damage survey, simplified assessment, and advanced seismic analyses of two masonry churches after the 2012 Emilia earthquake. International Journal of Architectural Heritage 2018. https://doi.org/10.1080/15583058.2018.1492646

[12] Calabrese A., Spizzuoco M.C., Serino G., Della Corte G., Maddaloni G. Shaking table investigation of a novel, low-cost, base isolation technology using recycled rubber. Structural Control and Health Monitoring 2015;22:107-122.

[13] Toopchi-Nezhad H., Tait M.J., Drysdale R.G. Bonded versus unbonded strip fiber reinforced elastomeric isolators: finite element analysis. Composite Structures 2011;93:850-859.

[14] Das A., Deb S.K., Dutta A. Comparison of numerical and experimental seismic responses of FREI-supported un-reinforced brick masonry model building. Journal of Earthquake Engineering 2016;20: 1239-1262.

[15] Das A., Deb S.K., Dutta A. Shake table testing of un-reinforced brick masonry building test model isolated by U-FREI. Earthquake Engineering & Structural Dynamics 2016;45:253-272.

[16] Thuyet V.N., Deb S.K., Dutta A. Evaluation of horizontal stiffness of fibre-reinforced elastomeric isolators. Earthquake Engineering & Structural Dynamics 2017;46:1747-1767.

[17] Chiozzi A., Simoni M., Tralli A. Base isolation of heavy non-structural monolithic objects at the top of a masonry monumental construction. Materials and Structures 2016;49:2113-2130.

[18] Seki M., Miyazaki M., Tsuneki Y., Kataoka, K. A masonry school building retrofitted by base isolation technology. 12th World Conference on Earthquake Engineering 2000.

[19] Habieb A.B., Milani G., Tavio T. Two-step advanced numerical approach for the design of low-cost unbonded fiber reinforced elastomeric seismic isolation systems in new masonry buildings. Engineering Failure Analysis 2018;90:380-396.

[20] Mishra H.K., Igarashi A., Matsushima H. Finite element analysis and experimental verification of the scrap tire rubber pad isolator. Bulletin of Earthquake Engineering 2013;11:687-707.

[21]   Thuyet V.N., Deb S.K., Dutta A. Mitigation of seismic vulnerability of a prototype low-rise masonry building using U-FREIs. Journal of Performance of Constructed Facilities 2018;32(2):1-13.

[22]   De Raaf M.G.P., Tait M.J., Toopchi-Nezhad H. Stability of fiber-reinforced elastomeric bearings in an unbonded application. Journal of Composite materials 2011;45:1873-1884.

[23]   Eurocode 8: Design of structures for earthquake resistance-part 1: general rules, seismic actions and rules for buildings. 2005.

[24]   S.N. Indonesia, Persyaratan Beton Struktural Untuk Bangunan Gedung, SNI 2847 2013.

[25]   Toopchi-Nezhad H., Tait M.J., Drysdale R.G. Testing and modeling of square carbon fiber-reinforced elastomeric seismic isolators. Structural Control and Health Monitoring 2008;15:876-900.

[26]   Simulia. ABAQUS 6.14 User's manual. Dassault Systems, Providence, RI, 2014.

[27]   Shahzad M., Kamran A., Siddiqui M.Z., Farhan M. Mechanical characterization and FE modelling of a hyperelastic material. Materials Research 2015;18:918-924.

[28]   Jerrams S.J., Kaya M., Soon K.F. The effects of strain rate and hardness on the material constants of nitrile rubbers. Materials & design 1998;19:157-167.

[29]   Osgooei P.M. Advanced numerical modeling of Fiber-Reinforced Elastomeric Isolators (FREIs). PhD Thesis, McMaster University, 2014.

[30]   Gunaratne M., Bandara N., Medzorian N., Chawla M., Ulrich P. Correlation of tire wear and friction to texture concrete pavements. Journal of Materials in Civil Engineering 2000; 12: 46-54.

[31]   Kelly J.M. Earthquake-resistant design with rubber, Springer-Verlag, 1993.

[32]   Van Engelen N.C., Konstantinidis D., Tait M.J. Structural and nonstructural performance of a seismically isolated building using stable unbonded fiber-reinforced elastomeric isolators. Earthquake Engineering & Structural Dynamics 2016;45:421-439.

[33]   Kumar M., Whittaker A.S., Constantinou M.C. An advanced numerical model of elastomeric seismic isolation bearings. Earthquake Engineering & Structural Dynamics 2014;43:1955-1974.

[34]   Al-Anany Y.M., Tait M.J. A numerical study on the compressive and rotational behavior of fiber reinforced elastomeric isolators (FREI). Composite Structures 2015;133:1249-1266.

[35]   Tiberti S., Acito M., Milani G. Comprehensive FE numerical insight into Finale Emilia Castle behavior under 2012 Emilia Romagna seismic sequence: damage causes and seismic vulnerability mitigation hypothesis. Engineering Structures 2016;117:397-421.

[36]   Milani G., Valente M., Alessandri C. The narthex of the Church of the Nativity in Bethlehem: a non-linear finite element approach to predict the structural damage. Computers & Structures 2018; 207:3-18.

[37]   Valente M., Milani G. Effects of geometrical features on the seismic response of historical masonry towers. Journal of Earthquake Engineering 2018; S1:2-34.

[38]   Sarhosis V, Bagi K, Lemos JV, Milani G, ed. Computational modeling of masonry structures using the discrete element method. USA: IGI Global, 2016

[39]   Habieb A.B., Milani G., Tavio T. Seismic performance of a masonry building isolated with low-cost rubber isolators. WIT Transactions on The Built Environment 2017;172:71-82.

[40]   Pauletta, M., Di Luca, D., Russo, E., Fumo, C. Seismic rehabilitation of cultural heritage masonry buildings with unbonded fiber reinforced elastomeric isolators (U-FREIs)–A case of study. Journal of Cultural Heritage, 2018;32:84-97.

[41]   Russo G., Pauletta M. Sliding instability of fiber-reinforced elastomeric isolators in unbonded applications. Engineering Structures 2013;48:70-80.

[42]   Calvi G.M. A displacement-based approach for vulnerability evaluation of classes of buildings. Journal of Earthquake Engineering 1999;3:411-438.

Chapter

6
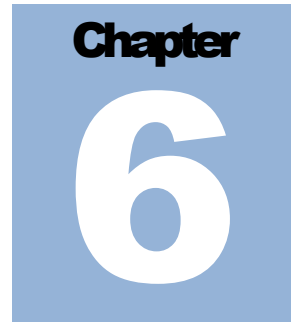
Effectiveness of different base isolation systems for seismic protection: Numerical insights into an existing masonry bell tower

Recent earthquakes in Italy have highlighted the particular vulnerability of historical masonry buildings and the need of effective retrofitting interventions. This paper investigates the possibility of improving the seismic performance of a historical masonry bell tower using different types of commercial isolators: High Damping Rubber Bearing (HDRB), Lead Rubber Bearing (LRB) and Friction Pendulum System (FPS) Isolator. Detailed three-dimensional (3D) finite element (FE) models are created to characterize the behavior of the three types of isolators. Then, an Abaqus User Element (UEL) is used to represent the 3D behavior of the isolators for global seismic analyses of isolated structures. The results of cyclic shear analyses show that the proposed UEL model can accurately predict the behavior obtained through detailed 3D FE models. Non-linear dynamic analyses are performed to investigate the seismic response of the historical masonry bell tower in the original and base-isolated configurations subjected to moderate-to-high seismic actions: moreover, the effects of near fault earthquakes are analyzed. The results obtained from the numerical simulations show that the HDRBs do not ensure an adequate seismic protection of the masonry bell tower in terms of damage patterns and top displacements. On the other hand, the LRBs and FPS isolators are very effective in reducing the earthquake effects on the masonry tower: residual displacements are negligible and the isolator displacements are limited. In case of near fault earthquakes, an isolation system with higher damping and larger dimension is required to reduce the drifts of the tower and to accommodate the large displacements of the isolators.

6.1. Introduction

Preservation of the historical and architectural heritage against seismic actions represents an actual and challenging issue: in particular, a large number of valuable historical constructions are located in earthquake-prone countries, such as Italy and South European territories. Recent Italian earthquakes have shown that historical

masonry constructions are very vulnerable to horizontal actions [1]-[10]. The collapses and extensive damages observed in historical masonry constructions highlight the importance of effective retrofitting interventions to protect cultural heritage.

Traditional retrofitting techniques are aimed at increasing the seismic capacity of the structure. Such methods generally increase the stiffness and strength of the structure, generating high seismic actions.

Differently from conventional retrofitting interventions, seismic base isolation decouples the structure from the ground motion by interposing isolator devices with low horizontal stiffness between the structure. Such a technique provides the structure a fundamental frequency that is much lower than that of the original configuration and different from the dominant frequency of seismic excitations, thus significantly reducing displacements and accelerations.

The utilization of base isolation for seismic protection of historical buildings and cultural heritage has become more popular among researchers in the last decades. Sorace and Terenzi [11] examined a special base-isolation technology as a viable retrofitting strategy for a historical church, as well as for a wide class of similar buildings that are highly vulnerable to seismic actions. Borri and Vetturini [12] and Vetturini et al. [13] described the different phases and the peculiar issues of a seismic base isolation intervention on a historical masonry building that was severely damaged during the 2009 L'Aquila earthquake. Chiozzi et al. [14] proposed base isolation as a very promising technique for the seismic protection of heavy non-structural monolithic objects, which are usually placed at the top of masonry monumental constructions. Sorace and Terenzi [15] analyzed a base-isolated floor strategy consisting of a system of double-friction pendulum isolators to protect historical and artistic statues exhibited in art museums, preventing overturning failures during earthquakes. Castellano et al. [16] proposed a low-cost typology of elastomeric isolators for the seismic protection of a typical historical masonry construction in Southern Italy. Habieb et al. [17] investigated the possibility of improving the seismic performance of a small historical masonry church using fiber reinforced elastomeric isolators in bonded and unbonded applications. The results showed that the application of base isolation can significantly mitigate the effects of earthquake on historical masonry buildings and cultural heritage.

This study investigates the possibility of improving the seismic performance of a historical masonry bell tower using different types of commercial isolators: High Damping Rubber Bearing (HDRB), Lead Rubber Bearing (LRB) and Friction Pendulum System (FPS) Isolator. The main characteristics of the isolators are selected on the basis of the products available on the market.

According to the literature, the application of base isolation is effective for low-to-medium rise structures having a low fundamental period [18][19]. Conversely, masonry towers are slender structures that are generally characterized by a large fundamental period. Strengthening methods are commonly adopted to protect masonry towers from damage due to earthquakes. Milani et al. [20] investigated the seismic strengthening through horizontal and vertical steel tie-rods to protect

masonry towers from several types of damage mechanisms. Valluzzi et al. [21] proposed a strengthening technique based on the insertion of steel bars in the bed joints. Cosenza and Iervolino [22] investigated a FRP tie system applied to the inner walls and anchored at the base by a reinforced concrete slab, independent of the tower foundation. Preciado et al. [23] proposed an approach for the seismic vulnerability reduction of masonry towers with external prestressing.

It is worth mentioning that the tower analyzed in this study does not exhibit a relevant height and presents a low fundamental period when compared with common masonry towers located in Italy. In such a case, the use of base isolation can be considered effective in significantly reducing the potential damage due to earthquakes.

The applicability of base isolation for structural retrofitting is related to the possibility of removing the ground floor for the installation of the isolators, which should be interposed between the superstructure and the substructure. The masonry wall should be cut and supported before the installation of the base isolators. A ring beam is required below the wall to distribute the weight of the structure on the isolation system. A practical explanation of a detailed procedure for the installation of base isolators into old masonry buildings can be found in [24].

This study starts from a 3D finite element (FE) modeling of each isolator in the software code Abaqus [25] to examine the cyclic shear behavior under constant vertical load. A simplified UEL model is then introduced in the FE model of the isolated masonry bell tower to represent the 3D behavior of each isolator. Such UEL model significantly reduces the computational effort when compared with the use of a detailed 3D FE model for a single isolator. Then, non-linear dynamic analyses are performed to investigate the seismic response of the historical masonry bell tower in the original and base-isolated configurations, evaluating the damage distribution, top displacements and accelerations of the bell tower as well as the displacements of the isolators.

The main objectives of the study are: (1) to evaluate the effectiveness of base isolation for seismic protection of a historical masonry bell tower; (2) to compare the performance of different types of isolators; (3) to investigate the effects of near fault earthquakes on the seismic response of the isolated tower.

6.2. Seismic protection of the bell tower under study

The case study is a masonry bell tower located in Southern Lombardia, Northern Italy. The geometry of the bell tower is schematically presented in Fig.7.1. The bell tower, which is characterized by a square plan with sides equal to about 4.6 m, reaches a maximum height of about 29 m. The walls thickness is equal to about 0.3-0.4 m and remains constant along the lower part of the tower: a significant increase of the thickness can be observed on the four corners of the square section. A small dome, which exhibits a diameter of about 3.4 m, is present on the top of the tower: it is supported by an octagonal tambour that is almost 3 m high. In the lower part of the tower, up to 20 m, only two small rectangular windows and the entrance door at the

base are present. In the upper part of the tower, each side presents a large arched opening that is about 2.4 m high: in addition, each side of the tambour exhibits a rectangular opening that is about 2 m high.
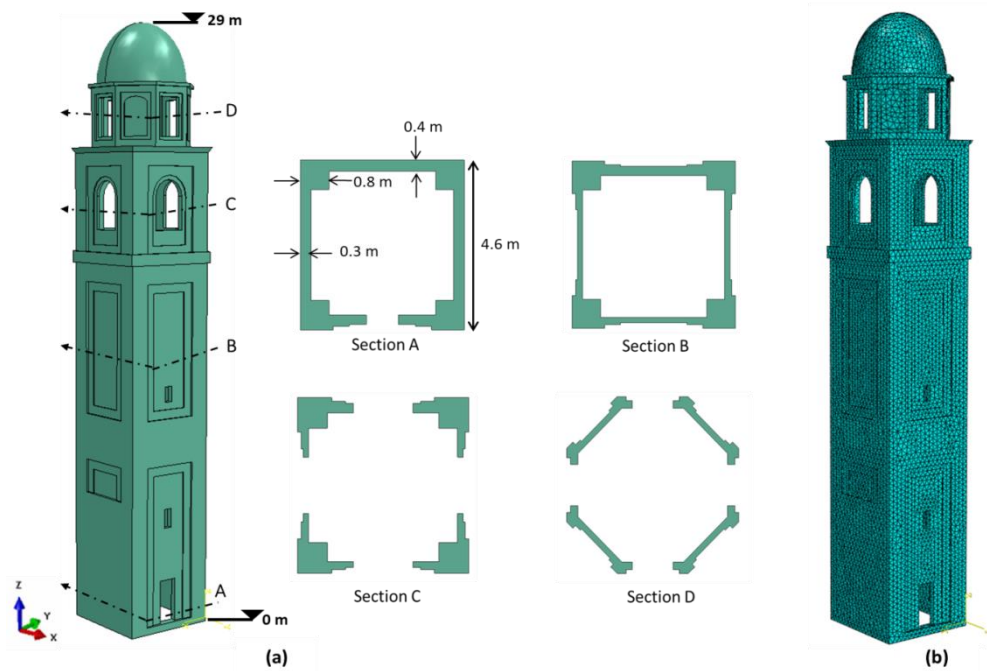

Fig.7.1 San Giovanni bell tower. (a) Geometrical model and different sections; (b) FE model.

The finite element (FE) model of the masonry bell tower, which consists of about 95000 four-node tetrahedral elements, is shown in Fig.7.1. The non-linear behavior of masonry is modeled through the Concrete Damage Plasticity (CDP) model proposed by [26] and then extended by [27], which is available within the ABAQUS software code. Although originally conceived to describe the non-linear behavior of concrete, the model can be used for masonry through a proper adaptation of the main parameters [28]-[30].

It is worth noting that masonry is typically orthotropic in both the elastic and inelastic field, the orthotropy ratio being ruled by the typology and geometry of the texture. Such a feature has been shown both experimentally (see for instance the pioneering research described in [31]) and numerically ([32]-[35]) in a recent and less recent past.

Table 6. 1. Values of the parameters adopted for the CDP model.

Dilatation angle	Eccentricity	σ_{b0}/σ_{c0}	K_c	Viscosity
10	0.1	1.16	0.667	0.0001

On the other hand, some considerations encourage the utilization of isotropic non-linear models. It should first be stated that when the texture is irregular (as it occurs in the majority of the cases for historical buildings) orthotropy progressively becomes smaller when the irregularity of the texture becomes larger, as recently shown in [36]. Moreover, there are still no available and robust routines to deal

specifically with masonry in a commercial –albeit advanced- FE software and the use of isotropic non-linear approaches (in the form of total strain, smeared crack and concrete damage plasticity models) is nowadays widespread to analyze the seismic response of large complex masonry structures. As a matter of fact, a further advantage of the utilization of a CDP model stands in the possibility to account properly for damage occurring in tension and compression, a feature that makes CDP particularly suited when dealing with cyclic problems and non-linear dynamic analyses.

Table 6. 1 summarizes the values of the parameters adopted for the CDP model in the non-linear dynamic simulations, in accordance with previous works [28]-[30]: (i) the dilation angle ψ, which is the angle due to a variation in volume of the material following the application of a shear force, is set equal to 10°, in agreement with experimental evidences available in the literature [37]; (ii) the strength ratio $\sigma b0/\sigma c0$, which is the ratio of initial equibiaxial compressive yield stress to initial uniaxial compressive yield stress, is assumed equal to 1.16, in agreement with some experimental data [38]; (iii) the KC parameter, which governs the shape of the yield surface in the deviatoric plane, is set equal to 0.666 in order to define an approximate Mohr-Coulomb strength domain; (iv) the correction parameter of the eccentricity μ is assumed equal to the default value 0.1, which implies that the material has almost the same dilation angle over a wide range of confining pressure stress values, [25]; (v) the viscosity parameter λ, which allows overcoming convergence difficulties, is assumed equal to 0.0001.

The main mechanical parameters of the masonry material are selected referring to the specifications of the Italian Code [39]-[41], considering a masonry typology constituted by clay bricks and lime mortar: (i) the density and the elastic modulus are equal to 1800 kg/m3 and 1500 MPa, respectively; (ii) the compressive strength is equal to σcu=2.4 MPa. The tensile strength is set equal to σto=0.19 MPa, obtaining a ratio between the tensile and compressive strength equal to about 0.07.

The simplified compressive and tensile uniaxial stress-strain relationships adopted for masonry are shown in Fig. 6.2. The uniaxial compression response is assumed linear until the value of the initial yield σco=1.9 MPa is reached. Then, the response is characterized by a linear strain hardening up to the ultimate stress σcu=2.4 MPa: the corresponding strain is assumed equal to five times the yield value. The bi-linear ascending part is followed by a softening behavior represented by a bi-linear descending branch up to a strain value equal to 0.032. Under uniaxial tension the stress-strain response follows a linear elastic relationship until the peak stress σto=0.19 Mpa is reached: it corresponds to a strain equal to 0.00013. The tensile post-peak behavior is approximated by a simplified tri-linear curve up to a strain equal to 0.0013 and corresponding stress equal to 0.012 MPa. It is worth noting that the trends and values adopted for the descending branches were chosen to provide smooth strength degradation necessary for convergence of the finite element analysis.
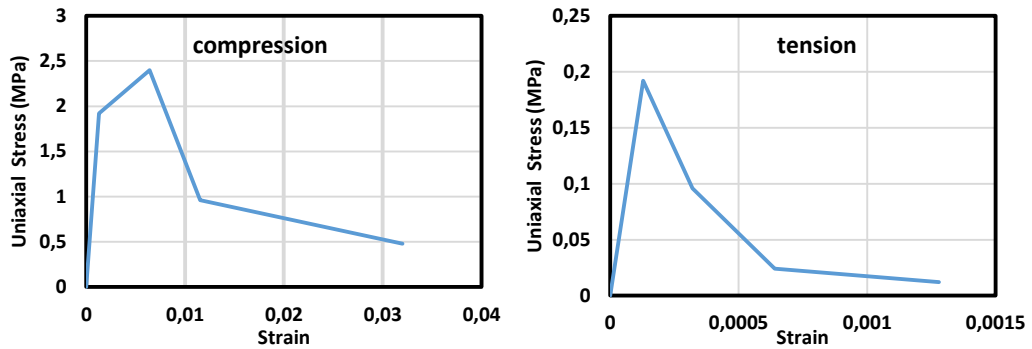
Fig. 6.2 Simplified uniaxial behavior of masonry in compression and tension

As already mentioned, unlike traditional retrofitting methods that are based on structural strengthening, base isolation significantly increases the fundamental period of the structure, then reducing the seismic demand. It is worth mentioning that base isolation is not suitable for slender structures that are characterized by high values of the fundamental period corresponding to the descending branch of the response spectrum. On the other hand, it has to be emphasized that the tower under study represents a specific case because it is characterized by a low value of the fundamental period when compared with common slender masonry towers. Therefore, the use of base isolation can be considered effective in significantly reducing the potential damage due to earthquakes.

A primary issue concerning base isolation is represented by the construction difficulties related to the insertion of the isolator devices at the base of the tower. The intervention requires the separation and support of the masonry wall of the tower during the isolators installation. A detailed description and explanation of such an intervention can be found in the literature for the base isolation of an old masonry building [24]. In the isolated model, two levels of reinforced concrete ring beams are required to separate the superstructure and the substructure in order to arrange the isolators, see Fig. 6.3a. The main details of the reinforced concrete ring beams and a sketch of the foundation system for the isolated tower are shown in Fig. 6.4. It can be noted that large footings should be arranged in correspondence with the corners to accommodate the concentrated load transferred by the four isolators.

To compare different available solutions for the isolation system, three types of commercial isolators are considered in this study: High Damping Rubber Bearing (HDRB), Lead Rubber Bearing (LRB) and Friction Pendulum System (FPS) Isolator. The choice of the isolator characteristics is made on the basis of the manufacturer's catalogue available on the market.

6.3. Design and 3D FE model of the isolators

A preliminary design is required to select the main geometrical and mechanical characteristics of the isolators for the seismic protection of the masonry tower. The design procedure of the isolation system is based on the prescriptions provided in EC8 [42] and on a simplified version reported in [43]. The target horizontal (T_h) and

vertical (T_v) periods of the isolated system define the required horizontal (K_h) and vertical (K_v) stiffness through Eq. 1 and Eq. 2, where M is the mass of the superstructure corresponding to the total weight of the tower. In this study, the target isolation periods are set equal to T_h=2.5 s and T_v=0.08 s, which are common values in practice, for the horizontal and vertical directions, respectively. The diameter of the bearing can be computed through Eq. 3, where A_i is the bearing area, G is the shear modulus of the rubber and t_r is the total thickness of the rubber pads. The required thickness of a single rubber pad (t_i) can be derived through Eq. 4, where E_c is the effective compression modulus of the elastomer constrained by steel shims.

$$K_h = \left(\frac{2\pi}{T_h}\right)^2 \cdot M \quad (1)$$

$$K_v = \left(\frac{2\pi}{T_v}\right)^2 \cdot M \quad (2)$$

$$K_{h,i} = \frac{G \cdot A_i}{t_r} \quad (3)$$

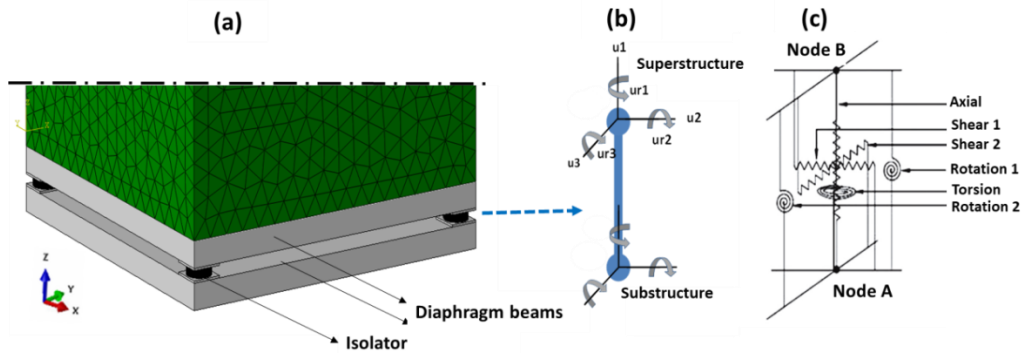$$K_{v,i} = \frac{E_c \cdot A_i}{t_i} \quad (4)$$

Fig. 6.3. (a) Sketch of the isolation system at the base of the bell tower; (b) representative UEL model; (c) discrete spring model of the UEL.
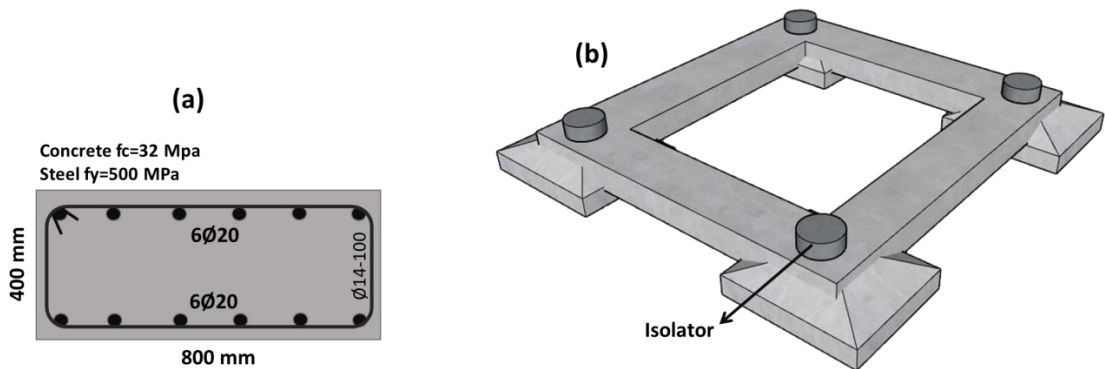

Fig. 6.4. (a) Detail of the reinforced concrete ring beam. (b) Sketch of the foundation system for the isolated tower.

The procedure requires the evaluation of the maximum relative horizontal displacements (S_d) in the isolator, which are a function of both the horizontal period T_h of the isolated system and the equivalent viscous damping ratio ξ_h of the isolation system. For isolated structures presenting a large horizontal period ($T_h > T_c$ where T_c is function of the soil type), the value of S_d in the isolation system can be computed as follows:

$$T_c \leq T_h \leq T_D \qquad S_d = \gamma_x\, \delta_i \left(\frac{2.5}{4\pi^2}\, a_g S \eta T_c \right) T_h \qquad (5)$$

$$T_h \geq T_D \qquad S_d = \gamma_x\, \delta_i \left(\frac{2.5}{4\pi^2}\, a_g S \eta T_c \right) T_D \qquad (6)$$

$$\eta = \sqrt{10/(5 + \xi_h)} \geq 0.55 \qquad (7)$$

where a_g is the peak ground acceleration, S is the soil factor, η is the damping correction factor. The values of the parameters adopted for the response spectrum are the following: a_g=0.25g, S=1.15, T_C=0.6 s, T_D=2 s. The importance factor of the masonry bell tower is assumed equal to γ_x=1.2, while the eccentricity parameter of the isolation system (δ_i) is set equal to 1: it means that the center of stiffness of the isolation system coincides with the vertical projection of the center of mass of the superstructure.

As shown in Fig. 6.3 and Fig. 6.4, four isolators are placed at each corner of the tower base: each isolator carries a load equal to about 650 kN. According to the preliminary design, each isolator presents a horizontal stiffness equal to about 0.5 kN/mm and the first shape factor is equal to 12.5 for elastomeric isolators. Potential isolators with different values of damping ratio are considered to investigate the effects of damping on the seismic behavior of the isolated tower.

The properties of the three possible isolators, as provided by the manufacturer, are presented in Fig. 6.5-Fig. 6.6. It can be noted that the HDRB and the LRB present similar horizontal stiffness and different damping ratio: on the other hand, the FPS isolator exhibits a damping ratio similar to that of the LRB and the smallest horizontal stiffness among the isolators considered. To investigate the behavior of each isolator, 3D FE models are created and cyclic analyses are performed using the software code Abaqus [25]. The isolators are subjected to 0.5 Hz cyclic shear tests with a maximum displacement equal to 100 mm under a constant vertical load equal to 650 kN.

6.3.1. High Damping Rubber Bearing (HDRB)

The HDRB consists of rubber layers and steel lamina. A circular HDRB is selected for this study according to the manufacturer's catalogue [44]. The rubber used is a soft high damping rubber with shear modulus equal to 0.4 MPa and damping ratio equal to 10%.

A Yeoh model is adopted to represent the hyperelasticity of the rubber, while the damping behavior is represented by the Prony series viscosity model. A comprehensive description of the Yeoh hyperelasticity model and Prony series

viscosity model can be found in [45] and [46], respectively. The Yeoh hyperelastic parameters are determined through the optimization of uniaxial tensile test data, while the Prony series coefficients can be derived from relaxation tests. Table 6. 2 and Table 6. 3 show the Yeoh hyperelastic and Prony parameters of the rubber used in this study, respectively. The steel lamina is modelled using a isotropic-elastic behavior with Young modulus equal to 210 GPa and Poisson ratio equal to 0.25.

Table 6. 2. Coefficients of the Yeoh Hyperelastic Model for the rubber.

C_{10}	C_{20}	C_{30}	D_1	D_2	D_3
0.22	0.0044	0.00013	0.0021	0.000086	-0.000018

C in MPa

Table 6. 3. Coefficients of the Prony-series for the rubber.

$g1$	$t1$	$g2$	$t2$
0.2	0.4	0.075	0.2

The geometry and mesh discretization of the HDRB are shown in Fig. 6.5. The FE model is composed of eight-node linear brick elements C3D8R: 2104 elements for a single rubber pad, 897 elements for a single steel reinforcement and 555 elements for a single rigid steel plate. Two elements are introduced along the thickness of a rubber pad to facilitate the lateral deformation against vertical pressure. All the parts of the HDRB are assumed perfectly bonded.

The deformation patterns and the stress distributions of the HDRB under cyclic shear analyses are shown in Fig. 6.5. At the initial stage (horizontal displacements equal to zero), the HDRB experiences compressive deformations due to only vertical loads, causing lateral deformations of the rubber pads. At high shear displacements, severe tensile stresses start from the vertical edges of the bearings.
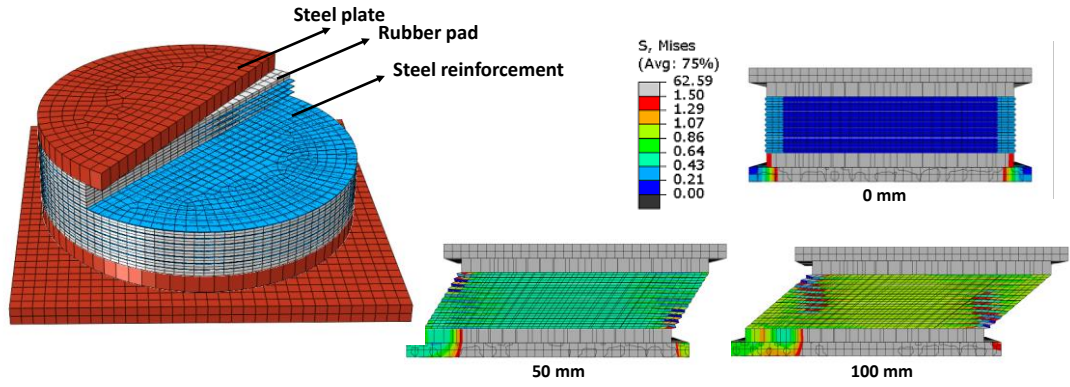
HDRB-350			
Diameter	350 mm	Maximum displacement	160 mm
Rubber layer thickness	7 mm	Nominal Effective stiffness	0.5 kN/mm
Number of rubber layer	11	Nominal damping ratio	10 %
G modulus Rubber	0.4 MPa	Max. Axial Load	1000 kN
Rubber damping	10 %		

Fig. 6.5. LRB isolator. Top: FE model, deformation patterns and Mises stress distribution. Bottom: main properties.

The shear force-horizontal displacement curve obtained for the HDRB (red line) during the cyclic shear analysis is presented in Fig. 6.8a. An elliptical hysteresis loop, which is the typical shear behavior of rubber bearings, can be observed. The effective stiffness and the damping ratio of the isolator are computed, at displacements equal to 100 mm, through the following equations [47]:

$$K_{h,eff} = (F_{max} - F_{min})/(\Delta_{max} - \Delta_{min}) \quad (8)$$

$$\xi = W_d/(4\pi W_s) \quad (9)$$

$$W_s = \frac{1}{2} K_{h,eff} \Delta^2_{max,ave} \quad (10)$$

$$\Delta_{max,ave} = \frac{1}{2}\left(\Delta_{max} + |\Delta_{min}|\right) \quad (11)$$

where F_{max}, F_{min}, Δ_{max} and Δ_{min} are the peak values of the horizontal force and displacement, respectively, W_d represents the dissipated energy (area within the loop) and W_s is the restored energy.

6.3.2. Lead Rubber Bearing (LRB)

The LRB, which is a more recent version of the elastomeric isolator, uses a lead core as dissipative device in addition to the rubber damping: steel reinforcements are also required to improve the vertical stiffness of the bearing, as in the case of elastomeric isolators.

The LRB used in this study can be found in the manufacturer's catalogue [48]. A soft high damping rubber with shear modulus equal to 0.4 MPa and damping ratio equal to 10% is used. The mechanical properties of the rubber and steel lamina in the LRB are similar to those of the HDRB, see Table 6. 2 and Table 6. 3. The elasto-plastic behavior of the lead core significantly contributes to the total damping ratio of the

LRB. The Young modulus and the yield stress of the lead core material are set equal to 15 GPa and 10 MPa, respectively: the Poisson ratio is equal to 0.42.

Fig. 6.6 shows the geometrical and mechanical properties along with the mesh of the LRB. Eight-node linear brick elements C3D8R are used: 2975 elements for the lead core, 2208 elements for a single rubber pad and 1104 elements for a single steel reinforcement. Unlike the HDRB model, the surface of the lead core is not bonded to the surrounding parts: a friction coefficient equal to 0.4 is assumed between the lead core and the rubber.

The deformation patterns and the shear behavior of the LRB are shown in Fig. 6.6 and Fig. 6.8b. At the beginning of the cyclic shear analysis, the stiffness of the LRB is mainly due to the high horizontal stiffness of the lead core, Fig. 6.8. After the yielding of the lead core, the stiffness is due to only the contribution of the elastomer, which is much lower than the initial one. The deformation patterns shown in Fig. 6.6 highlight the yielding of the lead core when subjected to shear displacements. The effective stiffness and damping ratio of the LRB isolator are computed using Eqs. 8-11.
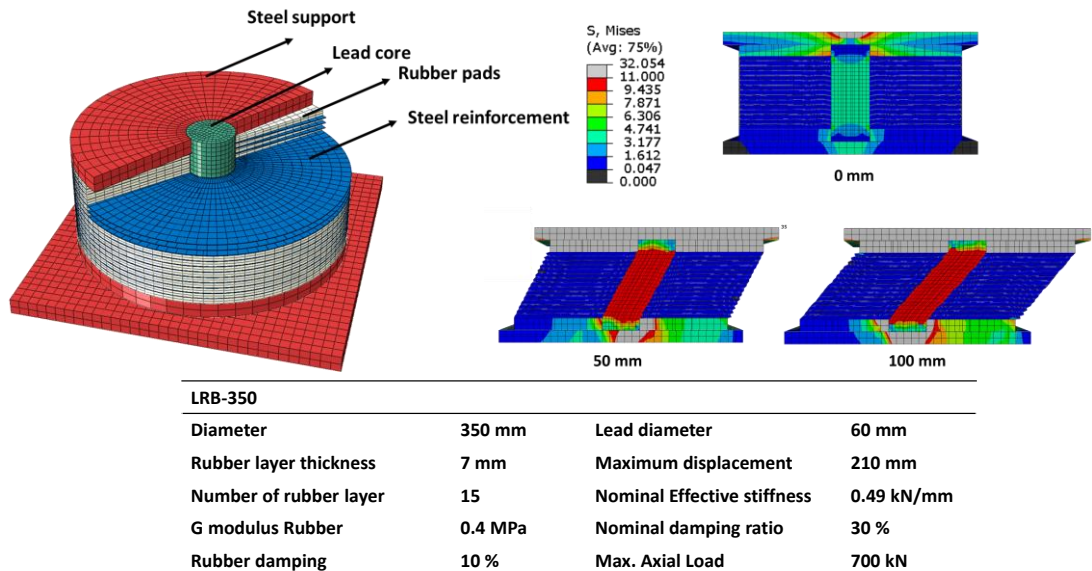

LRB-350			
Diameter	350 mm	Lead diameter	60 mm
Rubber layer thickness	7 mm	Maximum displacement	210 mm
Number of rubber layer	15	Nominal Effective stiffness	0.49 kN/mm
G modulus Rubber	0.4 MPa	Nominal damping ratio	30 %
Rubber damping	10 %	Max. Axial Load	700 kN

Fig. 6.6. LRB isolator. Top: FE model, deformation patterns and Mises stress distribution. Bottom: main properties.

6.3.3. Friction Pendulum System Isolator (FPS)

The FPS isolator is considered as an effective device for base isolation, considering its very low effective horizontal stiffness and high damping ratio. The horizontal stiffness is due to the sliding material relying on the curved pads. The FPS isolator used in this study has a double curvature and a sliding solid material. The nominal diameter and the friction coefficient are equal to 4000 mm and 3%, respectively, as stated in the manufacturer's catalogue [48]. The geometrical and mechanical properties along with the mesh of the FPS isolator model are shown in Fig. 6.7. The FE model is composed of eight-node linear brick elements C3DBR:

2736 elements for a single spherical plate and 1002 elements for the sliding bearing. All the parts of the FPS model present an isotropic-elastic behavior with Young modulus equal to 210 GPa and Poisson ratio equal to 0.25.

It is worth mentioning that the 3D FE model used in this study, although fairly simplified, may represent the mechanical behavior of the real FPS isolator by defining an equivalent friction coefficient, between the slider and the spherical plate, equal to 3%. In the real device, there is a thin interface layer that provides the same friction coefficient between the two surfaces.

As shown in Fig. 6.6, the sliding bearing can move freely following the curve of the double sliding surface. A high stiffness can be observed up to the yielding point, Fig. 6.8c, as in the case of the LRB. A significant reduction of stiffness takes place when the resisting friction force is exceeded. Fig. 6.8c shows the parallelogram hysteresis loop of the FPS isolator. Theoretically, the shear force-horizontal displacement curve of the FPS isolator can be expressed as follows [48]:

$$F = V\left(\mu + \frac{D}{R}\right) \qquad (12)$$

where F is the shear force, D is the displacement, V is the vertical load, μ is the friction coefficient and R is the radius of the sliding surface.

Finally, the effective stiffness and damping ratio obtained from the 3D FE analyses of the three isolators under study are summarized in Table 6. 4.

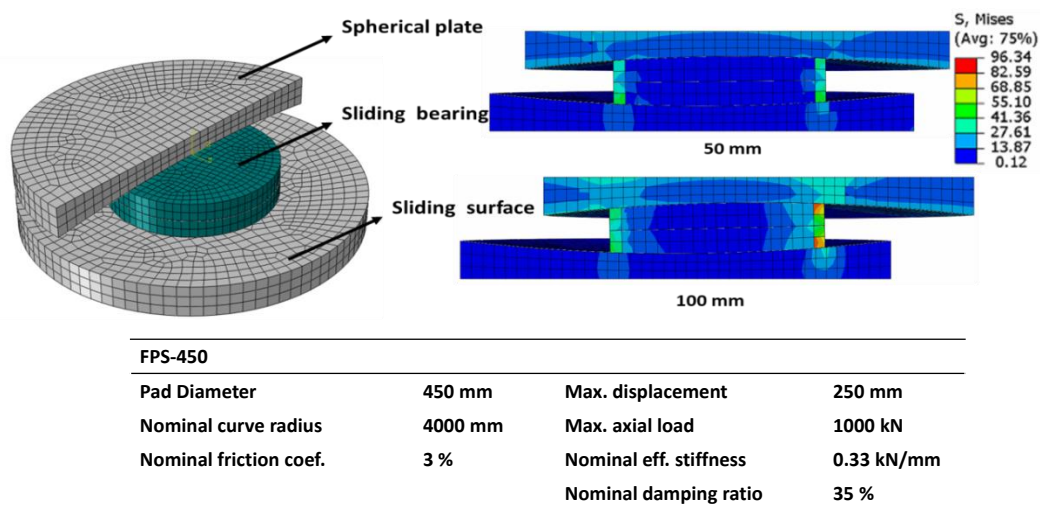| FPS-450			
Pad Diameter	450 mm	Max. displacement	250 mm
Nominal curve radius	4000 mm	Max. axial load	1000 kN
Nominal friction coef.	3 %	Nominal eff. stiffness	0.33 kN/mm
		Nominal damping ratio	35 %

Fig. 6.7. FPS isolator. Top: FE model, deformation patterns and Mises stress distribution. Bottom: main properties.

Table 6. 4.. Effective stiffness and damping ratio for the different isolators.

	Effective stiffness (kN/mm)			Damping ratio (%)		
	Manufacture	3D FE	UEL	Manufacture	3D FE	UEL
HDRB-350	0.50	0.52	0.51	10	10.85	9.96
LRB-350	0.49	0.52	0.45	28	26.91	27.89
FPS-450	0.35	0.36	0.33	33	33.25	31.07

6.4. Abaqus User Element (UEL) for Base Isolators

A single isolator in the isolated structure can be modeled either as a 3D solid part [49], which is computational demanding due to the fine mesh, or as a simplified element with representative behavior [50][51]. In order to reduce the computational effort of the numerical simulations, in this study the isolator is represented by an Abaqus User Element (UEL). The UEL model consists of a two-node beam element (with 12 DOFs) connecting the superstructure and the substructure, as shown in Fig. 6.3b. It can simulate the 3D behavior of a single isolator, taking into account the vertical and horizontal stiffness, the rotational and torsional stiffness, and the hysteresis shear behavior. The representative discrete spring model of the UEL is presented in Fig. 6.3c.

Kumar et al. [52] developed a UEL model for commercial isolators, such as HDRBs and LRBs. The hysteretic behavior of the UEL model in the two orthogonal horizontal directions is based on the Bouc-Wen formulation, Eqs. 13-14, where: F_i is the force; k_H is the horizontal stiffness; u_i is the displacement; c_d is the viscous damping coefficient; w, Y, A, β, and γ are the Bouc-Wen coefficients that control the hysteresis loop shape; z_i is a non-physical parameter that governs the differential equation. The hysteretic behavior of the UEL model is assigned only to the shear DOFs of the UEL model because the damping behavior in the other DOFs does not significantly affect the global behavior of the isolated structure.

To obtain an appropriate representative element, an optimization procedure is required to fit the behavior obtained through the 3D FE model.

Table 6. 5 summarizes the values of the horizontal stiffness, the viscous damping coefficient and the Bouc-Wen coefficients adopted for each UEL model of the three isolators under study. In HDRBs the hysteretic behavior is provided only by the inherent viscous damping of the rubber material, see also Fig. 6.8a. On the other hand, in LRBs a significant additional damping is provided by the yielding of the lead core. As seen also in Fig. 6.8b, the UEL model can capture the significant change of the initial and effective stiffness due to the yielding of the lead core. Moreover, the UEL model takes into account also the possibility of cavitation, which may reduce the tensile strength of elastomeric bearings. As the behavior of FPS isolators is similar to that of LRBs, the UEL model for LRBs can be suitable also for FPS isolators through a proper adaptation of some parameters, see also Fig. 6.8c.

$$\begin{bmatrix} F_x \\ F_y \end{bmatrix} = k_H \cdot \begin{bmatrix} u_x \\ u_y \end{bmatrix} + c_d \cdot \begin{bmatrix} \dot{u}_x \\ \dot{u}_y \end{bmatrix} + w \begin{bmatrix} z_x \\ z_y \end{bmatrix} \tag{13}$$

$$Y \begin{bmatrix} \dot{z}_x \\ \dot{z}_y \end{bmatrix} = \left(A[I] - \begin{bmatrix} z_x^{\;2}(\gamma . sign(\dot{u}_x z_x) + \beta) & z_x z_y(\gamma . sign(\dot{u}_x z_x) + \beta) \\ z_x z_y(\gamma . sign(\dot{u}_x z_x) + \beta) & z_y^{\;2}(\gamma . sign(\dot{u}_y z_y) + \beta) \end{bmatrix} \right) \begin{bmatrix} \dot{u}_x \\ \dot{u}_y \end{bmatrix} \tag{14}$$

Table 6. 5. Values of the parameters used in the UEL model for the isolators under study.

Isolator	k_H (kN/mm)	c_d (kN.s/mm)	w (kN)	A (-)	β (-)	Y (-)	γ (-)
HDRB-350	0.485	0.03	-	-	-	-	-
LRB-350	0.369	0.035	10	1	0.15	0.0005	0.45
FPS-450	0.158	-	20	1	0.15	0.0025	1

The comparative results obtained through the 3D FE and UEL models for the different isolators are presented in Fig. 6.8 and Table 6. 4. It can be noted that the UEL model can accurately represent the behavior of the three isolators in terms of effective stiffness and damping ratio when compared with the 3D FE model and the manufacturer data. Furthermore, it has to be pointed out that the differences in the shape of hysteresis loops are negligible.

Then, the UEL models are implemented in the detailed 3D FE model of the masonry bell tower, following the arrangement of four isolators at the base. It is important to highlight that the UEL model is very useful for the global seismic analysis of isolated structures in Abaqus environment, significantly reducing the computational effort of the numerical simulations.
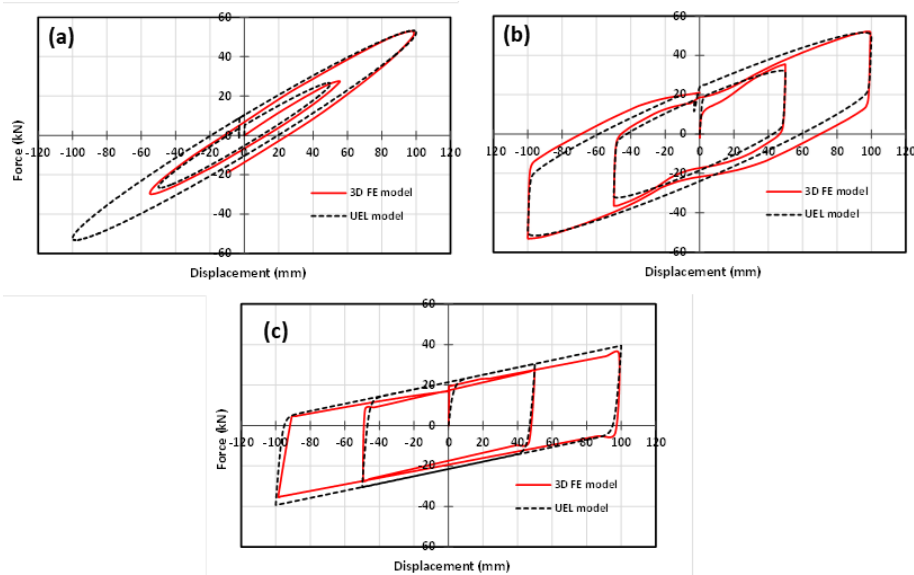

Fig. 6.8. Shear force – horizontal displacement curves obtained through 3D FE models and Abaqus User Element (UEL) for the three isolators under constant vertical load.

6.5. Modal analysis

A modal analysis is performed to evaluate the main vibration properties of the masonry bell tower without and with base isolation. Fig. 6.9 shows the deformed shapes, the corresponding periods and the participating mass ratio (PMR) of the main vibration modes for the fixed-base (FB) model and the base isolated (BI) models. It can be noted that the dynamic behavior of the tower is similar in both the directions because of the square cross-section of the tower.
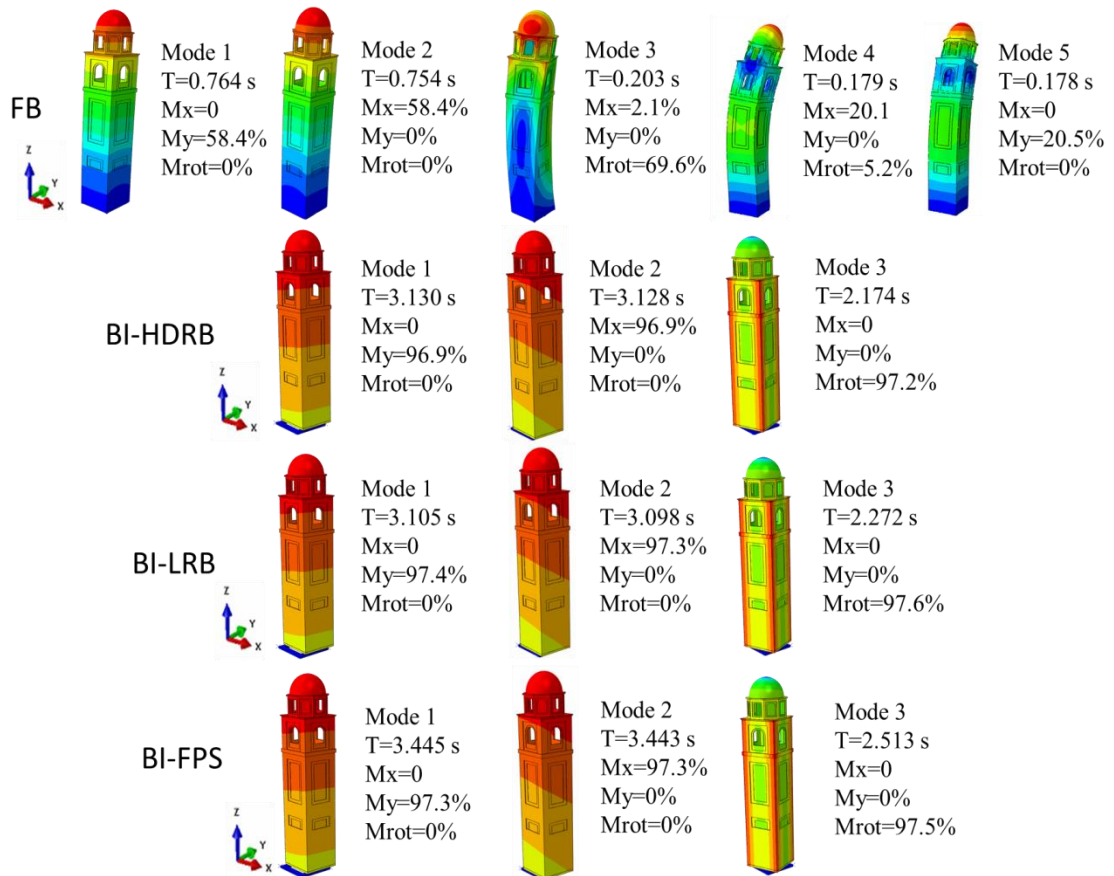

Fig. 6.9. Modal deformed shapes, corresponding period and participating mass ratio of the main vibration modes for the fixed-base (FB) model and the base isolated (BI) models.

In the model without base isolation (FB model), the first and second modes present similar periods (T=0.764 s and T=0.754 s) and are related to a modal shape mainly translational with a PMR equal to about 58% in the Y and X directions, respectively. The third mode with a period T=0.203 s is predominantly torsional. The fourth (T=0.179 s) and fifth (T=0.178 s) modes are mainly translational with a PMR equal to about 20% in the X and Y directions, respectively.

In the models with base isolation (BI models), the first two modes present high values of periods (larger than 3 s) and are mainly translational in the Y (mode 1) and X (mode 2) directions with a very large PMR equal to about 97%: the third mode is torsional with a period larger than 2 s and a very large PMR. As expected, the deformations are concentrated at the base level, where the isolation system is located

and the horizontal stiffness is significantly lower. The other modes of the BI models are characterized by very low values of the PMR. It can be noted that the first and second modes of the BI-HDRB and BI-LRB models exhibit similar values of periods because the two isolators have a similar effective stiffness equal to about 0.5 kN/mm. Moreover, it is worth mentioning that the fundamental periods of the base isolated (BI) models are higher than the target period (2.5 s) assumed in the preliminary design due to the flexibility of the masonry tower: in particular, the highest fundamental period (3.44 s) is obtained in the BI-FPS model due to the lower horizontal effective stiffness of FPS isolators.

6.6. Non-linear dynamic analyses

The seismic response of the masonry bell tower in the different configurations is investigated by performing bi-directional non-linear dynamic analyses. The real accelerogram registered in Mirandola on 29th May during the 2012 Emilia seismic sequence [53] is used for the numerical simulations: the time history accelerations (east-west and north-south components) with PGA=0.25g are shown in **Fig. 6.10**.
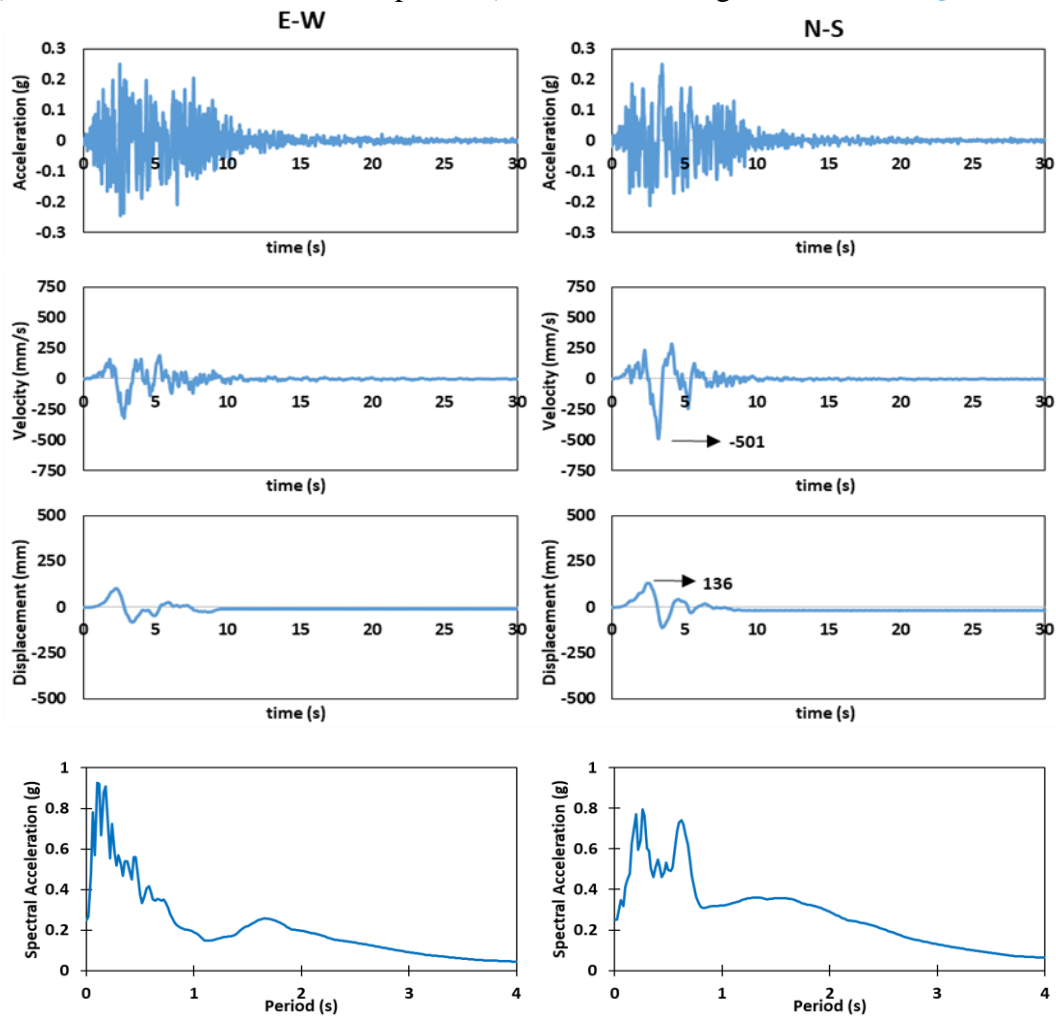

Fig. 6.10. Mirandola ground motion used in the numerical simulations: east-west component in the Y direction and north-south component in the X direction.

Fig. 6.11 shows the tensile damage distribution for the fixed-base (FB) model and the base isolated (BI) models at different time instants during the non-linear dynamic analyses. In the FB model damage starts from the corners of the openings in the upper part of the tower and then propagates along the whole height of the tower. In the BI-LRB and BI-FPS models tensile damage is significantly reduced in all the parts of the tower. Conversely, it can be noted that remarkable damage can be observed along the height of the BI-HRDB model. It is worth mentioning that the HDRBs and LRBs present a similar horizontal stiffness, but the damping ratio of the LRBs is higher than that of the HDRBs, justifying the lower damage level in the BI-LRB model.

Fig. 6.12 shows the top displacement time history obtained from the non-linear dynamic analyses for the fixed-base (FB) model and the base isolated (BI) models in the X and Y directions. The largest displacements are registered in the X direction for the FB and BI-HRDB models: a significant reduction is observed for the BI-LRB and BI-FPS models. Moreover, it can be noted that large residual drifts are registered at the end of the non-linear dynamic analyses for the FB and BI-HDRB models.

Fig. 6.13 shows the top acceleration time history obtained from the non-linear dynamic analyses for the fixed-base (FB) model and the base isolated (BI) models in the X and Y directions. All the BI models present a quite similar reduction (about 75%) of the peak accelerations. It is worth mentioning that a considerable reduction of the acceleration can lead to a notable damage mitigation of the non-structural components [54].
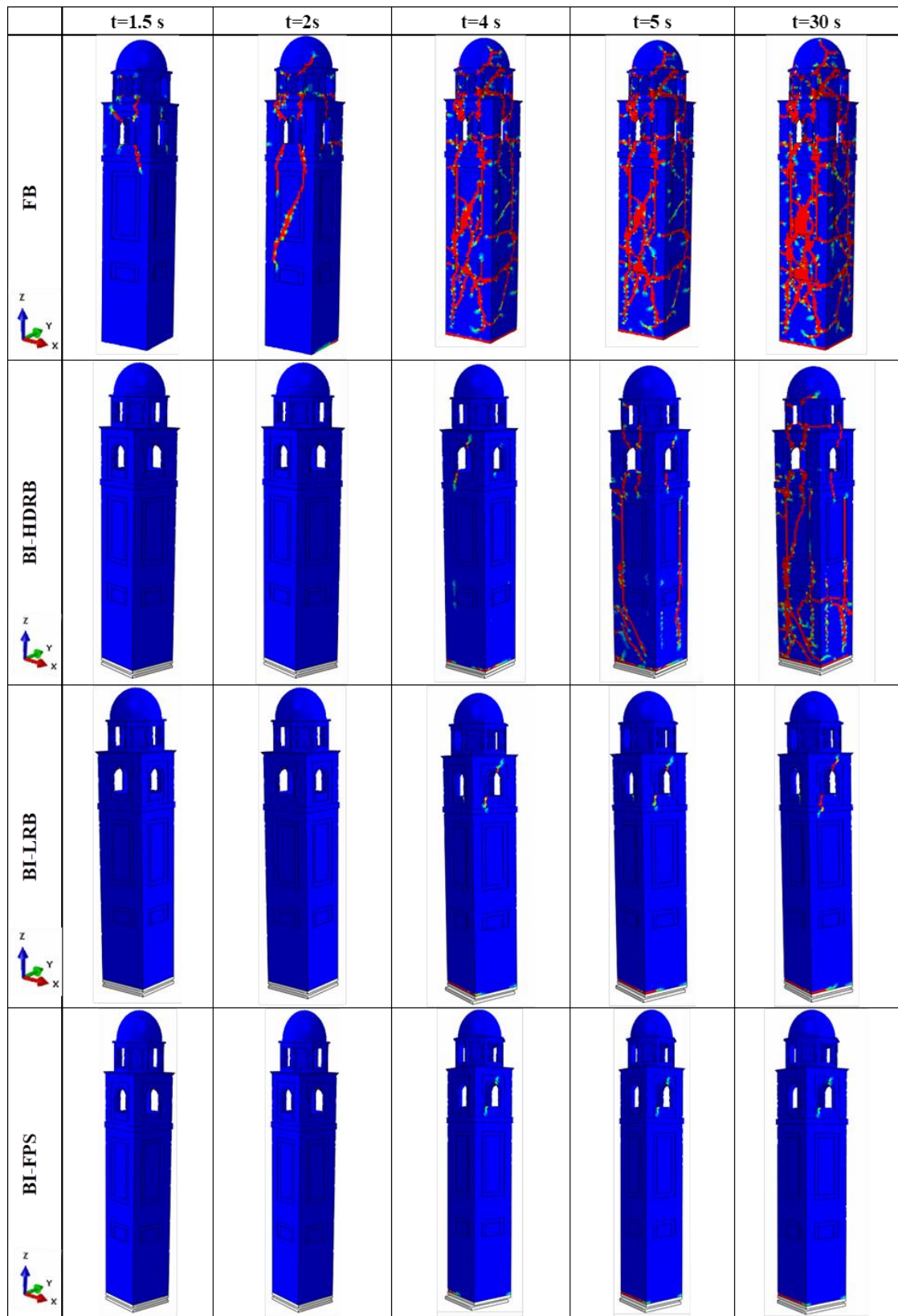
	t=1.5 s	t=2s	t=4 s	t=5 s	t=30 s
FB					
BI-HDRB					
BI-LRB					
BI-FPS					

Fig. 6.11. Tensile damage distribution for the fixed-base (FB) model and the base isolated (BI) models at different time instants during the non-linear dynamic analyses.
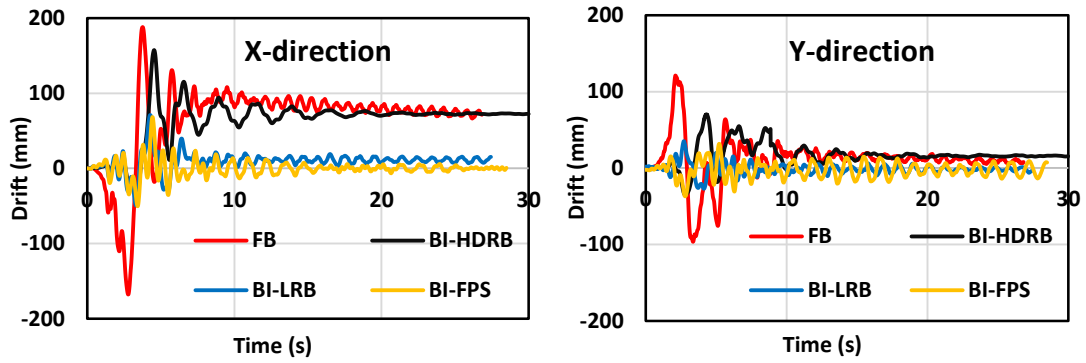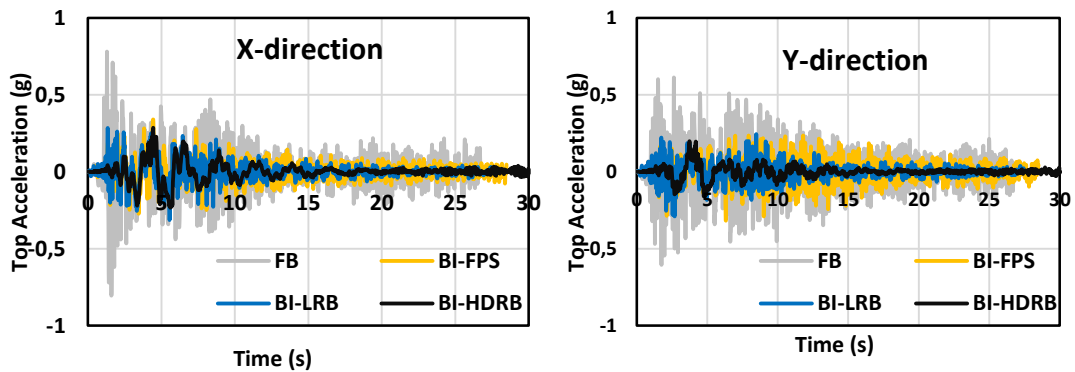
Fig. 6.12. Top displacement time history in the X and Y directions obtained from the non-linear dynamic analysis for the fixed-base (FB) model and the base isolated (BI) models.

Fig. 6.13. Top acceleration time history in the X and Y directions obtained from the non-linear dynamic analysis for the fixed-base (FB) model and the base isolated (BI) models.
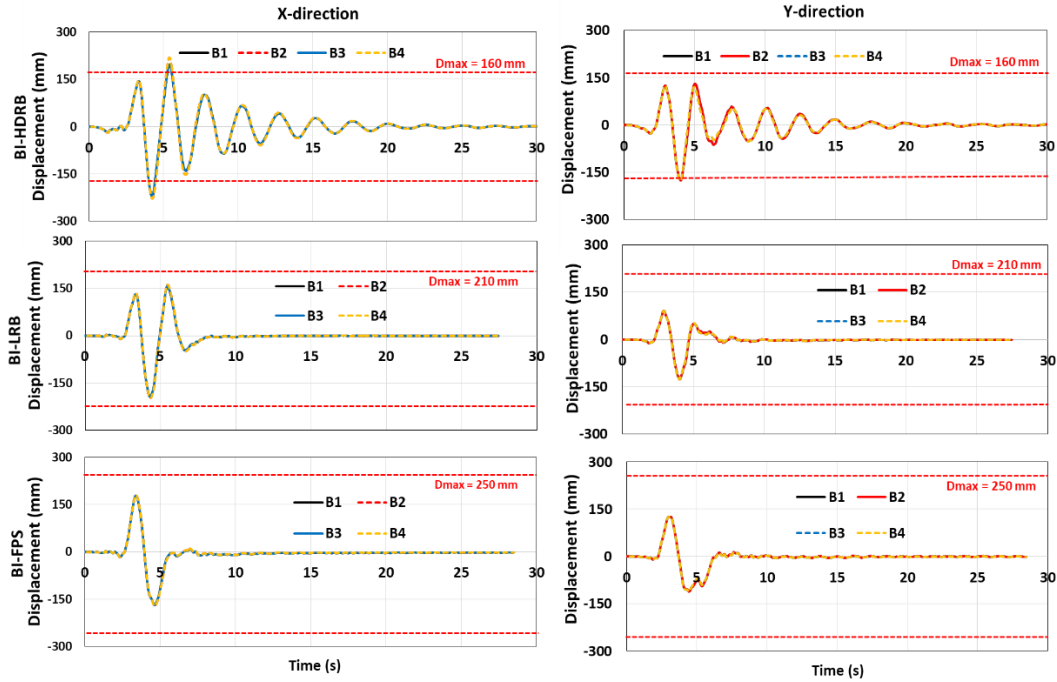
Fig. 6.14 shows the displacement time history obtained from the non-linear dynamic analyses for the different types of isolators in the X and Y directions. The horizontal red line indicates the maximum displacement provided by the manufacturer's brochure for the isolators considered. Numerical results show that the largest shear displacement (about 250 mm) is registered for the HDRB. The LRB and the FPS isolator, which are characterized by a similar high damping ratio, present similar peak shear displacements. Such results indicate that the shear displacements of the isolator is influenced mainly by the damping ratio of the isolation system. From the results obtained, it can be concluded that the HDRB cannot be used due to excessive shear displacements, while the other two isolators satisfy the displacement limits provided by the manufacturer.

Finally, a simplified overturning stability check is performed considering that the isolated structure presents high slenderness, see Eqs. 15-17. The overturning moment M_O is given by the product of the seismic force Fs and the height of the mass center of the superstructure h1, where the seismic force Fs is a function of the maximum response acceleration and the mass of the superstructure; the resisting moment M_R is given by the product of the superstructure weight Wt and half the width of the tower

base L/2; SF_O is the overturning safety factor that is defined as the ratio between the resisting moment MR and the overturning moment M_O.

$$M_O = F_s \cdot h_1 \quad (15); \qquad M_R = W_t \cdot L/2 \qquad (16); \quad SF_O = M_R/M_O \qquad (17)$$

Table 6. 6 summarizes the main results of the simplified overturning check of the isolated tower. The results show that under Mirandola earthquake the isolated tower can be considered stable against overturning because the values of the safety factor SF are larger than 1 [55].

Fig. 6.14. Displacement time history in the X and Y directions obtained from the non-linear dynamic analyses for the different types of isolators.

Table 6. 6. Simplified overturning check for the isolated tower under Mirandola earthquake.

	M_O (kN.m)	M_R (kN.m)	SF_O
BI-HDRB	5978	6095	1.01
BI-LRB	4379	6095	1.39
BI-FPS	4685	6095	1.30

6.7. Effects of near-fault earthquakes

Another aim of the present study is to investigate the effects of near fault (NF) earthquakes on the seismic response of the masonry tower, without and with base isolation. NF earthquakes are characterized by a long-period pulse in the acceleration time history and a large peak velocity. They may cause disruptive effects on isolated structures, especially in terms of isolators displacements: in particular, an

amplification of isolators displacements may take place due to the similar period values of the isolated structure and ground motion [56][57].

To this aim, the near fault (NF) El Centro ground motion is selected and scaled to the same PGA (PGA=0.25 g) as the far fault (FF) earthquake used for the analyses described in the previous section. Fig. 6.15 shows the main characteristics of the NF El Centro ground motion used in the numerical simulations. It can be noted that the NF record presents a larger peak ground velocity and displacement than the FF record, see Fig. 6.10. The NF ground motion is then applied to the masonry tower in the different (FB and BI) configurations.
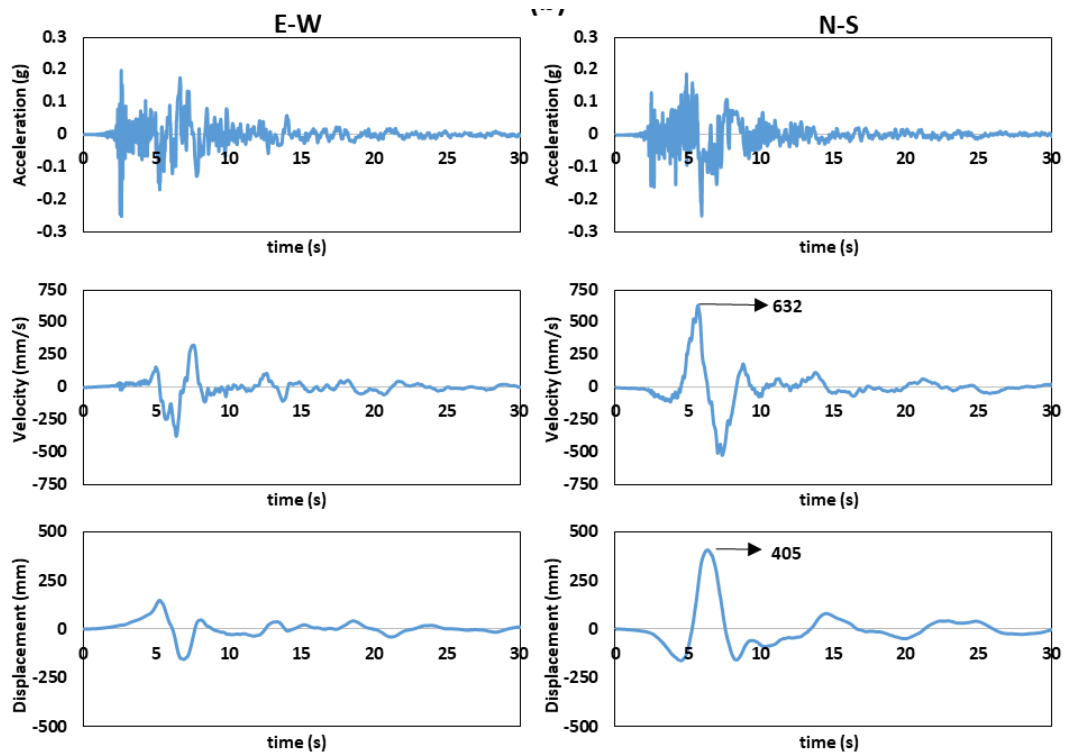
Fig. 6.15. El Centro ground motion used in the numerical simulations: east-west component in the Y direction and north-south component in the X direction.

Fig. 6.16 shows the tensile damage contour plots of the tower subjected to NF ground motions at the end of the seismic excitation. It can be noted that the damage level observed in the masonry tower under the NF earthquake is generally higher than that registered under the FF earthquake, see Fig. 6.11. The application of HDRBs seems not to mitigate the damage of the tower; conversely, the use of the other two isolation systems is effective in reducing the damage level of the tower.

Fig. 6.17 shows the top displacement time history under the NF earthquake for the fixed-base (FB) model and the base isolated (BI) models in the X and Y directions. The use of FPS isolators results in the largest reduction of the top displacement compared to the other isolation systems: moreover, the FPS isolation system considerably reduces the residual displacements at the end of the seismic excitation. Numerical results also highlight that the application of HDRBs causes an

amplification of the tower response: the peak top displacement of the BI-HDRB model is larger than that of the FB model.
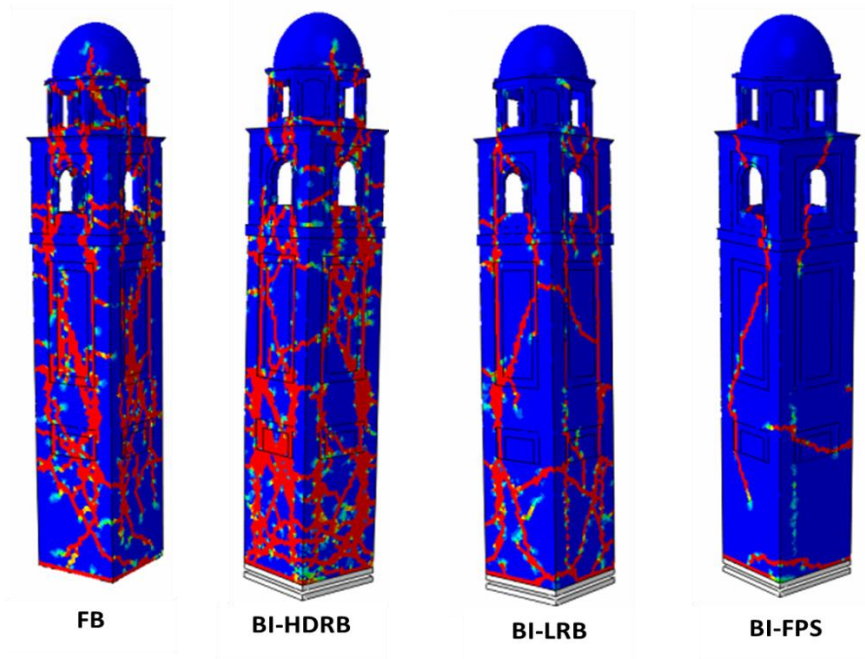

Fig. 6.16. Tensile damage distribution for the fixed-base (FB) model and the base isolated (BI) models at the end of the non-linear dynamic analyses with the NF earthquake.
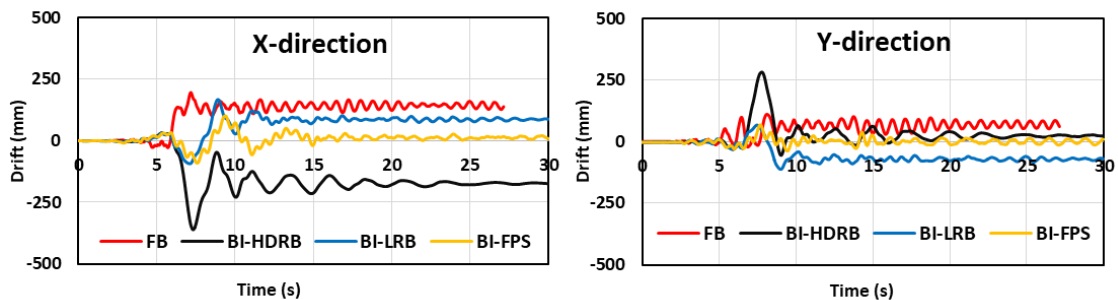

Fig. 6.17. Top displacement time history in the X and Y directions obtained from the non-linear dynamic analysis for the fixed-base (FB) model and the base isolated (BI) models under the NF earthquake.

Fig. 6.18 shows the top acceleration time history under the NF earthquake for the fixed-base (FB) model and the base isolated (BI) models in the X and Y directions. The FB model amplifies the acceleration response up to 1.0g, while all the isolation systems are able to significantly decrease the acceleration response in a similar way.

Fig. 6.19 shows the displacement time history obtained from the non-linear dynamic analyses for the different types of isolators under the NF earthquake. All the BI models exhibit large displacements of the isolators, being a common problem for isolation systems under NF ground motions. On the other hand, it can be noted that the LRBs and FPS isolators can mitigate the residual vibrations at about 15 s of the seismic excitation, due to their significantly higher damping ratio than that of the HDRBs.
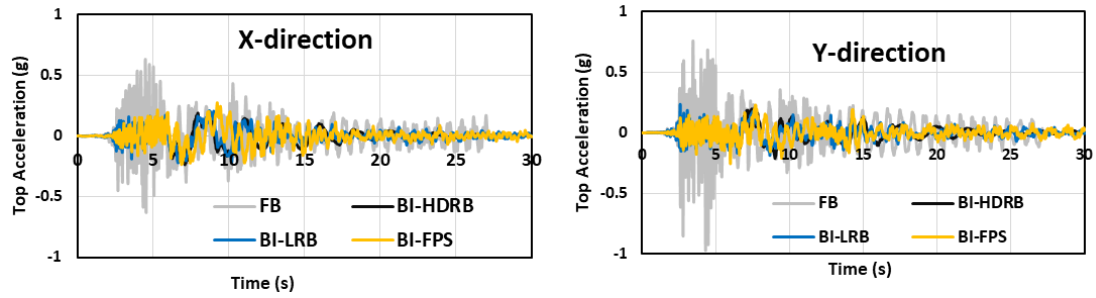
Fig. 6.18. Top acceleration time history in the X and Y directions obtained from the non-linear dynamic analysis for the fixed-base (FB) model and the base isolated (BI) models under the NF earthquake.
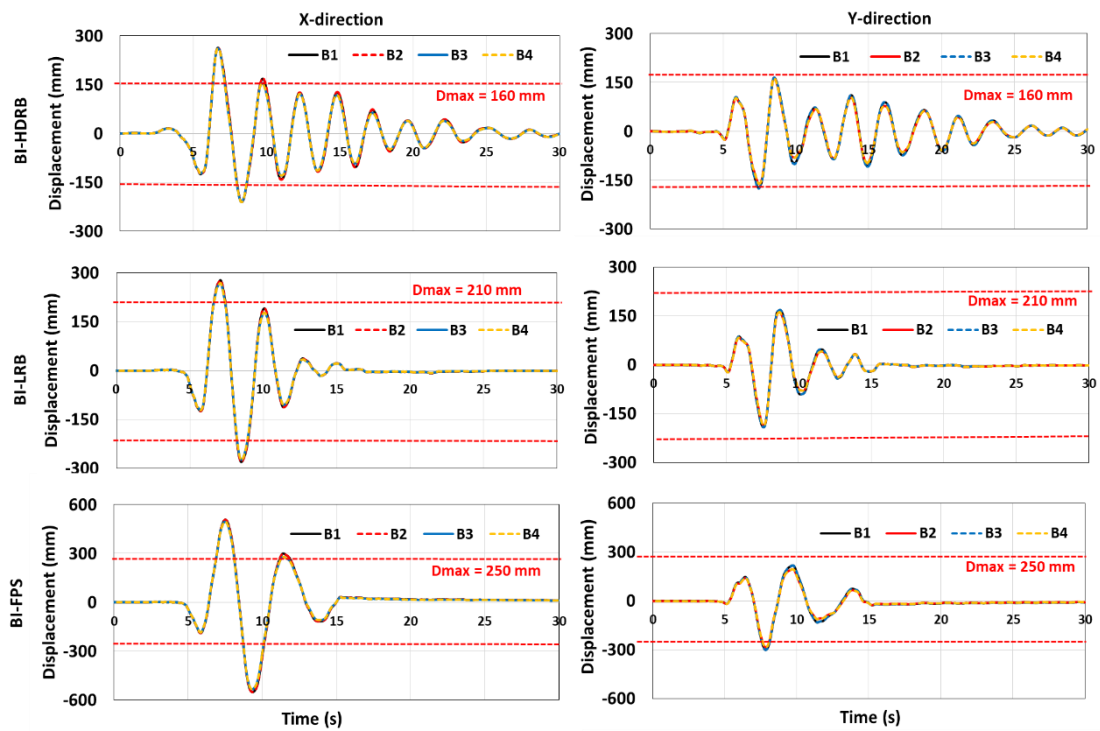

Fig. 6.19. Displacement time history in the X and Y directions obtained from the non-linear dynamic analyses for the different types of isolators under the NF earthquake.

Fig. 6.20 shows the comparative peak values of (a) top drift, (b) top acceleration and (c) ratio between the isolator displacement (u) and the corresponding critical value (umax), in case of FF and NF earthquakes.

Under the FF earthquake, the isolation systems can mitigate the drift of the tower: however, it can be noted that only a negligible drift reduction is registered for the BI-HDRB model. In the case of NF earthquake, the BI-HDRB model presents an increase of drift with respect to the FB model. Such results indicate that an adequate damping is required for the base isolation system to mitigate the earthquake effects on the structure, especially under NF ground motions. As presented in Section 3, LRBs exhibit significantly larger damping ratio but similar stiffness when compared to HDRBs. Numerical results show that there is no notable difference between the

BI-LRB and BI-FPS models in terms of tower drift under the FF earthquake. Conversely, under the NF earthquake, the BI-FPS model presents a larger drift reduction than the BI-LRB model. It is important to underline that FPS isolators exhibit less stiffness and almost similar damping when compared to LRBs.

Numerical results show that no relevant difference in terms of acceleration response reduction is observed at the top of the BI models for the two earthquakes: in fact, the peak acceleration values registered for all the three BI models are similar and lower than those observed for the FB model. It is interesting to observe that the FB model shows higher peak acceleration values under the NF earthquake than under the FF earthquake.
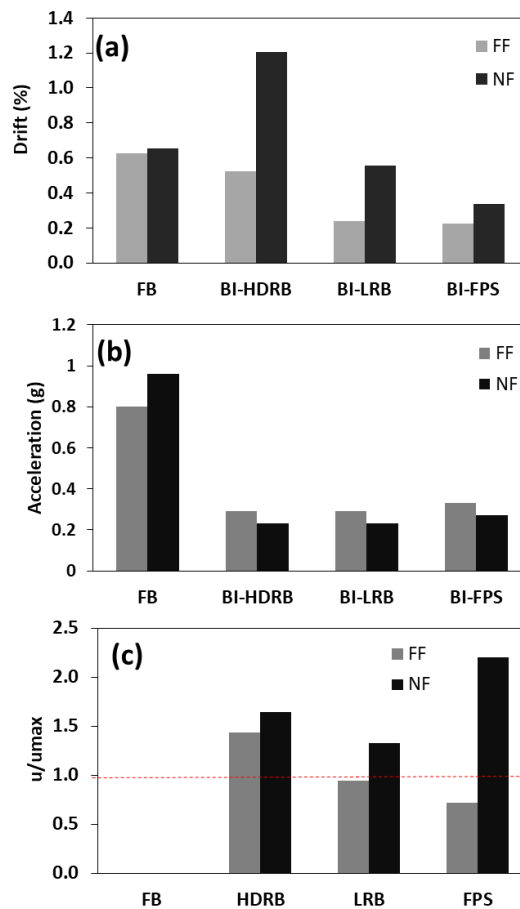

Fig. 6.20. Peak values of the seismic response of the tower under the FF and NF earthquakes: (a) top drift, (b) top acceleration, and (c) ratio between the isolator displacement and the corresponding limit value.

As regards the isolator displacements, the HDRBs show a ratio between the isolator displacement and the corresponding limit value larger than 1 for both FF and NF earthquakes. On the other hand, the LRBs and FPS isolators satisfy the limits under the FF earthquake: conversely, under the NF earthquake, the ratio between the isolator displacement and the corresponding critical value is larger than 1. Such a result implies that base isolation systems require larger isolators with higher damping to accommodate large displacement demands under NF earthquakes.

Table 6. 7 summarizes the main results of the simplified overturning check of the isolated tower under NF earthquake: as shown in the case of FF earthquake, it can be noted that the check is satisfied because the values of the safety factor SF are larger than 1.

Table 6. 7. Simplified overturning check for the isolated tower under the NF earthquake.

	M_O (kN.m)	M_R (kN.m)	SF_O
BI-HDRB	5737	6095	1.06
BI-LRB	4040	6095	1.51
BI-FPS	4583	6095	1.33

6.8. Conclusions

This study has provided a comprehensive evaluation of the base isolation effectiveness for the seismic protection of a historical masonry bell tower. Three types of isolators (HDRB, LRB, and FPS), which present different effective stiffness or damping ratio, have been considered and investigated. A 3D FE model has been developed for each type of isolator to obtain the cyclic shear behavior. For the global seismic analysis of the isolated masonry bell tower, each single isolator has been modeled through a representative UEL model. The seismic response of the tower in the different (fixed base and base isolated) configurations has been investigated performing non-linear dynamic analyses with far fault (FF) and near fault (NF) ground motions.

From an overall analysis of the results obtained in this study, the following remarks can be made.

-The results of cyclic shear analyses show that the proposed UEL model can accurately predict the behavior obtained through detailed 3D FE models. Such UEL model is effective to significantly reduce the computational effort in non-linear dynamic analyses.

-The HDRBs do not ensure an adequate seismic protection of the masonry bell tower, due to their smaller damping when compared with the other isolators considered, in terms of damage level and top displacement, in case of both FF and NF earthquakes. In case of the NF earthquake, larger top displacements are registered for the BI-HDRB model than for the FB model: furthermore, under both FF and NF earthquakes, the peak displacements of the HDRBs exceed the maximum value stated by the manufacturer.

-The BI-LRB and BI-FPS models show a similar good performance under the FF earthquake, despite a different horizontal stiffness: the residual displacements of the tower are negligible and the isolator displacements satisfy the limit values. Under the NF earthquake, the BI-LRB model presents a significantly larger top displacement than the BI-FPS model. In any case, both the BI-LRB and FPS models do not ensure

sufficient seismic protection under the NF earthquake in terms of tower drifts and isolator displacements.

-Numerical results indicate that, in case of NF earthquakes, an isolation system with higher damping and larger dimension is required to reduce the drifts of the tower and to accommodate the large displacements of the isolators. Consequently, an additional damper system can be considered to significantly increase the dissipation capacity of the isolation system.

- It is worth mentioning that a possible alternative installation layout consisting of a larger number of isolators (e.g eight isolators with smaller dimensions) could be adopted, especially in the case of far field earthquakes. In so doing, notably safer conditions of the isolation system and the superstructure would be reached, in the case of partial malfunctioning of an isolator.

- Finally, it is important to highlight that the expected costs of the base isolation intervention proposed for the tower may be higher than those of more traditional strengthening methods. However, base isolation may be really effective in terms of damage prevention and seismic protection, preserving the original artistic and structural features of the construction as well as overcoming some practical difficulties of traditional strengthening interventions.

References

[1] Clementi F, Pierdicca A, Formisano A, Catinari F, Lenci S. Numerical model upgrading of a historical masonry building damaged during the 2016 Italian earthquakes: the case study of the Podestà palace in Montelupone (Italy). Journal of Civil Structural Health Monitoring 2017;7(5):703-717.

[2] Sorrentino L, Liberatore L, Decanini LD, Liberatore D. The performance of churches in the 2012 Emilia earthquakes. Bulletin of Earthquake Engineering 2013;12:2299-2331.

[3] Ubertini F, Cavalagli N, Kita A, Comanducci G. Assessment of a monumental masonry bell-tower after 2016 central Italy seismic sequence by long-term SHM. Bulletin of Earthquake Engineering 2018;16 (2):775-801.

[4] Castellazzi G, D'Altri AM, De Miranda S, Chiozzi A, Tralli A. Numerical insights on the seismic behavior of a non isolated historical masonry tower. Bulletin of Earthquake Engineering 2018;16(2): 933–61.

[5] Formisano A. Theoretical and numerical seismic analysis of masonry building aggregates: case studies in San Pio Delle Camere (L'Aquila, Italy). Journal of Earthquake Engineering 2017; 21(2):227-245.

[6] Hofer L, Zampieri P, Zanini MA, Faleschini F, Pellegrino C. Seismic damage survey and empirical fragility curves for churches after the August 24, 2016 Central Italy earthquake. Soil Dynamics and Earthquake Engineering 2018;111:98-109.

[7] Gattulli V, Antonacci E, Vestroni F. Field observations and failure analysis of the Basilica S. Maria di Collemaggio after the 2009 L'Aquila earthquake. Engineering Failure Analysis 2013;34:715-734.

[8] Valente M, Milani G. Seismic response and damage patterns of masonry churches: seven case studies in Ferrara, Italy. Engineering Structures 2018;177:809-835.

[9] Valente M, Milani G. Damage assessment and partial failure mechanisms activation of historical masonry churches under seismic actions: three case studies in Mantua. Engineering Failure Analysis 2018;92:495-519.

[10] Valente M, Milani G. Damage survey, simplified assessment, and advanced seismic analyses of two masonry churches after the 2012 Emilia earthquake. International Journal of Architectural Heritage 2018, https://doi.org/10.1080/15583058.2018.1492646

[11] Sorace S, Terenzi G. Seismic evaluation and retrofit of historical churches. Structural Engineering International 2002;12(4):283-288.

[12] Borri A, Vetturini R. Isolamento sismico alla base di un edificio in muratura di pregio storico-artistico in L'Aquila. XIV Italian Conference ANIDIS, Bari, Italy, 18-22 September, 2011.

[13] Vetturini R, Cecchini W, Mariani R, Ciotti T, Agostini EM. Intervento di isolamento sismico alla base di un edificio in muratura di pregio storico-artistico in L'Aquila. Progettazione Sismica 2013;4(1):95-118.

[14] Chiozzi A, Simoni M, Tralli A. Base isolation of heavy non-structural monolithic objects at the top of a masonry monumental construction. Materials and Structures 2016;49:2113-2130.

[15] Sorace S, Terenzi G. Seismic performance assessment and base-isolated floor protection of statues exhibited in museum halls. Bulletin of Earthquake Engineering 2015;13:1873-1892.

[16] Castellano A, Foti P, Fraddosio A, Marzano S, Mininno G, Piccioni MD. Seismic response of a historic masonry construction isolated by stable unbonded fiber-reinforced elastomeric isolators (SU-FREI). Key Engineering Materials 2015;628:160-167.

[17] Habieb AB, Valente M, Milani G. Base seismic isolation of a historical masonry church using fiber reinforced elastomeric isolators. Soil Dynamics and Earthquake Engineering 2019;120:127-145.

[18] Kelly JM, Chalhoub MS. Earthquake Simulator Testing of a Combined Sliding Bearing and Rubber Bearing Isolation System. Report No. UCB/EERC-87/04, Earthquake Engineering Research Center, University of California at Berkeley, 1990.

[19] Jain SK, Shashi KT. Application of base isolation for flexible buildings. 13th World Conference on Earthquake Engineering, Vancouver, Canada, 1-6 August, 2004.

[20] Milani G, Shehu R, Valente M. A kinematic limit analysis approach for seismic retrofitting of masonry towers through steel tie-rods. Engineering Structures 2018;160:212-228.

[21] Valluzzi MR, Binda L, Modena C. Mechanical behaviour of historic masonry structures strengthened by bed joints structural repointing. Construction and Building Materials 2005;19(1):63-73.

[22] Cosenza E, Iervolino I. Case study: seismic retrofitting of a medieval bell tower with FRP. Journal of Composites for Construction 2007;11(3):319-327.

[23] Preciado A, Sperbeck ST, Ramírez-Gaytán A. Seismic vulnerability enhancement of medieval and masonry bell towers externally prestressed with unbonded smart tendons. Engineering Structures 2016;122:50-61.

[24]   Seki M, Miyazaki M, Tsuneki Y, Kataoka K. A masonry school building retrofitted by base isolation technology. 12th World conference on Earthquake Engineering, Auckland, New Zeland, 2000.

[25]   ABAQUS®, Theory Manual, Version 6.14, 2014.

[26]   Lubliner J, Oliver J, Oller S, Oñate E. A plastic-damage model for concrete. International Journal of Solids and Structures 1989;25:299-326.

[27]   Lee J, Fenves GL. Plastic-Damage Model for Cyclic Loading of Concrete Structures. Journal of Engineering Mechanics 1998;124:892-900.

[28]   Valente M, Milani G. Damage assessment and collapse investigation of three historical masonry palaces under seismic actions. Engineering Failure Analysis 2019;98:10-37.

[29]   Valente M, Barbieri G, Biolzi L. Damage assessment of three medieval churches after the 2012 Emilia earthquake. Bulletin of Earthquake Engineering 2017,15(7),2939-2980.

[30]   Valente M, Milani G. Earthquake-induced damage assessment and partial failure mechanisms of an Italian Medieval castle. Engineering Failure Analysis 2019;99:292-309.

[31]   Page AW. A biaxial failure criterion for brick masonry in the tension–tension range. International Journal of Masonry Constructions 1981;1:26-30.

[32]   de Buhan P, de Felice G. A homogenisation approach to the ultimate strength of brick masonry. Journal of the Mechanics and Physics of Solids 1997;45(7):1085-1104.

[33]   Milani G, Lourenco PB, Tralli A. Homogenised limit analysis of masonry walls, Part I: failure surfaces. Computers and Structures 2006;84(3-4):166-180.

[34]   Milani G, Milani E, Tralli A. Upper Bound limit analysis model for FRP-reinforced masonry curved structures. Part I: unreinforced masonry failure surfaces. Computers & Structures 2009;87(23-24):1516-1533.

[35]   Cecchi A, Milani G. A kinematic FE limit analysis model for thick English bond masonry walls. International Journal of Solids and Structures 2008;45(5):1302-1331.

[36]   Tiberti S, Milani G. 2D pixed homogenized limit analysis of non-periodic masonry walls. Computers & Structures 2019;219:16-57.

[37]   Van Der Pluijm R. Shear behaviour of bed joints. Proceedings of 6th North American Masonry Conference, Philadelphia, 1993, 125-136.

[38]   Page A. The biaxial compressive strength of brick masonry, Proc. Inst. Civ. Eng. 1981:871-893.

[39]   DM, Nuove norme Tecniche per le Costruzioni. Ministero Delle Infrastrutture (GU N.29 04/02/2008), 14/01/2008, Rome, Italy. [New Technical Norms on Constructions].

[40]   Circolare n° 617 del 2 Febbraio, Istruzioni per l'applicazione Delle Nuove Norme Tecniche per le Costruzioni di Cui al Decreto Ministeriale 14 Gennaio 2008, 2009, [Instructions for the Application of the New Technical Norms on Constructions].

[41]   DPCM, Linee guida per la valutazione e la riduzione del rischio sismico del patrimonio culturale con riferimento alle Norme tecniche delle costruzioni di cui al decreto del Ministero delle Infrastrutture e Dei trasporti del 14 gennaio 2008, 9/2/2011, [Italian guidelines for the evaluation and the reduction of the seismic risk for the built heritage with reference to the Italian norm of constructions].

[42] Eurocode 8. Design of structures for earthquake resistance-part 1: general rules, seismic actions and rules for buildings. Brussels: European Committee for Standardization, 2005.

[43] Losanno D, Hadad HA, Serino G. Design charts for Eurocode-based design of elastomeric seismic isolation systems. Soil Dynamics and Earthquake Engineering 2019;119:488-498.

[44] Elemka. Product Catalog: HDRB and LRB, 2018.

[45] Yeoh OH. Some forms of the strain energy function for rubber. Rubber Chemistry and technology 1993;66(5):754-771.

[46] Dill EH. Continuum mechanics: elasticity, plasticity, viscoelasticity. CRC press, 2006.

[47] Toopchi-Nezhad H, Tait MJ, Drysdale RG. Testing and modeling of square carbon fiber-reinforced elastomeric seismic isolators. Structural Control and Health Monitoring 2008;15:876-900.

[48] FPC-Italia, 2018. Seismic Isolator Products.

[49] Ohsaki M, Miyamura T, Kohiyama M, Yamashita T, Yamamoto M, Nakamura N. Finite-element analysis of laminated rubber bearing of building frame under seismic excitation. Earthquake Engineering & Structural Dynamics 2015;44(11):1881-1898.

[50] Habieb AB, Milani G, Tavio T. Two-step advanced numerical approach for the design of low-cost unbonded fiber reinforced elastomeric seismic isolation systems in new masonry buildings. Engineering Failure Analysis 2018;90:380-396.

[51] Habieb AB, Valente M, Milani G. Implementation of a simple novel Abaqus user element to predict the behavior of unbonded fiber reinforced elastomeric isolators in macro-scale computations. Bulletin of Earthquake Engineering 2019;17(5):2741-2766.

[52] Kumar M, Whittaker AS, Constantinou MC. An advanced numerical model of elastomeric seismic isolation bearings. Earthquake Engineering & Structural Dynamics 2014;43:1955-1974.

[53] Italian strong-motion database ITACA (Italian ACcelerometric Archive, http://itaca.mi.ingv.it)

[54] Van Engelen NC, Konstantinidis D, Tait MJ. Structural and nonstructural performance of a seismically isolated building using stable unbonded fiber-reinforced elastomeric isolators. Earthquake Engineering & Structural Dynamics 2016;45:421-439.

[55] Ehsani B, Toopchi-Nezhad H. Systematic design of unbonded fiber reinforced elastomeric isolators. Engineering Structures 2017;132:383-398.

[56] Jonsson MH, Bessason B, Haflidason E. Earthquake response of a base-isolated bridge subjected to strong near-fault ground motion. Soil Dynamics and Earthquake Engineering 2010;30:447-455.

[57] Providakis CP. Effect of LRB isolators and supplemental viscous dampers on seismic isolated buildings under near-fault excitations. Engineering Structures 2008;30:1187-1198.

Chapter

7
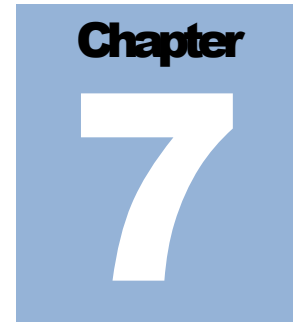
Hybrid seismic base isolation for a historical masonry church using fiber reinforced elastomers and shape memory alloy wires

One of the most promising devices for seismic base isolation of structures is the Unbonded Fiber Reinforced Elastomeric Isolator (UFREI) due to its low manufacturing cost and horizontal stiffness. This paper investigates the possibility of combining UFREIs and shape memory alloy (SMA) wires to increase the energy dissipation capacity of the isolation system for the seismic protection of a historical masonry church. Detailed 3D finite element (FE) analyses are performed to characterize the response of UFREIs under cyclic displacements. The behavior of SMA is simulated through a thermomechanical constitutive model implemented in a user-defined material (UMAT) subroutine available in the software package Abaqus. To reduce the computational effort in non-linear dynamic analyses of large isolated structures, an Abaqus user element (UEL) is developed to represent the 3D behavior of the isolation system proposed in this study. Non-linear dynamic time history analyses are then carried out to evaluate the seismic response of a historical masonry church in different configurations (fixed-base model and model equipped with different base isolation systems) for moderate and severe seismic intensity levels. Numerical results show that the damage observed in the masonry church can be considerably reduced through the insertion of UFREIs. The utilization of SMA wires with a specific pre-strain significantly increases the energy dissipation capacity of the base isolation system and decreases the horizontal displacements of the masonry church.

7.1. Introduction

Preservation of historical masonry buildings is still a critical issue in several countries, such as Italy. A large number of historical masonry structures, in particular churches, are highly vulnerable to damage and prone to partial or total collapse under seismic actions, as also reported after recent seismic events [1]-[4]. Different seismic protection strategies and techniques are available to increase the seismic capacity of existing masonry constructions, as widely reported in the literature: among many others, see [5]-[8]. Common retrofitting techniques are often invasive and generally

based on a strengthening approach, consequently increasing the seismic demand on the structure.

Another protection method is based on shifting the period of the structure through the insertion of base isolation devices that are characterized by low horizontal stiffness. Base isolation has become increasingly popular among engineers in designing important structures in high seismicity regions: however, although base isolation has been recognized as a promising alternative to protect structures against earthquakes, engineering research and practices on seismic isolation of historical masonry constructions remain limited. Moreover, seismic isolators are especially needed for unreinforced masonry structures, where the poor tensile strength may lead to low horizontal load carrying capacities [9]-[11].

The application of isolation systems has increased also in high seismicity regions of developing countries through the use of low cost devices. Fiber reinforced elastomeric isolators (FREIs) have been introduced as a potential low cost alternative to conventional steel reinforced elastomeric ones: they can be unbonded (UFREI) or bonded (BFREI) to both the superstructure and substructure. Conventional elastomeric isolators usually consist of several layers of high-damping rubber (pads) reinforced by interposed steel shims: the reinforcement has the role of improving the stability and limiting vertical deformations, while the horizontal deformations are controlled by the shear stiffness of the pads. Glass or carbon fiber material can be used as alternative reinforcement because it is more economical than its steel counterpart and provides comparable reinforcement effects [12]-[14].

The fiber reinforcement allows for the application of UFREIs, in which the upper and bottom surfaces are not glued to the structure: furthermore, steel reinforcing plates for the supports are not required. A shaking table test on a new masonry building supported on UFREIs has provided promising results, with a significant reduction of inter-story drifts and accelerations [15]. Moreover, a first full-scale application of base isolation to a two-story masonry building supported on UFREIs has been carried out in Tawang, India [16]. On the other hand, the application of base isolation in existing or historical masonry buildings seems a challenging task due to the need of separating the superstructure and foundation. The difficulty typically comes from the large thickness and weight of masonry walls. However, several construction methods have been proposed to implement the base isolation system into old masonry buildings [17]-[19].

The main advantages of UFREIs application are described in the literature [12][20][21]. The effective horizontal stiffness of UFREIs at medium to high displacements is considerably lower than that of BFREIs, thus decreasing the seismic demand. The reduction of the effective lateral stiffness is the result of the rollover deformation of the UFREI due to the absence of bonding. Some researchers have evaluated the UFREI stability limit at which the isolator can be subjected to damage or delamination. Lateral displacements equal to $1.7\text{-}2t_r$ (where t_r is the total thickness of rubber layers in the isolator) are considered as critical values [22],

while it is reported in [23] that even lateral displacements equal to $3t_r$ do not seem to cause any damage in the rubber-fiber interfaces. Such large critical values facilitate the utilization of UFREIs with small height, bearing in mind that commercial BFREIs typically exhibit critical lateral displacements equal to $1.5t_r$ [24][25].

In this paper, the UFREI system is implemented to base seismically isolate a historical masonry church loacted in the south part of Lombardia region, Northern Italy. The non-linear behavior of masonry is modeled as an isotropic material using the concrete damage plasticity (CDP) model that is available in the Abaqus standard package [26]. Although this is a simplified approach, the utilisation of CDP model is recommended in the literature for seismic analysis of large structures [27][28][29].

To increase the energy dissipation capacity of the isolation system, elastomeric isolators can be combined with shape memory alloy (SMA) wires according to specific configurations. SMA materials have a temperature-dependant behavior and are widely used for additional dissipative devices due to their superelastic effect and excellent recoverability under large strains. The utilisation of SMA materials for additional dissipative devices is reported in the literature: the combination of laminated high damping rubber bearings and SMA devices has been proposed to improve the seismic response of elevated highway bridges [30][31]. The SMA isolation system presents a stiff connection between the column and the deck under low seismic excitations. For high seismic actions, the system provides high damping and also acts as a displacement controlling device due to the hardening phase of the SMA. Experimental results reported in the literature [32] show that SMA dampers ensure a significantly better performance than typical steel devices. The NiTi-SMA presents an excellent recoverable elongation (about 8%), which is much larger than that (only 0.2%) of structural steel. In addition, durability tests show an excellent NiTi-SMA resistance against corrosion, which can be considered similar to that of stainless steel.

In this study, the combination of UFREIs and ferrous SMA wires is proposed and investigated for the seismic protection of a historical masonry church. In Section 2 a detailed 3D finite element (FE) model is developed and cyclic shear analyses are performed to characterize the behavior of UFREIs: the cyclic response of UFREIs is then reproduced by a simplified model developed by the authors. In Section 3 the behavior of SMA is simulated through a thermomechanical constitutive model implemented in a user subroutine (UMAT) available in the software package Abaqus. In Section 4 an Abaqus User Element (UEL) is proposed to represent the 3D behavior of UFREIs with SMA wires for large scale seismic analyses of complex isolated structures. In Section 5 the FE model of a historical masonry church with base isolation systems is developed. In Sections 6 and 7 the effectiveness of the isolation systems is then evaluated through non-linear dynamic analyses of the masonry church in the original and base-isolated configurations in terms of damage distribution, drifts and accelerations for two different seismic

intensity levels. Finally, Section 8 summarizes the main conclusions of this research work.

7.2. Numerical model of the unbonded fiber reinforced elastomeric isolator (UFREI)

Detailed 3D FE models are developed and cyclic shear FE analyses are performed through the software code Abaqus [26] to investigate the behavior of the UFREI. In the software code Abaqus, different types of hyperelastic material models are available and each model defines the strain energy function in a different way. In this study, the Yeoh hyperelastic material model is used to represent the properties of rubber, see Eq. 1, where W is the strain energy density, C_{i0} are material coefficients in MPa and I_1 is the first deviatoric strain invariant. The values of the material coefficients are assumed by referring to experimental studies reported in the literature [34]. The rubber considered in this study presents a shear modulus G equal to 0.4 MPa. Table 7.1 shows the values of the coefficients adopted for the Yeoh hyperelastic material model in the present FE simulations.

$$W = \sum_{i=1}^{3} C_{i0}(I_1 - 3)^i \qquad (1)$$

To characterize the damping behavior of rubber, the Prony-series model based on the viscoelastic generalized Maxwell model is used: it is a time-domain viscoelasticity available in Abaqus [26] to determine the time-dependent stress-strain relation, see Eq. 2. The generalized Maxwell model Fig. 7.1 represents the rheological model of the stress relaxation function G(t). The model is composed of a nonlinear elastic spring related to the hyperelastic part and a finite number of Maxwell elements (spring and dashpots) that describe the viscoelasticity [33]: G_∞ is the final or equilibrium modulus; G_k and η_k are the modulus and viscosity of the kth element, respectively; τ_k is the relaxation time defined as $\tau_k = \eta_k/G_k$. In Abaqus, the right hand side of Eq. 2 is applied: G_0 is the shear modulus at time t=0 and g_k is the dimensionless Prony coefficient. The parameters g_k and τ_k can be determined experimentally through relaxation test.
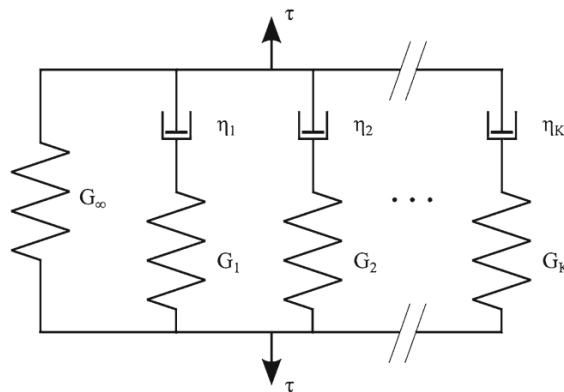

Fig. 7.1. Rheological model of the generalized Maxwell model.

$$G(t) = G_\infty + \sum_{k=1}^{K} G_k e^{-t/\tau_k} = G_0 \left[1 - \sum_{k=1}^{K} g_k\left(1 - e^{-t/\tau_k}\right)\right] \qquad (2)$$
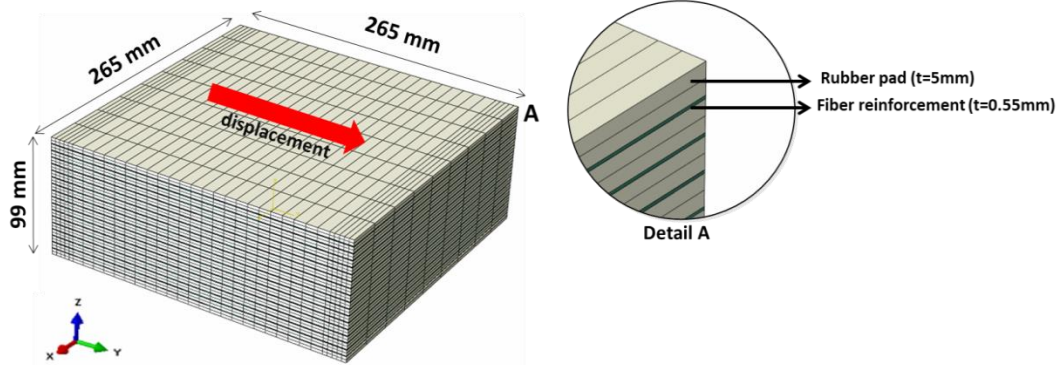

Fig. 7.2.Geometry and mesh of the FE model of the UFREI-265 with local detail.

For hyper-viscoelastic material models, the relaxation function G(t) in Eq. 2 is normally applied to the constant that describes the energy function [26]. Consequently, for the Yeoh hyperelastic model the relaxation form is given in Eq. 3.

$$C_{i0}^{R}(t) = C_{i0}^{0} \left[1 - \sum_{i=1}^{N} g_k\left(1 - e^{-\frac{t}{\tau_k}}\right)\right] \qquad (3)$$

The rubber considered in this study is a low-damping rubber, which is characterized by an equivalent damping ratio equal to about 3-5%. Table 7.2 shows the coefficients values of the Prony-series viscosity model adopted for rubber in this study: such coefficients values were obtained through short-term relaxation tests on low-damping rubber specimens.

The isolator investigated in this study uses bidirectional woven glass fibers as vertical reinforcement. The fibers are bonded to the rubber pads simply by using a polyurethane adhesive, as reported in the literature [12]. As already explained, the utilization of fibers may reduce the cost of the isolator when compared with steel laminas [13]. In the present numerical simulations, the glass fiber is assumed isotropic-elastic with Young modulus E_f equal to 40 GPa and Poisson's ratio equal to 0.2: it is considered perfectly bonded to the rubber pads, in accordance with some studies reported in the literature, [14][35].

Table 7.1. Coefficients of the Yeoh hyperelastic model for rubber UFREI-265 used in the numerical analyses.

C_{10}	C_{20}	C_{30}
0.21	0.0044	0.00013
C in Mpa		

Table 7.2. Coefficients of the Prony-series model for rubber UFREI-265 used in the numerical analyses.

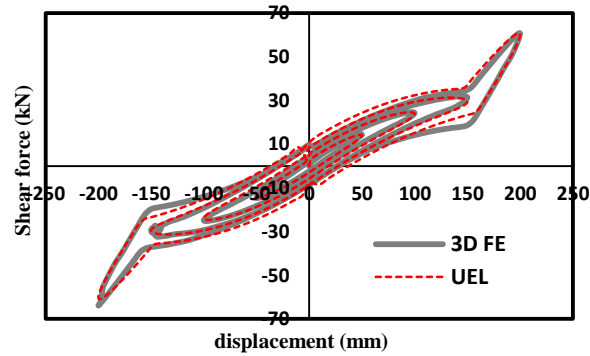| g_1	t_1	g_2	t_2
0.1	0.1	0.1	0.05

Fig. 7.3. Shear force – horizontal displacement curves of the UFREI-265 obtained through the 3D FE model and the simplified user element (UEL) model.
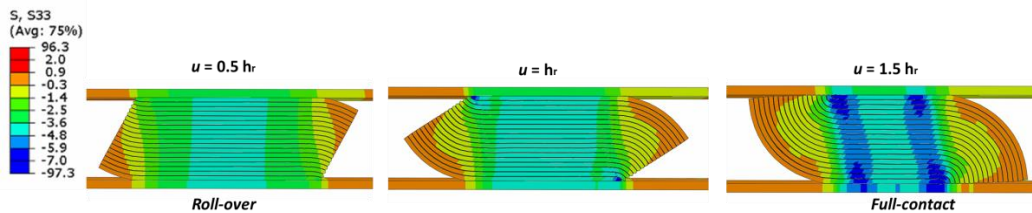

Fig. 7.4. Deformation patterns and vertical stress distribution of the UFREI-265 under constant vertical pressure.

Fig. 7.2 illustrates the FE model of the UFREI investigated in this study, denoted as UFREI-265, with indication of the main geometrical and mechanical characteristics: it consists of 18 square rubber pads that are 5 mm thick and 265 mm long, resulting in a shape factor (S) equal to 13.3. The thickness of the fiber reinforcement is equal to 0.55 mm: the total height (h_r) of the UFREI-265 is 99.35 mm.

The isolator is modelled using about 98000 eight-node brick elements with reduced integration (C3D8R): a perfect bond between rubber and fiber is adopted in the model. To obtain the unbounded system, no bonding is introduced between the rubber and the support. A penalty friction with coefficient μ=0.8 is applied: it corresponds to the friction between dry concrete and rubber [36].

A cyclic shear analysis with 0.75 Hz of frequency is conducted on the detailed 3D FE model of the UFREI up to lateral displacement equal to about $2h_r$, applying a constant vertical pressure equal to 2.5 MPa: such a pressure approximately corresponds to the load carried by a single isolator when inserted into the model of the masonry church that is analyzed in the following sections.

Fig. 7.3 presents the shear force - horizontal displacement curves of the UFREI-265 obtained through the 3D FE model (grey line). The UFREI shows an evident decrease of stiffness before a significant hardening occurs at displacements equal to about $u=1.5h_r$. The deformation patterns and vertical stress distribution of the UFREI during the shear test are presented in Fig. 7.4: roll-over and full-contact deformations can be observed at displacements equal to $u=0.5h_r$ and $u=1.5h_r$, respectively. During the roll-over deformation, a part of the rubber exhibits negligible stresses, generating a reduction of the lateral stiffness of the UFREI. Meanwhile, the full-contact phase triggers a significant hardening of the UFREI at large displacements.

For large scale seismic analyses of complex isolated structures, the use of detailed 3D FE models of isolators is very time-consuming because several isolator devices are generally inserted at the base of the building. Unfortunately, in the software code Abaqus there is no representative element available to model isolators in an effective way. Therefore, in this study an extended Abaqus User Element (UEL) is implemented to represent the 3D behavior of a single isolator UFREI with the aim of significantly reducing the computational effort in FE modeling and analysis, thus avoiding the use of a detailed 3D FE model for each single isolator. A detail discussion of the UEL model for UFREIs is reported in a previous work by the same authors [37].

The proposed UEL is in the form of a beam element, characterized by 12 degrees of freedom (DOF), which is able to capture the 3D behavior of a single isolator. The UEL takes into account the coupling behavior between two orthogonal displacements and between vertical stiffness and displacements. The UEL developed for a single UFREI along with the corresponding DOFs are shown in Fig. 7.5. Fig. 7.3 shows the comparative shear force-displacement curves of the UFREI-265 obtained from the detailed 3D FE and UEL models: a very good fitting of the UEL model against the 3D FE model can be observed.
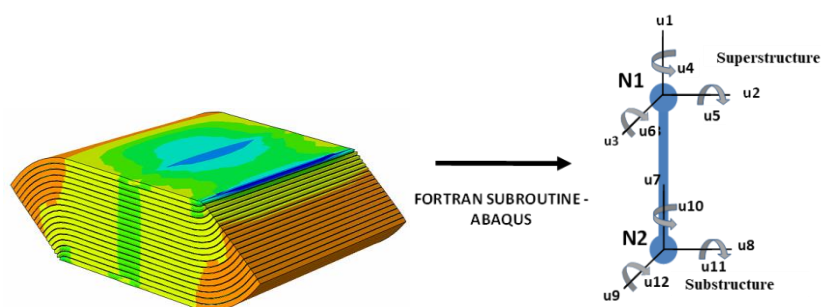

Fig. 7.5. Representative Abaqus user element (UEL) for a single UFREI.

7.3. Numerical model of the shape memory alloy (SMA)

The application of shape memory alloy (SMA) for seismic protection purposes has been introduced in recent decades. Thanks to its superelasticity and excellent

strain recovery, SMA materials are often used in combination with elastomeric bearings to improve the dissipation energy capacity of the isolation system.

The behavior of typical SMA materials is plotted in terms of strain-stress-temperature relationship in Fig. 7.6. SMA presents two solid phases: the martensite phase when the material is at temperature T below the martensite finishing temperature M_f; and the austenite phase at T above the austenite finishing temperature A_f [32][38]. They introduce the unique physical properties known as shape memory effect and superelastic effect, respectively. The shape memory effect can be described as the ability to regain its initial shape upon heating, while the superelasticity indicates the ability to recover its initial shape from large deformations just after the unloading step. The superelastic behavior of an SMA takes place only when the material is strained above the austenite finish temperature (A_f) and if the strain is lower than the maximum superelastic strain ε_s. Such a superelastic behavior becomes the basic of the SMA application for a additional seismic protection devices to improve the recentering capability.
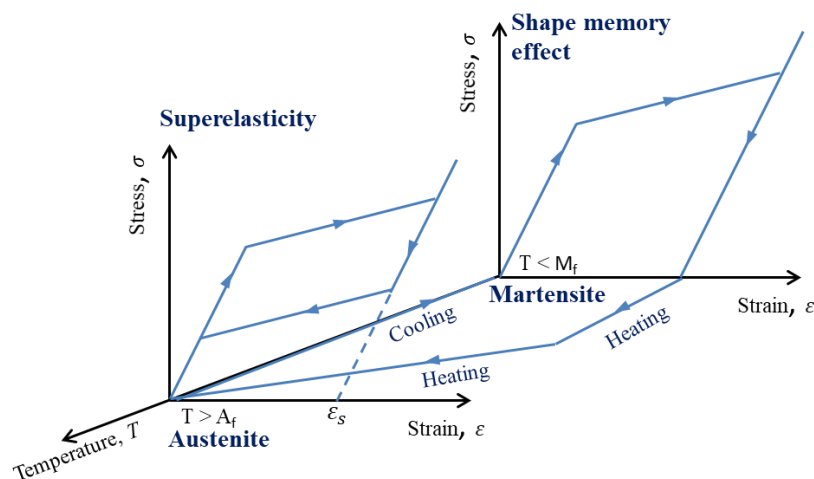

Fig. 7.6. A typical temperature-dependant superelasticity and shape memory behavior of SMA materials.

The cost of the SMA materials, such as NiTi-SMA, is commonly high because both nickel and titanium are expensive. Therefore, in this study the material considered for the isolation system is the ferrous alloy, FeNiCuAlTaB (FeTB), which has lower costs than Ni-TI, as reported in the literature [31]. Compared to other popular SMA materials for seismic devices, see Table 7.3, FeTB-SMA has the largest superelastic strain ε_s (13.5%) and maximum strain ε_{max} (15%), as well as a moderate Young modulus, E_A. Another beneficial feature of the FeTB-SMA is the very low austenite finish temperature A_f, about -62°C, which allows for an optimal performance even in extreme winter conditions. The stress-strain curve of the FeTB-SMA obtained from an experimental test at room temperature is presented in Fig. 7.7, [43]. In this study, the behavior of the FeTB SMA (hereinafter referred also to SMA) is evaluated using the thermomechanical constitutive model for SMA presented by Lagoudas et al. [39]: such a model is implemented in the user-defined

material (UMAT) subroutine for SMA that is available in Abaqus environment [40]. Table 7.4 presents the values of some material parameters for FeTB SMA implemented in Lagoudas model. Fig. 7.7 shows a good agreement between experimental and numerical results in terms of stress-strain curves obtained at room temperature.

Table 7.3. Mechanical properties of some well-known SMA materials for dissipative devices.

SMA	$\varepsilon_{max\ (\%)}$	$\varepsilon_{s\ (\%)}$	E_A (GPa)	A_f (°C)	Reference
NiTi$_{45}$	6.8	6.0	62.5	-10.0	[41]
CuAlBe	3.0	2.4	32.0	-65.0	[42]
FeTB	15.0	13.5	46.9	-62.0	[43]
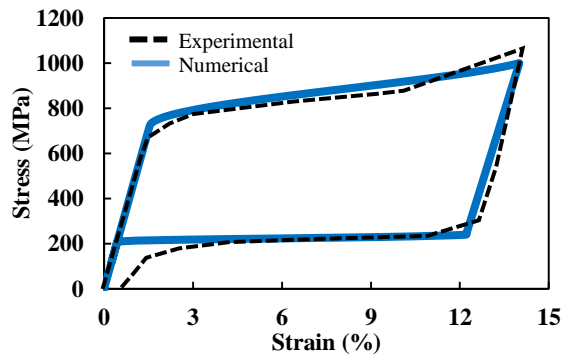
Fig. 7.7. Stress-strain curve of the FeTB SMA wire obtained at room temperature: experimental and numerical results.

Table 7.4. Values adopted for some material parameters of FeTB SMA in Lagoudas model.

Material Parameter	Value
Elastic stiffness of the austenite E^A	46.9 GPa
Elastic stiffness of the martensite E^M	42 GPa
Martensitic start temperature M^s	187 K
Austenitic finish temperature A^f	211 K
Maximum transformation strain H	0.135

7.4. Hybrid isolation system using UFREIs and SMA-wires

In the present work, a combination of unbonded fiber reinforced elastomeric isolators (UFREIs) and SMA-wires is proposed to isolate a historical masonry church. The SMA wire should be arranged in order to satisfy the permitted maximum strain of the wire under horizontal displacements of the isolation system. Therefore, a straight wire configuration with frictionless steel hooks is adopted in the proposed system, as recommended in the literature [31], see Fig. 7.8. Due to the arrangement of the frictionless steel hooks, a strain imposed in the wire can be uniformly

distributed along all the length of the wire. In addition, flange supports are required to facilitate the deformation of the SMA wire in the two orthogonal directions without being in contact with the support beam or foundation, which may lead to a failure of the SMA wire.
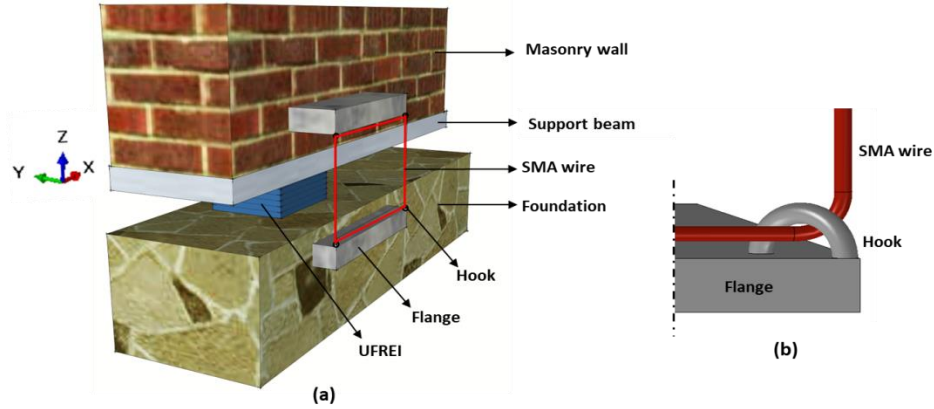

Fig. 7.8. (a) Arrangement of the combination of UFREI and SMA wire in the isolation system (UFREI-SMA) of masonry structures. (b) Detail of the hook and SMA wire.

In reality, a frictional force is generated between the wire and the hook in correspondence with the contact area. In such a situation, the relative displacement between the wire and the hook will be limited, or even negligible in the worst case. Therefore, further experimental investigations are required to obtain a proper design of the SMA wire system.

As seen in Fig. 7.9, the side length of an SMA wire s is set equal to 300 mm to satisfy the maximum strain of the SMA wire (15%) undergoing a displacement up to 2 h_r. The current total length l_t and strain ε of the wire as a function of isolator displacement u can be computed using Eq. 1 and Eq. 2: such equations apply also for the displacement in the orthogonal direction.

$$l_t = 2\left(s + \left(\sqrt{u^2 + s^2}\right)\right) \quad (1)$$

$$\varepsilon = (l_t - 4s)/4s \quad (2)$$

Fig. 7.10 shows the imposed strain on the SMA wires (with different lengths s) as a function of the isolator displacement. It is found that the SMA wire with a length equal to s=300 mm satisfies the maximum FeTB SMA strain (15%). The diameter of the wire is set equal to 4.5 mm so that the ratio between the lateral stiffness of the SMA wire and that of the UFREI is about 0.2 at the design displacement equal to $2h_r$.

Fig. 7.9. (a) Undeformed shape of the SMA-wire device; (b) deformed shape of the SMA-wire device subjected to horizontal displacement.
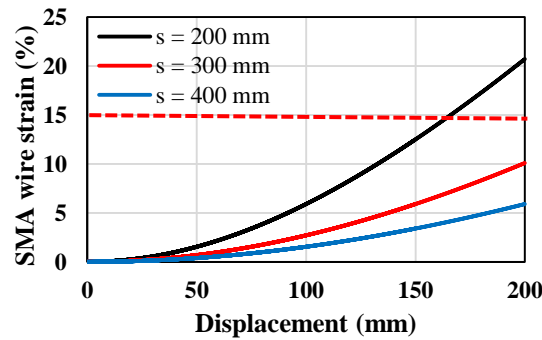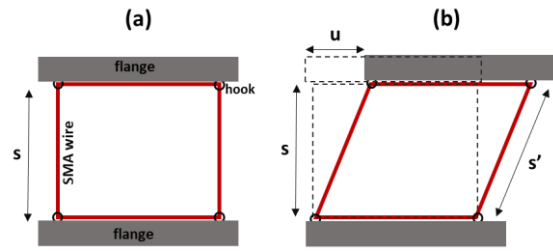

Fig. 7.10. Strain of the SMA-wire device with different lengths as a function of the isolator displacement.

In order to optimize the performance of the SMA-wire, some amount of pre-strain can be applied into the wire, as recommended in the literature [31]. This method can favorably shift the behavior of the SMA material, as seen in Fig. 7.11a, so that the stiffness of the pre-strained SMA wire can be significantly decreased, while the energy dissipation (area inside the hysteretic loop) remains the same, see Fig. 7.11b.
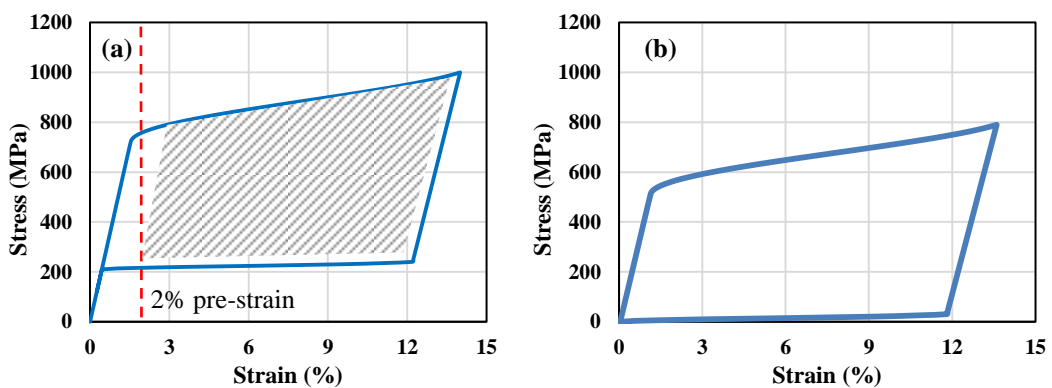
Fig. 7.11. (a) Stress-strain curve of the SMA wire with indication of pre-strain equal to 2%; (b) stress-strain curve of the SMA wire after a pre-strain equal to 2%.
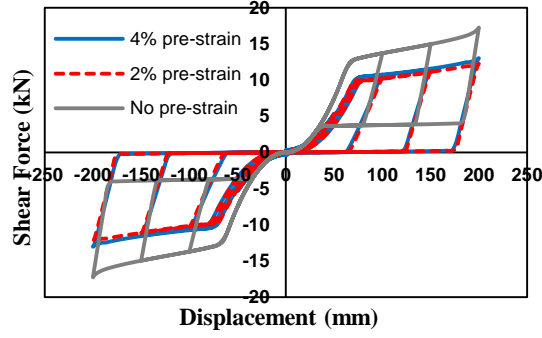
Fig. 7.12. Shear force – horizontal displacement curves of the SMA wire device with different values of pre-strain.

In order to investigate the effects of pre-strain amount on the SMA wire in the configuration described in Fig. 7.8, the shear force - horizontal displacement curves of the SMA wire (without and with a pre-strain equal to 2% and 4%) under cyclic displacements are shown in Fig. 7.12. The model with pre-strain shows a clear advantage as the effective stiffness of the SMA wire decreases, maintaining the large period of the isolation system. It can be noted that there is only a negligible difference between the models with a pre-strain equal to 2% and 4%: a pre-strain equal to 2% is then chosen for the UFREI-SMA isolation system.

The shear force-displacement curves of the SMA wire device presented in Fig. 7.12 are then combined with the shear force-displacement curve of the UFREI obtained through the 3D FE analysis in Fig. 7.3. The combined curves are shown in Fig. 7.14: UFREI is the model without SMA-wire, UFREI-SMA is the combination of UFREI and SMA wire without pre-straining, and UFREI-SMA-P2% is the combination of UFREI and SMA wire with a pre-strain equal to 2%.

Table 7.5 shows the performance of the three proposed isolation systems at different displacement magnitudes u, in terms of horizontal stiffness, damping ratio and energy dissipation. In Table 7.5, h_r is the total height of the bearing and Δ represents the percentage difference between the UFREI-SMA models and the UFREI model. The computation of the effective horizontal stiffness $K_{H,eff}$ and damping ratio ξ is based on Eqs. (6)-(9) [44].

$$K_{H,eff} = (F_{max} - F_{min})/(\Delta_{max} - \Delta_{min}) \qquad (6)$$

$$\xi = W_d/(4\pi W_s) \qquad (7)$$

$$W_s = \frac{1}{2}K_{h,eff}\,\Delta^2{}_{max,ave} \qquad (8)$$

$$\Delta^2{}_{max,ave} = (\Delta_{max} + |\Delta_{min}|)/2 \qquad (9)$$

where F_{max}, F_{min}, Δ_{max} and Δ_{min} are the peak values of the horizontal force and displacement, respectively, W_d represents the dissipated energy (area within the loop) and W_s is the restored energy, see Fig. 7.13.
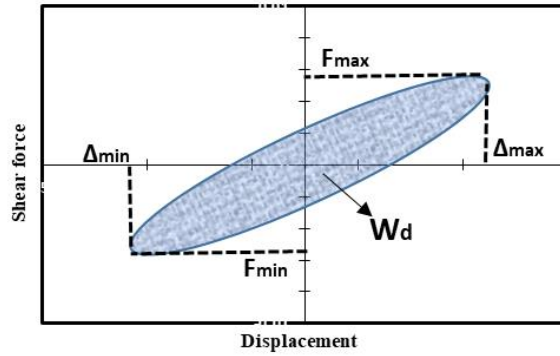
Fig. 7.13. Some notations for the calculation of isolator performances.
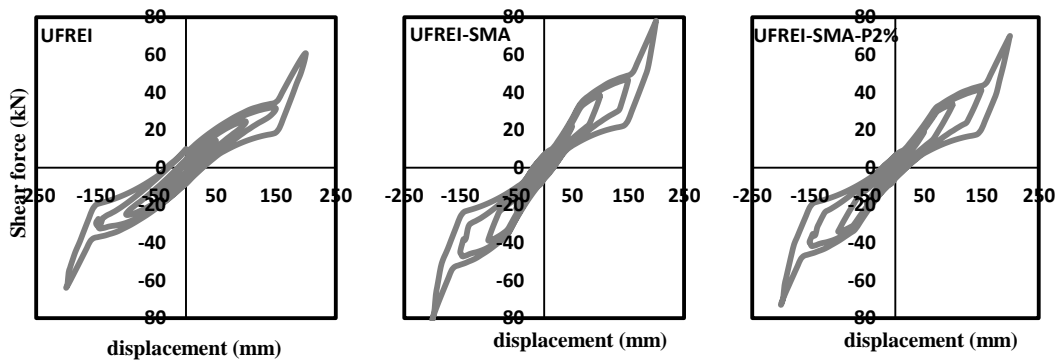

Fig. 7.14. Shear force – horizontal displacement curves obtained from 3D FE models of the three isolators under study.

The two UFREI-SMA models present significantly larger energy dissipation capacity, with an increase up to 78% compared to the UFREI model. However, the two UFREI-SMA models are characterized by higher stiffness: the application of a pre-strain equal to 2% can favorably reduce the stiffness of the hybrid isolation, as seen for the UFREI-SMA-P2% model.

As a consequence of higher stiffness, the damping ratio of the UFREI-SMA model may decrease, particularly at low displacements ($0.5h_r$ and h_r), when the SMA wire does not reach its yield strain yet. The application of a pre-strain equal to 2%, however, can decrease such a damping reduction, from 11.90% to 8.32% at $u=0.5h_r$. The SMA-wire contributes to the increase of the damping ratio at high displacements, $1.5h_r$ and $2h_r$. Significant increases of damping ratio (15% and 24.6% for the UFREI-SMA and UFREI-SMA-P2% models, respectively) are observed at displacements equal to $u=2h_r$.

Table 7.5. Comparative stiffness, damping ratio and energy dissipation of the three isolators obtained from 3D FE models.

u (h_r)	UFREI			UFREI-SMA						UFREI-SMA-P2%					
	k_H	ξ	W_d	k_H	$\Delta(\%)$	ξ	$\Delta(\%)$	W_d	$\Delta(\%)$	k_H	$\Delta(\%)$	ξ	$\Delta(\%)$	W_d	$\Delta(\%)$
0.5	0.29	5.58	0.19	0.44	50.88	4.92	-11.90	0.50	0.19	0.38	30.03	5.12	-8.32	0.19	0.00
1.0	0.25	7.28	0.93	0.39	54.80	6.94	-4.65	1.64	75.94	0.34	36.34	7.09	-2.59	1.56	67.41
1.5	0.21	8.39	2.28	0.31	46.24	9.16	9.21	4.06	78.32	0.28	30.64	9.72	15.83	3.92	72.19
2.0	0.31	6.26	4.27	0.40	27.63	7.20	15.01	7.20	68.48	0.36	15.37	7.80	24.61	7.22	68.81

Units: k_H [kN/mm] ; ξ [%] ; W_d [kJ]

To perform dynamic time-history analyses of isolated structures through the FE software code Abaqus, a simplified user element (UEL) for unbounded isolation systems is proposed and implemented to reproduce the behavior of the isolators [37]. The hysteresis model implemented in the UEL is based on the Bouc-Wen model that is governed by Eqs. (10)-(11) [45][46]: k is the horizontal stiffness in function of horizontal displacement u; c_d is the viscous damping coefficient; w, Y, γ, A and β are the Bouc–Wen coefficients controlling the shape of the hysteretic loop. The variable z is a non-physical parameter governing the isolator hysteretic loop based on the differential equation, Eq. (11). To solve numerically the Bouc-Wen equation, a standard Newton–Raphson procedure is executed.

$$F = k(u).u + c_d.\dot{u} + w.z \qquad (10)$$
$$Y\dot{z} = [A - z^2(\gamma.sign(\dot{u}z) + \beta)].\dot{u} \qquad (11)$$

A schematic representation of the shear force – horizontal displacement curves for UFREIs and SMA wires under study is shown in Fig. 7.15.

The UFREI isolator presents a non-linear behavior characterized by the stiffness k that is a function of the isolator displacement $\bar{u}$ due to the roll-over deformation; then, the hardening phase is governed by the stiffness k_{hd} due to the full-contact occurring at the displacement u_{hd}. The variation of stiffness k in the roll-over phase is governed by Eqs. (12)-(16).

$$A_r = b \cdot l_t \qquad (12)$$

$$l_t = l_0 - (|\bar{u}| \cdot m_l) \qquad (13)$$

$$k = G \cdot A_r \cdot \frac{\left(1 - \left(\frac{P_L}{P_{cr}}\right)^2\right)}{t_r} \qquad (14)$$

$$P_e = \pi^2 \cdot \frac{EI_{eff}}{t_r^2} \qquad (15)$$

$$P_{cr} = 2 \cdot \frac{P_e}{1 + \sqrt{\left(1 + 4\pi^2 \left(\frac{EI_{eff}}{G \cdot A_r \cdot t_r^2}\right)\right)}} \quad (16)$$

The main parameters are indicated in Fig. 7.16: A_r is the bearing area; b and l_0 are the sides lengths of a rectangular bearing (in 2D analyses, l_0 corresponds to the side parallel to the horizontal displacement); l_t is the effective length; u is the horizontal displacement; m_l is the modification factor to partially involve the effect of the free-stress zone; P_L is the applied vertical load; P_{cr} is the critical load; EI_{eff} is the effective flexural rigidity of the isolator; G is the shear modulus of rubber; t_r is the total thickness of the rubbers. The stiffness k_{hd} in the hardening phase is considered constant. Detailed explanations and validations of such expressions can be found in a previous work by the same authors [37]. The hysteresis loop of the UFREI is governed by the viscous damping coefficient c_d.

On the other hand, the SMA wire device is characterized by the bilinear stiffness k_1 and k_2, see Fig. 7.15, while the hysteresis loop is governed by the Bouc-Wen model (Eqs. (7)-(8)). Two different constants (w_1 and w_2) are introduced in order to capture the enlargement of the hysteresis loop at displacement u_y.
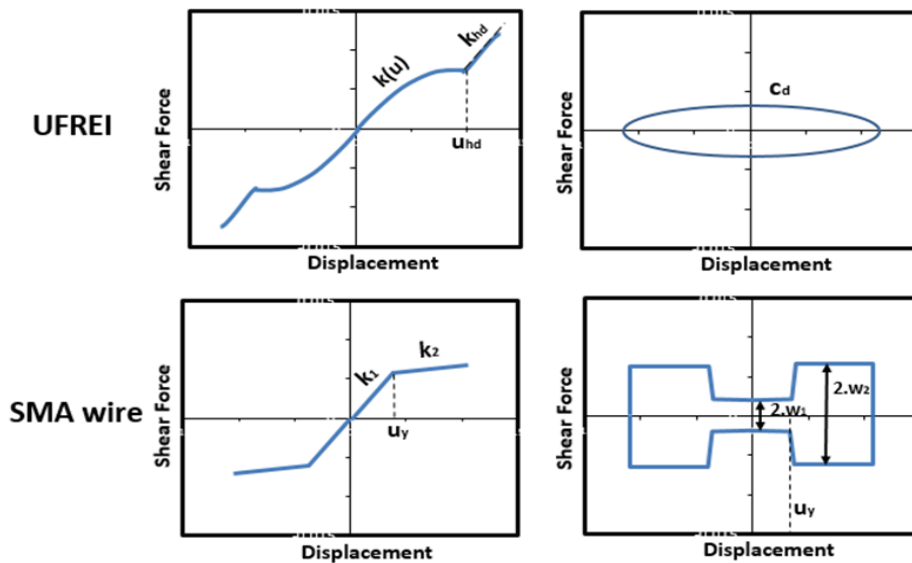

Fig. 7.15. Schematic representation of the shear force – horizontal displacement curves for UFREIs and SMA wires.
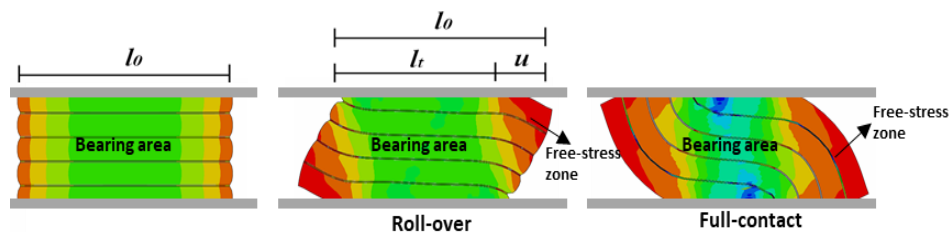

Fig. 7.16. Schematic representation of the deformed shapes of a typical UFREI undergoing shear displacement and indication of the parameters used in the UEL model.

Table 7.6 presents the parameters adopted in the UEL model for the three proposed isolators. Since all the three isolators use an identical UFREI device, the values of the parameters related to the UFREI (m_l, u_{hd}, k_{hd}, c_d) are equal. The coefficient of m_l is set equal to 0.75, which means that approximately 25% of the free-stress zone contributes to the horizontal stiffness of the UFREI, see Fig. 7.16. For the UFREI-SMA and UFREI-SMA-P2% models, the remarkable differences are related to the values of k_1 and u_y due to the pre-strain application. Moreover, the values of the Bouc-Wen coefficients are assumed equal because the hysteresis loop shapes are not significantly different.

Table 7.6. Values of the parameters used in the UEL model for the proposed isolators under study.

Isolators	m_l	u_{hd}	k_{hd}	c_d (kN.s/mm)	k_1	k_2	u_y	w_1	w_2	A	n	β	Y	γ
	(-)	(h_r)	(kN/mm)	)	(kN/mm)	(kN/mm)	(h_r)	(kN)	(kN)	(-)	(-)	(-)	(-)	(-)
UFREI	0.75	1.5	0.48	10.5	-	-	-	-	-	-	-	-	-	-
UFREI-SMA	0.75	1.5	0.48	10.5	0.155	0.025	0.5	0	3.65	1	1	0.15	0.005	0.45
UFREI-SMA-P2%	0.75	1.5	0.48	10.5	0.135	0.025	0.2	0	3.65	1	1	0.15	0.005	0.45

Fig. 7.17 shows the comparative shear force-displacement curves between the 3D FE and UEL models of the UFREI and the two UFREI-SMA systems. Table 7.7 quantifies the comparisons between the 3D FE and UEL models in terms of effective horizontal stiffness ($K_{h,eff}$) and damping ratio (ξ) for each cycle. An excellent performance of the UEL models can be observed: the percentage difference (Δ) with the 3D FE models are on average less than 10%. The utilization of the UEL model in seismic analyses of isolated structures significantly reduces the computational effort rather than using a 3D detailed FE model for a single isolator.
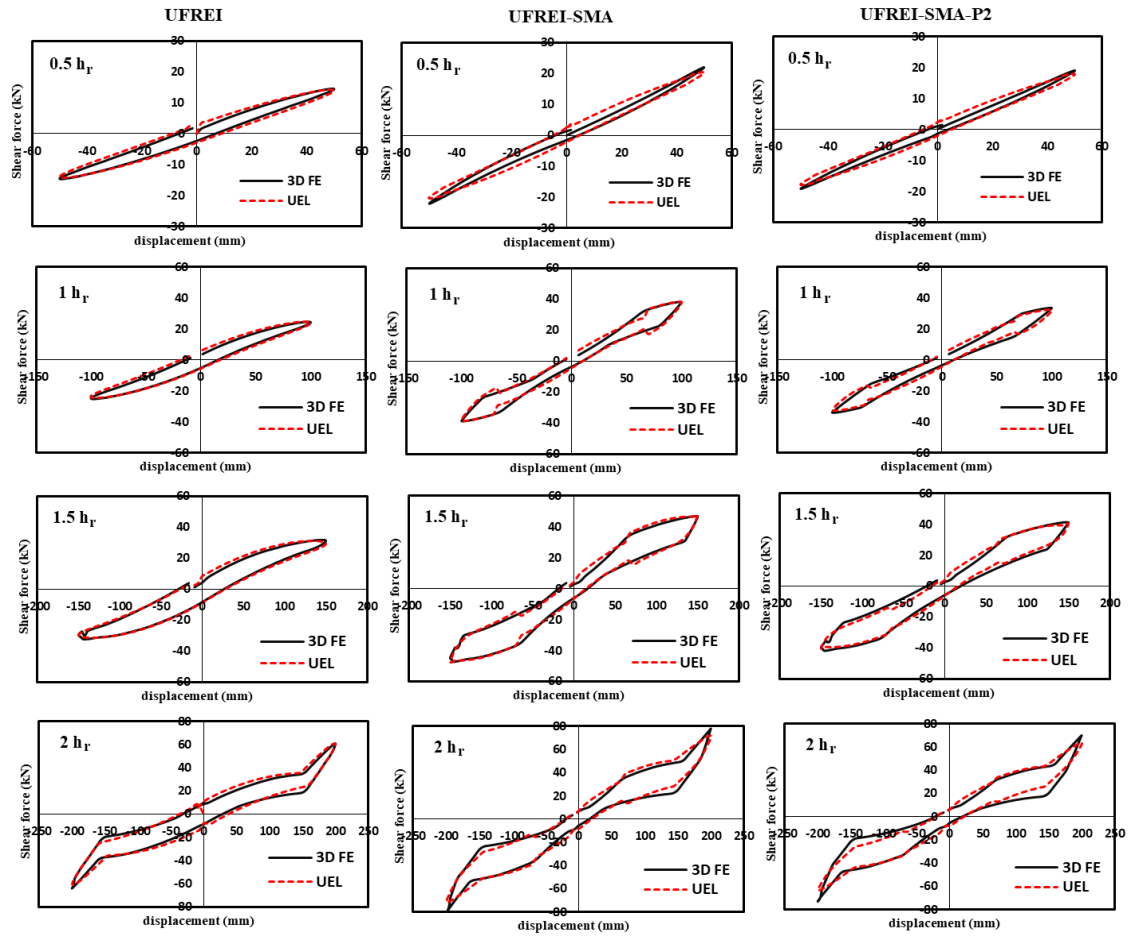
Fig. 7.17. Comparative shear force – horizontal displacement curves of the three isolators obtained from 3D FE and UEL models.

Table 7.7. Comparative stiffness and damping ratio of the three isolators obtained from 3D FE and UEL models.

	UFREI						UFREI-SMA						UFREI-SMA-P2%					
	kH (kN/mm)			ξ (%)			kH (kN/mm)			ξ (%)			kH (kN/mm)			ξ (%)		
u (hr)	3D FE	UEL	Δ(%)	3D-FE	UEL	Δ(%)	3D FE	UEL	Δ(%)	3D-FE	UEL	Δ(%)	3D FE	UEL	Δ(%)	3D-FE	UEL	Δ(%)
0.5	0.29	0.28	2.8	5.58	5.79	-3.7	0.44	0.41	7.7	4.92	5.28	-7.3	0.38	0.36	5.7	5.12	5.67	-10.7
1.0	0.25	0.24	2.2	7.28	6.88	5.5	0.39	0.38	0.4	6.94	7.78	-12.1	0.34	0.32	4.2	7.09	7.97	-12.4
1.5	0.21	0.20	4.8	8.39	7.40	11.8	0.31	0.32	-1.3	9.16	9.85	-7.4	0.28	0.27	2.0	9.72	9.55	1.7
2.0	0.31	0.30	2.4	6.26	5.63	10.1	0.40	0.36	9.9	7.20	7.93	-10.2	0.36	0.32	11.0	7.80	7.97	-2.2

7.5. Seismic isolation of a historical masonry church using UFREI-SMA

A historical masonry church located in the south part of Lombardia region, Northern Italy, is considered in this work to evaluate the performance of the proposed isolation systems. The geometry of the church is schematically illustrated in Fig. 7.18. The church, which is about 20.6 m long and 10.8 m wide, consists of a central nave, two small aisles and lateral chapels. The central nave, which is covered

by a barrel vault, is connected to the aisles through two large arches in correspondence with 15 the chapels and three small arches. Two openings are present in the upper part of the nave walls, while the aisles walls exhibit rectangular windows. The façade presents a triangular tympanum and is 11 m high. The presbytery, which is about 8 m long and 4.2 m wide, ends with a semicircular apse covered by a masonry semi-dome. A door, a rectangular window and a small circular opening are present on each side of the choir: the apse exhibits two small openings in the bottom part. The bell tower, which is located on the right side of the church, is 17.5 m high and presents four large openings in the upper part..

The seismic assessment of the isolated masonry church is performed thorugh non-linear dynamic time-history analyses. A 3D FE model of the church is created through the software code Abaqus, without and with base isolation. Masonry is considered as a homogenous isotropic material and is modeled in Abaqus using the Concrete Damage Plasticity (CDP) model: the main properties are presented in Table 7.8, according to previous works [4][11]. The uniaxial compressive and tensile strain-stress curves for masonry are presented in Fig. 7.19. The compressive and tensile strength are 2.4 MPa and 0.1 MPa, respectively. A fine meshing is applied to the masonry structure using about 220000 four-node tetrahedron elements (C3D4), as shown in Fig. 7.20: the average size of each element is about 20 cm.
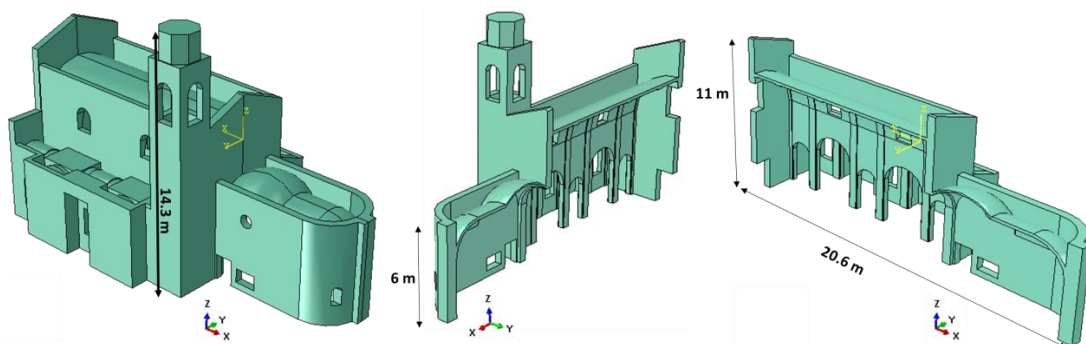

Fig. 7.18. Geometrical model and main dimensions of the church under study.

Table 7.8. Values of the parameters used for the CDP model in the numerical analyses.

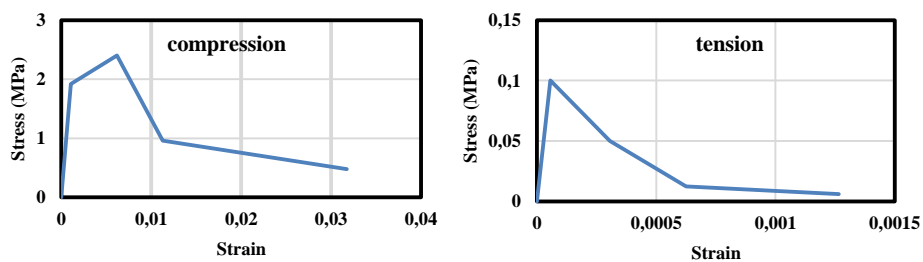| E (MPa)	v	Dilation angle	Eccentricity	σ_{b0}/σ_{c0}	K_c	Viscosity
1800	0.2	10	0.1	1.16	0.667	0.002

Fig. 7.19. Uniaxial stress-strain curves adopted for masonry in compression and tension.

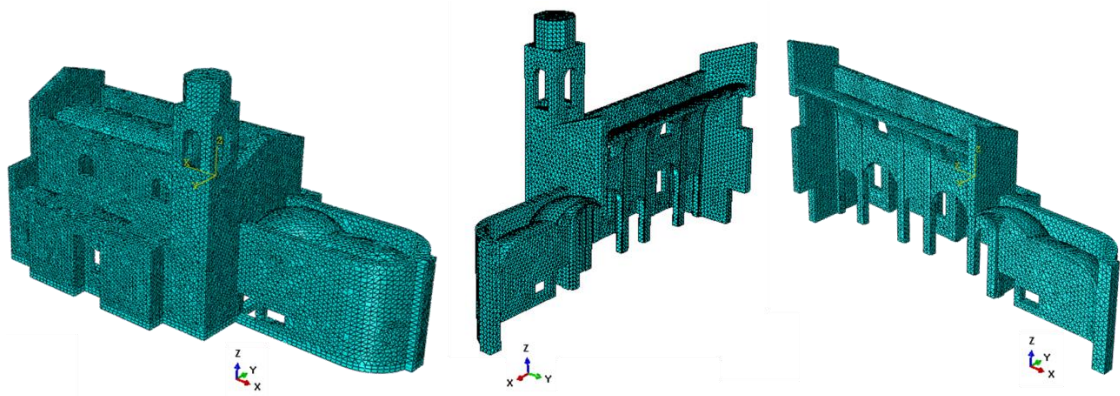Fig. 7.20. FE model of the church under study.

UFREI 265 x 265 x 100

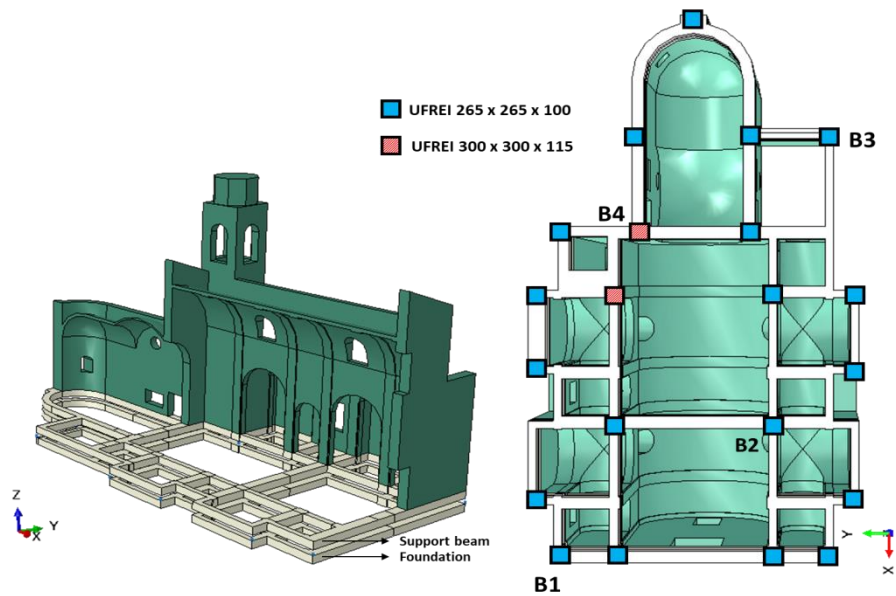UFREI 300 x 300 x 115

Support beam
Foundation

Fig. 7.21. Left: Geometrical model of the church with isolation system. Right: Arrangement of different UFREI isolators at the base of the church.

Fig. 7.21 shows the arrangement of the UFREIs in the isolation system of the masonry church. It can be noted that nineteen UFREI-265 isolators are used at the base of the structure: in addition, two larger UFREI-300 isolators are employed to carry the considerable weight of the tower. For the sake of conciseness, it is worth mentioning that the analysis of the UFREI-300 is not included in this paper because the procedure is similar and the horizontal stiffness is only slightly different. The target design period of the hybrid isolation system is set equal to 1.5 s at the design displacement equal to 2 h_r (h_r is the height of the bearing). In addition, a check should be made to ensure that the vertical load carried by a single bearing (UFREIs are subjected to a vertical stress varying from 2 MPa to 3 MPa) is smaller than the UFREI axial load capacity. The width of the support beam and foundation is set equal to 50 cm to accommodate the displacement of the UFREIs up to $2h_r$. In the case of hybrid isolation system, each UFREI is equipped with a SMA wire, as

illustrated in Fig. 7.8. The reference isolators (denoted as B1-B4) that are monitored in the numerical simulations are indicated in Fig. 19.

Non-linear dynamic time history analyses are performed considering the following different models: (1) fixed-base (FB) model; (2) UFREI model; (3) UFREI-SMA model; (4) UFREI-SMA-P2% (with a pre-strain equal to 2% imposed on the SMA wires) model. The effectiveness of the proposed isolation systems is evaluated considering two levels (PGA) of seismic actions.

A preliminary assessment of the dynamic behavior of the church models is carried out through modal analyses. Fig. 7.22 shows the first four vibration modes and the corresponding periods of the masonry church in the different configurations (fixed-base (FB) model and models (BI) with different isolation systems). In the fixed-base (FB) model, the first vibration modes involve mainly the tower as well as the nave and aisles of the church: conversely, the first vibration modes of the base isolated (BI) models concern the isolation system. The application of UFREIs significantly increases the fundamental period from T=0.225 s to T=1.685 s, considerably reducing the seismic demand on the church. The addition of SMA wires in the isolation system decreases the fundamental period to T=1.488 s, as a consequence of the higher stiffness when compared with the UFREI model. The application of a pre-strain equal to 2% in the SMA wires shifts the fundamental period to T=1.538 s.
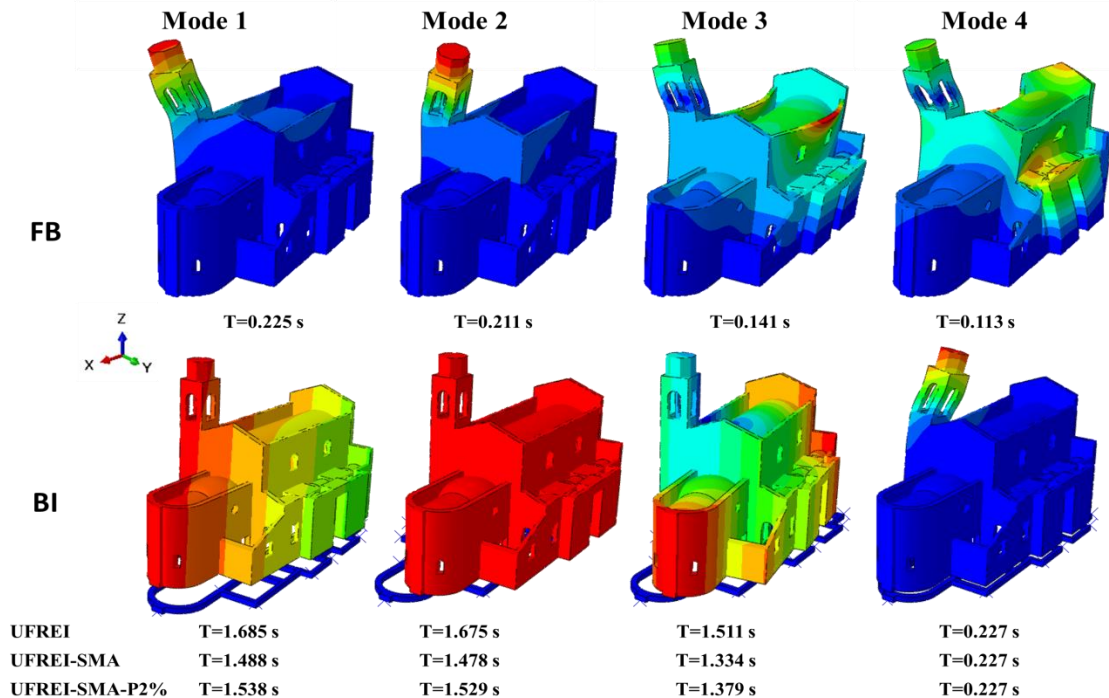

Fig. 7.22. First four vibration modes and corresponding periods of the masonry church in FB and BI models.

7.6. Non-linear dynamic analysis with PGA=0.15g

The seismic response of the church in the different configurations was studied through non-linear dynamic analyses using an artificial accelerogram generated through the software code Simqke (SIMQKE 1976) in order to match the Eurocode 8 response spectrum (soil type C). Fig. 7.23 shows the acceleration time histories with PGA=0.15g applied in the longitudinal (X) and transversal (Y) directions. The last 10 seconds of the acceleration time histories were added to observe the behavior of the proposed isolation system at the end of the earthquake loading.

Fig. 7.24 shows the tensile damage contour plots for the fixed-base (FB) model and the base isolated models at different time instants during the non-linear dynamic analyses with PGA=0.15g. The first cracks are registered in the coverings and in the connection region between the tower and the church. At the end of the analysis, severe damage is observed in the FB model, especially in the barrel vault of the nave and along the body of the tower. The application of UFREIs considerably reduces the damage in the church, above all in the barrel vault of the nave. It can be noted that in the UFREI-SMA model damage is slightly more widespread than in the UFREI model: such a result is mainly due to the higher stiffness of the UFREI-SMA isolation system. However, it is important to observe that the application of a pre-strain equal to 2% (UFREI-SMA-P2% model) can overcome such a problem, slightly reducing damage in the church when compared with the UFREI-SMA model.
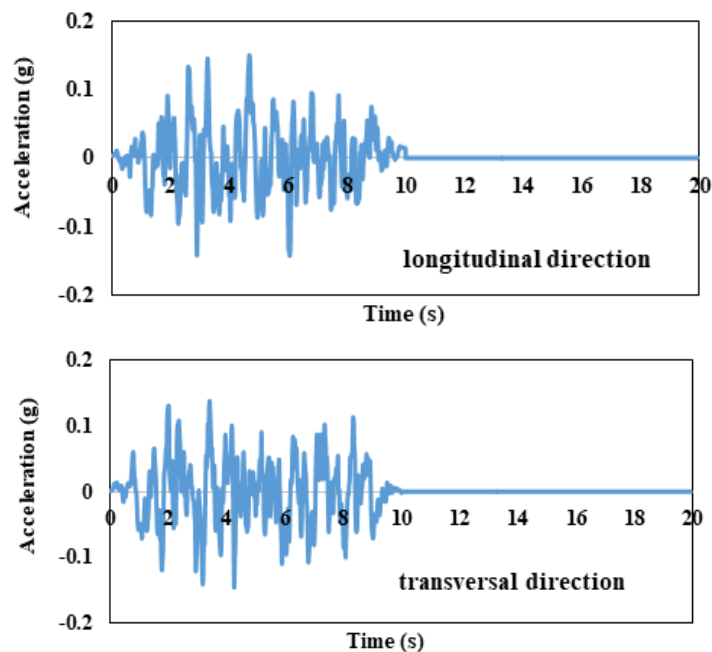

Fig. 7.23. Acceleration time histories (PGA=0.15g) used in the numerical simulations.
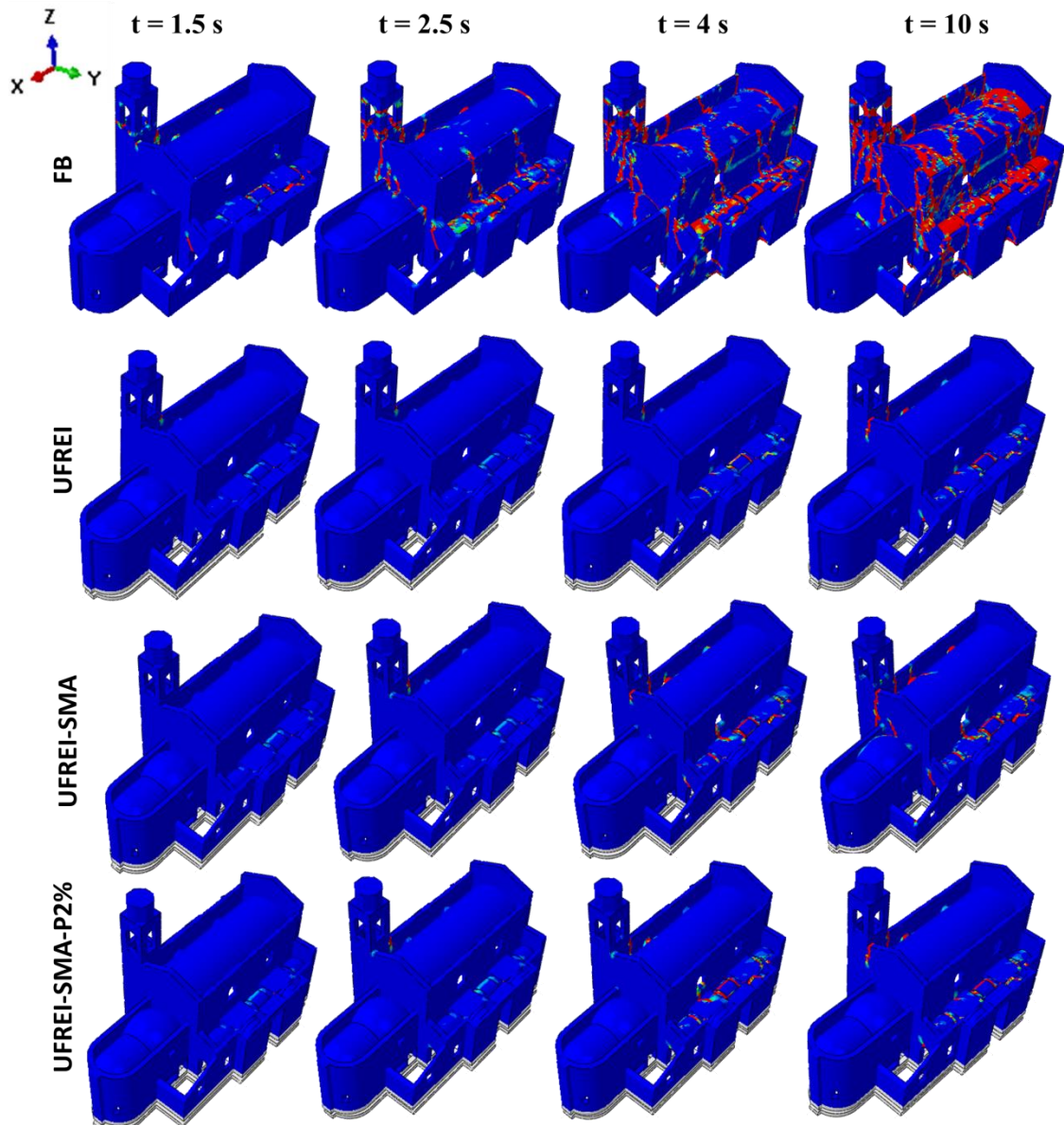
Fig. 7.24. Tensile damage contour plots for the fixed-base (FB) model and the base isolated (UFREI, UFREI-SMA, UFREI-SMA-P2%) models at different time instants during the non-linear dynamic analyses with PGA=0.15g.

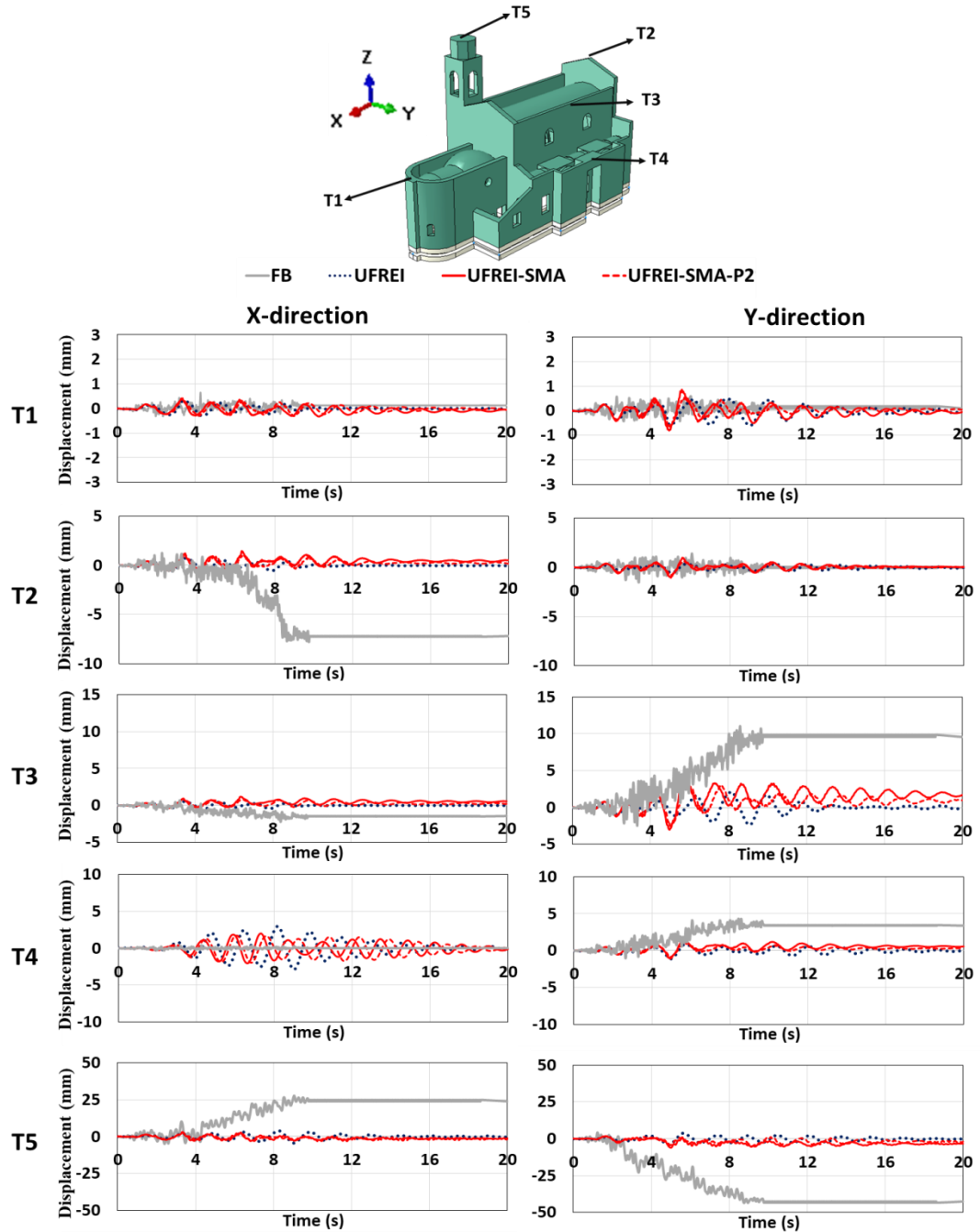Fig. 7.25 presents the displacement time history of five reference points in the longitudinal (X) and transversal (Y) directions obtained from non-linear dynamic analyses with PGA=0.15g for the fixed-base (FB) model and the base isolated (UFREI, UFREI-SMA, UFREI-SMA-P2%) models. Very large residual displacements are registered in the fixed-base (FB) model, for the façade in the longitudinal direction and the nave and the external walls in the transversal direction. As expected, the largest displacements are computed at the top of the masonry tower in both the directions. No significant displacements are observed for the apse (reference point T1) that is characterized by a thick and short masonry wall. All the base isolated models present a significant reduction of the displacements with negligible residual displacements when compared with the fixed-base model.

The difference in terms of peak drifts (defined as the ratio between the horizontal displacement at the top of the macro element and its corresponding height) of the reference points among the base isolated models can be seen more clearly in Fig. 7.26. It can be noted that smaller displacements are registered for the UFREI model than for the two other base isolated models, except for reference point T4. Such a result may indicate that the utilization of the SMA wires is not effective in terms of drift reduction for such earthquake levels. In any case, the application of a pre-strain equal to 2% can slightly decrease the peak drifts of the different macro-elements, as evidenced form the comparison with the UFREI-SMA model without pre-straining.

Fig. 7.25. Displacement time history of different reference points in the longitudinal (X) and transversal (Y) directions obtained from non-linear dynamic analyses with PGA=0.15g for the fixed-base (FB) model and the base isolated (UFREI, UFREI-SMA, UFREI-SMA-P2%) models.
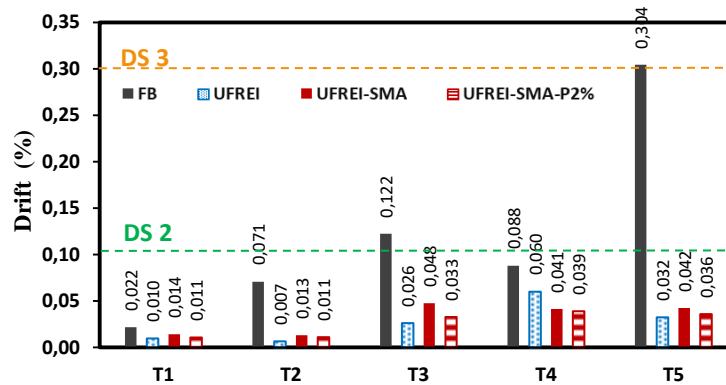
Fig. 7.26. Peak drifts registered for some reference points of the different church models during the non-linear dynamic analyses with PGA=0.15g.

The threshold values of drifts reported in the literature for masonry structures [47] are used to classify the damage state (DS) of the masonry church under study. A drift value smaller than 0.1% represents no or slight damage (DS1); a drift value between 0.1% and 0.3% corresponds to moderate damage (DS2); a drift value between 0.3% and 0.5% describes an extensive damage (DS3); a drift value larger than 0.5% indicates the structural collapse (DS4).

As shown in Fig. 7.26, the fixed base model presents moderate to extensive damage for the reference points and macro-elements, indicating the tower as the critical elements. Meanwhile, all the base isolated models can fairly mitigate the damage from extensive to slight levels under seismic excitation with PGA=0.15g.

For the sake of conciseness, in the following, the displacement and acceleration time histories are reported only for the most critical points T2, T3 and T5: on the other hand, the peak drifts and accelerations are presented for all the reference points.

Fig. 7.27 shows that the acceleration time history and the peak accelerations of different reference points in the longitudinal (X) and transversal (Y) directions obtained from non-linear dynamic analyses with PGA=0.15g for the fixed-base (FB) model and the base isolated (UFREI, UFREI-SMA, UFREI-SMA-P2%) models. Fig. 7.28 summarizes the peak accelerations registered for the same reference points of the different church models. The largest value of acceleration is registered for the fixed-base model, while the largest reduction of acceleration is observed for the UFREI model: the UFREI-SMA and UFREI-SMA-P2% models, which are characterized by higher stiffness, show higher values of acceleration than the UFREI model. However, the UFREI model presents remarkable residual vibrations during the recovery time (t=10-20s), as shown by reference points T2-T5 in the Y direction. On the other hand, both the UFREI-SMA and UFREI-SMA-P2% models can prevent any notable residual vibration after earthquake excitation due to their large energy dissipation capacity. The significant reduction of the accelerations imply that the proposed isolation systems can avoid considerable damages to the non-structural components in the historical masonry church.
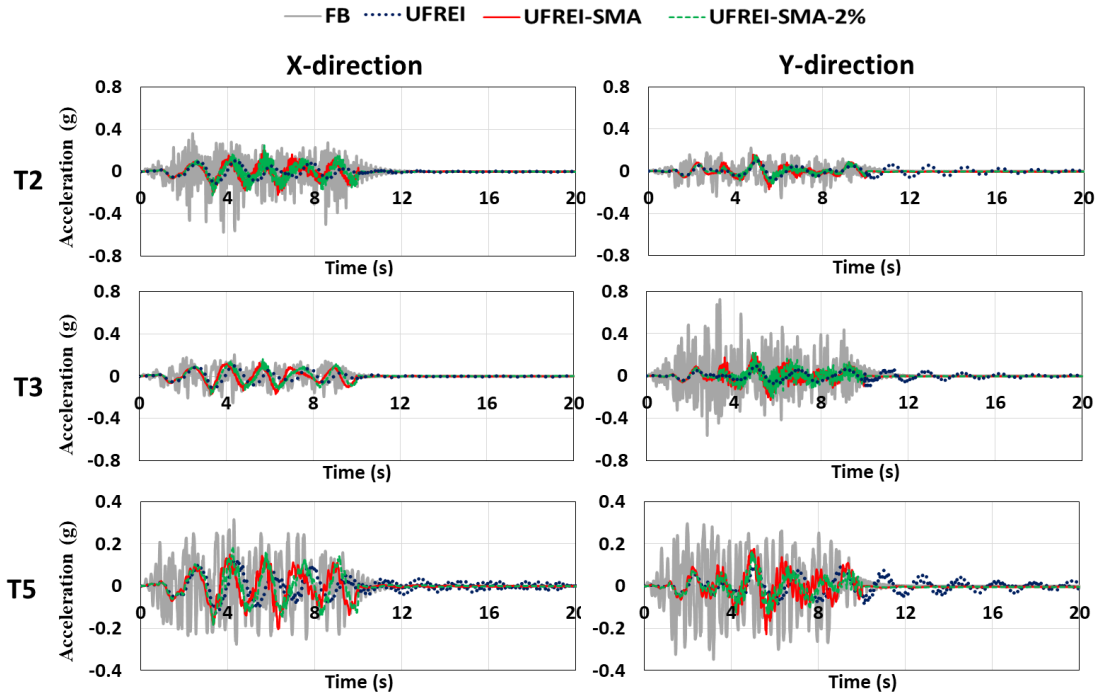
Fig. 7.27. Acceleration time history of different reference points in the longitudinal (X) and transversal (Y) directions obtained from non-linear dynamic analyses with PGA=0.15g for the fixed-base (FB) model and the base isolated (UFREI, UFREI-SMA, UFREI-SMA-P2%) models.
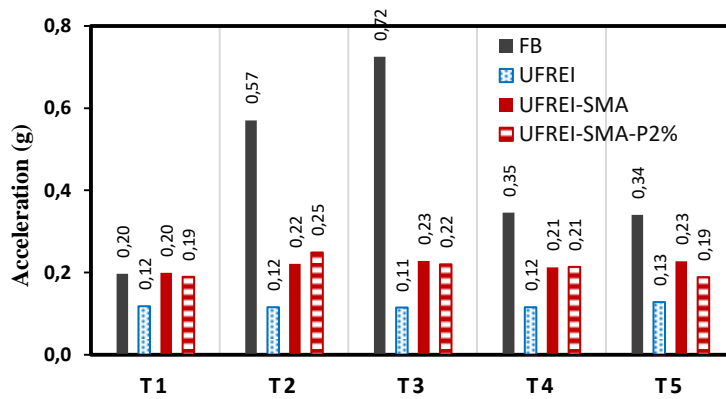

Fig. 7.28. Peak accelerations registered for some reference points of the different church models during the non-linear dynamic analyses with PGA=0.15g.

Fig. 7.29 shows the displacement time history in the X and Y directions obtained for four representative isolators (see Fig. 7.21) during the non-linear dynamic analyses with PGA=0.15g. Fig. 7.30 summarizes the peak displacements registered for the same representative isolators of the different church models. In general, the isolators of all the base isolated models present residual vibrations after the earthquake excitations until t=20s. The largest peak displacements of the isolators are registered in the UFREI model, as result of the lower horizontal stiffness. In any case, it is important to observe that for PGA=0.15g all the models exhibit peak displacements lower than $1.5h_r$, indicating that UFREIs do not reach their hardening phase. Moreover, it can be noted that the application of SMA wires considerably

reduces the displacement of UFREIs: the UFREI-SMA-P2% model shows larger peak displacement than the UFREI-SMA model due to its lower stiffness.
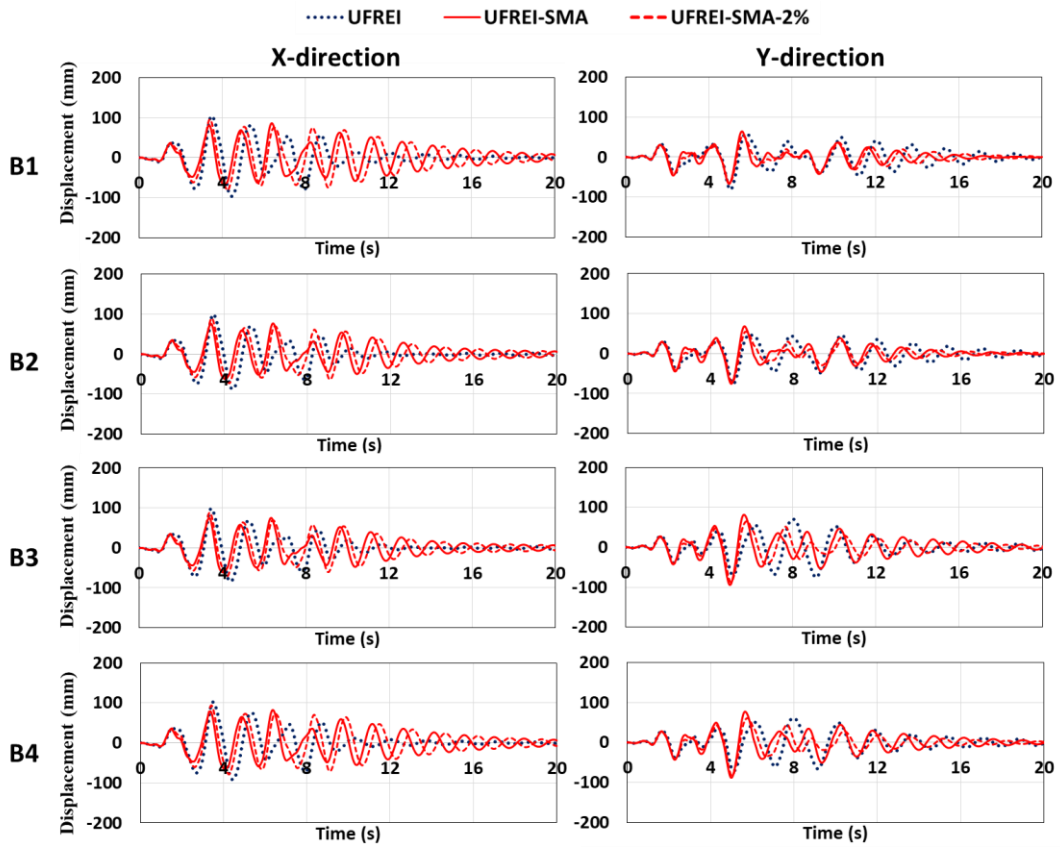

Fig. 7.29. Displacement time history in the X and Y directions obtained from non-linear dynamic analyses with PGA=0.15g for four representative isolators (see Fig. 21 for legend) of the different church models.
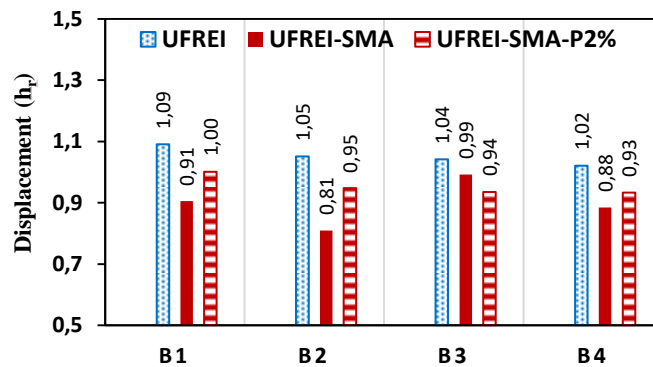

Fig. 7.30. Peak displacements registered for four representative isolators of the different church models during the non-linear dynamic analyses with PGA=0.15g (see Fig. 7.21 for legend).

7.7. Non-linear dynamic analysis with PGA=0.3g

To evaluate the effectiveness of the proposed isolation methods for higher seismic intensity levels, non-linear dynamic analyses with PGA=0.3g are performed.

Fig. 7.31 shows the tensile damage contour plots for the fixed-base (FB) model and the base isolated models at different time instants during the non-linear dynamic

analyses with PGA=0.3g. The fixed-base model presents extensive damage in correspondence with the central vaults, the lateral vaults, the longitudinal walls and the tower. The application of the isolation systems significantly decreases the tensile damage in the masonry church. The UFREI and UFREI-SMA-P2% models present the lowest damage level, showing moderate damage only in the lateral vaults.
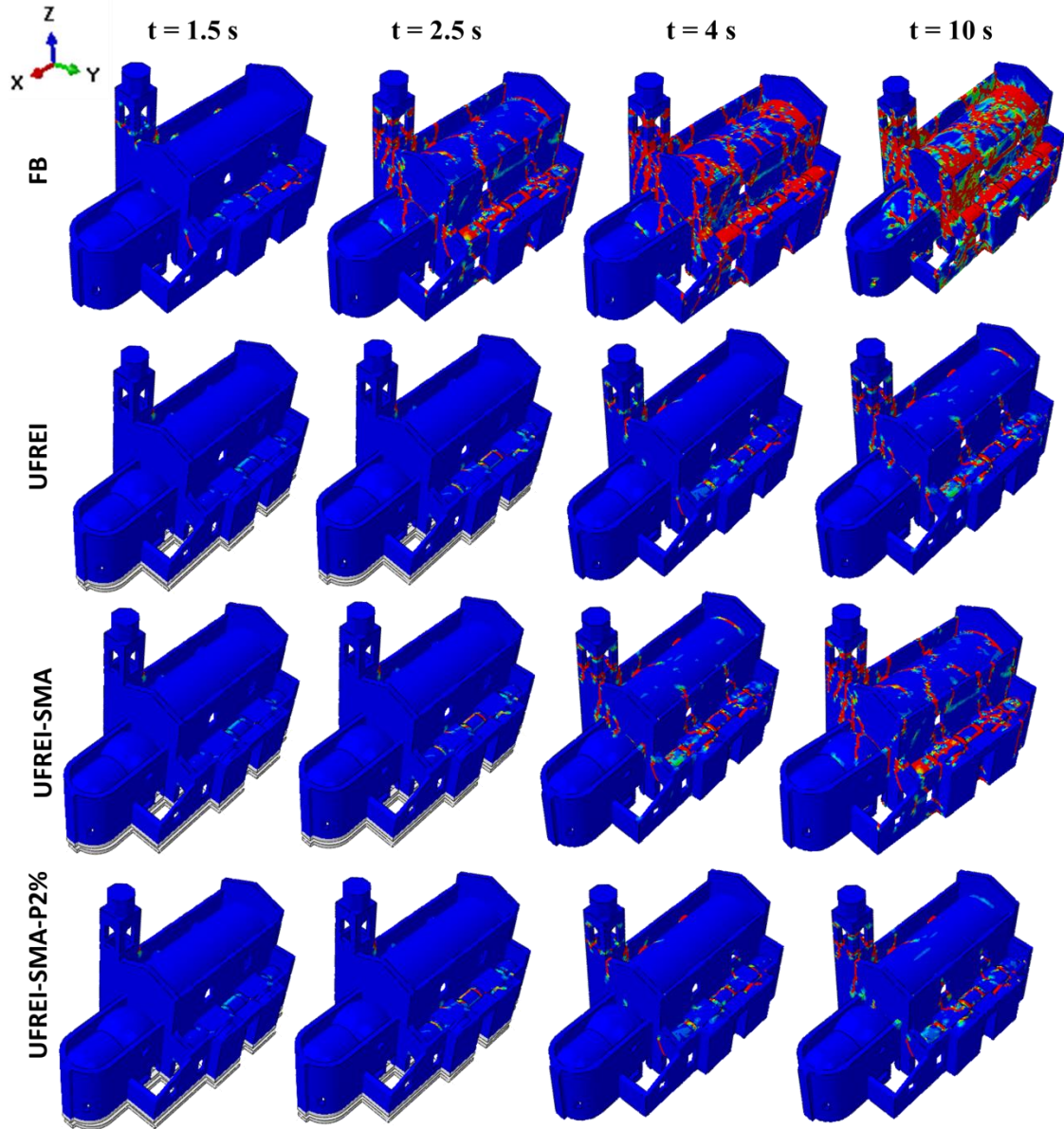

Fig. 7.31. Tensile damage contour plots for the fixed-base (FB) model and the base isolated (UFREI, UFREI-SMA, UFREI-SMA-P2%) models at different time instants during the non-linear dynamic analyses with PGA=0.3g.

Fig. 7.32 shows that the displacement time history and the peak accelerations of different reference points in the longitudinal (X) and transversal (Y) directions obtained from non-linear dynamic analyses with PGA=0.3g for the fixed-base (FB) model and the base isolated (UFREI, UFREI-SMA, UFREI-SMA-P2%) models. Fig. 7.33 summarizes the peak drifts registered for the same reference points of the different church models. It can be noted that almost all the reference points in the

fixed-base model show drifts that are larger than the limit value corresponding to collapse level. In general, the base isolated models significantly reduce the displacements from collapse to slight or moderate damage levels. The UFREI-SMA-P2% model presents the largest reduction of displacements among the base isolated models. On the contrary, quite large residual displacements are registered for the UFREI-SMA model, as observed for reference points T2 and T5. Such results may imply that the application of SMA-wires in the elastomeric isolation system is effective in the case of high seismic excitations and using a certain amount of pre-strain to maintain a low value of the isolation system stiffness.
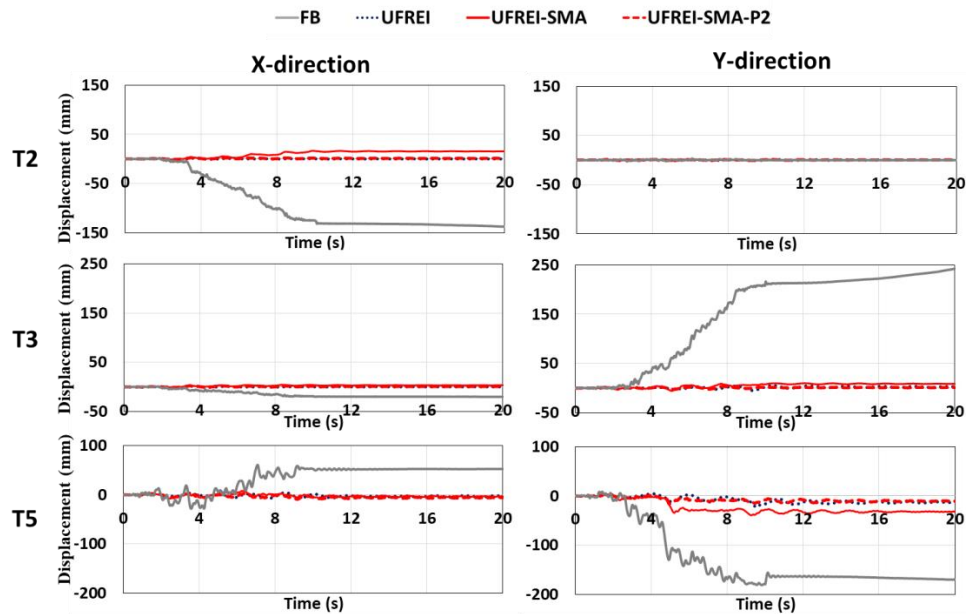

Fig. 7.32. Displacement time history of different reference points in the longitudinal (X) and transversal (Y) directions obtained from non-linear dynamic analyses with PGA=0.3g for the fixed-base (FB) model and the base isolated (UFREI, UFREI-SMA, UFREI-SMA-P2%) models. See Fig. 7.25 for legends.
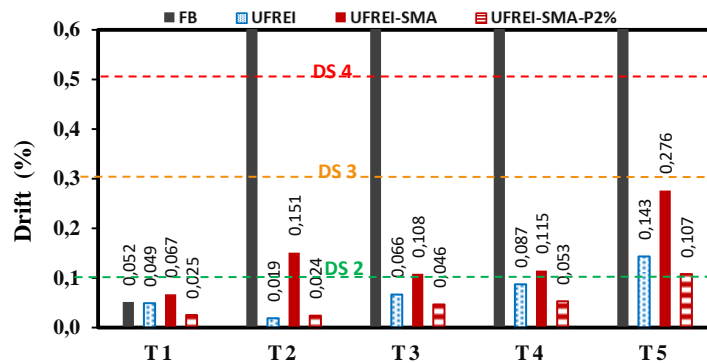

Fig. 7.33. Peak drifts registered for some reference points of the different church models during the non-linear dynamic analyses with PGA=0.3g.

Fig. 7.34 shows that the acceleration time history and the peak accelerations of different reference points in the longitudinal (X) and transversal (Y) directions obtained from non-linear dynamic analyses with PGA=0.3g for the fixed-base (FB)

model and the base isolated (UFREI, UFREI-SMA, UFREI-SMA-P2%) models. Fig. 7.35 summarizes the peak accelerations registered for the same reference points of the different church models. As shown in the case of PGA=0.15g, the application of the base isolation reduces the accelerations of the reference points of the masonry church: it can be noted that the three base isolated models show a quite similar reduction of the acceleration response.
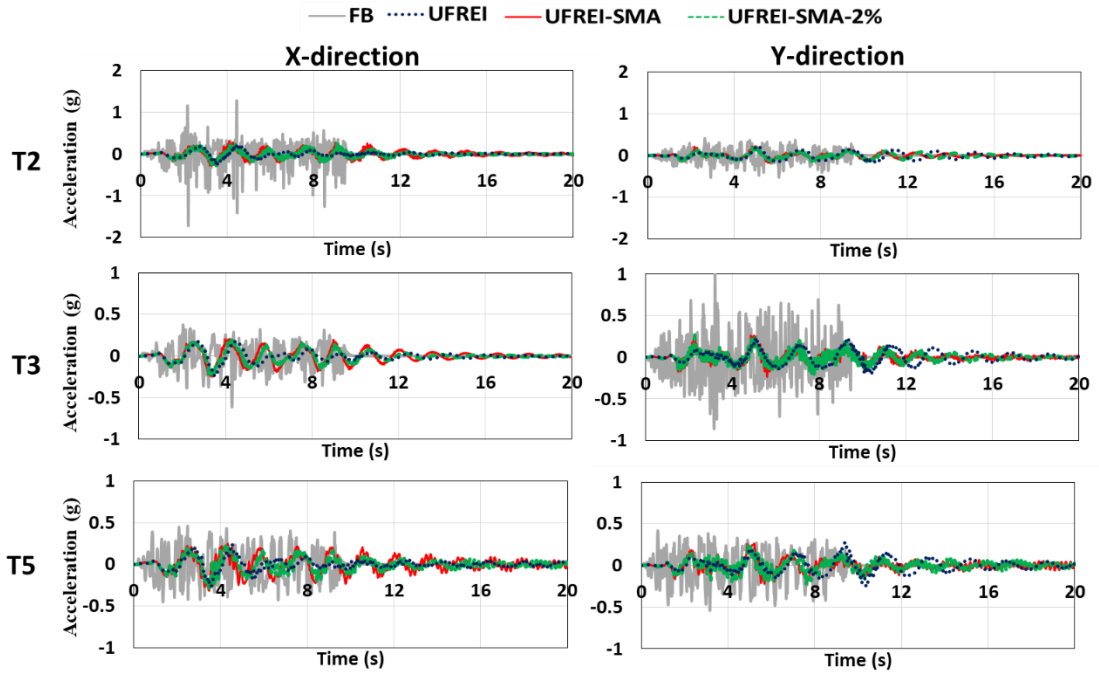

Fig. 7.34. Acceleration time history of different reference points in the longitudinal (X) and transversal (Y) directions obtained from non-linear dynamic analyses with PGA=0.3g for the fixed-base (FB) model and the base isolated (UFREI, UFREI-SMA, UFREI-SMA-P2%) models.
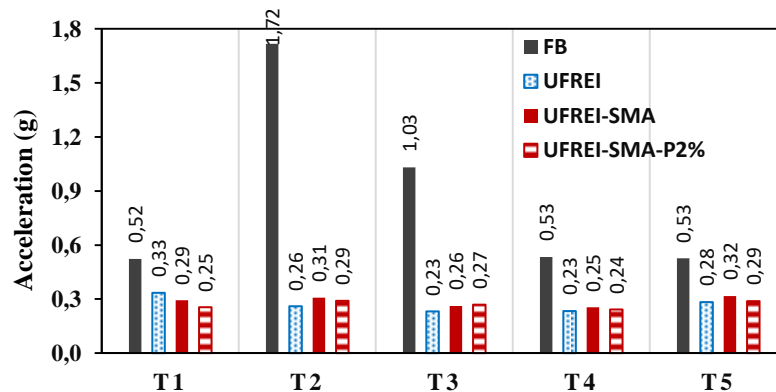

Fig. 7.35. Peak accelerations registered for some reference points of the different church models during the non-linear dynamic analyses with PGA=0.3g.

Fig. 7.36 shows the displacement time history in the X and Y directions obtained for four representative isolators during the non-linear dynamic analyses with PGA=0.3g. Fig. 7.37 summarizes the peak displacements registered for the same

representative isolators of the different church models. As obtained in the case of PGA=0.15g, the UFREI model shows larger peak displacements of the isolators than the other two base isolated models. Both UFREI-SMA and UFREI-SMA-P2% exhibit almost similar response during and after earthquake excitation in terms of displacement history. In the case of PGA=0.3g, the utilization of SMA brings clear benefits. In the UFREI model, after the end of the earthquake excitation, large residual vibrations take place and gradually decrease until t=20s. On the other hand, the other two models show very small residual vibrations after the earthquake excitation thanks to the higher damping and energy dissipation capacity of the SMA wires at large displacements.
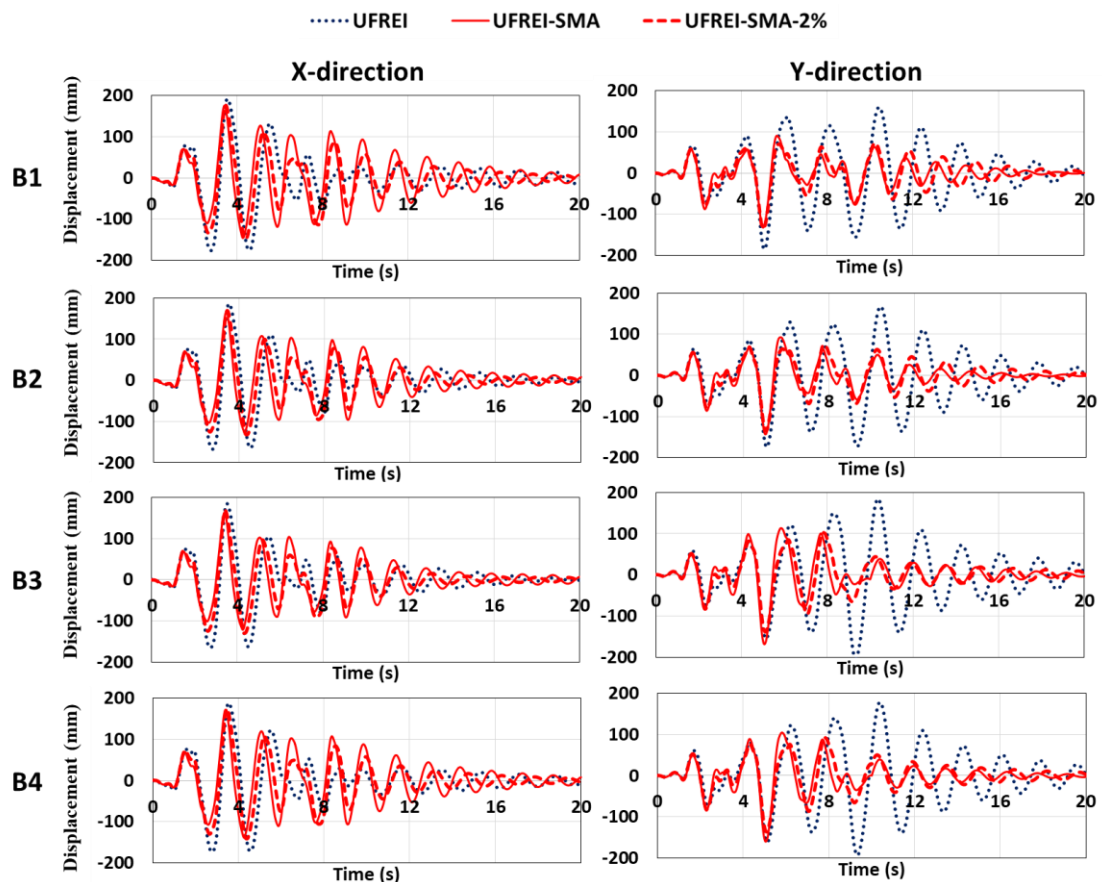

Fig. 7.36. Displacement time history in the X and Y directions obtained from non-linear dynamic analyses with PGA=0.15g for four representative isolators (see Fig. 21 for legend) of the different church models.

7.8. Conclusions

A hybrid isolation system consisting of unbounded fiber reinforced elastomeric isolators (UFREIs) and shape memory alloy (SMA) wires as additional dissipative device is proposed and investigated to seismically isolate a historical masonry church. UFREIs presents a significantly lower horizontal stiffness than typical commercial bonded isolators: in addition, UFREIs costs are considerably lower because glass fibers are used instead of steel shims as vertical reinforcement and

thick steel plates are not required for the supports. In particular, a ferrous SMA material (FeTB-SMA) is adopted in this study as dissipative device due to its lower cost and significantly larger maximum and superelastic strains than other common SMA materials.
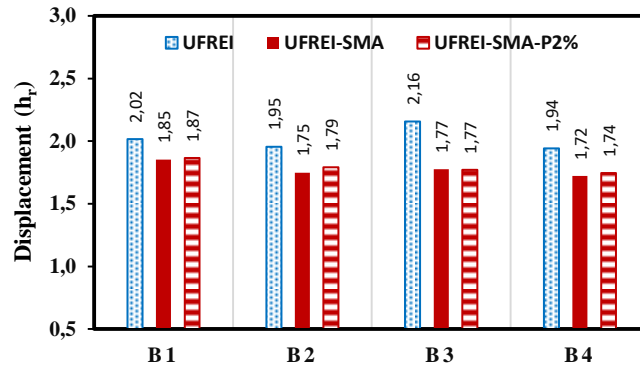

Fig. 7.37. Peak displacements registered for four representative isolators of the different church models during the non-linear dynamic analyses with PGA=0.3g (see Fig. 7.21 for legend).

Detailed 3D FE models are developed and cyclic shear analyses are carried out to characterize the response of UFREIs. The behavior of SMA is described using a thermomechanical constitutive model implemented in a user-defined material (UMAT) subroutine that is available in the software package Abaqus: a specific configuration is proposed for the SMA wire. The results of cyclic shear analyses show that the addition of the SMA wire can significantly increase the energy dissipation capacity of the isolation system. However, a considerable increase of the horizontal stiffness can be observed in the UFREI-SMA isolation system: such an increase can be reduced through the application of a specific pre-strain level in the SMA wire.

In order to reduce the computational effort in advanced numerical simulations of large isolated structures, an Abaqus User Element (UEL) is developed to represent the behavior of the isolators under study. Non-linear dynamic time history analyses are then performed to investigate the seismic response of a historical masonry church in the original and base-isolated configurations employing three different isolation systems. The numerical results show that the extensive damage observed in the fixed-base model of the church can be substantially reduced through the application of the three isolation systems.

In case of moderate earthquakes, the UFREI model represents the most effective isolation system in decreasing the horizontal displacements of the church due to its low horizontal stiffness. In case of strong earthquakes, the UFREI-SMA-P2% model (with a pre-strain equal to 2% in the SMA wire) exhibits the largest reduction of the horizontal displacements of the church and considerably decreases damage (from collapse to slight damage level) due to its high energy dissipation capacity. It has to be noted that the UFREI-SMA model (without pre-strain in the SMA wire) is less effective in reducing damage and horizontal displacements of the structure than the

UFREI and UFREI-SMA-P2% models. The utilization of SMA wires in the UFREI system is more effective by applying a specific amount of pre-strain and in case of strong earthquakes.

The UFREI model shows the largest reduction of accelerations in the church under moderate earthquakes, while a similar mitigation of accelerations is observed for all the base isolated church models under strong earthquakes. In any case, the accelerations registered for the fixed-base model are markedly reduced for all the base isolated models in case of both moderate and strong earthquakes: such result shows that the proposed base isolation systems can mitigate the damage of valuable non-structural components inside the church.

In case of strong earthquakes, the UFREI-SMA models can prevent significant vibrations at the end of the earthquake excitation due to their higher energy dissipation capacity when compared with the UFREI model.

In general, the seismic response of the isolated church is not much different when comparing the use of UFREI and UFREI-SMA-P2%, even for high PGA. However, the fair reduction of the isolation system displacement, especially under high PGA, may be considered as an important benefit because unbonded isolators are vulnerable to sliding instability when subjected to large displacements. In any case, future investigations are required to better understand the limitations and effectiveness of the proposed UFREI-SMA system for different types of structures subjected to various ground motions.

References

[1] Lagomarsino S. Damage assessment of churches after L'Aquila earthquake (2009). Bulletin of Earthquake Engineering 2012;10(1):73-92.

[2] Brandonisio G., Lucibello G., Mele E., De Luca A. Damage and performance evaluation of masonry churches in the 2009 L'Aquila earthquake. Engineering Failure Analysis 2013;34:693-714.

[3] Valente M., Barbieri G., Biolzi L. Seismic assessment of two masonry Baroque churches damaged by the 2012 Emilia earthquake. Engineering Failure Analysis 2017;79:773-802.

[4] Valente M., Milani G. Damage assessment and partial failure mechanisms activation of historical masonry churches under seismic actions: Three case studies in Mantua. Engineering Failure Analysis 2018;92:495-519.

[5] Choudhury T., Milani G., Kaushik H.B. Comprehensive numerical approaches for the design and safety assessment of masonry buildings retrofitted with steel bands in developing countries: The case of India. Construction and Building Materials 2015;85:227-246.

[6] Murtyl C.V.R., Dutta J., Agrawal S.K. Twin lintel belt in steel for seismic strengthening of brick masonry buildings. Earthquake Engineering and Engineering Vibration 2004;3:215-222.

[7] Milani G., Shehu R., Valente M. A kinematic limit analysis approach for seismic retrofitting of masonry towers through steel tie-rods. Engineering Structures 2018;160:212-228.

[8] Milani G., Shehu R., Valente M. Possibilities and limitations of innovative retrofitting for masonry churches: Advanced computations on three case studies. Construction and Building Materials 2017;147:239-263.

[9] Feng Y., Yi D., Bi Q. Seismic design analysis of the country masonry school buildings in the meizoseismal area. Earthquake Engineering and Engineering Vibration 2011;10:359-367.

[10] Barbieri G., Valente M., Biolzi L., Togliani C., Fregonese L., Stanga G. An insight in the late Baroque architecture: an integrated approach for a unique Bibiena church. Journal of Cultural Heritage 2017;23:58-67.

[11] Valente M., Milani G. Damage survey, simplified assessment, and advanced seismic analyses of two masonry churches after the 2012 Emilia earthquake. International Journal of Architectural Heritage 2018. https://doi.org/10.1080/15583058.2018.1492646

[12] Calabrese A., Spizzuoco M.C., Serino G., Della Corte G., Maddaloni G. Shaking table investigation of a novel, low-cost, base isolation technology using recycled rubber. Structural Control and Health Monitoring 2015;22:107-122.

[13] Toopchi-Nezhad H., Tait M.J., Drysdale R.G. Bonded versus unbonded strip fiber reinforced elastomeric isolators: finite element analysis. Composite Structures 2011;93:850-859.

[14] Das A., Deb S.K., Dutta A. Comparison of numerical and experimental seismic responses of FREI-supported un-reinforced brick masonry model building. Journal of Earthquake Engineering 2016;20: 1239-1262.

[15] Das A., Deb S.K., Dutta A. Shake table testing of un-reinforced brick masonry building test model isolated by U-FREI. Earthquake Engineering & Structural Dynamics 2016;45:253-272.

[16] Thuyet V.N., Deb S.K., Dutta A. Evaluation of horizontal stiffness of fibre-reinforced elastomeric isolators. Earthquake Engineering & Structural Dynamics 2017;46:1747-1767.

[17] Chiozzi A., Simoni M., Tralli A. Base isolation of heavy non-structural monolithic objects at the top of a masonry monumental construction. Materials and Structures 2016;49:2113-2130.

[18] Seki M., Miyazaki M., Tsuneki Y., Kataoka, K. A masonry school building retrofitted by base isolation technology. 12th World Conference on Earthquake Engineering 2000.

[19] Habieb A.B., Valente M., Milani G. Base seismic isolation of a historical masonry church using fiber reinforced elastomeric isolators. Soil Dynamic and Earthquake Engineering 2018: Accepted.

[20] Habieb A.B., Milani G., Tavio T. Two-step advanced numerical approach for the design of low-cost unbonded fiber reinforced elastomeric seismic isolation

systems in new masonry buildings. Engineering Failure Analysis 2018;90:380-396.

[21] Mishra H.K., Igarashi A., Matsushima H. Finite element analysis and experimental verification of the scrap tire rubber pad isolator. Bulletin of Earthquake Engineering 2013;11:687-707.

[22] Thuyet V.N., Deb S.K., Dutta A. Mitigation of seismic vulnerability of a prototype low-rise masonry building using U-FREIs. Journal of Performance of Constructed Facilities 2018;32(2):1-13.

[23] De Raaf M.G.P., Tait M.J., Toopchi-Nezhad H. Stability of fiber-reinforced elastomeric bearings in an unbonded application. Journal of Composite materials 2011;45:1873-1884.

[24] Eurocode 8: Design of structures for earthquake resistance-part 1: general rules, seismic actions and rules for buildings. 2005.

[25] S.N. Indonesia, Persyaratan Beton Struktural Untuk Bangunan Gedung, SNI 2847 2013.

[26] Simulia. ABAQUS 6.14 User's manual. Dassault Systems, Providence, RI, 2014.

[27] Minghini, F., Bertolesi, E., Del Grosso, A., Milani, G., & Tralli, A. Modal pushover and response history analyses of a masonry chimney before and after shortening. Engineering Structures 2016: 110: 307-324.

[28] Tiberti, S., Acito, M., & Milani, G. Comprehensive FE numerical insight into Finale Emilia Castle behavior under 2012 Emilia Romagna seismic sequence: damage causes and seismic vulnerability mitigation hypothesis. Engineering Structures 2016: 117: 397-421.

[29] Valente M., Milani G. (2018). Seismic response and damage patterns of masonry churches: seven case studies in Ferrara, Italy. Engineering Structures, 177, 809-835.

[30] Wilde, K., Gardoni, P., & Fujino, Y. Base isolation system with shape memory alloy device for elevated highway bridges. Engineering structures 2000: 22(3): 222-229.

[31] Dezfuli, F. H., & Alam, M. S. Performance-based assessment and design of FRP-based high damping rubber bearing incorporated with shape memory alloy wires. Engineering Structures 2014: 61: 166-183.

[32] DesRoches, R., McCormick, J., & Delemont, M. Cyclic properties of superelastic shape memory alloy wires and bars. Journal of Structural Engineering 2004: 130(1): 38-46.

[33] Kraus, M. A., Schuster, M., Kuntsche, J., Siebert, G., & Schneider, J. Parameter identification methods for visco-and hyperelastic material models. Glass Structures & Engineering 2017: 2(2): 147-167.

[34] Shahzad M., Kamran A., Siddiqui M.Z., Farhan M. Mechanical characterization and FE modelling of a hyperelastic material. Materials Research 2015;18:918-924.

[35] Osgooei P.M. Advanced numerical modeling of Fiber-Reinforced Elastomeric Isolators (FREIs). PhD Thesis, McMaster University, 2014.

[36] Gunaratne M., Bandara N., Medzorian N., Chawla M., Ulrich P. Correlation of tire wear and friction to texture concrete pavements. Journal of Materials in Civil Engineering 2000; 12: 46-54.

[37] Habieb A. B., Valente M., Milani G., Implementation of a simple novel Abaqus user element to predict the behavior of unbonded fiber reinforced elastomeric isolators in macro-scale computations. Bulletin of Earthquake Engineering 2018: In Press

[38] Song, G., Ma, N., & Li, H. N. Applications of shape memory alloys in civil structures. Engineering structures 2006: 28(9): 1266-1274.

[39] Lagoudas D.C. Shape Memory Alloys (New York: Springer Science and Business Media 2008, LLC.

[40] Lagoudas, D., Bo, Z., Qidwai, M., & Entchev, P. SMA-UM: User Material Subroutine for Thermomechanical Constitutive Model of Shape Memory Alloys (College Station 2003: TexasA&M).

[41] Alam, M. S., Youssef, M. A., & Nehdi, M. Analytical prediction of the seismic behaviour of superelastic shape memory alloy reinforced concrete elements. Engineering Structures 2008: 30(12): 3399-3411.

[42] Zhang, Y., Hu, X., & Zhu, S. Seismic performance of benchmark base-isolated bridges with superelastic Cu–Al–Be restraining damping device. Structural Control and Health Monitoring 2009: 16(6): 668-685.

[43] Tanaka, Y., Himuro, Y., Kainuma, R., Sutou, Y., Omori, T., & Ishida, K. Ferrous polycrystalline shape-memory alloy showing huge superelasticity. Science 2010: 327(5972): 1488-1490.

[44] Kelly J.M. Earthquake-resistant design with rubber, Springer-Verlag, 1993.

[45] Wen, Y. K. Method for random vibration of hysteretic systems. Journal of the engineering mechanics division 1976: 102(2): 249-263.

[46] Kumar, M., Whittaker, A. S., & Constantinou, M. C. An advanced numerical model of elastomeric seismic isolation bearings. Earthquake Engineering & Structural Dynamics 2014: 43(13): 1955-1974.

[47] Calvi G.M. A displacement-based approach for vulnerability evaluation of classes of buildings. Journal of Earthquake Engineering 1999;3:411-438.

Chapter

8
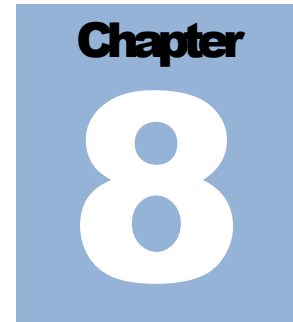
The effect of ageing on the recycled rubber pads in base seismic isolation of a historical masonry church

Base seismic isolation is one of the efficient technical solutions to reduce the vulnerability of new and existing structures. The designs of the base isolation device have been developed in the past decades by many researchers. In this work, a recycled rubber material in the form of reactivated EPDM is used for rubber pad to reduce significantly the cost of isolator devices. A series of uniaxial tensile test and relaxation test is conducted to characterize the hyperelasticity and viscosity of the recycled rubber, both in fresh and aged condition to evaluate its durability. The recycled rubber specimens are then used to fabricate an unbonded fiber reinforced elastomeric isolator (UFREI), which does not need any thick steel plate for the installation. It may reduce significantly the cost and weight of the isolation system. The proposed UFREI is investigated through a shear test simulation, both in fresh and aged condition, to investigate the behavior after long-term use. The proposed UFREI is then implemented to isolate a historical masonry church in the center of Italy. A time-history analysis is performed in Abaqus FE software, by applying a concrete damage plasticity (CDP) model for the masonry material. The results of the dynamic analysis show that the application of such low-cost isolation system can mitigate the damage of the masonry church under 0.25 g of PGA, from extensive damage to slight damage. The proposed UFREI shows also a negligible reduction of the isolation performance under ageing effect. The results reveal a promising advantage of the UFREI system using recycled rubbers.

8.1. Introduction

By recent earthquakes, numerous historical masonry buildings in Italy were subjected to severe damages or even total collapse [1]. Different seismic protection methods were proposed to increase the seismic capacity of existing masonry constructions, see [[5]-[8]]. Common retrofitting techniques are generally invasive

and based on a strengthening approach, increasing the seismic demand on the structure.

On the other hand, base isolation system can be used as an alternative solution to mitigate the effects of earthquakes on new and existing. It has been widely accepted as an effective method for the protection of structures against seismic actions: the isolation devices, typically placed at the base of the structure, increase the flexibility of the structure and shift its fundamental frequency away from the dominant frequency of seismic excitations, thus significantly reducing inter-story drifts and accelerations. However, although base isolation has been recognized as a promising method, research and practices on seismic isolation of historical masonry constructions remain limited. Moreover, seismic isolation system is especially needed for masonry structures, where the poor tensile strength may lead to low horizontal load carrying capacities [9]-[11].

The application of isolation systems has increased also in high seismic regions of developing countries by using low cost devices. Fiber reinforced elastomeric isolators (FREIs) have been introduced as a potential economical alternative to conventional steel reinforced elastomeric ones: they can be unbonded (UFREI) or bonded (BFREI) to both the superstructure and substructure. Conventional elastomeric isolators usually consist of several layers of high-damping rubber (pads) reinforced by interposed steel shims: the reinforcement has the role of improving the stability and limiting vertical deformations, while the horizontal deformations are controlled by the shear stiffness of the pads. Glass or carbon fiber material can be used as alternative reinforcement because it is more economical than its steel counterpart and provides a comparable reinforcement effect [12]-[14]. The fiber reinforcement allows the application of UFREIs, in which the upper and bottom surfaces are not glued to the structures: furthermore, the rigid steel plates for supports are not required.

A shaking table test on a new masonry building supported on UFREIs has provided promising results, with a significant reduction of inter-story drifts and accelerations [15]. Moreover, a first full-scale application of base isolation to a new two-story masonry building supported on UFREIs has been carried out in Tawang, India [16]. On the other hand, the application of base isolation in existing or historical masonry buildings seems a challenging task due to the need of separating the superstructure and foundation. The difficulty typically derives from the large thickness and the massive weight of masonry walls. However, several construction methods have been proposed to implement the base isolation system into old masonry buildings [17][18].

The main advantages of UFREIs application are described in the literature [12][19][20]. The effective horizontal stiffness of UFREIs is considerably lower than that of the bonded fiber reinforced elastomeric isolators (BFREIs), decreasing the seismic demand. The reduction of the effective lateral stiffness is the result of the rollover deformation of the UFREI due to the absence of bonding. Some researchers have evaluated the UFREI stability limit at which the isolator can be subjected to damage or delamination. Lateral displacements equal to 1.7-$2t_r$ (where t_r is the total thickness of rubber layers in the isolator) are considered as critical values [21], while it is reported in [22] that even lateral displacements equal to $3t_r$ don't seem to cause any damage in the rubber-fiber interfaces. Such large critical values facilitate the utilization of UFREIs with small height. Moreover, such a remarkable feature cannot be found in commercial BFREIs that typically exhibit critical lateral displacements equal to $1.5t_r$ [23][24].

In this work, UFREIs with only a few rubber pads is proposed to isolate a small Italian historical masonry church located in the area with 0.25g of PGA. Moreover, to drop down the isolator cost, the rubber is produced using recycled material in the form of reactivated EPDM from industrial waste.

To reduce significantly the computational time, in the nonlinear time history analyses in Abaqus, a single UFREI is modeled using representative user-element which was developed by the author.

Another important issue is related to the effect of ageing on the performance of the UFREIs using recycled rubber. Therefore, in this study the effect of ageing is taken into account in the nonlinear time-history analyses based on several parameters obtained from experimental aging tests.

8.2. Experiments and numerical modeling of the fiber reinforced elastomeric isolators (FREIs) made from recycled rubber

8.2.1. Uniaxial tensile and relaxation test on recycled rubber specimens

Two rubber specimens tested are RR30 and RR70, which represent the rubber with 30% and 70% of recycled material, respectively. The shear modulus of the specimen according to the manufacturer is 0.7 and 0.35 MPa, for RR30 and RR70, respectively. The specimen is in the form of dumb-bell test type 2 according to the code [25]. Three specimens are taken for each test. The result highlighted in this paper is the average of the three tests. The accelerated ageing condition is performed by storing the specimen at 70˚C for 7x24 hours [26]. This ageing simulation may represent the long-term degradation after 60 years of normal use of the rubber pad.

The uniaxial tensile test is performed until the failure of rubber according to the code [25][8]. Fig. 8. 1 shows the result of tensile test of fresh and aged specimens. The failure characteristics of both specimens are summarized in Table 8. 1. The result confirms that the specimen RR-30 and RR-70 satisfy the requirement of ultimate strength and strain evolution after accelerated ageing condition, as stated in the code [26].

Table 8. 1 Failure strain and tensile strength of the rubber RR-30 and RR-70 in before and after aging.

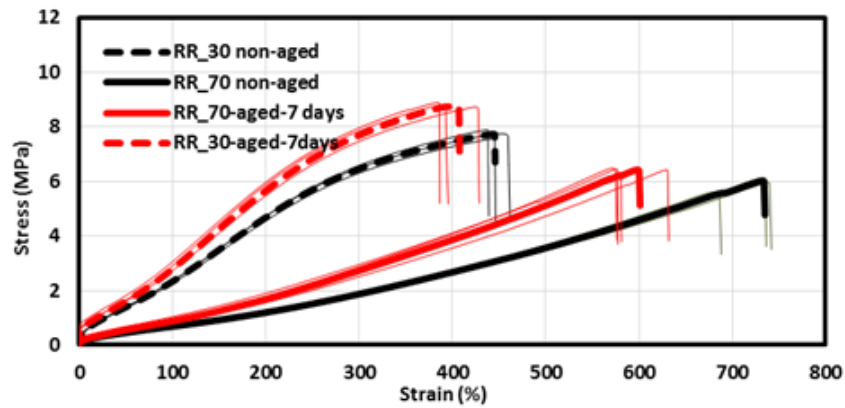| **RR-30**	Fresh	Aged	**Δ (%)**	
Failure strain (%)	446.183	408.101	**-8.535**	OK <25%
Tensile Strength (MPa)	7.726	8.807	**13.979**	OK <15%
RR-70	Fresh	Aged	**Δ (%)**	
Failure strain (%)	730	600	**-17.808**	OK <25%
Tensile Strength (MPa)	6.032	6.4 3	**6.490**	OK <15%

Fig. 8. 1 The results of tensile test on rubber RR30 and RR70 at fresh and aged condition.

The relaxation test is performed to characterize the viscosity of the rubber. With a higher viscosity of rubber, the damping ratio of the isolator increases. To represent the condition under seismic action, the relaxation test is performed by firstly pulling the specimen as fast as possible and then maintaining the strain at 100% and recording the evolution of the stress for 100 seconds [27]. In this study, the maximum speed of the tensile device used is 40 mm/s. The result of the relaxation test is shown in Fig. 8. 2, presenting the evolution of the normalized uniaxial stress in function of time. The ageing effect decreases slightly the viscosity of the two rubber specimens.

The data from uniaxial tensile and relaxation tests are used as the inputs for the finite element (FE) modeling in Abaqus.
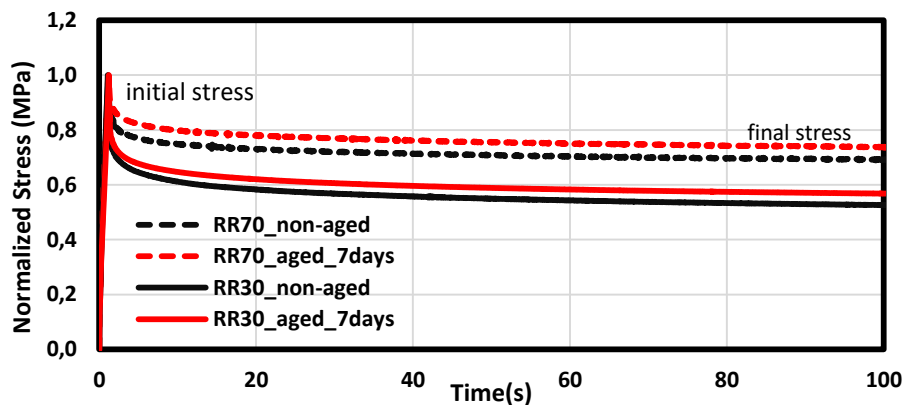

Fig. 8. 2 The results of relaxation test on rubber RR30 and RR70 at fresh and aged condition.

8.2.2. Performance of the UFREIs and the effect of ageing

A prototype of UFREI with dimension shown in Fig. 8. 3 is presented in this paper. This dimension results in a bearing with low-shape isolator, which can reduce the fabrication cost by minimizing the bonding surface and reinforcement. The utilization of this low-cost UFREI for masonry structures can be found in the literature [19][28][28].

For the 3D FE modeling, the data from the uniaxial tensile test is used to determine the hyperelasticity behavior of the rubber according to Yeoh model and the relaxation data is inputted as the viscosity behavior according to Prony-series model [29]. The fiber reinforcement is considered isotropic elastic with 210 GPa of Young modulus and 0.25 of Poisson ratio.

Two prototypes considered are UFREIs using rubber RR30 and RR70, at fresh and aged condition. To apply the unbounded condition, a frictional contact between rubber pads and the supports is applied with 0.7 of friction coefficient. The constant vertical pressure is 2.1 MPa to represent the gravity load carried by a single isolator in the isolation system of the masonry church that is discussed in the next section. The UFREI is then subjected to a gradual cyclic shear test with 0.5 Hz of frequency and 140% of maximum shear displacement.

Fig. 8. 3 and Fig. 8. 4 show the deformation patterns and shear behavior of the two UFREIs at fresh and aged condition. The evolution of effective stiffness and damping ratio after ageing is reported in Table 8. 2. The result shows that only UFREI-RR30 which satisfies the ageing effect requirements: stiffness evolution under 20% and damping evolution under 15% as stated in the code [26]. Therefore in this study, UFREI-RR30 is proposed as the isolation device of the historical masonry church.

Dimension 150.150.54 mm
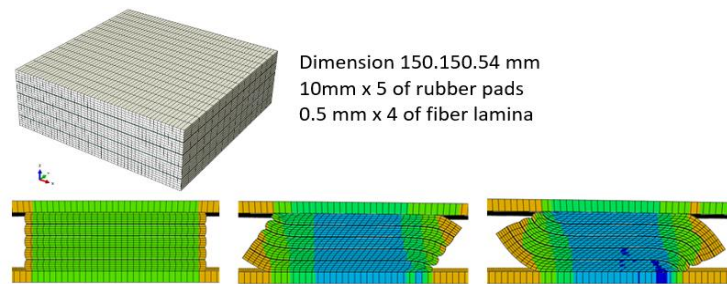10mm x 5 of rubber pads
0.5 mm x 4 of fiber lamina

Fig. 8. 3 Dimension of the UFREI and the deformation patterns under shear test.

The performance of the isolated masonry church using UFREIs is then analyzed through FE modeling in Abaqus. Unfortunately, in the software code Abaqus there is no representative element available to model isolators in an effective way. Therefore, in this study a new Abaqus User Element (UEL) is proposed and implemented to represent the 3D behavior of a single UFREI with the aim of significantly reducing the computational effort in FE analysis, thus avoiding the use of a detailed 3D FE model for each single isolator. The detail discussion of the proposed UEL for UFREIs is presented in the previous work [30]. The proposed UEL is in the form of a beam element, characterized by 12 degrees of freedom (DOF), which is able to capture the 3D behavior of a single isolator, as well as the nonlinearity and hardening of the horizontal stiffness.
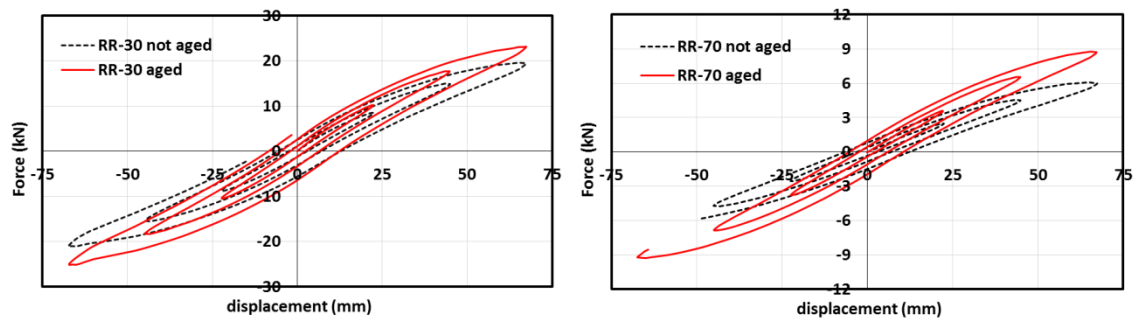
Fig. 8. 4 Shear behavior of UFREI using rubber RR30 and RR70 at fresh and aged condition, obtained from 3D FE analysis.

Table 8. 2 Effective stiffness and damping ratio of two UFREIs in fresh and aged condition.

UFREI	Stiffness (N/mm)		Δk (%)	Damping ratio (%)		$\Delta\xi$ (%)
	not aged	aged		not aged	aged	
RR-30	291.04	337.31	15.89 (OK)	10.28	9.15	-11.04 (OK)
R -70	102.14	134.17	31.35 (NO)	9.39	6.85	-27.02 (NO)

8.3. UFREI-RR30 for base seismic isolation of a historical masonry church

In this study the seismic performance of a small historical masonry church located in Lazio region, Central Italy, is investigated. The church dates back to the XIX century and presents a rectangular plan with two naves: it is 11.4 m long and 9.9 m width. The facade presents two side doors and a tympanum that is surmounted by a bell gable that is about 2 m high: the overall maximum height is 10.25 m. The naves longitudinal walls present two rectangular openings and are about 0.6 m thick. The two naves are covered by four cross vaults and present a central square column with sides equal to 0.5 m. The building is composed of masonry bricks and lime mortar.

Advanced numerical analyses of the church under study were performed through a detailed 3D FE model created by means of the software code Abaqus [28]. Fig. 8. 5 shows a general view of the FE model of the church under study, consisting of about 110000 tetrahedron elements. To simulate the non-linear response of masonry, the Concrete Damaged Plasticity (CDP) model available in the software code ABAQUS is used. In this model, masonry is considered as an isotropic material exhibiting damage in both tension and compression. Although this is a simplification, such an assumption is commonly accepted in engineering practice [31][32][33]. The CDP model is originally conceived for isotropic fragile materials (typically concrete), but

it can be adapted to masonry because the orthotropy ratio in brickworks is moderate (around 1.2) under biaxial stress states in the compression–compression region. Orthotropy is lost in CDP but the use of the isotropic model is accepted after an adaptation of the parameters to fit an average behavior between vertical and horizontal values.
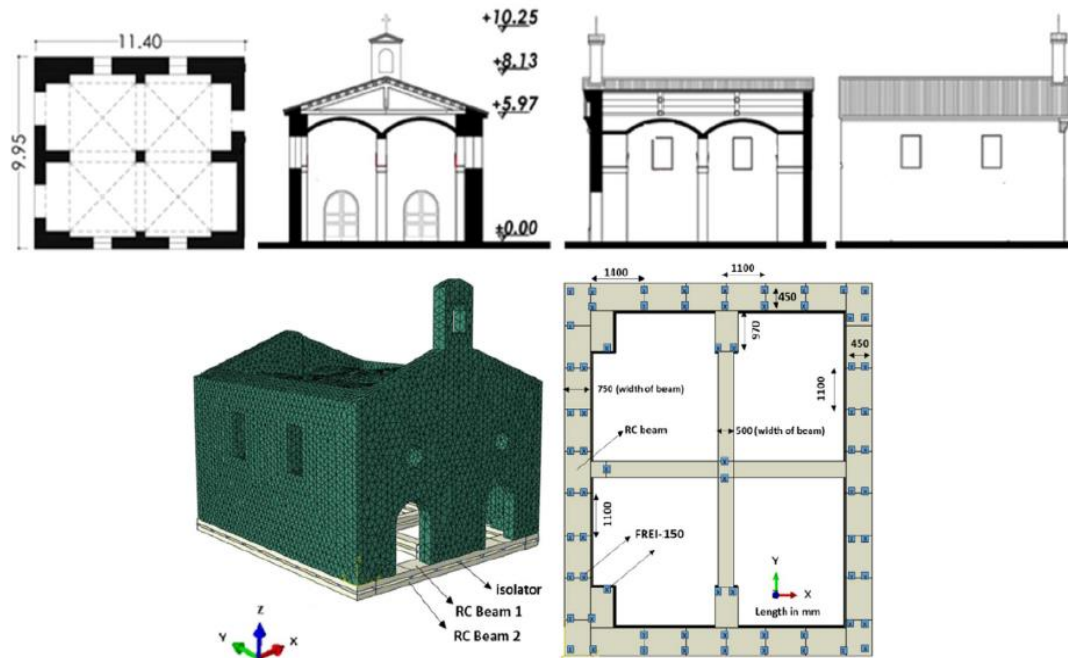

Fig. 8. 5 Top: drawings of the masonry church: plan, two sections and an elevation lateral view. Bottom: FE model of the isolated masonry church and arrangement of FREIs.

The tensile damage is considered to evaluate the overall damage state of masonry since mortar tensile strength is considerably low. The stress-strain curve in tension exhibits a peak stress $f_t = 0.19$ MPa, see Fig. 8. 6 : this value corresponds to the tensile strength of mortar and is taken in agreements with experimental data available in the literature for a medium/high strength mortar and codes of practice indications. Then micro-cracks start to propagate within the material, leading to a macroscopic softening. Softening in tension is typically exponential and approximated in the computations with a trilinear behavior for the sake of simplicity. In compression, the response is linear up to the yield stress $f_y = 1.9$ MPa, followed by a crushing stress $f_u =2.4$ MPa and a softening branch which is supposed linear again for simplicity. Other parameters of the CDP model are assumed according to previous studies, [3][7][34], and utilized in the computations are summarized in Table 8. 3.
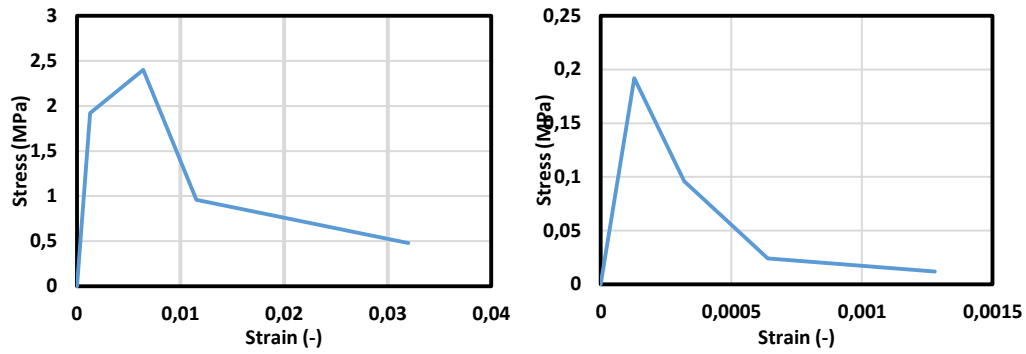
Fig. 8. 6 Simplified uniaxial behavior of masonry material in compression (left) and tension (right).

Table 8. 3 Values of the parameters used for the CDP model in the numerical analyses.

E (MPa)	v	Dilatation angle	Eccentricity	σ_{b0}/σ_{c0}	K_c	Viscosity
1800	0.2	10	0.1	1.16	0.667	0.001

The masonry church is base isolated using isolators see 8.5: as already mentioned, Fig. 8. 4 shows the shear behavior of UFREI up to lateral displacements equal to 1.4 t_r. To facilitate the application of the base isolators, reinforced concrete beams are placed at the base of the walls: such a configuration allows the UFREIs to work properly between the foundation and the superstructure. The method to decouple the super and substructure and to insert the unbonded isolation system into an existing masonry building can be found in the literature [35].

The number of UFREIs inserted into the numerical model is equal to 73, as shown in Fig. 8. 5. It is worth mentioning that the number of required isolators depends on the weight of the isolated structure and the target period of the isolation system. The target period of the isolation system is set to about 1 second. In such a configuration, a single UFREI carries 2.1 MPa of vertical pressure, approximately. A single isolator should be loaded by a stress value not larger than 2.5 MPa to avoid buckling of the isolator resulting in a negative horizontal stiffness. At the same time, the vertical load should be also large enough to prevent any sliding between unbonded isolators and supports: to this aim, some researchers suggest a minimum value of vertical stress on unbonded FREIs equal to 0.5 MPa, [36].

8.4. Nonlinear time history analyses

To evaluate the seismic performance of the church in the three different configurations, full-scale non-linear time-history (NLTH) analyses are performed using the accelerogram registered during the 2009 L'Aquila earthquake, Central Italy. The two horizontal components of the accelerogram with Peak Ground Acceleration (PGA) scaled to 0.25g are illustrated in Fig. 8. 7: a part (10 s) of the real registration is used in the numerical simulations. The structural behavior of the church and the damage distribution in the different macro-elements are investigated in the case of fixed-base and isolated models.

Fig. 8. 8 illustrates the tensile damage contour plots for the three models at different time instants during the non-linear dynamic analyses: red color is associated to full damage and blue color to zero damage. In the fixed-base model (FB), tensile damage initially develops in the bell gable at the top of the façade and then propagates in the cross vaults, the façade and lateral walls, especially near the openings: at the end of the non-linear dynamic analysis, significant damage is registered in the model, mainly in the masonry cross vaults. It can be noted that in the base isolated models tensile damage is significantly reduced. In the model with UFREIs, small damage appears only near the openings of the façade: it is worth mentioning that in the first part of the analysis no damage is observed. These results show the effectiveness of the isolation system in reducing damage, in the case of UFREIs.
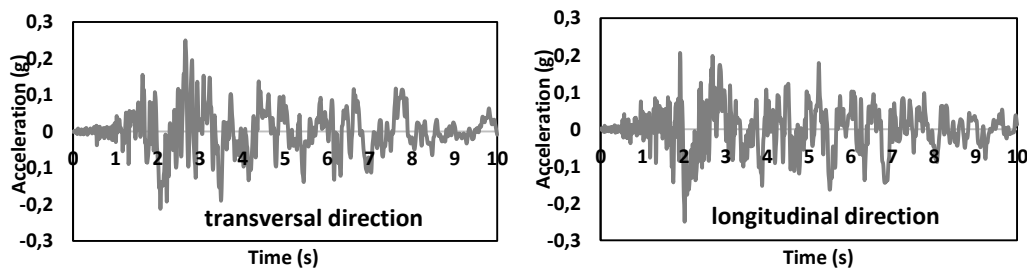

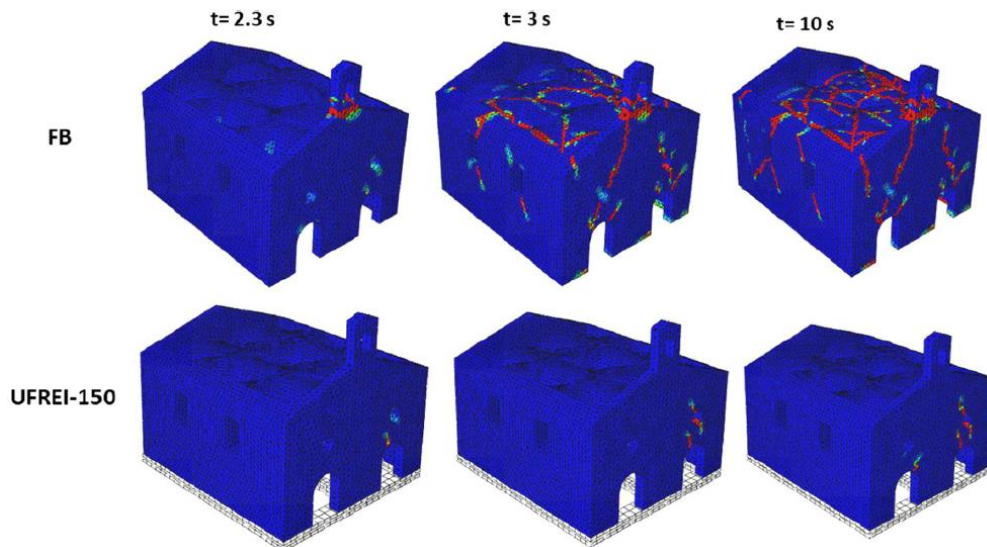Fig. 8. 7 Horizontal components of the accelerogram used in the numerical simulations.

Fig. 8. 8 Tensile damage contour plots for the fixed-base (FB) model and the base isolated (UFREI-150) model at different time instants during the non-linear dynamic analyses with PGA=0.25g.

Fig. 8. 9 compares the displacement time history of some reference points obtained from non-linear dynamic analyses for the FB and UFREI models (red and blue line, respectively). The measured displacement in this case is the relative displacement between the reference point and the base of the super-structure (upper-part of the isolation system). The fixed-base model (FB) shows very large displacements (about 9 cm) in the longitudinal direction at the top of the bell gable (P4), indicating a clear collapse of such element: large displacements (1.4 cm) in the longitudinal direction

are registered also at the top of the façade in correspondence with the base of the bell gable (P1). It can be noted that notable residual displacements are computed at the end of the non-linear dynamic analyses, revealing significant permanent damage: such results are consistent with the damage concentration observed in the bell gable. In the transversal direction the largest displacement (about 1 cm) is registered for the right lateral wall. In the base isolated models a remarkable reduction of the peak displacements can be observed, mainly at the top of the bell gable (P4) and at the top of the façade (P1): in particular, residual displacements are negligible for both the base isolated models at the end of the non-linear dynamic analyses. It can be noted that the response of the base isolated model is characterized by a significant frequency reduction.

Another interesting parameter is the acceleration, typically responsible for the damage of non-structural components inside the building. Fig. 8. 10 shows the acceleration time history of some reference points (base, cross vaults and bell gable) obtained from non-linear dynamic analyses for the FB and UFREI models (red and blue line, respectively). Numerical results show that the acceleration values at the cross vaults and at the bell gable are significantly reduced due to the application of the isolation system: consequently, the use of base isolation can fairly mitigate the damage of non-structural components inside the building, such as historical furniture, lamps and paintings.

Finally, the horizontal displacements of the base isolators are computed to check the maximum displacement requirements. Fig. 8. 11 shows the displacement time history in the X and Y directions for four representative isolators (B1,B2,B3 and B4), in unbonded (UFREI) case, during the non-linear dynamic analyses.

In the UFREI case, according to some experimental works [22], the critical displacement can be assumed equal to about 2.5-3t_r: consequently, in this study it may be assumed equal to 125 mm because the total height of rubber is 50 mm. The numerical results show that all the isolators satisfy the maximum displacement requirements. It is worth mentioning that the sliding displacement of the UFREI is not taken into account in the UEL model because it can be considered as negligible under a vertical pressure larger than 0.5 MPa, as reported in [36].

8.5. Nonlinear time history analyses taking into account the ageing effect to the rubber pads

Another NLTH analysis is carried out by considering the ageing effect, as reported in section 2.2. Such an ageing consideration represents the condition after 60 years of installation, approximately. Therefore, the mechanical properties of the rubber after accelerated ageing are taken into account in this section. As shown in Table 8. 2, the ageing effect increases the effective stiffness of UFREI-RR30 by 15.89% and reduces its damping ratio by 11.04%.

The displacement time history of some reference points obtained from NLTH analysis for Aged-UFREI model is shown in Fig. 8. 9 (black line). In general, there is no remarkable difference of the peak displacements between the UFREI and Aged-UFREI models. In addition, Fig. 8. 10 shows that the acceleration responses of the two models, before and after ageing, are not significantly different. These results imply that the seismic response of the isolated church before and after ageing effect remains quite similar. However, remarkable differences are depicted between Fig. 8. 11 and Fig. 8. 12, where the peak values of isolator displacements are reduced due to the increase of isolator stiffness after ageing.
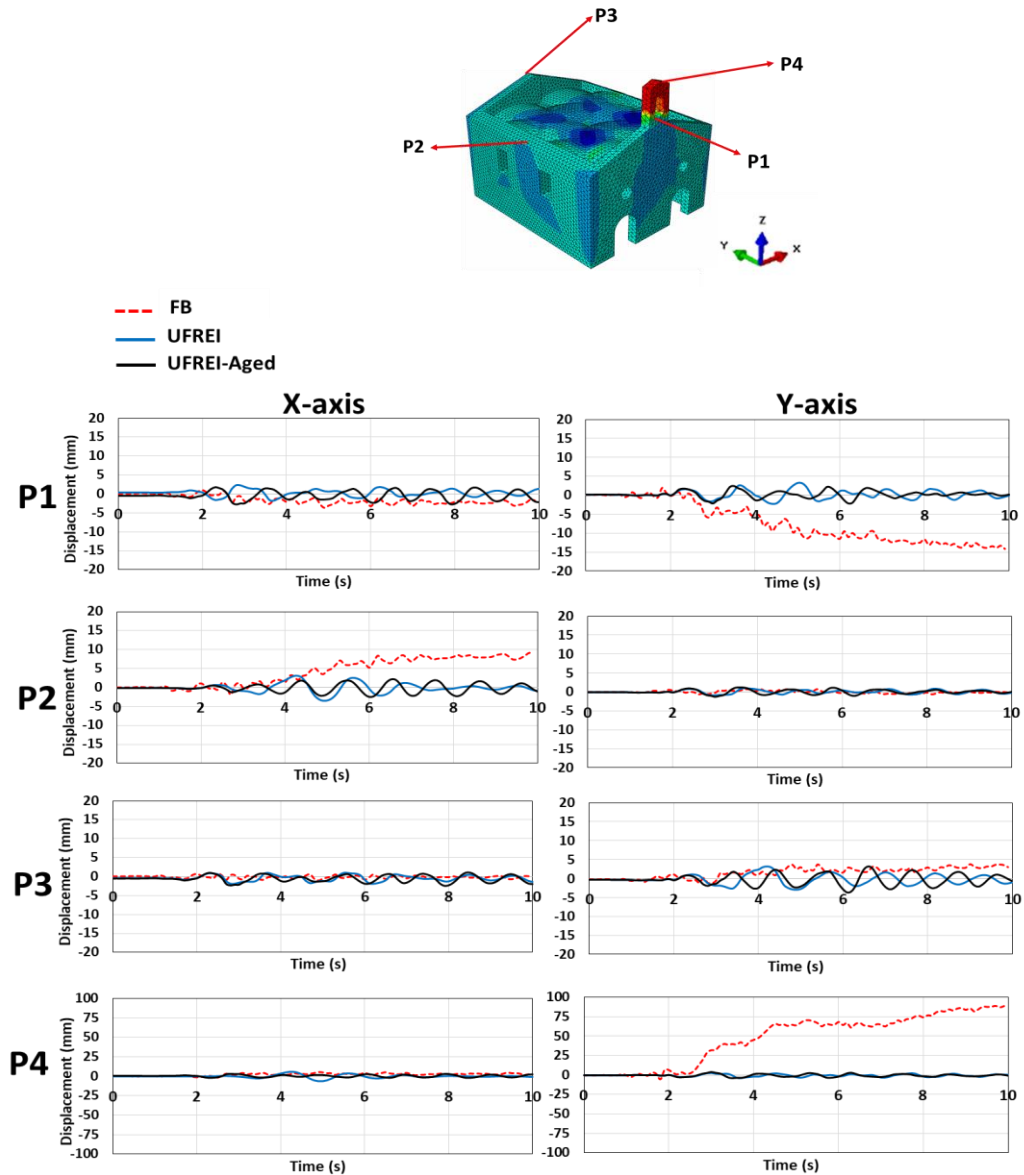

Fig. 8. 9 Displacement time history of different reference points in the longitudinal (Y) and transversal (X) directions obtained from non-linear dynamic analyses with PGA=0.25g for the fixed-base (FB) model and the base isolated (UFREI and UFREI-Aged) models
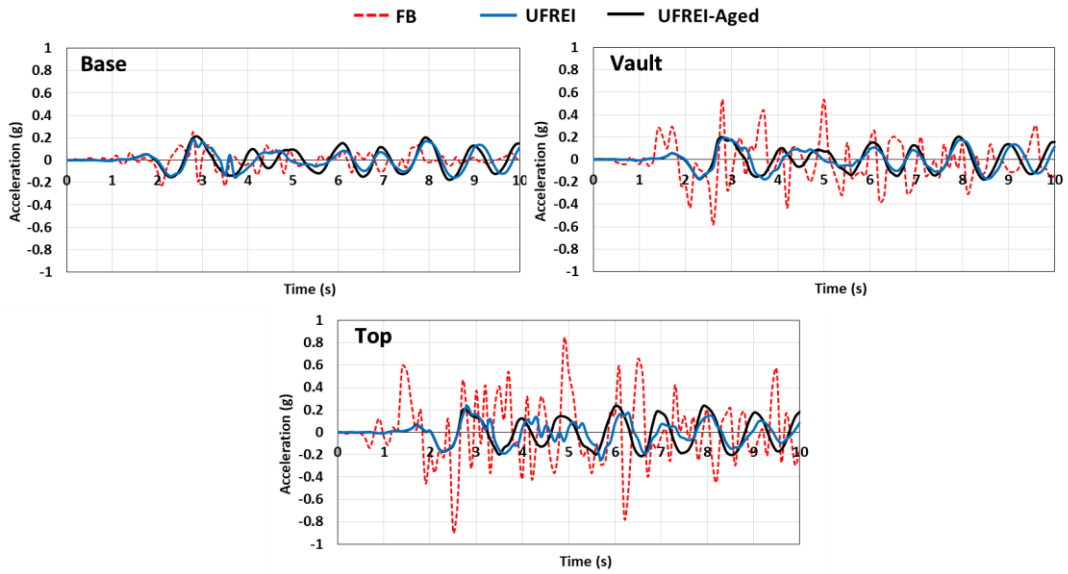
Fig. 8. 10 Acceleration time history of different reference points (base, vault and top level) in the transversal direction obtained from non-linear dynamic analyses with PGA=0.25g for the fixed-base (FB) model and the base isolated (UFREI and UFREI-Aged) models.
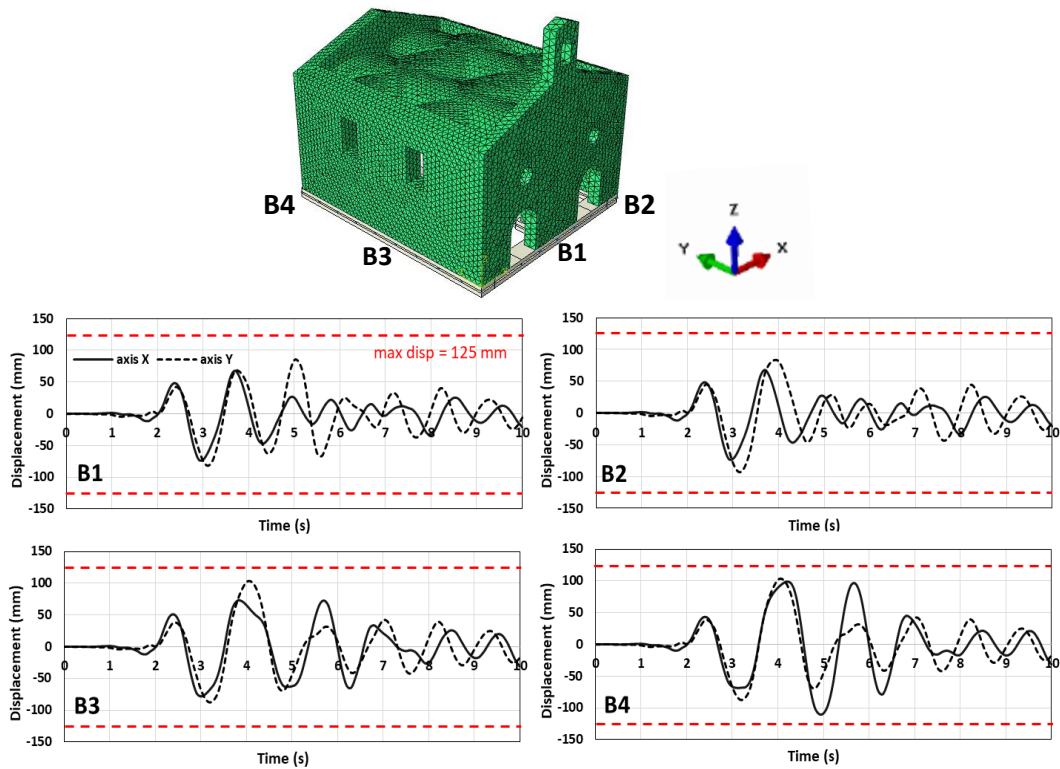

Fig. 8. 11 Displacement time history in the X and Y directions obtained from non-linear dynamic analyses with PGA=0.25g for four representative isolators UFREI.
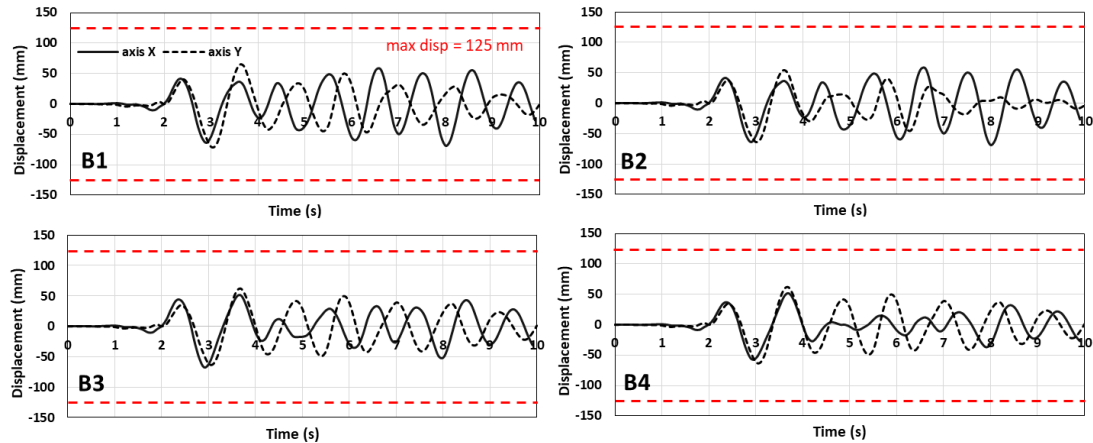
Fig. 8. 12 Displacement time history in the X and Y directions obtained from non-linear dynamic analyses with PGA=0.25g for four representative isolators UFREI-Aged.

8.6. Conclusions

A series of experimental test and numerical analyses were carried out to investigate the effect of aging on the UFREI isolation system applied on a historical masonry church. The experimentation includes uniaxial tensile test and relaxation tests on the rubber compounds used in the isolation system, taking into account the ageing effect. Rubber compound with the best performance after ageing is selected as the material of the UFREI system applied in a historical masonry church.

Based on the recorded ground motion, the performances of the UFREI system before and after ageing are compared. In general, there is no remarkable difference of the peak structure displacements between the UFREI and the Aged-UFREI models. The result shows that the acceleration responses of the two models, before and after ageing, are not significantly different. These results imply that the seismic response of the isolated church before and after ageing effect remains quite similar. However, remarkable differences are reported where the peak values of isolator displacements are reduced due to the increase of isolator stiffness after ageing. These results reveal that the requirement of rubber ageing resistance stated in the code is suitable to assure the durability of the isolation system undergoing ageing effect.

REFERENCES

[1] S. Lagomarsino, Damage assessment of churches after L'Aquila earthquake 2009. Bulletin of Earthquake Engineering 2012;10(1):73-92.
[2] Brandonisio G., Lucibello G., Mele E., De Luca A. Damage and performance evaluation of masonry churches in the 2009 L'Aquila earthquake. Engineering Failure Analysis 2013;34:693-714.
[3] Valente M., Barbieri G., Biolzi L. Seismic assessment of two masonry Baroque churches damaged by the 2012 Emilia earthquake. Engineering Failure Analysis 2017;79:773-802.

[4] Valente M., Milani G. Damage assessment and partial failure mechanisms activation of historical masonry churches under seismic actions: Three case studies in Mantua. Engineering Failure Analysis 2018;92:495-519.

[5] Choudhury T., Milani G., Kaushik H.B. Comprehensive numerical approaches for the design and safety assessment of masonry buildings retrofitted with steel bands in developing countries: The case of India. Construction and Building Materials 2015;85:227-246.

[6] Murtyl C.V.R., Dutta J., Agrawal S.K. Twin lintel belt in steel for seismic strengthening of brick masonry buildings. Earthquake Engineering and Engineering Vibration 2004;3:215-222.

[7] Milani G., Shehu R., Valente M. A kinematic limit analysis approach for seismic retrofitting of masonry towers through steel tie-rods. Engineering Structures 2018;160:212-228.

[8] Milani G., Shehu R., Valente M. Possibilities and limitations of innovative retrofitting for masonry churches: Advanced computations on three case studies. Construction and Building Materials 2017;147:239-263.

[9] Feng Y., Yi D., Bi Q. Seismic design analysis of the country masonry school buildings in the meizoseismal area. Earthquake Engineering and Engineering Vibration 2011;10:359-367.

[10] Barbieri G., Valente M., Biolzi L., Togliani C., Fregonese L., Stanga G. An insight in the late Baroque architecture: an integrated approach for a unique Bibiena church. Journal of Cultural Heritage 2017;23:58-67.

[11] Valente M., Milani G. Damage survey, simplified assessment, and advanced seismic analyses of two masonry churches after the 2012 Emilia earthquake. International Journal of Architectural Heritage 2018. https://doi.org/10.1080/15583058.2018.1492646

[12] Calabrese A., Spizzuoco M.C., Serino G., Della Corte G., Maddaloni G. Shaking table investigation of a novel, low-cost, base isolation technology using recycled rubber. Structural Control and Health Monitoring 2015;22:107-122.

[13] Toopchi-Nezhad H., Tait M.J., Drysdale R.G. Bonded versus unbonded strip fiber reinforced elastomeric isolators: finite element analysis. Composite Structures 2011;93:850-859.

[14] Das A., Deb S.K., Dutta A. Comparison of numerical and experimental seismic responses of FREI-supported un-reinforced brick masonry model building. Journal of Earthquake Engineering 2016;20: 1239-1262.

[15] Das A., Deb S.K., Dutta A. Shake table testing of un-reinforced brick masonry building test model isolated by U-FREI. Earthquake Engineering & Structural Dynamics 2016;45:253-272.

[16] Thuyet V.N., Deb S.K., Dutta A. Evaluation of horizontal stiffness of fibre-reinforced elastomeric isolators. Earthquake Engineering & Structural Dynamics 2017;46:1747-1767.

[17] Chiozzi A., Simoni M., Tralli A. Base isolation of heavy non-structural monolithic objects at the top of a masonry monumental construction. Materials and Structures 2016;49:2113-2130.

[18] Seki M., Miyazaki M., Tsuneki Y., Kataoka, K. A masonry school building retrofitted by base isolation technology. 12th World Conference on Earthquake Engineering 2000.

[19] Habieb A.B., Milani G., Tavio T. Two-step advanced numerical approach for the design of low-cost unbonded fiber reinforced elastomeric seismic isolation

systems in new masonry buildings. Engineering Failure Analysis 2018;90:380-396.

[20] Mishra H.K., Igarashi A., Matsushima H. Finite element analysis and experimental verification of the scrap tire rubber pad isolator. Bulletin of Earthquake Engineering 2013;11:687-707.

[21] Thuyet V.N., Deb S.K., Dutta A. Mitigation of seismic vulnerability of a prototype low-rise masonry building using U-FREIs. Journal of Performance of Constructed Facilities 2018;32(2):1-13.

[22] De Raaf M.G.P., Tait M.J., Toopchi-Nezhad H. Stability of fiber-reinforced elastomeric bearings in an unbonded application. Journal of Composite materials 2011;45:1873-1884.

[23] Eurocode 8: Design of structures for earthquake resistance-part 1: general rules, seismic actions and rules for buildings. 2005.

[24] S.N. Indonesia, Persyaratan Beton Struktural Untuk Bangunan Gedung, SNI 2847 2013.

[25] ISO. 37: 2011. Rubber, vulcanized or thermoplastic—Determination of tensile stress-strain properties. British Standards Institution: London, UK, 2011.

[26] Comite Europe en de Normalisation TC, 340, European Code UNI EN 15129: 2009 Anti-seismic devices, Brussels, 2009.

[27] T. Dalrymple, J. Choi and K. Miller, "Elastomer rate-dependence: A testing and material modeling methodology," in *172nd Technical Meeting of the Rubber Division of the American Chemical Society (ACS),* Cleveland, OH, Oct, 2007.

[28] Habieb A.B., Valente M., Milani G. Base seismic isolation of a historical masonry church using fiber reinforced elastomeric isolators. Soil Dynamics and Earthquake Engineering 2019: 120: 127-145.

[29] Simulia. ABAQUS 6.14 User's manual. Dassault Systems, Providence, RI, 2014.

[30] Habieb A.B., Valente M., Milani G. Implementation of a simple novel Abaqus User Element to predict the behavior of unbonded fiber reinforced elastomeric isolators in macro-scale computations. Bulletin of Earthquake Engineering 2019: 17(5): 2741-2766.

[31] Tiberti S., Acito M., Milani G. Comprehensive FE numerical insight into Finale Emilia Castle behavior under 2012 Emilia Romagna seismic sequence: damage causes and seismic vulnerability mitigation hypothesis. Engineering Structures 2016;117:397-421.

[32] Milani G., Valente M., Alessandri C. The narthex of the Church of the Nativity in Bethlehem: a non-linear finite element approach to predict the structural damage. Computers & Structures 2017, http://dx.doi.org/10.1016/j.compstruc.2017.03.010.

[33] Valente M., Milani G. Effects of geometrical features on the seismic response of historical masonry towers. Journal of Earthquake Engineering 2017, http://dx.doi.org/10.1080/13632469.2016.1277438.

[34] Habieb A.B., Milani G., Tavio T. Seismic performance of a masonry building isolated with low-cost rubber isolators. WIT Transactions on The Built Environment 2017;172:71-82.

[35] Pauletta, M., Di Luca, D., Russo, E., Fumo, C. Seismic rehabilitation of cultural heritage masonry buildings with unbonded fiber reinforced elastomeric isolators (U-FREIs)–A case of study. Journal of Cultural Heritage, 2018;32:84-97.

[36] Russo G., Pauletta M. Sliding instability of fiber-reinforced elastomeric isolators in unbonded applications. Engineering Structures 2013;48:70-80.

Chapter

9
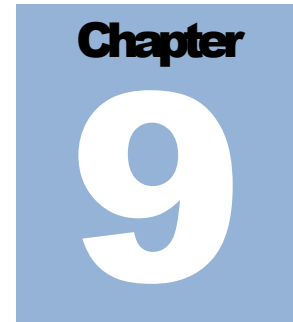
Conclusions and Recommendations

9.1. Conclusions

A series of experimental tests and numerical analyses were conducted to investigate the feasibility of reactivated EPDM rubber to fabricate fiber reinforced elastomeric isolators (FREIs). The proposed FREIs are implemented mainly in unreinforced masonry buildings to significantly improve their seismic response. The experimental part consists of the production of the recycled rubber using reactivated EDPM, the preparation of GFRP and fabrication of FREIs, and some rubber testing including hardness test, compression set, rheometer test, uniaxial tensile test, shear test, and relaxation test. The performances of the proposed isolation system implemented in various type of structures are investigated through finite element (FE) analyses based on the proposed user element model for FREIs developed by the author.

9.2.1 Experimental study

Regarding the results of the experimental study on the FREIs using reactivated EDPM, some conclusions can be drawn:

1. As discussed in Chapter 2, the vulcanization at 150°C seem to be the most optimum method when compared to other vulcanization temperature in producing the reactivated EDPM compound.

2. It is found that the ageing on rubber has the effect in increasing the stiffness and decreasing the viscousity of the rubber. In the same time, a slight increase of hardness after ageing indicates that additional crosslinking is provided during ageing process, increasing the vulcanization degree of the compound.

3. Rubber compound no. 4B (composition: Dutral 4038+regenerated EPDM type B) presents the most satisfactory results before and after aging. It approximates better the performance of the corresponding virgin material, Dutral 4038. Quite satisfactory result is provided by compound 2B (Vistalon 3666 + regenerated EPDM type B), which presents allowable variation of tensile strength and elongation at break after ageing.

4. In the compression set test, all rubber compounds satisfy the requirement of compression set for rubber seismic isolators, where all the thickness variations after compression test are less than 30%.

5. The relaxation test performed with 100% of strain and 40mm/s of strain rate results in the most accurate data used in predicting the damping behavior of the rubber through FE modeling.

6. In the production of the FREIs, the bonding between GFRP and rubber pad can be provided using cover-coat adhesive used in combination with an adhesive primer. After the vulcanization, hardness test is performed at several points on the sliced FREI specimen. The shore A hardness at the middle of the pad is found considerably lower than which near the edge of the pad. On the other hand, a rubber cube without GFRP presents an identical hardness at any point. It confirms that the presence of GFRP sheets isolates further the core of the samples. However, the variation of the hardness in the rubber core are still in the acceptable range. It indicates that the performed production method in fabricating FREIs is suitable to produce standardized industrial items.

7. The relaxation test performed with 100% of strain and 40mm/s of strain rate results in the most accurate data for predicting the damping behavior of the rubber through FE modeling.

9.2.2 Numerical study

Based on the results of the numerical study on the proposed FREIs implemented in several type of unreinforced masonry structures, some considerations ca be drawn:

1. The user element (UEL) model to predict the behavior of the unbonded FREIs discussed in chapter 3 present a good agreement with the available experimental data and with the detailed 3D FE model. Therefore, the proposed UEL model can be particularly suitable for 3D analyses of complex isolated structures through the software code Abaqus, with a significant computational efficiency.

2. The implementation of unbonded FREIs in a two-story residential unreinforced building is discussed in chapter 4. It has been found that, for the selected seismic zone, the proposed isolators significantly improved the seismic behavior: the structure resulted only moderately damaged whereas collapse was avoided, and so any casualty. In addition, the maximum deformations of isolators during seismic motion did not exceed the critical limit, so allowing the re-utilization of the isolation system.

3. The use of FREIs significantly reduces the cost of the isolation system due to the absence of thick steel plates for the supports. In particular, this research has investigated the unbonded FREIs behavior that is characterized by a marked non-linear range and hardening phase: the former allows for a decrease of the effective horizontal stiffness, thus reducing the seismic demand, while the latter plays an

important role in limiting the shear displacement of the isolation system under strong earthquakes.

4. As reported in chapter 5, FREI system can be effectively used to protect the small historical masonry church against severe seismic actions, reducing damage considerably. In the non-linear dynamic analyses with PGA=0.25g, the church does not present any significant damage for both unbonded and bonded FREIs. However, in the non-linear dynamic analyses with PGA=0.35g, some evident damage can be observed in the case of bonded FREIs, while only a very limited damage is registered in the case of unbonded FREIs. The analysis of the displacements of some reference points of the church shows that both the isolation systems significantly reduce the residual drifts of the different macro-elements.

5. Additional dissipative device such as shape memory alloy (SMA) wires can be suitably used in combination with the unbonded FREIs, as discussed in chapter 7. However, the application of SMA wires is only effective when a specific amount of pre-strain is applied to the wire.

6. The performances of the FREI system before and after ageing are compared in chapter 8. Rubber with sufficient resistance against ageing is used the model. There is no remarkable difference of the peak structure displacements between the FREI and the Aged-FREI models. The result shows that the acceleration responses of the two models, before and after ageing, are not significantly different. These results imply that the seismic response of the isolated church before and after ageing effect remains quite similar. However, remarkable differences are reported where the peak values of isolator displacements are reduced due to the increase of isolator stiffness after ageing. These results reveal that the requirement of rubber ageing resistance stated in the code is suitable to assure the durability of the isolation system undergoing ageing effect.

9.2. Recommendations

Regarding the limitation of the present doctoral thesis, the followings are some recommendations for the future works:

1. The experimental test on the prototypes of the FREI are continued.

2. It is interesting to investigate the ageing resistance of the GFRP itself and to develop a more detail numerical model of the FREI device, taking into account the ageing effect on the rubber and GFRP.

3. Tensile strength of the bonded FREI could be investigated to develop the numerical model considering the tensile damage of the device.

4. The fire resistance of the FREI device could be investigated.

5. Re-centering capability of the FREI device could be investigated.

6. The coupling behavior of the FREI in two-orthogonal direction should be investigated through an experimental test.